Analysis of discrete reaction-diffusion equations for autocatalysis and continuum diffusion equations for transport

by

Chi-Jen Wang

A dissertation submitted to the graduate faculty

in partial fulfillment of the requirements for the degree of

DOCTOR OF PHILOSOPHY

Major: Applied Mathematics

Program of Study Committee:
James Evans, Major Professor
Michael Smiley
Paul Sacks
Jue Yan
Alexander Roitershtein

Iowa State University
Ames, Iowa
2013

TABLE OF CONTENTS

Page

Page

Page

ACKNOWLEDGEMENTS

This dissertation is dedicated to my parents Chin-Shan Wang and Hung-Yu Chen, and my wife Yi-Hsiu Liu.

First of all, I would like to take this opportunity to express my sincere appreciation to my advisor Dr. Jim Evans for his excellent teaching, expert guidance and continuous encouragement throughout my graduate study. I always feel so comfortable and encouraged to discuss with him and love to learn from him.

Secondly, I would like to thank my committee members: Dr. Michael Smiley, Dr. Paul Sacks, Dr. Jue Yan and Dr. Alexander Roitershtein for their precious advice and suggestions. Also, I would like to give my thanks to our research group: Dr. Da-Jiang Liu, Dr. Xiaofang Guo, Dr. Yong Han, David Ackerman, and Jing Wang for their efforts and contributions to this work.

In addition, I would like to thank my friends at the ISU Math Department and the CrossRoad Baptist Church for everything they have done for me. Further, I would like to give my deepest appreciation to my parents, my brothers and sisters, my wife, and our children for their love, care, understanding, and patience throughout these years.

Finally, I am especially grateful for the beautiful land−IOWA and the beautiful island−TAIWAN.

This work was performed at the Ames Laboratory under contract number DE-AC02-07CH11358 with the U.S. Department of Energy.

ABSTRACT

We analyze both the spatiotemporal behavior of non-linear "reaction" models utilizing reaction-diffusion equations, and spatial transport problems on surfaces and in nanopores utilizing the relevant diffusion or Fokker-Planck equations.

The non-linear "reaction" models involve spatial discrete systems where "particles" reside at the sites of a periodic lattice: particles, X, spontaneously annihilate ($X \rightarrow \varnothing$) at a specified rate *p*, and are autocatalytically created given the presence of nearby pairs of particles ($\varnothing + 2X \rightarrow 3X$) at rates depending on the local configuration. [This reaction model is equivalent to a spatial epidemic model where sick individuals spontaneously recover ($S \rightarrow H$), and healthy individuals are infected by pairs of sick neighbors ($H + 2S \rightarrow 3S$).] The model exhibits a non-equilibrium phase-transition from a populated state to a vacuum state (with no particles) with increasing *p*. Near this transition, one can consider the propagation of interfaces separating the two states. Planar interfaces exhibit an orientation-dependence (leading to so-called generic two-phase coexistence), and curved interfaces enclosing droplets exhibit even richer behavior. These phenomena are analyzed utilizing the appropriate set of discrete reaction-diffusion equations (corresponding to lattice differential equations).

Diffusive transport of particles between islands or clusters of particles on a surface leads to coarsening of island arrays which can be analyzed by solution of an appropriate boundary value problem for the surface diffusion equation. We extend previous treatments to strongly anisotropic systems. Diffusion and passing of pairs of

overdamped Langevin molecules in narrow nanopores can be described by the appropriate Fokker-Planck equations (corresponding to a high-dimensional diffusion equation). We provide the first analysis of this problem focusing on a characterization of the propensity of passing as a function of pore diameter.

CHAPTER 1

GENERAL INTROCUTION

Background

In this thesis, we analyze both the spatiotemporal behavior of: (A) non-linear "reaction" models utilizing (discrete) reaction-diffusion equations; and (B) spatial transport problems on surfaces and in nanopores utilizing the relevant (continuum) diffusion or Fokker-Planck equations. Thus, there are some common themes in these studies, as they all involve partial differential equations or their discrete analogues which incorporate a description of diffusion-type processes. However, there are also some qualitative differences, as shall be discussed below.

In the first component (A) of these studies, the non-linear "reaction" models involve spatially discrete systems where "particles" reside at the sites of a periodic lattice or grid. In the most general models particles are added to (creation reaction), removed from (annihilation reaction), or shifted between (diffusive hopping) such sites. In the most basic model of interest here [1-4], particles, X, spontaneously annihilate ($X \rightarrow \varnothing$) at a specified rate p, and are autocatalytically created given the presence of nearby pairs of particles ($\varnothing + 2X \rightarrow 3X$) at rates which depend on the local configuration. See **Fig.1.** It is appropriate to note that this reaction model is equivalent to a spatial epidemic model where individuals reside in households which are distributed on a periodic grid (as in most towns); individuals can be either sick or healthy, and sick

individuals spontaneously recover (S→H) at rate *p*, and healthy individuals are infected by pairs of sick neighbors (H+2S→3S) at rates depending on the local configuration.

The basic reaction model exhibits a discontinuous non-equilibrium phase-transition from a populated state to a vacuum state (with no particles) with increasing *p* [4]. Near this transition, one can consider the propagation of interfaces separating the two states. Expansion of the vacuum state by displacement of the populated state would correspond to extinction of the reaction (or extinction of the particle population). [In the spatial epidemic analogue, the opposite situation of expansion of the infected state would correspond spreading of the epidemic as in the spread of the Black Death across Europe in the 12^{th} century.] In contrast to analogous phenomena in spatially continuous models, we find that the propagation of planar interfaces exhibits an orientation-dependence [4]. This leads to so-called generic two-phase coexistence [4-6], where each phase is stable against local perturbations by the other phase for a finite range of "control parameter" *p*. This behavior is in stark contrast to that for thermodynamic systems exhibiting discontinuous transitions where a fundamental principle of thermodynamics enforces the requirement that two states can only coexist (being equally or equi-stable) at a single point in parameter space.

Discontinuous phase transitions and associated nucleation phenomena (i.e., analysis of the formation of droplets of the more stable phase embedded in a less stable or metastable phase) have been studied for decades. These analyses have been performed almost exclusively for thermodynamic systems and often within a quasi-continuum framework. The general view from these studies is that there is a unique critical size

above which droplets grow and below which they shrink. However, for the discrete non-equilibrium model analyzed here, we find much richer behavior as a result of both generic two-phase coexistence and propagation failure. In the two-phase coexistence region, droplets always shrink (i.e., droplets of the populated state embedded in the vacuum state shrink, and also droplets of the vacuum state embedded in the populated state always shrink). Outside this region, sometimes entire families of stationary droplets exist as a direct consequence of propagation failure for planar interfaces.

Although not emphasized above, our discrete reaction model should be regarded as a stochastic Markov processes, particle creation and annihilation occurring "randomly" with specified rates. (More explicitly, each of these processes occurs stochastically according to an exponential waiting time distribution with mean waiting time determined by the relevant rate.) A precise determination of behavior can be achieved via kinetic Monte Carlo simulations. However, in this thesis we focus on analytic techniques in an attempt to provide a more fundamental understanding of behavior (although we caution that the analysis involves approximations). Specifically, exact behavior of the model can be described by master equations for the stochastic process, which we generally write in hierarchical form. These equations are most familiar for spatially homogeneous states. However, in this work we typically utilize the natural extension to spatially heterogeneous states (so we can assess interface formation and droplet dynamics). Exact analysis of the hierarchical equations is typically not possible. Thus, factorization approximations (which either completely neglect spatial correlations or introduce some approximations for these) are implemented to truncate or

close the hierarchy. For spatially heterogeneous states, this produces a set of set of discrete reaction-diffusion type equations [7] (which are typically referred to as lattice differential equations by the mathematical community [8]).

In the second component (B) of these studies, transport problems are analyzed (in the absence of reaction) which involve diffusion of atoms or molecules on surfaces or in nanopores. Spatially continuous (rather than discrete) models are utilized and thus analysis involves the appropriate (continuum) diffusion or Fokker-Planck equations. One class of problems involves diffusive transport of atoms on flat surfaces, whereas atoms attach and detach from two-dimensional (single atom high) islands or clusters of such atoms [9,10]. This leads to coarsening or ripening of island arrays since there is a bias for atoms to detach from smaller islands and attach to larger ones. Thus, larger islands tend to grow at the expense of smaller islands which shrink and disappear. This process is called Ostwald ripening (OR) [11]. Almost all previous studies of OR have been for isotropic systems where at least diffusion on the surface is isotropic (although islands may have non-circular shapes reflecting the crystallinity of the surface). We extend previous treatments to strongly anisotropic systems by analyzing the solution of an appropriate boundary value problem for the surface diffusion equation. In fact, a key advance is the use of appropriate non-traditional boundary conditions for these equations [12]. Our analysis successfully describes and elucidates experimental scanning tunneling microscopy (STM) observations for the Ag/Ag(110) system [13,14]. **Fig.2** provides an example of the type of analysis where we model island decay in this experimental system.

Another class of transport problems which we consider involves diffusion and passing of pairs of overdamped Langevin molecules [15] in narrow nanopores. See **Fig.3** for an example of passing versus separating spheres in a cylindrical pore. The propensity for reactant and product molecules to pass each other within the pores of catalytic nanoporous materials strongly impacts reaction yield [16,17]. For overdamped Langevin molecular dynamics, we describe the dependence of the passing propensity, P, on pore radius, R, including the scaling, $P \sim (R-R_c)^{\sigma}$, as $R \to R_c$ from above (where R_c the critical radius below which passing is sterically blocked). We find that the exponent, σ, is generally lower than transition state type theory predictions [18]. Precise numerical analysis of the Langevin [15] and equivalent Fokker-Planck [19] equations is provided for rotationally symmetric molecules. This facilitates development of a general picture for the dependence of passing propensity on molecular degrees of freedom including shape and rotational motion.

Thesis Organization

The main body of this dissertation is based on two published papers (Chapter 2 and 3), three additional contributions on a related topics (Chapter 4, 5 and 6) for reaction models. The last two chapters relate to transport studies. The first (Chapter 7) is a submitted paper and the second (Chapter 8) will soon be submitted.

Chapter 2 reprints the published paper “Schloegl's Second Model for Autocatalysis on a Cubic Lattice: Mean-Field-Type Discrete Reaction-Diffusion Equation Analysis”, by C.-J. Wang, X. Guo, D.-J. Liu and J.W. Evans in J. Stat. Phys.

144 (2011), 1308-1328. This paper gives a detailed description and analysis of generic two-phase coexistence on a cubic lattice.

Chapter 3 reprints the published paper "Schloegl's Second Model for Autocatalysis on Hypercubic Lattices: Dimension-Dependence of Generic Two-Phase Coexistence", by C.-J. Wang, D.-J. Liu and J.W. Evans in Phys. Rev. E 85, 041109 (2012). This paper extend Schloegl's second model in any dimension and gives an analysis of two-phase coexistence and artificial propagation failure as $d\to\infty$,

Chapter 4 focuses on the threshold version of Schloegl's second model. This version reveals analogous behavior to the basic model.

Chapter 5 presents a detailed discussion on the perturbations of Schloegl's second model. These refined models remove the quirk in the vertical interfaces but still reveal propagation failure behavior.

Chapter 6 studies discontinuous phase transitions and associated nucleation phenomena in Schloegl's second model. And we illustrate the behavior of stationary droplets inside and outside of the generic two-phase coexistence region.

Chapter 7 reprints a submitted paper "Analytic Formulations for One-Dimensional Decay of Rectangular Homoepitaxial Islands During Coarsening on Anisotropic fcc(110) Surfaces" by C.-J. Wang, Y. Han, H. Walen, S.M. Russell, P.A. Thiel, and J.W. Evans to Physical Review B. This paper provides an effective and instructive modeling tool capturing the basic features of 1D decay of islands in strongly anisotropic fcc(110) homoepitaxial systems.

Chapter 8 corresponds to the unpublished manuscript “Langevin and Fokker-Planck Analysis of Inhibited Molecular Passing Processes Controlling Reactivity in Nanoporous Catalytic Materials”. This paper gives a general picture for the behavior of molecular passing processes in narrow pores.

References

[1] F. Schloegl, Z. Phys. 253, 147 (1972).

[2] P. Grassberger, Z. Phys. B Cond. Matt. 47, 365 (1982).

[3] R. Durrett, SIAM Rev. 41, 677 (1999).

[4] D.-J. Liu, Xiaofang Guo, and J.W. Evans, Phys. Rev. Lett. 98, 050601 (2007).

[5] A.L. Toom, in Multicomponent random systems, edited by R.L. Dobrushin and Y.G. Sinai Marcel Dekker, New York, 1980).

[6] C.H. Bennett and G. Grinstein, Phys. Rev. Lett. 55, 657 (1985).

[7] C.-J. Wang, D.-J. Liu, and J.W. Evans, Phys. Rev. E 85, 041109 (2012).

[8] S.-N. Chow, J. Mallet-Paret, and E. S. Van Vleck, Int. J. Bifurc. Chaos 6, 1605 (1996).

[9] K. Morgenstern, Phys. Stat. Sol. (b) 242, 773 (2005) Feature Article

[10] P.A. Thiel, M. Shen, D.-J. Liu, and J.W. Evans, J. Phys. Chem. C 113, 5047 (2009) Feature Article

[11] W. Ostwald, “Lehrbuch der Allgemeinen Chemie” (Leipzig, Germany, 1896) Vol.2, Part 1.

[12] D. M. Ackerman and J. W. Evans, SIAM Multiscale Model. Simul. 9, 59 (2011).

[13] K. Morgenstern, E. Laegsgaard, I. Stensgaard, and F. Besenbacher, Phys. Rev. Lett. 83, 1613 (1999).

[14] Y. Han, S.M. Russell, A.R. Layson, H. Walen, C.D. Yuen, P.A. Thiel, and J.W. Evans, Phys. Rev. B, 87, 155420 (2013).

[15] I. Snook, "The Langevin and Generalized Langevin Equation Approach to the Dynamics of Atomic, Polymeric, and Colliodal Systems", (Elsevier, Amsterdam, 2007).

[16] C. Rodenbeck, J. Karger, and K. Hahn, J. Catal. 157, 656 (1995).

[17] D.M. Ackerman, J. Wang, and J.W. Evans, Phys. Rev. Lett., 108, 228301 (2012).

[18] D.S. Sholl, Chem. Eng. J. 74, 25 (1999).

[19] C.W. Gardiner, "Handbook of Stochastic Methods" (Springer, Berlin, 2002).

MRS Symp. Proc. Vol. 1423 (MRS, Pittsburgh, 2012) DOI: 10.1557/opl.2012.229

Figures

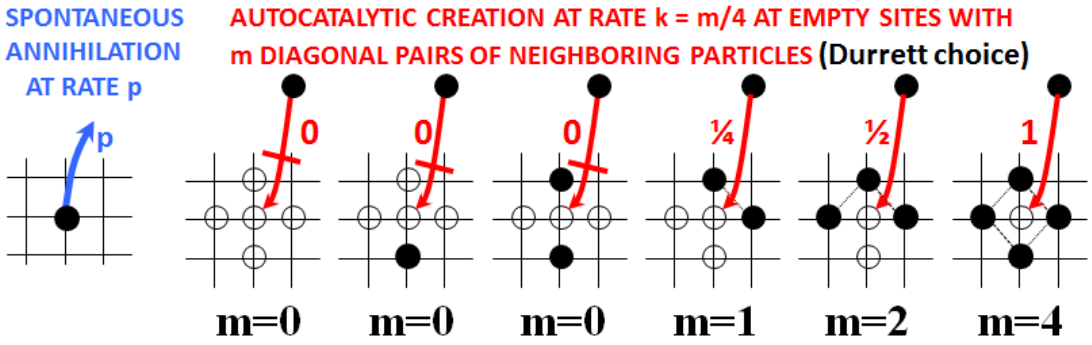

Fig.1. Schematic of the Durrett version of the basic reaction model including spontaneous annihilation of particles at rate p, and autocatalytic creation provided there is a suitable pair of neighboring particles.

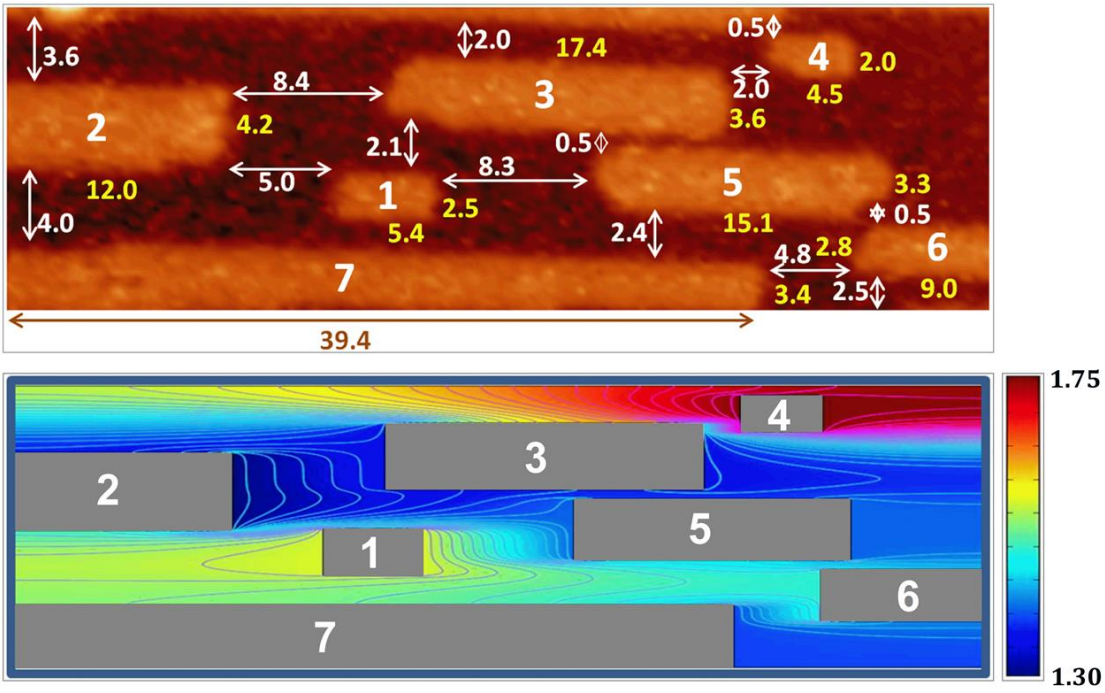

Fig.2. Top: Magnified STM image (50.0×15.5 nm2) for the local environment of the small narrow island decaying 1. Island dimensions are shown in yellow and separations in white (in nm). Bottom: FEMLAB results for the rescaled adatom density from our solution of the appropriate boundary value problem for the surface diffusion equation. The simulation cell has zero-flux boundary conditions at the outer edges.

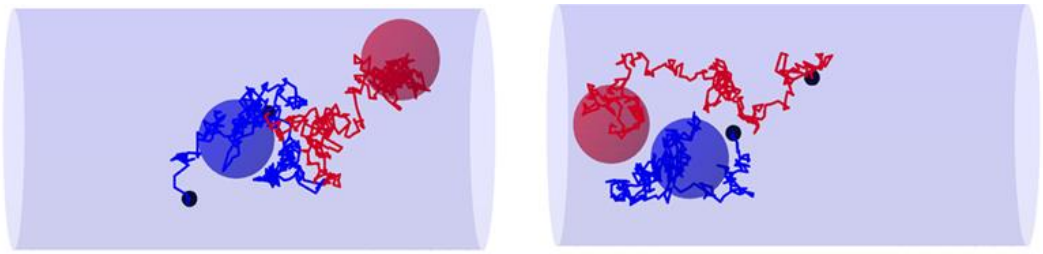

Fig.3. Simulated trajectories for separating spheres (left) and passing spheres (right) in a cylindrical pore for gap size equal to the particle diameter where passing probability 0.20.

CHAPTER 2

SCHLOEGL'S SECOND MODEL FOR AUTOCATALYSIS ON A CUBIC LATTICE: MEAN-FIELD-TYPE DISCRETE REACTION-DIFFUSSION EQUATION ANALYSIS

A paper published in *Journal of Statistical Physics*

Chi-Jen Wang,[1,2] Xiaofang Guo,[1,2,3] Da-Jiang Liu,[1] and J.W. Evans[1,2,3]

Ames Laboratory – USDOE[1] and Departments of Mathematics[2] and Physics & Astronomy[3], Iowa State University, Ames, Iowa 50011

Abstract

Schloegl's second model for autocatalysis on a hypercubic lattice of dimension $d \geq 2$ involves: (i) spontaneous annihilation of particles at lattice sites with rate p; and (ii) autocatalytic creation of particles at vacant sites at a rate proportional to the number of diagonal pairs of particles on neighboring sites. Kinetic Monte Carlo simulations for a $d=3$ cubic lattice reveal a discontinuous transition from a populated state to a vacuum state as p increases above $p=p_e$. However, stationary points, $p=p_{eq}$ ($\leq p_e$), for planar interfaces separating these states depend on interface orientation. Our focus is on analysis of interface dynamics via discrete reaction-diffusion equations (dRDE's) obtained from mean-field type approximations to the exact master equations for spatially inhomogeneous states. These dRDE can display propagation failure absent due to fluctuations in the stochastic model. However, accounting for this anomaly, dRDE

analysis elucidates exact behavior with quantitative accuracy for higher-level approximations.

Keywords

Schloegl's second model, Generic two-phase coexistence, Discrete reaction-diffusion equations, Interface propagation

1. Introduction

Stochastic lattice-gas "reaction" models prescribe kinetic rules and rates for the creation and annihilation of one or more types of species residing on a lattice [1]. Often, the reaction steps are cooperative, i.e., dependent on the local environment, and sometimes irreversible. Typically, no Hamiltonian is prescribed for the models, so the rates do not satisfy any detailed-balance conditions. These systems may evolve to non-equilibrium steady-states which are not characterized by an equilibrium Gibbs measure. Nonetheless, these non-equilibrium steady states can display phase transitions, as some control parameter is varied, somewhat analogous to those in equilibrium Hamiltonian systems [1]. Some progress has been made in elucidating such phenomena despite the lack of a thermodynamic free energy framework. The most extensive analysis has been directed towards characterization of universality associated with continuous transitions or critical points [1-3]. However, there have also been some investigations of discontinuous transitions [1,4-7], where issues of metastability and nucleation, and of the structure and dynamics of interfaces separating phases are of natural interest [8-11].

One surprising recent discovery was the occurrence of generic two-phase coexistence (2PC) associated with a discontinuous transition in a realization of Schloegl's second model involving spontaneous annihilation and autocatalytic creation of particles X on a square lattice [7,11]. 2PC means that the two distinct phases associated with the transition coexist and are stable for a finite range of annihilation rate. 2PC behavior was traced to an orientation-dependence of the value of the annihilation rate corresponding to a stationary planar interface separating the two phases. This contrasts phase coexistence at a unique point corresponding to equality of chemical potentials in an equilibrium Hamiltonian system. Such 2PC behavior had been observed and analyzed previously in Toom's model for voter dynamics where the kinetic rules have a broken symmetry, in contrast to Schloegl's second model [12,13].

The conventional mean-field formulation of a restricted version Schloegl's second model includes the mechanistic steps [7,11,14-18]:

$$X \rightarrow \varnothing \text{ (spontaneous annihilation @ rate p);}$$

$$2X \rightarrow 3X \text{ (autocatalytic creation).}$$

For the latter, nearby pairs of particles (2X) can create an additional particle. Off-lattice formulations include the autocatalytic annihilation process $3X \rightarrow 2X$ to avoid population explosion. However, in lattice versions considered here [7,11,18], particle creation requires an empty site, $\varnothing$, which automatically limits population growth, so autocatalytic particle creation might be better represented as $\varnothing + 2X \rightarrow 3X$. The lattice versions specify the rate of autocatalytic creation at an empty site as proportional to the number of

suitable pairs of particles on neighboring sites. Such models are also known as Quadratic Contact Processes (QCP) [18].

A mean-field (MF) rate equation treatment for either lattice or off-lattice versions reveals bistability, where a stable active populated steady-state and stable vacuum steady-state coexist over a range of smaller p>0. This feature is readily understood. The particle annihilation rate, $R_-(C) = pC$ is exactly linear in particle concentration, C. The particle creation rate has the qualitative non-linear non-monotonic form $R_+(C) \sim C^2(1-C)$ for lattice models where C=1 corresponds to a completely filled lattice. Thus, for large enough p, one has that $R_-(C) > R_+(C)$ for all C>0, and C=0 is the unique stable steady state. However, for smaller p, one has that $R_+(C) > R_-(C)$ for a range of intermediate C, leading to an additional stable populated state with C>0. Note that C=0 is always a stable absorbing "vacuum" state.

Bistability in a MF treatment is often the signature of a discontinuous transition in a stochastic model. Thus, given the MF bistability for this model and the discontinuous transition for a d=2 square lattice, one naturally expects that the model will also display a discontinuous transition and perhaps 2PC for a d=3 cubic lattice and for a d>3 dimensional hypercubic lattice. The current paper considers the case of a d=3 cubic lattice, although some of the formalism is developed for general d≥2.

In Sec.2, we provide a detailed description of our stochastic realization of Schloegl's second model on d≥2 dimensional hypercubic lattices. We present new Kinetic Monte Carlo (KMC) simulation results for d=3 and review previous results for d=2. In Sec.3, we present the exact master equations for spatially homogeneous states of

the model and perform MF and pair truncation approximation analyses. From these approximations to the master equations for spatially heterogeneous states, we develop discrete reaction-diffusion equations (dRDE) in Sec.5. The dRDE are used to assess the propagation of planar interfaces between active and vacuum states, specifically stationarity and propagation failure. This is done at the MF level in Sec.6, and for the pair approximation in Sec.7. The interpretation of the dRDE results and their relationship to exact behavior of the stochastic reaction model is described in Sec.7. Further discussion and conclusions are provided in Sec.8.

2. Model Prescription and KMC Simulation Results

Our lattice-gas realization of Schloegl's second model as a stochastic Markov process on a d-dimensional hyper-cubic lattice with sites labeled by $\underline{i} = (i_1, i_2, i_3,\ldots, i_d)$ generalizes Durrett's prescription [18] for a d=2 square lattice. It involves the following components: (i) spontaneous creation of particles at unoccupied sites at rate p; (ii) autocatalytic annihilation of particles at empty sites at rate k/k_{max}, where k is the number of "diagonal" pairs of particles on neighboring sites, and k_{max} is the maximum possible value. Such "diagonal" pairs neighboring the empty site $\underline{i}$ have one particle at one of $(i_1, i_2,\ldots, i_j\pm1,\ldots, i_d)$ and another at one of $(i_1, i_2,\ldots, i_k\pm1,\ldots, i_d)$ where $j\neq k$. The number of pairs of sites of any type selected from the 2d neighbors of an empty site satisfies $k_{tot} = (2d)(2d-1)/2! = d(2d-1)$, and the number of linear pairs is $k_{lin} = d$. Thus, the maximum number of diagonal pairs of particles satisfies $k_{max} = k_{tot} - k_{lin} = 2d(d-1)$, corresponding to the case where all 2d neighboring sites are occupied.

Consider a d=3 cubic lattice where k_{max}=12. If only n = 0 or 1 of the six neighboring sites of an empty site $\underline{i}$ are occupied, then k=0 and a particle cannot be created at $\underline{i}$. If n=2 non-adjacent neighbors are occupied, e.g., (i_1+1, i_2, i_3) and (i_1-1, i_2, i_3), then again k=0. If n=2 diagonally adjacent neighbors are occupied, then k=1 and a particle is created at rate 1/12. The different possibilities with k=0 (n=0, 1, or 2), k=1 (n=2), k=2 (n=3), k=3 (n=3), k=4 (n=4), k=5 (n=4), k=8 (n=5), or k=12=k_{max} (n=6) are enumerated in **Fig.1**.

Considering steady-state behavior for any d≥2, we expect that a stable populated steady-state exists for a range of "low" annihilation rates, $0 \le p \le p_e$. We describe this state as "active" since particles are continually created and annihilated. For higher $p>p_e$, only the particle-free "vacuum" state will exist as a stable state. However, a somewhat ill-defined metastable extension of the active state should also exist for a small range of $p_e<p<p_s$, where $p=p_s$ denotes the spinodal point [11,19]. Previous KMC simulation studies for d=2 revealed a discontinuous transition from the active state to the vacuum state at $p_e(d=2) = 0.09443$ [7] with $p_s(d=2) \approx 0.101$ [19]. New KMC simulations for a d=3 cubic lattice yield $p_e(d=3) = 0.13939$ with $p_s(d=3) \approx 0.15$. Similar to d=2 [7], we find 2PC for d=3 between the stable active and vacuum states for a finite range $p_f \le p \le p_e$ (see below), noting that the vacuum state exists for all p as an absorbing state. See **Fig.2**.

Another quantity of fundamental interest is the "equistability" value of $p=p_{eq}$ corresponding to a stationary planar interface separating active and vacuum states. In these models, one finds that p_{eq} depends on interface orientation, and that necessarily p_e

= max p_{eq} and p_f = min p_{eq} [7]. For a specific orientation, when $0 \le p < p_{eq}$, the active state is more stable and displaces the absorbing vacuum state leading to perpetual interface propagation. For $p_{eq} < p < p_e$, the vacuum state is more stable and displaces the active state leading to perpetual interface propagation. For $p_e < p < p_s$, the vacuum state displaces the metastable active state more quickly until the latter spontaneously converts to a vacuum state. See [11,19] and **Fig.2**.

One caveat to the above picture derives from a "quirk" in the reaction model. For a vertical interface corresponding to $i_1=0$, say, on a hypercubic lattice for any $d \ge 2$, the active state can *never* displace the vacuum state. This follows since empty sites within but at the edge of the vacuum state have at most one neighboring occupied site (and those in the interior have none). Thus, vertical interfaces are stationary for all $p \le p_{eq}$, but propagation of the vacuum state into the active state still occurs for $p > p_{eq}$.

Given the above observations regarding vertical interfaces, one might anticipate that p_{eq} would be the highest for interface orientations "furthest from vertical" where the active state can "most easily" displace the vacuum state. This has been confirmed for the d=2 square lattice. For a diagonal interface with (11) orientation, and for a vertical interface with (10) orientation, previous KMC simulation analysis yielded [7]

$$p_{eq}(10) = \min p_{eq} = p_f(d=2) = 0.0869, \text{ and}$$

$$p_{eq}(11) = \max p_{eq} = p_e(d=2) = 0.09443.$$

Correspondingly, for a d=3 cubic lattice, one might anticipate that a "skew" interface with (111) orientation would have the highest p_{eq}. Indeed, for this orientation,

for a diagonal interface with (110) orientation, and for a vertical interface with (100) orientation, our new KMC simulation analysis reveals that

$$p_{eq}(100) = \min p_{eq} = p_f(d=3) = 0.13529,$$

$$p_{eq}(110) = 0.13903, \text{ and}$$

$$p_{eq}(111) = \max p_{eq} = p_e(d=3) = 0.13939.$$

One could modify the rules for autocatalytic creation still within the framework of a Schloegl model of the second type to require only that the empty site has at least 2 occupied neighbors (i.e., to drop the diagonal pair constraint). The basic behavior of the model should be preserved (including the quirk), as already demonstrated for d=2 [20]. What motivates our specific choice of autocatalytic creation rates counting diagonal pairs of particles? This generalization of Durrett's specification of the QCP for d=2 [18] produces a simple universal d-independent form for the mean-field kinetics of the model. Furthermore, the choice has perhaps a deeper significance in enabling an exact simplification of the master equations, as described in Sec.3 and Appendix B.

As an aside, all KMC simulations described above were performed on finite lattice with periodic boundary conditions. In conventional constant-p ensemble simulations, processes are implemented with probabilities proportional to their rates. For any finite system, our reaction model must eventually evolve to the absorbing vacuum state. However, for large systems, this takes very long and constant-p simulations reach a quasi-steady state mimicking the true steady state of an infinite system. For analyses of equistability values of $p=p_{eq}$, we have implemented alternative and particularly effective

constant-concentration or constant-C ensemble simulations [7,11,21]. This analysis and further refinements for vertical interfaces will be discussed in detail elsewhere.

3. Master Equations: Spatially Homogeneous States

3.1 Exact master equations

For spatially homogeneous states on infinite lattices, the probability that a single site, or cluster of sites, is occupied is independent of location. The exact master equations for the reaction model can then be written in the form of an infinite coupled hierarchy for the evolution of the probability of a single filled site, a filled pair, etc. Equivalently, one can consider empty configurations. It will be convenient to introduce the following notation. Let x (o) denote a filled (empty) site, and let P's denote probabilities of various configurations of such sites. For example, P[x] = C (particle concentration) and P[x x] denote the probabilities of that a single site and that a neighboring pair is filled, respectively. Similarly, P[o] = 1-C and P[o o] denote the probability that a single site and neighboring pair are empty, respectively. Conservation of probability implies that P[x] + P[o] = 1, P[x o] + P[o o] = P[o], P[x x] + P[x o] = P[x], etc. Then, in terms of probabilities for empty configurations, the exact master equations have the form

$$d/dt\ P[o] = p \cdot P[x] - \{\text{autocatalytic particle creation terms}\}, \qquad (1)$$

$$d/dt\ P[o\ o] = 2p \cdot P[x\ o] - \{\text{autocatalytic particle creation terms}\}, \qquad (2)$$

with analogous equations for larger configurations of empty clusters.

The first gain terms in (1) and (2) correspond to spontaneous particle annihilation producing desired empty configurations. The second loss terms correspond to autocatalytic particle creation destroying the empty configurations under consideration, and come from summing over various relevant configurations multiplied by the appropriate rates. For a d=3 cubic lattice, these are shown in **Fig.1** for (1), and will be discussed below for (2). As an aside, we favor empty configurations in formulating (1) and (2) as all terms can be recast in terms of probabilities of connected empty configurations. This feature also applies for irreversible particle creation processes (without particle annihilation) with nearest-neighbor cooperativity [22].

Our choice for particle creation rates enables an exact reduction or simplification of the particle creation terms in these master equations. This exact reduction not only allows simple derivation of the universal mean-field kinetics, but also facilitates generation of higher-order approximations for the kinetics, as discussed below. One can show that the particle creation terms in (1) for P[o] (shown in **Fig.1** for d=3) sum exactly to $P\begin{bmatrix} x & \\ o & x \end{bmatrix}$, the probability of an empty site with a diagonal pair of particles on neighboring sites. See Appendix A. This leads to the simple and intuitive exact equation

$$d/dt\ P[o] = p \cdot P[x] - P\begin{bmatrix} x & \\ o & x \end{bmatrix} \qquad (3)$$

An analogous exact reduction is possible for the particle creation in (2) for P[oo] (shown in **Fig.3a** for d=3). See Appendix A. This yields the exact equation

$$d/dt\ P[o\ o] = 2p \cdot P[x\ o] - [4(d-1)/k_{max}]\, P\begin{bmatrix} & x & \\ o & o & x \end{bmatrix} - [4(d-1)(d-2)/k_{max}]\, P\begin{bmatrix} & x \\ o & \otimes \end{bmatrix}. \quad (4)$$

Here $P\begin{bmatrix} & x & \\ o & o & x \end{bmatrix}$ and $P\begin{bmatrix} & x \\ o & \otimes \end{bmatrix}$ represent probabilities of an empty pair where one site in this pair has a diagonal pair of particles on neighboring sites. The first is where one filled site forms a linear triple with the empty pair. The second where both filled sites form bent triples with the empty pair. These are shown in **Fig.3b** for a d=3 cubic lattice.

3.2 Approximations

The simplest *mean-field* (MF) *approximation* ignores all spatial correlations in occupancy of different sites and thus factors multi-site probabilities in terms of P[x] = C and P[o] = 1-C. Applying factorization directly to the exact equation (3), and noting that d/dt P[o] = -dC/dt yields the MF kinetic equation

$$d/dt\ C = -pC + C^2(1-C) = -C[p-C(1-C)] \equiv R(C), \qquad (5)$$

i.e., universal d-independent kinetics. Note that $R(C) = R_+(C) - R_-(C)$ corresponds to the difference in creation and annihilation rates described in Sec.1. Analysis of the steady-states of (5) yields

$$C(1-C) = p \text{ for populated state, or } C=0 \text{ for the stable vacuum state.} \qquad (6)$$

A stable active state is given by $C_{act}(MF) = 1/2 + 1/2(1-4p)^{1/2}$, revealing bistability for $0 \le p \le p_s(MF)$, where $p_s(MF) = 1/4$ denotes the MF spinodal point. The large discrepancy from the KMC estimates of p_s for d=2 and 3 is expected since MF treatments generally produce an artificially extended regime of bistability.

Next, we describe a more sophisticated *pair-approximation* where probabilities for configurations or triples (and larger clusters) of sites are factorized in terms of those for constituent pairs. For example,

$$P\begin{bmatrix} & x & \\ o & o & x \end{bmatrix} \approx P\begin{bmatrix} & x \\ o & \otimes \end{bmatrix} \approx P[o\ o]P[x\ o]^2/P[o]^2. \qquad (7)$$

It is convenient to introduce the conditional concentration, K = P[x o]/P[o], representing the probability of finding a particle next to a site specified empty. Then, one has that P[o o]/P[o] = 1-K. The pair approximation leads to the equations

$$d/dt\ P[o] = -p\ C + K^2(1-C) \qquad (8)$$

, and

$$d/dt\ P[o\ o] = 2K(1-C)[p - c_d\ K(1-K)], \qquad (9)$$

with $c_d = (d-1)/d$. Equations (8) and (9) can be rewritten as a closed pair of equations for C and K using that P[o] = 1-C and P[o o] = (1-C)(1-K).

A steady-state analysis yields the relations

$$pC - K^2(1-C) = 0 \text{ and } c_d\ K(1-K) = p \text{ for active states,} \qquad (10)$$

and C = K = 0 for the vacuum state. Note that (10) implies $K_{act}(pair) = c_dC/[1-(1-c_d)C]$ in contrast to K(MF) = C. More specifically, one has that $K_{act}(pair) = 1/2 + 1/2(1-4p/c_d)^{1/2}$ and then $C_{act}(pair)$ follows from (10). Also from (10), one finds that the bistability regime in the pair-approximation exists for $0 < p < p_s(pair)$, where

$$p_s(pair) = c_d/4 = (d-1)/(4d) \rightarrow p_s(MF) = 1/4, \text{ as } d\rightarrow\infty. \qquad (11)$$

Note also that $K_{act}(pair) \rightarrow C = K(MF)$, as $d\rightarrow\infty$. For a d=2 square lattice, $p_s(pair) = 1/8 = 0.125$ is fairly close to the KMC estimate of $p_s \approx 0.101$. For a d=3 cubic lattice, $p_s(pair)$

$= 1/6 = 0.166^{\bullet}$ is even closer to the KMC estimate of $p_s \approx 0.15$. This demonstrates the significantly improved accuracy of the pair-approximation relative to MF.

4. Master Equations: Spatially Inhomogeneous States

4.1 Exact master equations

For spatially inhomogeneous states, the probability that a site is occupied depends on its location. Thus, we let $P[o_{\underline{i}}] = P[o_{i1,i2,\ldots,id}]$ denote the probability that site $\underline{i} = (i_1, i_2,\ldots, i_d)$ is empty, etc. Then, $C_{i1,\, i2,\, \ldots,id} = P[x_{\underline{i}}] = 1 - P[o_{\underline{i}}]$ is the probability that site $\underline{i}$ is occupied. One can still write down an exact set of master equations in *hierarchical form* [22]. For the autocatalytic particle creation terms, now many of the configurations described for the homogeneous case are degenerate. For example, in the equation for $P[o_{\underline{i}}]$, there are now 2d distinct terms corresponding to particle creation with exactly 2d-1 particles neighboring the empty site, $\underline{i}$. These differ in the location the neighboring unoccupied site. In all these cases, one has $k = (2d-1)(d-1)$ so that a particle can be created with rate at $\underline{i}$ with $(2d-1)(d-1)/k_{max}$. Analogous to the case of homogeneous states, an exact reduction of these autocatalytic creation terms is possible. See Appendix A. One can also obtain equations for probabilities of adjacent pairs of empty sites, e.g., $P[o_{i1,i2,\ldots,id}\, o_{i1+1,i2,\ldots,id}]$, and for larger clusters of empty sites, accounting for gain and loss contributions due to particle annihilation and creation. Again, an exact reduction applies. See Appendix A. It should be noted that probabilities of pairs of empty sites with different orientations, as well as different locations, will in general have different values.

As an example, for a *d=3 cubic lattice*, one obtains the exact equation

$$d/dt\, P[o_{i1,\,i2,\,i3}] = p \cdot P[x_{i1,\,i2,\,i3}] - (1/12) \cdot \{ P\begin{bmatrix} x_{i1,\,i2\,+\,1,\,i3} & \\ o_{i1,\,i2,\,i3} & x_{i1\,+\,1,\,i2,\,i3} \end{bmatrix} + P\begin{bmatrix} o_{i1,\,i2,\,i3} & x_{i1\,+\,1,\,i2,\,i3} \\ x_{i1,\,i2\,-\,1,\,i3} & \end{bmatrix} + \ldots \} \tag{12}$$

where we have shown explicitly only 2 out of the 12 creation terms with different diagonal pairs of particles in sites neighboring $\underline{i} = (i_1, i_2, i_3)$. For interfaces with specific orientations, the $C_{i1,\,i2,\,i3}$ can be independent of some i_k or dependent only on certain combinations of them. Also, some probabilities for configurations of clusters of sites become identical. For example, for one class of vertical interfaces, one has that $C_{i1,\,i2,\,i3} = C_{i1}$ and the first two particle creation terms in (12) are equivalent. For the reaction model in general dimension d, one has an analogous equation to (12) but with k_{max} separate autocatalytic creation terms multiplied by the coefficient $1/k_{max}$. Similarly, one can develop equations for the probability of empty pairs $P[o_{i1,i2,i3}\, o_{i1+1,i2,i3}]$, etc.

4.2 Approximations: Discrete Reaction-Diffusion Equations (dRDE)

One can extend the *mean-field (MF) approximation* to treat spatially inhomogeneous states, again by simply ignoring all spatial correlations in occupancy of different sites. Thus, multi-site probabilities factor in terms of $P[x_{i1,i2,\ldots,id}] = C_{i1,i2,\ldots,id}$ and $P[o_{i1,i2,\ldots,id}] = 1\text{-}C_{i1,i2,\ldots,id}$ for various sites $\underline{i}$. Applying this procedure to (12) produces discrete reaction-diffusion (dRDE) type equations for d=3. In this case, the "diffusion" type terms are not due to particle hopping, but rather due to spatial coupling in the model which derives from cooperativity in particle creation. These type of dRDE have been developed and explored previously for other lattice-gas reaction models [23-25]. If one

refines the reaction model to include particle hopping to nearby empty sites, then this results in additional terms in the dRDE which have a conventional discrete diffusion form [11,19]. One can also extend the *pair-approximation* to treat spatially inhomogeneous states thereby obtaining sets of dRDE for the $C_{i1,i2,\ldots,id}$ and well as various pair quantities.

For a *d=3 cubic lattice* considered exclusively below, it is straightforward to write down the general form of the MF dRDE's starting from (12). A key component of this study is the use of these equations to analyze the propagation of planar interfaces between active and vacuum states for $0 < p < p_s(MF)$, and in particular to determine the stationary values of $p = p_{eq}$. We shall consider interfaces of general orientation such that $a\, i_1 + b\, i_2 + c\, i_3 = m$, where a, b, c, and m are integers. In this case, one has that $C_{i1,i2,i3} = C_m$ depends only on m. The MF dRDE's can then be conveniently recast as

$$d/dt\, C_m = -pC_m + (1/12)(1-C_m)h(m) \qquad (13a)$$

, where

$$h(m) = [C_{m-a} + C_{m+a}][C_{m-b} + C_{m+b}] + [C_{m-b} + C_{m+b}][C_{m-c} + C_{m+c}] + [C_{m-c} + C_{m+c}][C_{m-a} + C_{m+a}] \qquad (13b)$$

It is instructive to introduce a normalized discrete Laplacian

$$\Delta_{abc}C_m = (d_{abc})^{-2}\, \Delta C_m \text{ with } \Delta C_m = C_{m+1} - 2C_m + C_{m-1}. \qquad (14)$$

where d_{abc} denotes distance between adjacent planes m and m±1. Then, for the key low-index (a b c) = (100) "vertical", (110) "diagonal", and (111) "skew" orientations, (14) can be further rewritten in a particularly simple reaction-diffusion equation type form

$$d/dt\, C_m = R(C_m) + D(C_m)\, \Delta_{abc}C_m + f_{abc}\, (1-C_m)\, (\Delta_{abc}C_m)^2, \qquad (15)$$

where again $R(C) = -pC+C^2(1-C)$ describes the MF kinetics, and $D(C) = C(1-C)/3$ is an effective diffusion type coefficient. Also, one has that $d_{100} =1$, $d_{110} =\sqrt{2}$, and $d_{111} =\sqrt{3}$, and $f_{100} =0$, $f_{110} = 1/48$, and $f_{111} = 1/36$.

The dRDE from the pair-approximation for the $C_{i1,i2,i3}$ and well as various pair quantities are given in Appendix B. The complex form of these equations is similar to those analyzed previously for a d=2 square lattice [23]. Predicted behavior should be qualitatively similar to the MF dRDE, but quantitatively more accurate.

5. Discrete RDE Analysis: d=3 Mean-Field Results

We consider the evolution of planar interfaces between the active and vacuum states with orientation corresponding to constant $m = a\ i_1 + b\ i_2 + c\ i_3$ for the reaction model on a *d*=3 *cubic lattice*. Results presented below are obtained from numerical integration of various forms of the MF dRDE's (13). The initial data corresponds to a sharp interface with the active state $C_m = C_{act} = 1/2 + 1/2(1-4p)^{1/2}$ on the left $m<m^*$ and the vacuum state on the right $C_m = 0$ for $m>m^*$. The interface location is determined the center of mass, $\langle m \rangle = \sum_m C_m/C_{act}$ for a large finite system of ~1000 sites. The asymptotic interface velocity, $V(p) = d/dt \langle m \rangle$, for large t is determine by integrating the dRDE's up to time $t \approx 4\times10^4$. Note that, e.g., $V(p) < 0$ corresponds to the vacuum state displacing the active state, a scenario which occurs for larger p (but with $p<p_s$). These MF results will be summarized again and compared with KMC results in Sec.7.

Our focus is on assessing variation of V(p) versus p to determine stationarity and propagation failure. Since these features correspond to time-independent steady-states of

the dRDE's, one could anticipate that direct analysis is possible without consideration of interface evolution. This can be achieved using iterated map techniques described in Appendix C. Results are consistent with those from numerical integration of (13), but the latter also have the advantage of characterizing the dependence of V(p) on p.

5.1 Skew (111) orientation

In this case (a=b=c=1), one has that $m = i_1+i_2+i_3$ and $d_{111} = \sqrt{3}$. Analysis of (13) with $f_{111}=1/36$ reveals a unique MF stationary point $p_{eq}(111) = 0.211377 \pm 10^{-6}$. For $0 < p < p_{eq}(111)$, the active state displaces the vacuum state and $V(p)>0$. For $p_{eq}(111) < p < p_s(MF)=1/4$, the vacuum state displaces the active state and $V(p)<0$. See **Fig.4a**. The form of stationary interface is shown in **Fig.4d**. Deviating from a skew (111) orientation produces continuous deviations from the above behavior with p_{eq} shifting to lower values.

5.2. Diagonal (110) and near-diagonal orientations

The diagonal case (a=b=1, c=0) has $m = i_1+i_2$ and $d_{110} = \sqrt{2}$. Analysis of (13a)-(13b) with $f_{110} = 1/48$ reveals MF propagation failure for $p_-(110) < p < p_+(110)$, where $p_-(110) = 0.21023$ and $p_+(110) = 0.21037$. For $0 < p < p_-(110)$, the active state displaces the vacuum state and $V(p)>0$. For $p_+(110) < p < p_s(MF)=1/4$, the vacuum state displaces the active state and $V(p)<0$. See **Fig.4b**. The form of the stationary interface roughly in the middle of the propagation failure regime is shown in **Fig.4e**. Interface motion for p

just above $p_+(110)$ and just below $p_-(110)$ exhibits a stop-and-go motion. See **Fig.5a-b**. The waiting period, $\tau^{\pm}$, between jumps of distance $\delta m=1$ scales like

$$\tau^{\pm}(p) \sim |p - p_{\pm}(110)|^{-n\pm} \text{ as } p \to p_{\pm}(110), \text{ where } n_+ = 1.56 \text{ and } n- = 1.68, \qquad (16)$$

outside the region of propagation failure. Corresponding velocity scaling is determined from $V(p) \sim 1/\tau^{\pm}(p)$. Note that this scaling is only achieved for p very close to $p_{\pm}(110)$. See **Fig.5c**. Such non-analytic behavior is familiar from previous studies of propagation failure for dRDE's where the specific form is known to depend on the detailed structure of the dRDE [26,27].

Deviation from a diagonal orientation with rare steps. Orientations defined by $S(i_1+i_2)\pm i_3=m$ with large S correspond to a diagonal interface $i_1+i_2=0$ misoriented by occasional horizontal steps separated by S lattice constants vertically. See **Fig.6a**. If $p_{eq}(S)$ denotes the stationary value of p, then numerical analysis reveals the MF result $p_{eq}(110H) = \lim_{S\to\infty} p_{eq}(S) = 0.21030$. This limiting value corresponds to stationarity of an isolated horizontal step on a diagonally oriented interface. See Table 1 and Sec.7 for further discussion. Note that $p_{eq}(110H) \approx 1/2[p_-(110) + p_+(110)]$ lies close to the center of the regime of propagation failure for diagonal interfaces.

One can consider slight deviations from a diagonal orientation in other directions producing differently oriented far-separated steps. For example, analysis for orientations defined by $S(i_1+i_2)+i_2=m$, corresponds to a diagonal interface misoriented by occasional vertical double steps. This yields a limiting MF p_{eq} as $S\to\infty$ of $p_{eq}(110D) =0.21029$, very close to $p_{eq}(110H)$.

5.3 Vertical (100) and near-vertical orientations

The vertical case (a=1, b=c=0) has m = i_1 and d_{100} =1. Analysis of (13a)-(13b) with f_{100} =0 reveals MF propagation failure for $p < p_{eq}(100) = 0.21038$. This feature which mimics exact behavior is clear from the structure of the MF dRDE. For $p_{eq}(100) < p < p_s(MF)=1/4$ the vacuum state displaces the active state and V(p)<0. See **Fig.4c**. The interface for p just above $p_{eq}(100)$ exhibits a stop-and-go motion. See **Fig.5d-e**. The waiting time, τ, between jumps of distance δm=1 scales like

$$\tau(p) \sim [p - p_{eq}(100)]^{-n}, \text{ as } p \to p_{eq}(100)+ \text{ with } n=1.98, \qquad (17)$$

and velocity behavior follows from and $V(p) \sim 1/\tau(p)$. See **Fig.5f**.

Deviation from a vertical orientation with rare horizontal or vertical steps. Orientations defined by $Si_1+i_2=m$ with large S correspond to a vertical interface $i_1=0$ misoriented by occasional horizontal steps separated by S lattice constants vertically. See **Fig.6b**. If $p=p_{eq}(S)$ corresponds to stationarity, then numerical analysis reveals the MF result $p_{eq}(100H) = \lim_{S\to\infty} p_{eq}(S) = 0.20602$ which is strictly below the MF $p_{eq}(100) = 0.21038$. This limiting value corresponds to stationarity of an isolated horizontal step on a vertical interface. See Table 2 and Sec.7 for further discussion.

Deviation from a vertical orientation with rare diagonal steps. Orientations defined by $Si_1+i_2+i_3=m$ with large S correspond to a vertical interface i=0 misoriented by occasional diagonal steps separated by S lattice constants vertically. See **Fig.6c**. If stationarity occurs for $p=p_{eq}(S)$, then numerical analysis reveals the MF result $p_{eq}(100D) = \lim_{S\to\infty} p_{eq}(S) = 0.20605$ which is again strictly below the MF $p_{eq}(100) = 0.21038$. See Table 3 and Sec.7 for further discussion. This limiting value corresponds to stationarity

of an isolated diagonal step on a vertical interface. We note, however, that p_{eq}(100D) is above p_{eq}(100H), a feature reminiscent of behavior for the reaction model on a d=2 square lattice where the value of p for a stationary diagonal interfaces is above that for a horizontal interface [7,22].

6. Discrete RDE Analysis: d=3 Pair Approximation Results

Again, we consider the evolution of planar interfaces between the active and vacuum states with orientation corresponding to constant $m = a\, i_1 + b\, i_2 + c\, i_3$ for the reaction model on a *d*=3 *cubic lattice*. Results presented below are obtained from numerical integration of the dRDE's obtained in the pair approximation as described in Appendix B. The initial data corresponds to a sharp interface with the active state on the left $m<m^*$ with site occupations $C_m = C_{act}$(pair) and pair occupations obtained from $K_{act}(pair) = 1/2 + 1/2(1-p/6)^{1/2}$. The vacuum state on the right for $m>m^*$ with $C_m = 0$ and vanishing pair occupations. The interface location, $\langle m \rangle = \sum_m C_m/C_{act}$, and velocity, $V(p) = d/dt \langle m \rangle$, for large t are determined by integrating the dRDE's for a large finite system of ~1000 sites up to time $t \approx 4\times10^4$. These results will be summarized again and compared with KMC results in Sec.7.

6.1 Skew (111) orientation

Analysis of the dRDE for the pair approximation reveals a unique stationary point $p_{eq}(111) = 0.142942\pm10^{-6}$. For $0 < p < p_{eq}(111)$, the active state displaces the vacuum state and $V(p)>0$. For $p_{eq}(111) < p < p_s(pair)=1/6$, the vacuum state displaces the

active state and V(p)<0. Deviating from a skew (111) orientation produces continuous deviations from the above behavior with p_{eq} shifting to lower values. This behavior is entirely analogous to the MF predictions.

6.2 Diagonal (110) orientation

Analysis of the pair approximation dRDE reveals a unique stationary point $p_{eq}(110) = 0.142508 \pm 10^{-6}$. For $0 < p < p_{eq}(110)$, the active state displaces the vacuum state and V(p)>0. For $p_{eq}(110) < p < p_s(\text{pair})=1/6$, the vacuum state displaces the active state and V(p)<0. Note that the narrow regime of propagation failure observed in the MF treatment has disappeared in the pair approximation.

6.3 Vertical (100) and near-vertical orientations

Analysis of the pair approximation dRDE reveals propagation failure for $p < p_{eq}(100) = 0.14123$. This feature which mimics exact behavior is clear from the structure of the pair dRDE. For $p_{eq}(100) < p < p_s(\text{pair})=1/6$, the vacuum state displaces the active state and V(p)<0. The interface for p just above $p_{eq}(100)$ exhibits a stop-and-go motion.

Deviation from a vertical orientation with rare steps. Orientations defined by $Si_1+i_2=m$ with large S correspond to a vertical interface i=0 misoriented by occasional horizontal steps. See **Fig.6b**. If $p_{eq}(S)$ denotes the stationarity value of p, then numerical analysis reveals that $p_{eq}(100H) = \lim_{S\to\infty} p_{eq}(S) = 0.1391$ which is strictly below the $p_{eq}(100) = 0.14123$ for the pair approximation. This limiting value corresponds to stationarity of an isolated horizontal or vertical step on a vertical interface. See Table 4

and Sec.7 for further discussion. One can of course consider deviations from a vertical interface with rare steps of other orientations. From analysis above at the MF level, we anticipate only a weak dependence of the stationarity on this step orientation the pair level, so that, e.g., $p_{eq}(100D) \approx 0.1391$ for rare diagonal steps in the pair approximation.

7. Relating dRDE and KMC Resluts

Mean-field (MF) type treatments of stochastic lattice-gas models with discontinuous transitions are expected to predict bistability. One must perform a Maxwell construction to locate the transition for equilibrium models, or a kinetic analogue of this construction for non-equilibrium steady-states of reaction models. A kinetic Maxwell construction follows from applying MF type dRDE's to determine the condition for stationary interfaces between coexisting phases. In general, such an analysis for lattice models would predict an orientation dependence of the stationary point, a feature not seen in traditional equilibrium Hamiltonian systems. However, for Schloegl's second model, such orientation dependence does occur and underlies 2PC. Thus, the MF-type dRDE do produce at least qualitatively the appropriate behavior. However, these dRDE can also produce propagation failure not seen in the stochastic lattice-gas models. Thus, the correspondence of behavior in MF-type dRDE to that in the stochastic model not transparent. However, we show here that an appropriate correspondence can be made, as is summarized schematically in **Fig.7**.

For a detailed correspondence between MF-type dRDE predictions and stochastic reaction model behavior for the d=3 cubic lattice, it is instructive to focus on the three

principal orientations (skew, diagonal, and vertical) and nearby orientations. For *skew* (111) *interfaces*, the situation is unambiguous as there is no propagation failure for the MF-type dRDE, so the predicted stationary $p_{eq}(111)$ corresponds to that in the stochastic model. A large discrepancy occurs at the MF level (as expected), but there is good agreement between $p_{eq}(111) \approx 0.14294$ (pair approx.) and $p_{eq}(111) \approx 0.13939$ (KMC).

For *diagonal* (110) *interfaces*, the lowest MF-level treatment predicts "artificial" propagation failure not seen in the stochastic model. One could argue that fluctuations in the stochastic model mean that one never has a perfectly flat (110) interface as in MF treatments, but rather an interface with steps. From this perspective, the condition for stationarity of a slightly misoriented (110) interface in the MF treatment would better reflect the situation in the stochastic model. Thus, one might identify the (almost identical) MF $p_{eq}(110H)$ or $p_{eq}(110D)$ with the KMC $p_{eq}(110)$. Significantly, propagation failure disappears at the pair-level treatment, and we unambiguously identify $p_{eq}(110) \approx 0.14251$ (pair approx.) with $p_{eq}(110) \approx 0.13903$ (KMC).

Finally, for *vertical* (100) *interfaces*, recall that propagation failure is expected for p below some critical value as the active state cannot displace the vacuum state for any $p \geq 0$. This feature applies to both the stochastic model and to various MF-type dRDE's. However, we claim that $p_{eq}(100)$ from the MF or pair approximation does <u>not</u> correspond to the KMC $p_{eq}(100)$ since MF type formulations "artificially extend" the regime of propagation failure. Analogous to the discussion of diagonal interfaces, we argue that fluctuations in the stochastic models always produce a roughened (100) interface with steps, a feature not reflected in MF-type analysis of a perfectly vertical

interface. Thus, p_{eq} for stationarity of a slightly misoriented (100) interface in the MF-type treatments better reflects the KMC $p_{eq}(100)$. Specifically, we identify $p_{eq}(110D)$ from MF or pair approximations, which corresponds to stationarity of a (100) interface with rare diagonal steps, with the KMC $p_{eq}(110)$. Why? If $p_{eq}(100H) < p < p_{eq}(100D)$, 2D vacuum islands in the layer adjacent to the vacuum state might initially expand their horizontal and vertical steps, but then they will convert to a shrinking diamond shape bordered by diagonal steps. Thus, $p > p_{eq}(100D)$ is required for expansion of the vacuum state. A large discrepancy occurs between these quantities at the MF level (as expected), but there is good agreement between $p_{eq}(100D) \approx 0.1391$ (pair approx.) and $p_{eq}(100) \approx 0.1353$ (KMC).

In the above picture, the extent of *artificial propagation failure* (*apf*) for vertical interfaces in MF-type treatments is measured by $\Delta p_{apf}(100) = p_{eq}(100) - p_{eq}(100D)$. This difference decreases from $\Delta p_{apf}(100) = 0.0044$ for the MF treatment to $\Delta p_{apf}(100) = 0.0021$ for a pair treatment. This trend is reminiscent of the disappearance of artificial propagation failure for (110) interfaces going from the MF to the pair treatment.

Finally, we summarize the effectiveness of MF-type dRDE analysis. While absolute values of various stationary points are dramatically shifted from KMC values at the lowest MF level, there is only a slight shift at the pair level. Furthermore, considering only the relative positions of these stationary points and the extent of 2PC regime, trends are already described in the MF treatment. Specifically, consider KMC values for $\Delta p_{eq}(111\text{-}110) = p_{eq}(111)\text{-}p_{eq}(110)$, $\Delta p_{eq}(110\text{-}100) = p_{eq}(110)\text{-}p_{eq}(100)$, and the sum of these $\Delta p_{eq} = p_{eq}(111)\text{-}p_{eq}(100)$ corresponding to the width of the 2PC regime. In

Table 5, these quantities are compared with the corresponding MF-type predictions. This comparison demonstrates the success of our MF-type dRDE analysis, especially at the pair-level, in capturing exact KMC behavior.

8. Conclusions

Our stochastic lattice-gas realization of Schloegl's second model for autocatalysis on a d=3 cubic lattice exhibits generic 2PC associated with an orientation dependence of the stationary point for planar interfaces separating coexisting active and vacuum states. We have demonstrated that dRDE associated with MF-type approximations to the master equations for spatially non-uniform states of the reaction model are effective in capturing and elucidating this behavior. The higher-order pair-approximation exhibits quantitative predictive capability.

A broader range of phenomena could be analyzed for the dRDE associated with our reaction model on a d=3 cubic lattice. Just considering time-independent solutions, in addition to stationary planar interfaces, one could consider "critical" planar, tubular, or droplet like perturbations from uniform states. Consider "planar" solutions to the dRDE for a d-dimensional hypercubic lattice where $C_{i1,i2,i3}$ depends only on $m = a\, i_1 + b i_2 + c\, i_3$. For p below the corresponding p_{eq}, the active state is more stable in the sense that it displaces the vacuum state separated by an appropriately oriented planar interface. However, a "small localized perturbation" with non-zero particle population of the vacuum state will not necessarily grow, but rather shrink. There is a critical size and profile (which is a stationary solution) above which growth and spreading occurs

[23,28]. Likewise, one can consider critical planar perturbations of the active state for $p_{eq} < p < p_s$. Furthermore, one could explore stationary solutions where $C_{i1,i2,i3} = C_{i1,i2}$ is independent of i_3, say, which correspond to a critical tubular perturbation deviating from a uniform stable state for a restricted range of i_1 and i_2. There are also stationary solutions correspond to critical droplets and where $C_{i1,i2,i3}$ deviates from a uniform stable state only in a region localized in d=3. Preliminary investigations reveal a rich phenomenology.

Finally, it is appropriate to comment on whether the phenomenology and dRDE methodology discussed here apply for broader classes of reaction models. As noted in Sec.1, previous analysis of Schloegl's second model on a d=2 square lattice [23,29] reveals analogous behavior to d=3. MF-type dRDE analysis shows that diagonal (11) interfaces exhibit no propagation failure so, e.g., $p_{eq}(11) = 0.1083$ (pair approx.) corresponds to $p_{eq}(11) = 0.0944$ (KMC). MF dRDE analysis for near-vertical interfaces with slope S shows that $\lim_{S\to\infty} p_{eq}(S)$ (= 0.1056 in the pair approximation) lies strictly below $p_{eq}(10)$ (= 0.1060 in the pair approximation) for an exactly vertical interface. The former corresponds to the p-value where an isolated kink on a vertical interface is stationary, and we associate this value with the KMC $p_{eq}(10) =0.0869$.

We can also extend Schloegl's second model in any dimension to include particle hopping to adjacent empty sites [11,19] and/or spontaneous particle creation [7,30]. Generic 2PC and orientation dependence of interface propagation is preserved at least for small hop rate or creation rate, and this behavior has been successfully described by MF-type dRDE including hopping [19]. We have speculated that 2PC phenomenon

could be quite general for non-equilibrium lattice-gas reaction models exhibiting discontinuous phase transitions. However, additional studies are required to support this claim. The Ziff-Gulari-Barshad (ZGB) model is a well-known two-species monomer-dimer reaction model which exhibits a discontinuous transition [4], although there is some debate about the detailed nature of the transition [5,6]. Stationarity or equistability of coexisting phases in the ZGB model has been assessed for this model via MF-type dRDE of the type described here [24]. Previous limited analysis of interface propagation for the ZGB model and its generalizations with particle hopping [8,9] have not reported orientation dependence or 2PC. However, further detailed analysis is required.

Acknowledgements

This work was supported by the Division of Chemical Sciences (Basic Energy Sciences), U.S. Department of Energy (USDOE) through the Ames Laboratory Chemical Physics and PCTC projects. Ames Laboratory is operated for the USDOE by Iowa State University under Contract No. DE-AC02-07CH11358.

Appendix A: Exact Reduction in Hierarchical Master Equations

Consider general spatially inhomogeneous states of the reaction model on a d-dimensional hypercubic lattice. For the loss terms due to particle creation in the rate equation for $P[o_{\underline{i}}] = P[o_{i1,i2,\ldots,id}]$, we enumerate all configurations of neighboring sites which include a *specific diagonal pair* of particles: (i) One such configuration has all other 2d-2 neighboring sites empty so k=1, yielding a creation rate of $1/k_{max}$. (ii) Two

other configurations have one extra particle (and the remaining 2d-3 sites empty) which creates exactly one additional diagonal pair, so k=2 with creation rate $2/k_{max}$. We associate one half of this contribution with the specific pair under consideration, and the other half with the second pair. (iii) There are multiple other configurations with one extra particle which create two additional diagonal pairs, so k=3 with creation rate $3/k_{max}$. One third of this contribution is associated with the specific pair under consideration, and the rest is equally divided between the other two pairs. (iv) The general term has k-1 additional pairs with creation rate k/k_{max}. We associate a fraction 1/k of this contribution with the specific pair under consideration, and the rest is equally distributed between the other pairs. Summing all contributions associated with the specific pair thus yields $1/k_{max}$ times the probability that site i is empty and the specific diagonal pair is occupied (with all other neighbors of the empty site unspecified). This result is illustrated in (12) for d=3.

Derivation of the autocatalytic particle creation terms in the rate equation for $P[o_{i1,i2,\ldots,id}\ o_{i1+1,i2,\ldots,id}]$ follows a similar strategy. Each term corresponds to a sum of contributions associated with different configurations of the 2d-1 sites at one end of the empty pair $o_{i1,i2,\ldots,id}\ o_{i1+1,i2,\ldots,id}$ which all include a specific diagonal pair of particles. Summing all contributions associated with the specific pair yields $1/k_{max}$ times the probability that the pair is empty and the specific diagonal pair is occupied (with other neighbors of the empty pair unspecified). In 4(d-1) of these terms, one filled site forms a linear triple with the empty pair. In the other 4(d-1)(d-2) terms, this is not the case.

Appendix B: dRDE in the Pair Approximation: d=3 Cubic Lattice

For planar interfaces with a *skew orientation*, so that $C_{i1,i2,i3} = C_{m=i1+i2+i3}$, we let $\varepsilon_m = 1-C_m$ denote the probability that a site on the skew plane $m=i_1+i_2+i_3$ is empty. The probability of a nearest-neighbor empty pair with one site in plane m and the other in plane m+1 is denoted by $\phi_{m+1/2}$. Note that all nearest-neighbor empty pairs can be described by these ϕ's. The corresponding dRDE have the form

$$d/dt\ \varepsilon_m = p(1-\varepsilon_m) - (2\varepsilon_m - \phi_{m+1/2} - \phi_{m-1/2})^2/(4\varepsilon_m), \tag{18a}$$

$$\begin{aligned} d/dt\ \phi_{m-1/2} = {} & p(\varepsilon_m + \varepsilon_{m-1} -2\phi_{m-1/2})-\phi_{m-1/2}[3(\varepsilon_m - \phi_{m+1/2})^2 + 4(\varepsilon_m - \phi_{m+1/2})(\varepsilon_m - \phi_{m-1/2}) \\ & + (\varepsilon_m - \phi_{m-1/2})^2/[12(\varepsilon_m)^2]-\phi_{m-1/2}[3(\varepsilon_{m-1} - \phi_{m-3/2})^2 + 4(\varepsilon_{m-1} - \phi_{m-3/2})(\varepsilon_m - \phi_{m-1/2}) \\ & + (\varepsilon_m - \phi_{m-1/2})^2/[12(\varepsilon_{m-1})^2]. \end{aligned} \tag{18b}$$

For a *diagonal interface* where $C_{i1,i2,i3} = C_{m=i1+i2}$, we let $\varepsilon_m = 1-C_m$ denote the probability that a site on the vertical plane $m=i_1$ is empty. The probability of nearest-neighbor empty pair with one site in plane m and the other in plane m+1 [i.e., sites (i_1,i_2,i_3) and (i_1,i_2+1,i_3) or (i_1+1,i_2,i_3)] is denoted by $\phi_{m+1/2}$. In addition, we must consider the probability of a nearest-neighbor empty pair with both sites in plane m [i.e., sites (i_1,i_2,i_3) and (i_1+1,i_2-1,i_3) or (i_1-1,i_2+1,i_3) or $(i_1,i_2,i_3\pm1)$] which is denoted by ψ_m. The corresponding dRDE have the form

$$d/dt\ \varepsilon_m = p(1-\varepsilon_m) - (2\varepsilon_m - \phi_{m+1/2} - \phi_{m-1/2})(6\varepsilon_m - 4\psi_m - \phi_{m+1/2} - \phi_{m-1/2})^2/(12\varepsilon_m), \tag{19a}$$

$$\begin{aligned} d/dt\ \phi_{m-1/2} = {} & p(\varepsilon_m + \varepsilon_{m-1} -2\phi_{m-1/2})-\phi_{m-1/2}\,[(\varepsilon_m - \phi_{m-1/2})(3\varepsilon_m - 2\psi_m - \phi_{m+1/2}) + (\varepsilon_m - \phi_{m+1/2}) \\ & (5\varepsilon_m - 4\psi_m - \phi_{m+1/2})]/[12(\varepsilon_m)^2] - \phi_{m-1/2}\,[(\varepsilon_{m-1} - \phi_{m-1/2})(3\varepsilon_{m-1} - 2\psi_{m-1} - \phi_{m-3/2}) \\ & +(\varepsilon_{m-1} - \phi_{m-3/2})(5\varepsilon_{m-1} - 4\psi_{m-1} - \phi_{m-3/2})]/[12(\varepsilon_{m-1})^2], \end{aligned} \tag{19b}$$

$$d/dt\ \psi_m = 2p(\varepsilon_m - \psi_m) - \psi_m(\varepsilon_m - \psi_m)(8\varepsilon_m - 2\psi_m - 3\phi_{m+1/2} - 3\phi_{m-1/2})/[6(\varepsilon_m)^2]. \quad (19c)$$

For a *vertical interface* where $C_{i1,i2,i3} = C_{m=i1}$, we let $\varepsilon_m = 1-C_m$ denote the probability that a site on the vertical plane $m=i_1$ is empty. The probability of a nearest-neighbor empty pair with one site in plane m and the other in plane m+1 [i.e., sites (i_1,i_2,i_3) and (i_1+1,i_2,i_3)] is denoted by $\phi_{m+1/2}$. In addition, we must consider the probability of nearest-neighbor empty pair with both sites in plane m [i.e., sites (i_1,i_2,i_3) and $(i_1,i_2\pm1,i_3)$ or $(i_1,i_2,i_3\pm1)$] which is denoted by ψ_m. The corresponding dRDE have the form

$$d/dt\ \varepsilon_m = p(1-\varepsilon_m) - (3\varepsilon_m - \psi_m - \phi_{m+1/2} - \phi_{m-1/2})^2/(3\varepsilon_m), \quad (20a)$$

$$d/dt\ \phi_{m-1/2} = p(\varepsilon_m + \varepsilon_{m-1} - 2\phi_{m-1/2}) - \phi_{m-1/2}(\varepsilon_m - \psi_m)(2\varepsilon_m - \psi_m - \phi_{m+1/2})/[3(\varepsilon_m)^2]$$
$$- \phi_{m-1/2}(\varepsilon_{m-1} - \psi_{m-1})(2\varepsilon_{m-1} - \psi_{m-1} - \phi_{m-3/2})/[3(\varepsilon_{m-1})^2], \quad (20b)$$

$$d/dt\ \psi_m = 2p(\varepsilon_m - \psi_m) - \psi_m(\varepsilon_m - \psi_m)(8\varepsilon_m - 2\psi_m - 3\phi_{m+1/2} - 3\phi_{m-1/2})/[6(\varepsilon_m)^2]. \quad (20c)$$

Appendix C: Iterated Map Analysis of Steady-States: d=3 MF dRDE

To characterize stationarity and propagation failure for planar interfaces with orientation $ai_1+bi_2+ci_3 = m$ in d=3, it suffices to analyze the steady-state form of (13) which corresponds to a second-order recurrence relation. This relation can be converted to an *iterated map* for $[u_m, v_m] = [C_{m-1}, C_m]$ of the form [23,26]

$$u_{m+1} = v_m \text{ and } v_{m+1} = F(u_m, v_m, p). \quad (21)$$

The uniform active and vacuum steady-states correspond to fixed points of the map, $[u,v] = [C_{act}(p), C_{act}(p)]$, with $C_{act}(p) = 1/2 + 1/2(1-4p)^{1/2}$, and $[u,v] = [0,0]$, respectively.

Except for vertical interface, the stationary concentration profiles smoothly approach the active and vacuum state away from the interface. Correspondingly, orbits of the above map smoothly connect the fixed points, while remaining within the physical domain $0 \leq u, v \leq 1$. For a vertical interface, the concentration profile does not smoothly approach the vacuum state. The orbit goes through the active fixed point and intersects physical domain boundary for $p \leq p_{eq}(100)$, tangentially for $p = p_{eq}(100)$ (cf. [23]).

Near the active state fixed point, behavior of the orbit is determined by the asymptotic form of the solution

$$C_m \approx C_{act} + \kappa\lambda^m, \text{ where } \lambda^{+a} + \lambda^{-a} + \lambda^{+b} + \lambda^{-b} + \lambda^{+c} + \lambda^{-c} = 3/(1-C_{act}). \quad (22)$$

Thus, one has that $\lambda = 1/2\ r - 1/2\ (r^2-4)^{1/2}$ with $r = (1-C_{act})^{-1}$, $3(1-C_{act})^{-1}/2 - 1$, $3(1-C_{act})^{-1} - 4$ (≥ 2) for skew, diagonal, and vertical interfaces, respectively. Thus, we consistently choose an initial point $[u_1, v_1] = [C_{act} + \varepsilon, C_{act} + \varepsilon\lambda]$ for small ε, iterate the map for a selected value of p, and determine whether the orbit has the desired form. For example, in the case of a *skew interface*, if one chooses $p > p_{eq}(111)$, the orbit remains within the physical domain (see **Fig.8a**), and for $p < p_{eq}(111)$, the orbit exits this domain (see **Fig.8b**). At the unique value of $p = p_{eq}(100)$, the orbit will smoothly approach [0,0] (see **Fig.9a**). For a *diagonal interface*, the orbit smoothly approaches [0,0] for any p in the propagation failure regime, $p_{-}(110) < p < p_{+}(110)$ (see **Fig.9b**). The *vertical interface*, we show the orbit for $p = p_{eq}(100)$ in **Fig.9c**.

References

[1] Marro, J., Dickman, R.; *Nonequilibrium Phase Transitions in Lattice Models* Cambridge University Press, Cambridge (1999)

[2] Hinrichsen, H.; Adv. Phys. **49**, 815 (2000)

[3] Odor, G.; Rev. Mod. Phys. **76**, 663 (2004)

[4] Ziff, R.M., Gulari, E., Barshad, Y.; Phys. Rev. Lett. **56**, 2553 (1986)

[5] Evans J.W.; Miesch, M.S.; Phys. Rev. Lett. **66**, 833 (1991)

[6] Loscar, E., Albano, E.V.; Rep. Prog. Phys. **66**, 1343 (2003)

[7] Liu, D.-J., Guo, X., Evans, J.W.; Phys. Rev. Lett. **98**, 050601 (2007)

[8] Evans, J.W., Ray, T.R., Phys. Rev. E **50**, 4302 (1994)

[9] Goodman, R.H., Graff, D.S., Sander, L.M., Leroux-Hugon, P., Clément, E.; Phys. Rev. E **52**, 5904 (1995)

[10] Machado, E., Buendia, G.M., Rikvold, P.A.; Phys. Rev. E **71**, 031603 (2005)

[11] Guo, X., Liu, D.-J., Evans, J.W.; J. Chem. Phys. **130**, 074106 (2009)

[12] Toom, A.L.; in Dobrushin, D.L.; Sinai, Y.G. (eds.) *Multicomponent Random Systems: Advances in Probability and Related Topics*, vol. 6, pp. 549-575. Dekker, New York (1980), Chap. 18

[13] Bennett, C.H, Grinstein, G.; Phys. Rev. Lett. **55**, 657 (1985)

[14] Schloegl, F.; Z. Phys. **253**, 147 (1972)

[15] Grassberger, P.; Z. Phys. B Cond. Matt. **47**, 365 (1982)

[16] Boon, J.P., Dab, D., Kapral, R., Lawniczak, A.; Rep. Mod. Phys. **273**, 55 (1996)

[17] Prakash, S., Nicolis, G.; J. Stat. Phys. **86**, 1289 (1997)

[18] Durrett, R.; SIAM Rev. **41**, 677 (1999)

[19] Guo, X., de Decker, Y., Evans, J.W.; Phys. Rev. E **82**, 021121 (2010)

[20] Guo, X., Liu D.-J., Evans, J.W.; Phys. Rev. E **75**, 061129 (2007)

[21] Ziff, R.M., Brosilow, B.J.; Phys. Rev. A **46**, 4630 (1992)

[22] Evans, J.W.; Rev. Mod. Phys. **65**, 1281 (1993)

[23] Guo, X., Evans, J.W., Liu, D.-J.; Physica A **387**, 177 (2008). Note the error in site labeling in the last two loss terms in (17): replace i with i-1.

[24] Fischer, P., Titulaer, U.M.; Surf. Sci. **221**, 409 (1989)

[25] De Decker, Y., Tsekouras, G.A., Provata, A., Erneux, Th., Nicolis, G.; Phys. Rev. E **69**, 036203 (2004)

[26] Keener, J.P.; SIAM J. Appl. Math. **47**, 556 (1987)

[27] Fath, G.; Physica D **116**, 176 (1998).

[28] Mikhailov, A.S.; *Introduction to Synergetics* (Springer, Berlin, 1990).

[29] Liu, D.-J.; J. Stat. Phys. **135**, 77 (2009)

Figures

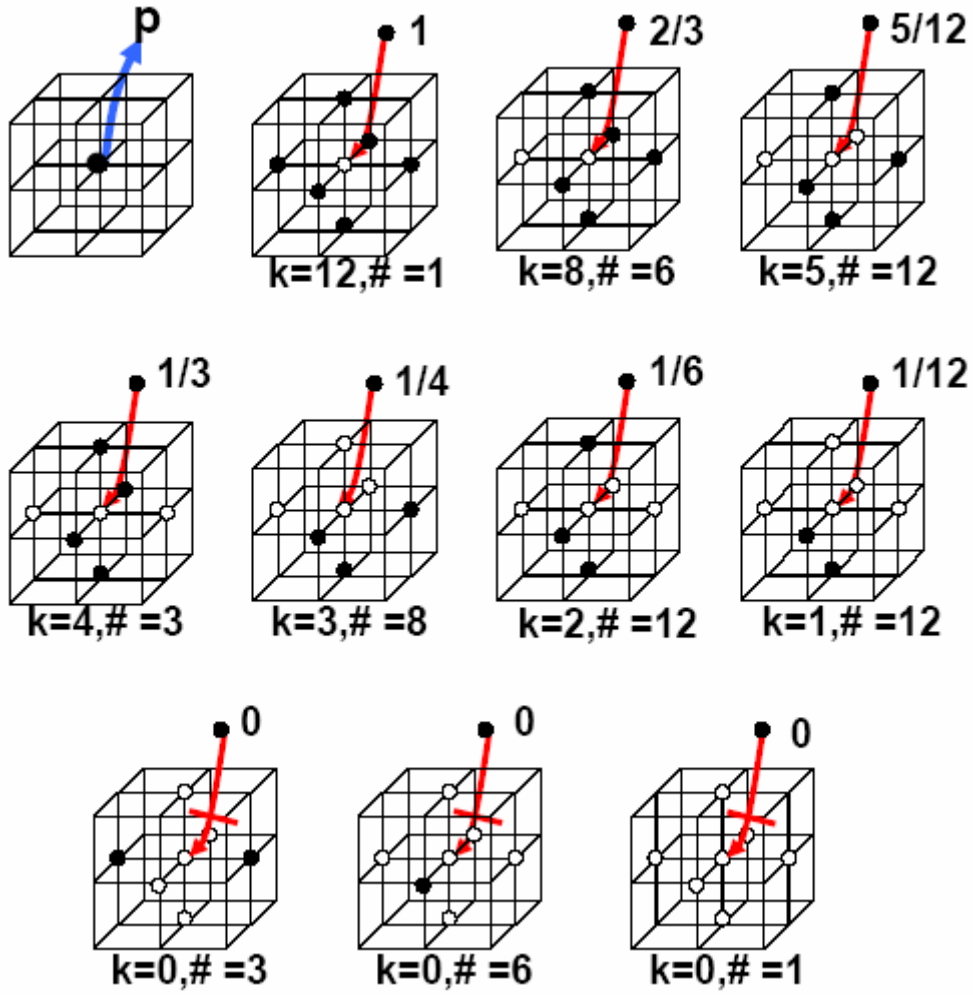

Fig.1. Schematic of spontaneous particle annihilation (at rate p) and configurations for autocatalytic particle creation (at rate k/12) for our realization of Schloegl's second model on a d=3 cubic lattice. k is the number of diagonal neighboring pairs of particles, and # is the configurational degeneracy.

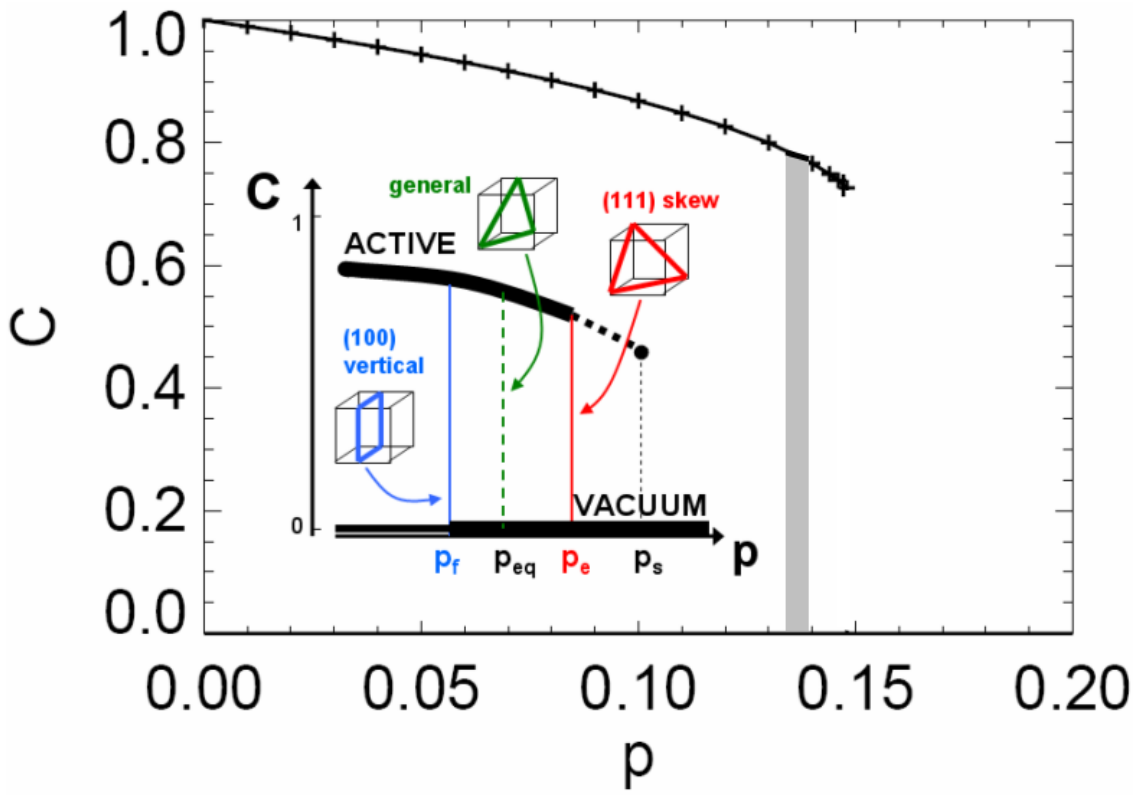

Fig. 2. KMC simulation results for the steady-state particle concentration, C, versus annihilation rate, p, for the active state in Schloegl's second model on a d=3 cubic lattice. The grey vertical band represents the regime of generic two-phase coexistence. Inset: schematic indicating values of p for stationary planar interfaces separating active and vacuum states of different orientations. The ill-defined spinodal point terminating the metastable active state (thick dashed line) is also indicated.

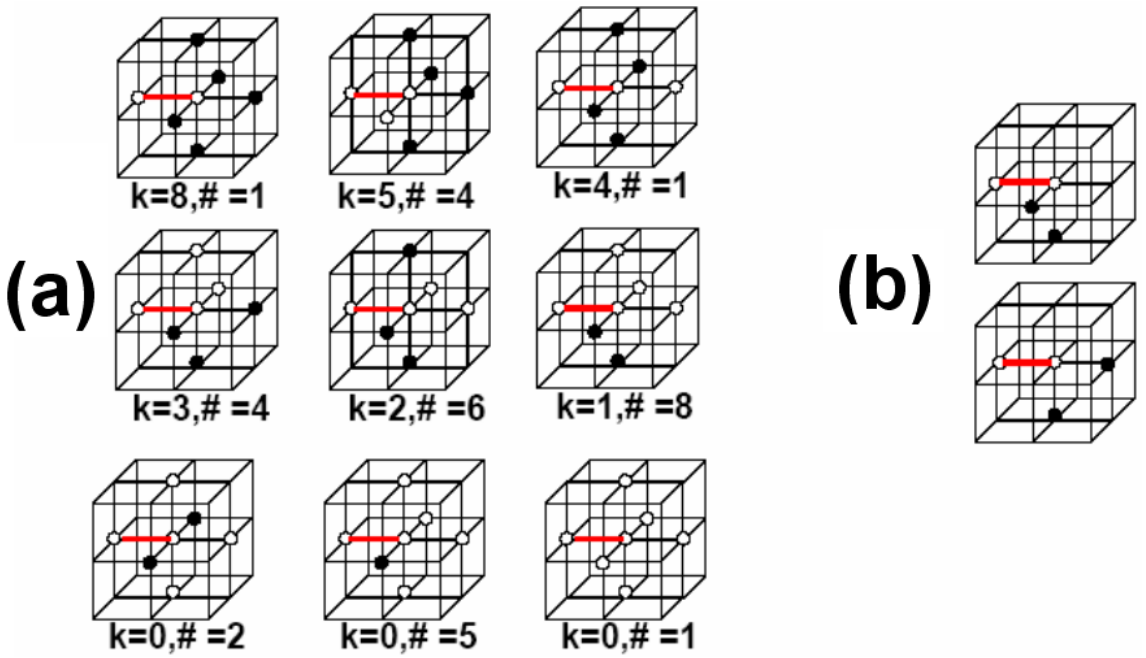

Fig. 3. (a) Configurations relevant for particle creation in the d/dt P[o o]-equation for Schloegl's second model on a d=3 cubic lattice. Here, a thicker red bond is drawn to indicate the empty pair for which particle creation occurs on the right site. Also, k/12 gives creation rate and # the configurational degeneracy. In (b), we show the reduced forms $P\begin{bmatrix} & x \\ o & \otimes \end{bmatrix}$ (top) and $P\begin{bmatrix} & x & \\ o & o & x \end{bmatrix}$ (bottom) obtained from summing these terms.

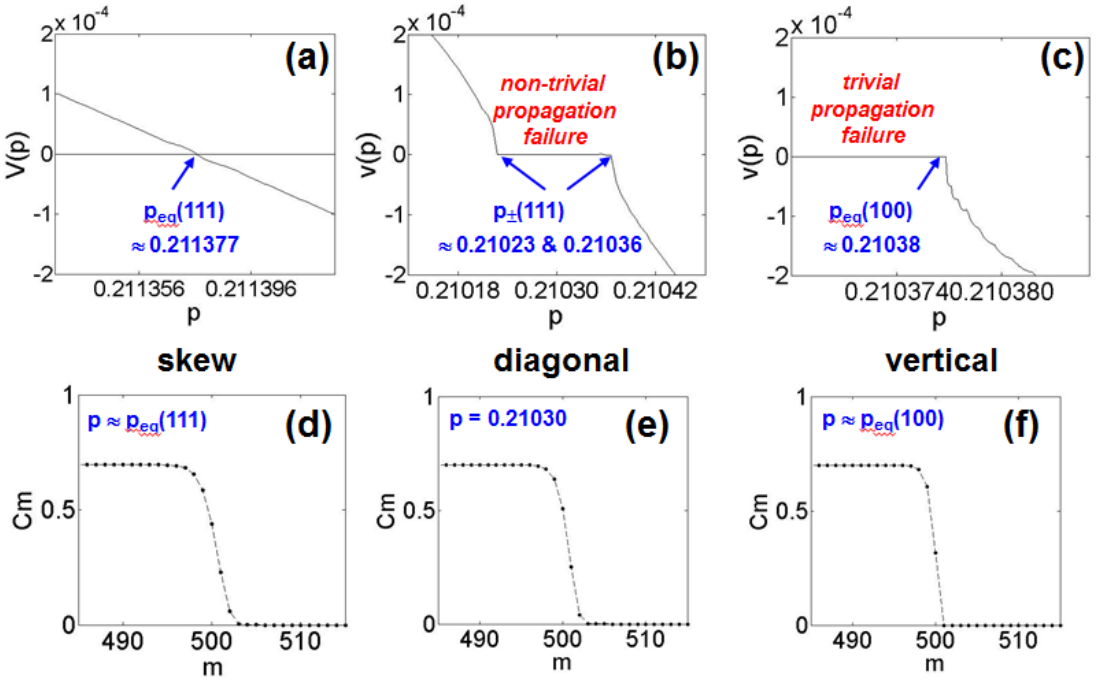

Fig. 4. MF dRDE predictions for planar interface propagation velocity, V(p), versus p in the d=3 reaction model for: (a) skew; (b) diagonal; (c) vertical orientations. Corresponding examples (d-f) of stationary interface profiles for the p-values indicated.

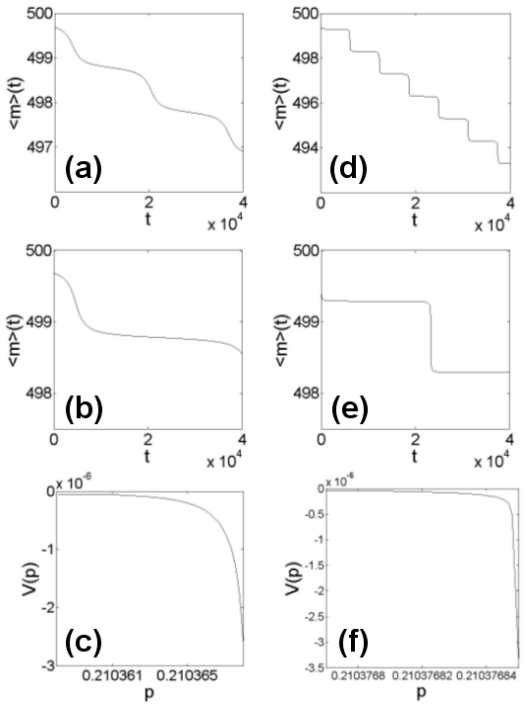

Fig. 5. Stop-and-go motion of planar interfaces near regimes of MF dRDE propagation failure. Location of a vertical interface versus t: (a) p = 0.210380, (b) p = 0.210377 versus $p_{eq}(100)$ = 0.2103767. Location of a diagonal interface versus t: (d) p=0.210377; (e) p=0.210369 versus $p_{+}(110)$=0.210363. V(p) versus p for vertical (c) and diagonal (f) interfaces.

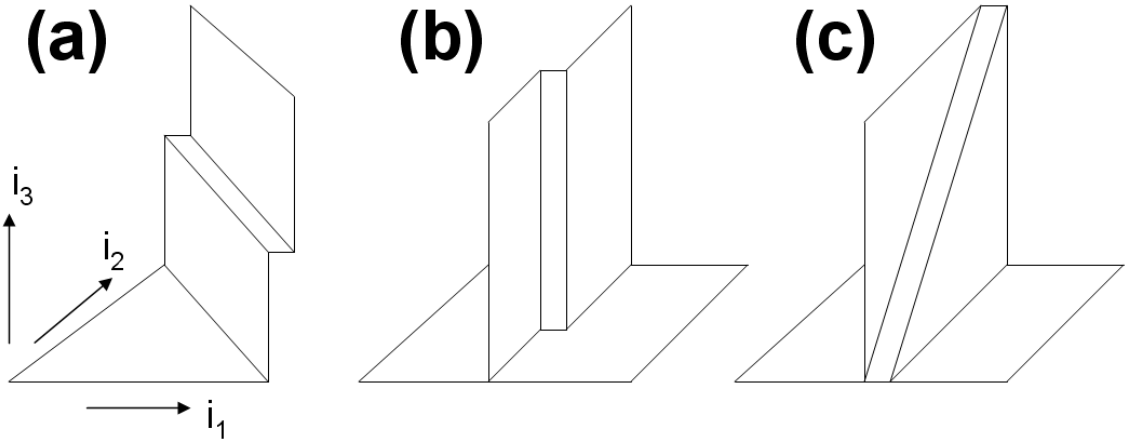

Fig. 6. Schematics for: near diagonal interfaces with isolated horizontal steps (a); and near vertical interfaces with isolated vertical (b), and diagonal (c) steps.

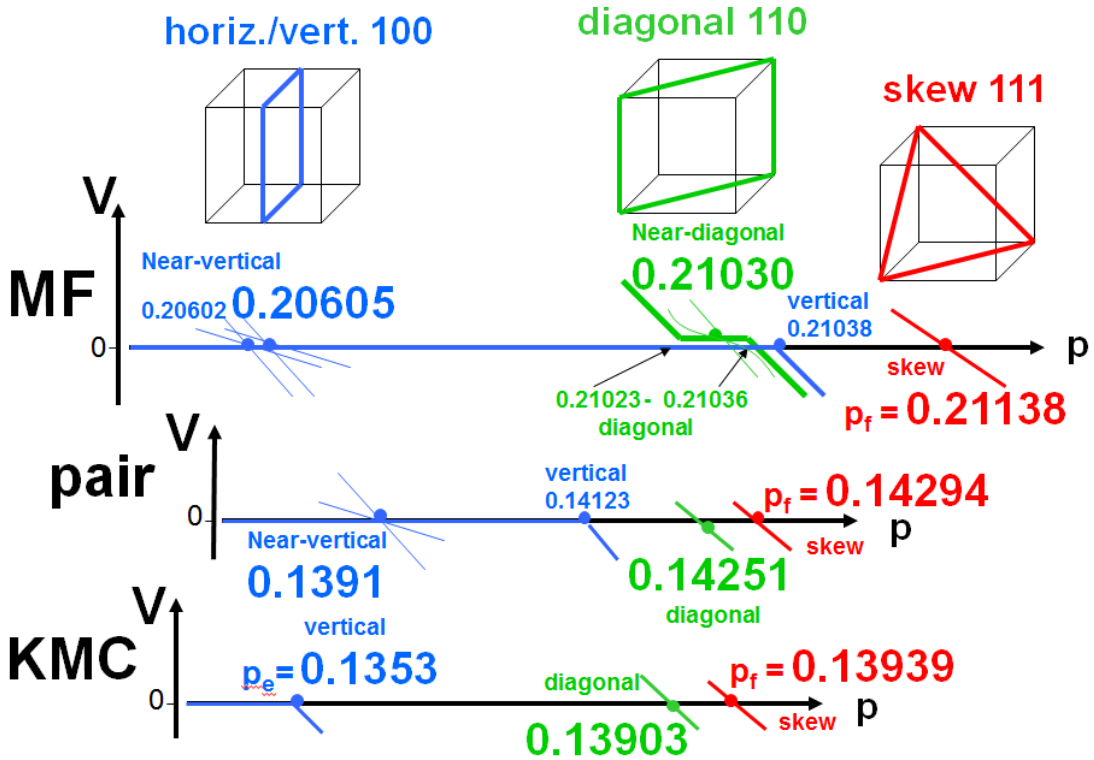

Fig. 7. Schematic summary of results for propagation velocity, V(p), versus particle annihilation rate, p, of planar interfaces separating the active and vacuum states for various orientations: comparison of MF dRDE, pair dRDE, and KMC predictions.

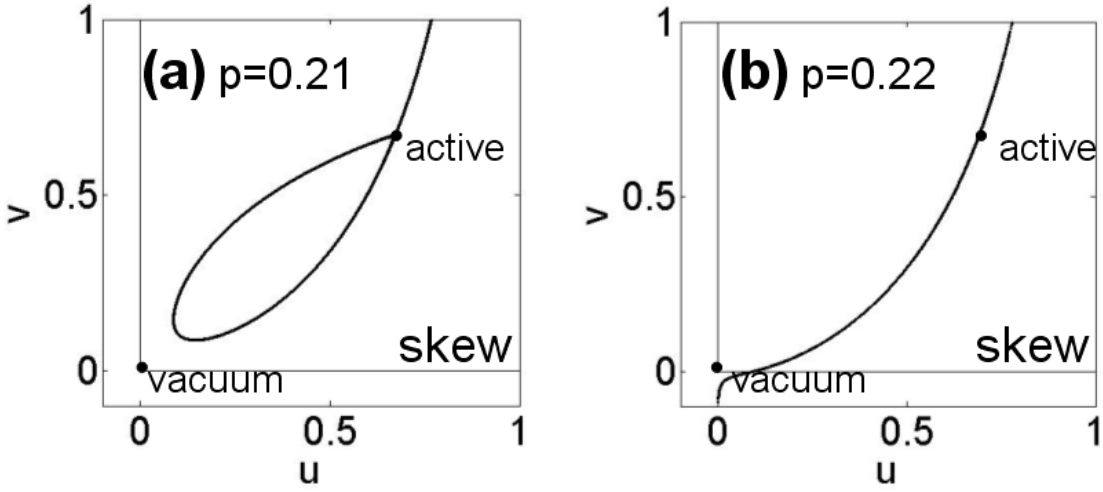

Fig. 8. Orbits of the iterated map associated with the MF dRDE for a skew interface in d=3 with: (a) $p = 0.220 > p_{eq}(111) \approx 0.211377$; (b) $p = 0.210 < p_{eq}(111)$.

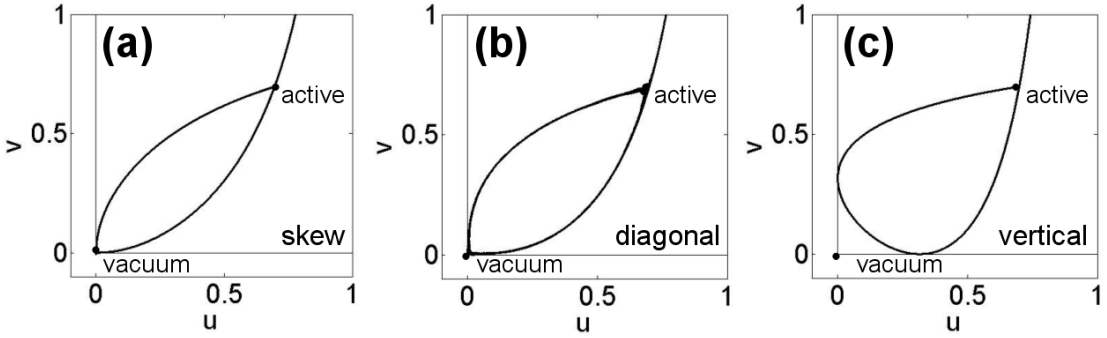

Fig. 9. Orbits of the iterated map associated with the MF dRDE for planar interfaces in d=3 for: (a) a skew orientation with $p = 0.21137770 \approx p_{eq}(111)$; (b) a diagonal orientation with $p = 0.21035$ in the middle of the propagation failure regime; (c) a vertical orientation with $p = 0.2103767 \approx p_{eq}(100)$.

Tables

Table 1. MF p_{eq} versus S for near-diagonal interfaces with orientation $S(i_1+i_2)\pm i_3=m$

$S(i_1+i_2)\pm i_3=m$	S=1	S=4	S=16	S≥64
MF $p_{eq}(S)$	0.21138	0.21053	0.21031	0.21030

Table 2. MF p_{eq} versus S for near-vertical interfaces with orientation $Si_1+i_2=m$

$Si_1+i_2=m$	S=1	S=4	S=16	S≥64
MF $p_{eq}(S)$	0.21023-0.21037	0.20729	0.20602	0.20602

Table 3. MF p_{eq} versus S for near-vertical interfaces with orientation $Si_1+i_2+i_3=m$

$Si_1+i_2+i_3=m$	S=1	S=4	S=16	S≥64
MF $p_{eq}(S)$	0.21138	0.20843	0.20606	0.20605

Table 4. Pair p_{eq} versus S for near-vertical interfaces with orientation $Si_1+i_2=m$

$Si_1+i_2=m$	S=1	S=4	S=16	S=1024	S=4096
pair $p_{eq}(S)$	0.14251	0.14097	0.13989	0.1395	0.1391

Table 5. Differences in stationary values for p for various interface orientations.

Treatment	MF	Pair	KMC
Δp_{eq}(111-110)	0.0011	0.00043	0.00036
Δp_{eq}(110-100)	0.0043	0.0034	0.0037
Δp_{eq} (2PC width)	0.0054	0.0038	0.0041

CHAPTER 3

SCHLOEGL'S SECOND MODEL FOR AUTOCATALYSIS ON HYPERCUBIC LATTICES: DIMENSION-DEPENDENCE OF PHASE COEXISTENCE

A paper published in *Physical Review E*

Chi-Jen Wang,[1,2] Da-Jiang Liu,[1] and J.W. Evans[1,2,3]

Ames Laboratory – USDOE[1] and Departments of Mathematics[2] and Physics & Astronomy[3], Iowa State University, Ames, Iowa 50011

Abstract

Schloegl's second model on a $d \geq 2$ dimensional hypercubic lattice involves: (i) spontaneous annihilation of particles with rate p; and (ii) autocatalytic creation of particles at vacant sites at a rate proportional to the number of suitable pairs of neighboring particles. This model provides a prototype for non-equilibrium discontinuous phase transitions. However, it also exhibits non-trivial generic two-phase coexistence: stable populated and vacuum states coexist for a finite range, $p_f(d) < p < p_e(d)$, spanned by the orientation-dependent stationary points for planar interfaces separating these states. Analysis of interface dynamics from Kinetic Monte Carlo (KMC) simulation, and from discrete reaction-diffusion equations (dRDE) obtained from truncation of the exact master equation, reveals that $p_{e(f)} \sim 0.2113765 + c_{e(f)}/d$, as $d \to \infty$, where $\Delta c = c_e - c_f \approx 0.014$. An metastable populated state persists above $p_e(d)$ up to a spinodal $p = p_s(d)$, which has a well-defined limit $p_s(d \to \infty) = ¼$. The dRDE

display artificial propagation failure, absent in the stochastic model due to fluctuations, a feature which is amplified for increasing d thus complicating our analysis.

1. Introduction

Stochastic lattice-gas reaction and reaction-diffusion models prescribe kinetic rules and rates for the creation and annihilation of various species residing on a lattice [1,2]. The reaction steps are often cooperative and sometimes irreversible. The lack of detailed-balance condition on the governing rates means that these systems may evolve to non-equilibrium steady-states which are not characterized by a Gibbs measure familiar for thermodynamic equilibrium in Hamiltonian models. However, these steady states can display phase transitions somewhat analogous to those in thermodynamic systems [1,2]. For both equilibrium [3] and non-equilibrium [1] lattice-gas models, it can be instructive to consider behavior as a function of lattice dimension, d. For models exhibiting continuous transitions or criticality, an upper critical dimension exists above which fluctuations are weak and mean-field (MF) behavior applies [1,3]. One also expects that either equilibrium or non-equilibrium discontinuous transitions may be erased due to strong fluctuations below some critical $d = d^*$ [1-3].

A candidate for non-equilibrium discontinuous transitions is Schloegl's second model for autocatalysis [4-13] on a hypercubic lattice which involves: (i) spontaneous annihilation of particles, X, at occupied sites at rate p; and (ii) autocatalytic creation of particles at vacant sites, $\varnothing$, induced by suitable nearby pairs of particles [8,9-13]. Schematically, the reaction steps are:

$X \rightarrow \varnothing$ (spontaneous annihilation @ rate p);

$\varnothing + 2X \rightarrow 3X$ (autocatalytic creation).

MF analysis suggests the existence of a discontinuous transition between an active state with particle concentration $C>0$, for $0<p<p_e$, and an absorbing vacuum state $C=0$, for all $p>0$. However, Kinetic Monte Carlo (KMC) analysis of Grassberger's version of this model found only a continuous transition for $d<4$ suggesting a critical $d^* = 4$ [5]. In contrast, our KMC analysis for a version of the model based on Durrett's Quadratic Contact Process or QCP (see below) revealed a discontinuous transition for $d=2$ [9] and $d=3$ [13], suggesting that $d^* =2$.

In addition, our analysis of the QCP version revealed a *non-trivial* generic two-phase coexistence (2PC) for $d=2$ and $d=3$ wherein the stable populated and vacuum phases coexist for a finite range of annihilation rate, p [9-13]. (Trivial 2PC occurs due to a "quirk" in the QCP rules. For any $p>0$, the vacuum state can always resist the growth of active droplets which cannot escape any rectangular region containing them [8]. Trivial 2PC disappears upon perturbing the model, e.g., to include particle hopping or spontaneous creation.) The non-trivial 2PC derives from an orientation-dependence of the value of the annihilation rate $p=p_{eq}$ corresponding to a stationary planar interface separating the two phases. This non-trivial generic 2PC feature may persist for $d>3$. This behavior contrasts phase coexistence in an equilibrium Hamiltonian system where planar interface separating phases is stationary at a unique point corresponding to equality of chemical potentials. As an aside, generic 2PC was first explored in Toom's model for voter dynamics [14,15] where the kinetic rules have an unappealing [16] asymmetry.

Our goal here is to elucidate fundamental aspects of the dependence on dimension, d, of discontinuous transitions in lattice-gas reaction models which display generic 2PC. In this paper, we consider only our QCP version of Schloegl's second model, but the features displayed and issues analyzed will undoubtedly have broad applicability. Analogous studies for equilibrium systems would be performed using the ferromagnetic Ising model. One might expect the kinetics to approach mean-field behavior, and also enhanced metastability, as $d \to \infty$. However, the d-dependence of features related to equistability of distinct phases is perhaps less clear, and is the focus of the current contribution. Although contentious [22], we claim that equistability for infinite lattices should be determined by stationarity of planar interfaces separating coexisting states (cf. [4,17-21]). Consideration of equistability is complicated by the presence of generic 2PC for which we provide the first analysis of its d-dependence and disappearance as $d \to \infty$.

With regard to development and application of general methodologies, we apply discrete reaction-diffusion equations (dRDE) to elucidate interface dynamics. dRDE are derived from truncation approximations to the exact master equations for spatially inhomogeneous states. This approach has received little attention previously, and then only for d=1-3 and mainly using the lowest-order mean-field truncation approximation. We exploit the dRDE to obtain exact limiting behavior as $d \to \infty$. However, we find that these dRDE can display artificial propagation failure (APF), an effect which is absent due to fluctuations in the stochastic model and which is strongly amplified with increasing d. Nonetheless, dRDE analysis of suitable interface orientations avoiding

APF is shown to still capture behavior in the stochastic model. While we treat only our QCP model, this dRDE methodology and the observed APF behavior and its resolution should have broad applicability.

In Sec.2, we provide a detailed description of our stochastic reaction model for general $d \geq 2$. New KMC simulation results are reported for d = 2-5. In Sec.3, we present the exact master equations for general d, and develop dRDE for spatially heterogeneous states by applying the MF and pair approximations. The dRDE are used to assess the propagation of planar interfaces between active and vacuum states, specifically stationarity and artificial propagation failure (APF), in Sec.4. The interpretation of the dRDE results and their relationship to exact behavior of the stochastic reaction model is described in Sec.5. Conclusions are provided in Sec.6.

2. Model Prescription for General Dimension and KMC Analysis

Our model involves particle annihilation and creation at the sites of an infinite d-dimensional hyper-cubic lattice with sites labeled by $\underline{i} = (i_1, i_2, i_3, \ldots, i_d)$. Note that the total number of pairs of sites selected from the $2d$ nearest-neighbors (NN) of any site satisfies $k_{tot} = (2d)(2d\text{-}1)/2! = d(2d\text{-}1)$. We divide all such pairs into two subsets: linear pairs where one site is $(i_1, i_2, \ldots, i_j + 1, \ldots, i_d)$ and the other is $(i_1, i_2, \ldots, i_j\text{-}1, \ldots, i_d)$; and "diagonal" pairs with one site is at one of $(i_1, i_2, \ldots, i_j \pm 1, \ldots, i_d)$ and another at one of $(i_1, i_2, \ldots, i_k \pm 1, \ldots, i_d)$ and where $j \neq k$. The number of linear pairs satisfies $k_{lin} = d$, and thus the number of diagonal pairs satisfies $k_{max} = k_{tot} - k_{lin} = 2d(d\text{-}1)$. Our QCP version of Schloegl's second model for any $d \geq 2$ generalizes Durrett's prescription [18] for a d=2. It

involves: (i) spontaneous creation of particles at unoccupied sites at rate p; (ii) autocatalytic annihilation of particles at empty sites at rate k/k_{max}, where k is the number of "diagonal" pairs of particles on neighboring sites. This prescription produces a simple d-independent form for the mean-field kinetics of the model. Furthermore, it enables an exact simplification of the master equations, as described in Sec.3.

For spatially homogeneous states, we define the particle concentration, C, as the mean probability that a site is occupied, so that $0 \leq C \leq 1$. We find that a stable populated steady-state with concentration $C>0$ exists for a range of annihilation rates, $0 \leq p \leq p_e(d)$. Previous KMC studies found $p_e(d=2) = 0.09443$ [9] and $p_e(d=3) = 0.13939$ [13]. Below we report behavior for $d>3$. In the "active" populated state, particles are continually created and annihilated. Increasing p to higher $p > p_e(d)$ results in a discontinuous transition to a stable absorbing "vacuum" state with $C=0$. An ill-defined metastable extension of the active state exists for a small range of $p_e(d) < p < p_s(d)$, where $p_s(d)$ denotes the spinodal with $p_s(d=2)\approx 0.101$ [12] and $p_s(d=3)\approx 0.15$ [13].

Previous studies for $d=2$ and 3 [9,12] found non-trivial generic 2PC wherein stable active and vacuum states coexist for a finite range $p_f(d) \leq p \leq p_e(d)$. This range is spanned by the orientation-dependent "equistability" values $p = p_{eq}$ for stationary planar interfaces separating these states, where $p_e(d) = max\ p_{eq}$ corresponds to a diagonal ($d=2$) or skew ($d=3$) interface. For a general orientation, when $0 \leq p < p_{eq}$, the active state displaces the vacuum state. For $p_{eq} < p < p_e(d)$, the vacuum state displaces the active state. For $p_e(d) < p < p_s$, the vacuum state transiently displaces the metastable active state until the latter spontaneously converts to the vacuum. One caveat is that for an

exactly vertical interface ($i_1=0$), the active state can never propagate into the vacuum (empty sites in this vacuum state have at most one occupied neighbor). More precisely, a vertical interface is stationary for all $p \leq p_f(d)$, but the vacuum state expands for $p > p_f(d)$. See [9-13] and **Fig.1**. As noted above, trivial 2PC occurs for all $p \leq p_e(d)$ as the vacuum state is stable against expansion of droplets of the active state. These features are shown to persist for $d>3$.

Model behavior is characterized by performing KMC simulations on finite hypercubic lattices of L^d sites with periodic boundary conditions. In conventional constant-p ensemble simulations, processes are implemented with probabilities proportional to their rates. However, to assess p_{eq}, we implement alternative constant-C ensemble simulations [9,23]. System sizes were typically L = 1024, 128, 48, and 20, for d = 2, 3, 4, and 5, respectively. Simulation data was collected over times ~10^6 Monte Carlo steps (MCS) for d = 2 - 4 and ~10^4 MCS for d=5.

For $d\geq2$ dimensions, the interface orientation where $a\ i_1 + b\ i_2 + c\ i_3 + \ldots = m$ is constant (with $a, b, c, \ldots,$ and m as integers) is labeled by ($abc\ldots$). Vertical interfaces correspond to a=1 and $b=c=\ldots=0$ (so $i_1 = m$) are (10), (100), (1000), etc. for d=2, 3, 4,…, respectively, and have $p_{eq}(d) = p_f(d)$ defined us the upper boundary of the region of propagation failure $0<p<p_f(d)$. We define a "hyperskew" orientations as that where $a=b=c=\ldots=1$ (so $i_1+i_2+i_3+\ldots+i_d=m$) which constitutes the furthest-from-vertical orientation. This hyperskew orientation corresponds to diagonal (11), skew (111), 4^{th}-order skew (1111),…, for d=2, 3, 4,…, respectively, and have $p_{eq}(d) = p_e(d)$, i.e., p_{eq} is highest for orientations furthest-from-vertical where the active state can most easily

displace the vacuum state. New results for $p_{eq}(d=2\text{-}5)$ for various interface orientations are shown in **Table I**. In Sec.5, we show that $p_{eq}(d\to\infty)=0.2113765$ for all orientations. Our data suggests that $p_{eq}(d) \approx p_{eq}(d\to\infty) + c/d$, where c depends weakly on orientation. See **Fig.2**. The width of the 2PC region satisfies $\Delta p_{eq}(d) = p_e(d) - p_f(d) \approx 0.014/d$.

3. Master Equations for Homogeneous and Inhomogeneous States

Let *x (o)* denote a filled (empty) site, and let *P*'s denote the probabilities for various configurations of clusters of sites. For general spatially inhomogeneous states, the probability that a site is occupied or vacant depends on its location. Thus, we let $C_{\underline{i}} = P[x_{\underline{i}}]$ denote the probability that site $\underline{i} = (i_1, i_2, \ldots, i_d)$ is occupied. Then, $P[o_{\underline{i}}] = 1 - P[x_{\underline{i}}]$ is the probability that site $\underline{i}$ is empty. Let $\underline{e}_1 = (1,0,0,\ldots)$, $\underline{e}_2 = (0,1,0,\ldots)$, etc., denotes vectors between NN sites. Then $P[x_{\underline{i}}\, x_{\underline{i}+\underline{e}1}]$ ($P[o_{\underline{i}}\, o_{\underline{i}+\underline{e}1}]$) denotes the probability that sites in the NN pair $\underline{i}$, $\underline{i}+\underline{e}_1$ are both occupied (empty). Also, $P[x_{\underline{i}}\, o_{\underline{i}+\underline{e}1}]$ and $P[o_{\underline{i}}\, x_{\underline{i}+\underline{e}1}]$ denote the probabilities of mixed occupied-empty pairs. Conservation of probability implies that $P[x_{\underline{i}}] + P[o_{\underline{i}}] = 1$, $P[x_{\underline{i}}\, o_{\underline{i}+\underline{e}1}] + P[x_{\underline{i}}\, x_{\underline{i}+\underline{e}1}] = P[x_{\underline{i}}]$, $P[o_{\underline{i}}\, x_{\underline{i}+\underline{e}1}] + P[o_{\underline{i}}\, o_{\underline{i}+\underline{e}1}] = P[o_{\underline{i}}]$, etc. For the special case of spatially homogeneous states, these quantities do not depend on site location, so $P[x_{\underline{i}}] = P[x] = C$, $P[o_{\underline{i}}] = P[o] = 1\text{-}C$ ($= C'$), etc.

The exact master equations for our reaction model can be written as a coupled hierarchy for the evolution of the probabilities for empty single sites, empty pairs, etc. [24]. Terms in these equations simply account for all possible gain pathways due to spontaneous particle annihilation, and all possible loss pathways associated with autocatalytic particle creation.

3A. Lowest-order hierarchical equation for single-site probabilities

For spatially inhomogeneous states, the equations for single empty sites have the exact form

$$d/dt\, P[o_{\underline{i}}] = p\, P[x_{\underline{i}}] - (1/k_{max})\{P[o_{\underline{i}}\, x_{\underline{i}+\underline{e}1}\, x_{\underline{i}+\underline{e}2}] + P[o_{\underline{i}}\, x_{\underline{i}+\underline{e}1}\, x_{\underline{i}-\underline{e}2}] + P[o_{\underline{i}}\, x_{\underline{i}+\underline{e}1}\, x_{\underline{i}+\underline{e}3}] + \ldots\}. \quad (1)$$

The first gain term on the right-hand-side (RHS) of (1) corresponds to spontaneous particle annihilation at site $\underline{i}$ at rate p. The other loss terms correspond to autocatalytic particle creation at empty site $\underline{i}$ where one term appears for each of the k_{max} possible configurations of diagonal pairs of particles on sites NN to $\underline{i}$. We have shown explicitly only three out of these k_{max} creation terms. From (1), it is clear that for a spatially homogeneous state, the evolution equation for the probability of a single empty site has the d-independent exact form

$$d/dt\, P[o] = p\, P[x] - P\begin{bmatrix} x & \\ o & x \end{bmatrix}. \quad (2)$$

The loss term on the right-hand-side denotes the probability of a filled site with a specific diagonal pair of filled sites, where the state of the $2d$-2 other neighboring sites is unspecified.

In deriving the loss terms in (1), $P[o_{\underline{i}}\, x_{\underline{i}+\underline{e}1}\, x_{\underline{i}+\underline{e}2}]$ corresponds to a sum of contributions for different configurations of the $2d$ sites surrounding $o_{\underline{i}}$, but all including a diagonal pair of particles at sites $\underline{i}+\underline{e}_1$ and $\underline{i}+\underline{e}_2$. One case is the configuration with all other $2d$-2 neighboring sites empty so k=1, associated with a creation rate of $1/k_{max}$. The

general case has k-1 additional diagonal pairs with creation rate k/k_{max}. We associate a fraction 1/k of this contribution with the term $P[o_{\underline{i}}\, x_{\underline{i}+\underline{e}1}\, x_{\underline{i}+\underline{e}2}]$, and the rest is equally distributed between the other terms. Summing all contributions associated with $P[o_{\underline{i}}\, x_{\underline{i}+\underline{e}1}\, x_{\underline{i}+\underline{e}2}]$ thus yields $1/k_{max}$ times the probability that site $\underline{i}$ is empty and the indicated diagonal pair is occupied (with all other neighbors of the empty site in an unspecified state). A similar analysis generates $P[o_{\underline{i}}\, x_{\underline{i}+\underline{e}1}\, x_{\underline{i}-\underline{e}2}]$ and the other terms.

For spatially inhomogeneous states corresponding to planar interfaces between populated and vacuum states, (1) adopt a simpler form. For specific orientations, the $C_{i1\,i2,\ldots,id}$ and related probabilities can be independent of some i_k or dependent only on certain combinations of them. Also, some probabilities for configurations of clusters of sites become identical. For example, for vertical interfaces where $C_{i1,i2,\ldots,id} = C_{i1}$, the first two particle creation terms in (1) are equivalent.

3B. Hierarchical equation for pair probabilities

One can also obtain equations for probabilities of adjacent empty pairs of sites, and for larger clusters of empty sites. For a spatially <u>inhomogeneous</u> state, the evolution equation for the pair probability $P[o_{\underline{i}}\, o_{\underline{i}+\underline{e}1}]$ has the exact form

$$d/dt\, P[o_{\underline{i}}\, o_{\underline{i}+\underline{e}1}] = p\,\{P[x_{\underline{i}}\, o_{\underline{i}+\underline{e}1}] + P[o_{\underline{i}}\, x_{\underline{i}+\underline{e}1}]\} - (1/k_{max})\,\{P[o_{\underline{i}}\, o_{\underline{i}+\underline{e}1}\, x_{\underline{i}+2\underline{e}1}\, x_{\underline{i}+\underline{e}1+\underline{e}2}] + \ldots\}$$
$$- (1/k_{max})\,\{P[x_{\underline{i}+\underline{e}1+\underline{e}2}\, x_{\underline{i}-\underline{e}1}\, o_{\underline{i}}\, o_{\underline{i}+\underline{e}1}] + \ldots\}. \qquad (3)$$

The first two gain terms on the RHS corresponds to spontaneous particle annihilation at site $\underline{i}$ and $\underline{i}+\underline{e}_1$ at rate p. The next group of loss terms correspond to autocatalytic particle creation at empty site $\underline{i}+\underline{e}_1$ where one term appears for each of the 2(d-1) possible

configurations of diagonal pairs of particles NN to this site, where neither particle is on the neighboring site $\underline{i}$. We have shown explicitly only one out of the subset of 2(d-1) configurations where one particle forms a linear triple with the empty pair. There is another larger subset of 2(d-1)(d-2) configurations where neither particle forms a linear triple with the empty pair. The analogous last group of loss terms correspond to autocatalytic particle creation at empty site $\underline{i}$, where one term appears for each of the total of $2(d\text{-}1)^2$ possible configurations of diagonal pairs of particles NN to this site.

From (3), it follows that for a spatially homogeneous state, the equation for evolution of the probability of an empty pair has the exact form

$$d/dt\, P[o\ o] = 2p\cdot P[x\ o] - \{4(d\text{-}1)/k_{max}\}\, P\begin{bmatrix} & x & \\ o & o & x \end{bmatrix} - \{4(d\text{-}1)(d\text{-}2)/k_{max}\}\, P\begin{bmatrix} & x \\ o & \otimes \end{bmatrix}, \tag{4}$$

where $P\begin{bmatrix} & x & \\ o & o & x \end{bmatrix}$ and $P\begin{bmatrix} & x \\ o & \otimes \end{bmatrix}$ represent probabilities of an empty pair where the right site in this pair has a diagonal neighboring pair of particles. In the first, one filled site forms a linear triple with the empty pair. In the second, both filled sites form bent triples with the empty pair.

Derivation of the loss terms in (3) due to autocatalytic particle creation follows a similar strategy to that for (1) above. Each term corresponds to a sum of contributions associated with different configurations of the 2d-1 sites at the relevant end the empty pair $o_{\underline{i}}\ o_{\underline{i}+\underline{e}1}$ but which all include the diagonal pair of particles indicated explicitly in (3). Summing all contributions associated with the specific pair thus yields $1/k_{max}$ times the

probability that the pair is empty and the specific diagonal pair is occupied (with other neighbors of the empty pair unspecified).

4. Approximations and Discrete Reaction-Diffusion Equations

4A. Truncation approximations

In the simplest mean-field (MF) or site approximation, one neglects all correlations in the occupancy of different sites. Thus, for example, one has that

$$P[o_{\underline{i}}\, x_{\underline{i}+\underline{e}1}\, x_{\underline{i}+\underline{e}2}] \approx P[o_{\underline{i}}]\, P[x_{\underline{i}+\underline{e}1}]\, P[x_{\underline{i}+\underline{e}2}] \quad (\text{reducing to } P\begin{bmatrix} x & \\ o & x \end{bmatrix} \approx P[o]\, P[x]^2), \quad (5)$$

for inhomogeneous (homogeneous) states. In the next higher-order pair approximation, probabilities configurations of clusters of sites are factorized in terms of those for all constituent pairs where one also compensates for double-counting of some sites. Thus, one has that

$$P[o_{\underline{i}}\, x_{\underline{i}+\underline{e}1}\, x_{\underline{i}+\underline{e}2}] \approx P[o_{\underline{i}}\, x_{\underline{i}+\underline{e}1}]\, P[o_{\underline{i}}\, x_{\underline{i}+\underline{e}2}] / P[o_{\underline{i}}], \text{ and}$$

$$P[o_{\underline{i}}\, o_{\underline{i}+\underline{e}1}\, x_{\underline{i}+2\underline{e}1}\, x_{\underline{i}+\underline{e}1+\underline{e}2}] \approx P[o_{\underline{i}}\, o_{\underline{i}+\underline{e}1}]\, P[o_{\underline{i}+\underline{e}1}\, x_{\underline{i}+2\underline{e}1}]\, P[o_{\underline{i}+\underline{e}1}\, x_{\underline{i}+\underline{e}1+\underline{e}2}] / P[o_{\underline{i}+\underline{e}1}]^2 \quad (6)$$

(reducing to $P\begin{bmatrix} x & \\ o & x \end{bmatrix} \approx P[xo]^2/P[o]$ and $P\begin{bmatrix} & x & \\ o & o & x \end{bmatrix} \approx P\begin{bmatrix} & x \\ o & \otimes \end{bmatrix} \approx P[o\ o]P[x\ o]^2/P[o]^2$), for inhomogeneous (homogenous) states.

4B. Mean-field type kinetics for homogeneous states

The MF site-approximation to (2) yields the d-independent MF kinetics

$$d/dt\ C = -p\ C + C^2(1\text{-}C) \equiv R(C), \text{ so } d/dt\ ln\ C' = (C/C')[p - CC'], \quad (7)$$

where $C' = 1\text{-}C$ gives the probability of an empty site. Steady-state analysis reveals a stable vacuum state with C=0 for all p>0, and a stable active state with $C = C_{act}(\text{MF}) = ½ + ½(1 - 4p)^{1/2}$ for a bistability regime $0 \le p \le p_s(\text{MF}) = ¼$ [4,8-10]. In the pair approximation, a natural variable is the conditional concentration, $K = P[x\ o]/P[o]$, representing the probability of finding a particle next to a site specified empty. Setting $K' = 1\text{-}K$ (the conditional probability of an empty site) and $c_d = (d\text{-}1)/d$, the pair kinetics can be instructively formulated as

$$d/dt\ ln\ C' = (C/C')[p - CC'(K/C)^2] \text{ and } d/dt\ ln\ K' + d/dt\ ln\ C' = 2(K/K')[p - c_d KK'].$$

(8)

A steady-state analysis yields a stable vacuum state with $C = K = 0$ for all p>0, and a stable active state $K = K_{act}(\text{pair}) = ½ + ½(1 - 4p/c_d)^{1/2}$ for a bistability regime $0 \le p \le p_s(\text{pair}) = c_d/4$. Since $c_d \to 1$ as $d \to \infty$, it is clear comparing (7) and (8) that site and pair approximations converge.

More generally, consider the evolution of the probability, $P[\{o\}_n]$, of finite connected cluster of n vacant sites, $\{o\}_n$. The key observation is that as $d \to \infty$, all sites are on the perimeter and almost fully coordinated with sites not in the cluster. More precisely, the fractional deficit from full coordination scales like $1/d$. Thus, the structure of the evolution equation is similar to that for the probability, $(P[o])^n$, for n isolated far separated sites. It follows that $P[\{o\}_n] \to (P[o])^n$, as $d \to \infty$, a general feature applying for any lattice-gas reaction model.

4C. Mean-field-type discrete reaction-diffusion equations (dRDE)

We will consider only spatially inhomogeneous states corresponding to planar interfaces between active and vacuum states. As in Sec.2, interface orientations where $a\ i_1 + b\ i_2 + c\ i_3 + \ldots = m$ is constant is labeled by $(abc\ldots)$ for $d \geq 2$ dimensions. In these case, the concentrations $C_{i1,i2,\ldots,id} = C_{ai1+bi2+ci3\ldots=m} = C_m$ are labeled by a single integer m. Applying MF factorization to (1) produces closed discrete reaction-diffusion (dRDE) type equations for the C_m. The "diffusion" type terms reflect spatial coupling in the reaction model rather than particle hopping. These type of MF dRDE have been explored previously for other reaction-diffusion models, but just for $d \leq 3$ [25-27]. It is convenient to define a pseudo-diffusion coefficient $D_j(C)=C(1-C)/j$, and the discrete Laplacian

$$\Delta C_m = C_{m+1} - 2C_m + C_{m-1}, \text{ so that } (C_{m+1}+C_{m-1})^2 - (2C_m)^2 = 4C_m\,\Delta C_m + (\Delta C_m)^2. \quad (9)$$

For hyper-skew (1111…) interfaces where $C_{i1,i2,\ldots,id} = C_{i1+i2+\ldots+id=m}$, one obtains the MF dRDE

$$d/dt\ C_m = -pC_m + \tfrac{1}{4}(1-C_m)(C_{m+1} + C_{m-1})^2$$

$$= R(C_m) + D_1(C_m)\,\Delta C_m + \tfrac{1}{4}(1-C_m)\,(\Delta C_m)^2, \quad (10)$$

which have a form independent of d. As a consequence, the MF-value of p_{eq} for the d=2 diagonal, d=3 skew, and d>3 hyperskew orientations will identical. It should be noted that the physical Euclidean distance between adjacent planes, m and m+1, equals $d^{-1/2}$, and thus the physical width of the concentration profile across the interface also scales like $d^{-1/2}$.

For vertical (1000…) interfaces where $C_{i1,i2,\ldots,id} = C_{i1=m}$, one obtains the distinct MF dRDE

$$d/dt\ C_m = R(C_m) + D_d(C_m)\ \Delta C_m, \qquad (11)$$

incorporating weak spatial coupling for large d due to small $D_d \sim 1/d$. Since $R(0) = 0$ and $D_d(0) = 0$, (10) appropriately ensures that the active state cannot displace the vacuum state.

Next, consider more general low-index interfaces including diagonal (11000…) interfaces where $C_{i1,i2,\ldots,id} = C_{i1+i2=m}$, skew (11100…) interfaces $C_{i1,i2,\ldots,id} = C_{i1+i2+i3=m}$, and the natural generalization to n^{th}-order skew interfaces where $C_{i1,i2,\ldots,id} = C_{i1+i2+i3+\ldots+in=m}$. For the general n^{th}-order skew case, one obtains the MF RDE

$$d/dt\ C_m = R(C_m) + n\ D_d(C_m)\ \Delta C_m + \tfrac{1}{4}\ n(n\text{-}1)d^{-1}(d\text{-}1)^{-1}\ (\Delta C_m)^2. \qquad (12)$$

This result includes vertical (n=1), diagonal (n=2), skew (n=3) orientations as special cases, and reveals weak spatial coupling in all cases with n=O(1) and large d, in contrast to (9).

For reasons discussed below, it will also be instructive to consider near-vertical orientations. When $Si_1 + i_2 = m$, corresponding to a near-vertical interface with large slope S and far-spaced rare "horizontal steps" (see **Fig.3a**), one obtains the MF dRDE

$$\begin{aligned} d/dt\ C_m = &-pC_m + d^{-1}(d\text{-}1)^{-1}(d\text{-}2)(d\text{-}3)(1\text{-}C_m)(C_m)^2 \\ &+ d^{-1}(d\text{-}1)^{-1}(d\text{-}2)(1\text{-}C_m)C_m(C_{m-1}+C_{m+1}+C_{m-S}+C_{m+S}) \\ &+ \tfrac{1}{2}\ d^{-1}(d\text{-}1)^{-1}(1\text{-}C_m)(C_{m-1}+C_{m+1})(C_{m-S}+C_{m+S}). \end{aligned} \qquad (13)$$

When $Si_1 + i_2 + \ldots + i_d = m$, corresponding to a near-vertical interface with large slope S and far-spaced rare "maximally kinked" or hyperskew steps" (see **Fig.3b**), one obtains the MF dRDE

$$d/dt\ C_m = -pC_m + \tfrac{1}{4}\ d^{-1}(d\text{-}2)(1\text{-}C_m)(C_{m-1}+C_{m+1})^2$$

$$+ \tfrac{1}{2}\, d^{-1}(1-C_m)(C_{m-1}+C_{m+1})(C_{m-S}+C_{m+S}). \qquad (14)$$

Writing (13) and (14) in the form $d/dt\ C_m = R(C_m)$ + "diffusion-type terms", these diffusion terms are of order 1/d in (13), but of order unity in (14) (which reduces to (9) as $d \to \infty$).

One can also apply the pair approximation to (1) and (3) for planar interfaces between active and vacuum states to obtain pair dRDE for C_m and related pair probabilities. See **Appendix A** for the special cases of hyperskew (1111…) and vertical (1000…) interfaces.

5. Discrete RDE Analysis: Mean-Field and Pair Results

We now present results from numerical integration of the dRDE's for evolution of planar interfaces between the active and vacuum states. The initial data are chosen as a sharp interface between the active state $C_m = C_{act}$, for $m<m^*$, and the vacuum state $C_m = 0$, for $m \geq m^*$. In the pair approximation, we also specify certain pair occupations determined from K_{act}(pair). The interface location is determined from $\langle m \rangle = \sum_m C_m/C_{act}$ for a large finite system of ~1000 sites. The interface velocity, $V(p) = d/dt \langle m \rangle$, is determined for long times $t \approx 4\times10^4$. Our focus is on assessing variation of $V(p)$ with p to determine stationarity and propagation failure.

5A. Hyperskew (1111…) orientation

The MF dRDE for the hyperskew orientation where $m = i_1+i_2+\ldots+i_d$ have the special feature of being independent of d. Analysis of interface propagation reveals that

V(p) vanishes at a single stationary point which has the d-independent MF value $p_{eq}(111\ldots) = 0.2113765(4)$. See **Table II**. The pair dRDE for the hyperskew orientation predict qualitatively similar interface evolution with *V(p)* vanishing at a single stationary point. However, the pair $p_{eq}(111\ldots)$ depends on dimension and increases smoothly to converge to the MF value as $d\to\infty$. See **Table III**. Continuously deviating from a hyperskew orientation produces continuous deviations from the above behavior either at the MF or pair level with p_{eq} shifting to lower values.

5B. Vertical (1000…) and near-vertical orientations

The MF dRDE for vertical interfaces where $m = i_1$ predict propagation failure for $0 < p < p_{eq}(100\ldots)$ where MF $p_{eq}(100\ldots)$ increases with *d*. In fact, MF $p_{eq}(100..) \to p_s(\mathrm{MF}) = ¼$, as $d\to\infty$, where the interface is stationary over the entire bistability regime. See **Table II**. Additional analysis elucidates the sharpening of the stationary interface at $p = p_{eq}$ as d increases. See **Appendix B**. Analysis of the pair dRDE (15) reveals the same qualitative behavior where the pair $p_{eq}(100\ldots) \to p_s(\mathrm{MF}) = ¼$, as $d\to\infty$, but the rate of convergence is slower. See **Table III**.

Deviation from a vertical orientation with rare horizontal (H) "steps" (cf. **Fig.3a**). Both MF and pair analysis for near-vertical orientations with rare horizontal steps ($Si_1+i_2=m$ with large $S = 1024$) *indicates a unique stationary point* $p_{eq}(100\ldots H)$ *for d=2-5 which shifts upward with d*. For $d\geq 6$, a finite range of propagation failure emerges over a regime $p_-(100\ldots H) < p < p_+(100\ldots H)$. This regime expands with increasing d to

cover the entire region of bistability, i.e., $p_-(100\ldots H) \to 0$ and $p_+(100\ldots H) \to p_s(\mathrm{MF}) = ¼$, as $d\to\infty$. See **Tables II-III**.

Deviation from a vertical orientation with rare hyperskew (HS) steps (cf. **Fig.3b**). Orientations defined by $Si_1+i_2+\ldots+i_d = m$ with large S correspond to a vertical interface i_1=0 mis-oriented by occasional hyperskew (maximally kinked) "steps" separated by vertically S lattice constants. Analysis based on both the MF and pair dRDE for S=1024 indicates a unique stationary point for which $p_{eq}(100..HS) \to \lim_{d\to\infty} p_{eq}(111\ldots) = 0.2113765$, as $d\to\infty$. See **Tables II-III**.

5C. Diagonal (11000…), skew (11100..), and other orientatons

Analysis of the MF and pair dRDE for diagonal (11000…) interfaces where $m = i_1+i_2$ reveals that except for small d, one has propagation failure over a regime $p_-(1100\ldots) < p < p_+(1100\ldots)$. The regime of propagation failure expands with increasing d to cover the entire region of bistability, i.e., $p_-(1100\ldots) \to 0$ and $p_+(1100\ldots) \to p_s(\mathrm{MF}) = ¼$, as $d\to\infty$. See **Tables II-III**. Motivated by the analysis of near-vertical interfaces, we also consider deviations from diagonal orientations associated with rare hyperskew (maximally kinked) steps as a route to eliminate propagation failure. These orientations are described by $S(i_1+i_2)+i_3+i_4+\ldots+i_d = m$, where we choose S=1024. Analysis for the MF and pair dRDE reveals a lack of propagation failure with stationary point $p_{eq}(1100..HS) \to \lim_{d\to\infty} p_{eq}(111\ldots) = 0.2113765$, as $d\to\infty$. See **Tables II-III**.

Analysis of both MF and pair dRDE for skew (11100…) interfaces reveals that except for small d, one has propagation failure over a regime $p_-(1110\ldots) < p <$

$p_+(1110\ldots)$. Again, the regime of propagation failure expands with increasing d to cover the entire region of bistability, i.e., $p_-(1110\ldots) \to 0$ and $p_+(1110\ldots) \to p_s(\mathrm{MF}) = ¼$, as $d\to\infty$. It is also the case that propagation failure can be eliminated by deviating from skew orientations with rare hyperskew steps. These orientations are described by $S(i_1+i_2+i_3)+i_4+\ldots+i_d = m$, where we choose S=1024. The stationary point $p_{eq}(1110..HS) \to \lim_{d\to\infty} p_{eq}(111\ldots) = 0.2113765$, as $d\to\infty$. See **Table II-III**.

One can extend the above investigations to consider n^{th}-order skew orientations as defined in Sec.4B. One anticipates analogous behavior, i.e., development of propagation failure with increasing d which engulfs the entire bistable regime as $d\to\infty$. It is also anticipated that deviating from these orientation with rare hyperskew steps will eliminate propagation failure.

6. Relating dRDE Predictions to Stochastic Model Behavior

In relating MF-type dRDE predictions to stochastic reaction model behavior, it is instructive to first focus on two key interface orientations, hyperskew and vertical.

For hyperskew (111…) interfaces, the correspondence is unambiguous: there is no propagation failure for MF or pair dRDE, and the predicted $p_{eq}(111\ldots)$ corresponds to that in the stochastic model. The large discrepancy between the d-independent MF predictions and KMC values of $p_{eq}(111\ldots)$ for smaller d is largely removed in the pair approximation. As noted previously, the simple form $p_{eq}(111\ldots) \approx 0.2113765 + c/d$ describe well observed d-dependence.

For vertical (100…) interfaces, recall that propagation failure is expected for p below some critical value, $p_{eq}(1000\ldots)$ as the active state cannot displace the vacuum state for any p≥0. For $p > p_{eq}(1000\ldots)$, the vacuum state displaces the populated state. This feature applies to both the stochastic model and to various MF-type dRDE. However, $p_{eq}(1000\ldots)$ from MF-type treatments does not correspond to that for the stochastic model as estimated by KMC simulations. Specifically, MF-type formulations "artificially extend" the regime of propagation failure. This feature is amplified for increasing d, recalling that MF-type $p_{eq}(1000\ldots) \to p_s(\text{MF}) = ¼$, as $d \to \infty$.

Artificial propagation failure (APF) in MF-type dRDE treatments can be understood as follows. For smooth vertical interfaces in the stochastic lattice-gas reaction model, propagation of the vacuum state into the populated state for $p > p_{eq}$ is associated with fluctuation-mediated nucleation and growth of (d-1)-dimensional droplets of the vacuum state in the layer adjacent to the completely empty edge layer of the vacuum state. This feature not reflected in MF-type treatments where more difficult "spatially homogeneous propagation" of the vacuum state into the next layer is required. Considering near-vertical interfaces in MF-type treatments, i.e., vertical interfaces with far-separated "steps", could potentially avoid APF. However, introducing "smooth" horizontal steps does not avoid APF. Why? Step propagation must still occur "spatially homogeneous" propagation rather than by fluctuation-mediated nucleation and growth of new rows of empty sites adjacent to the step as in the stochastic reaction model. However, introducing more easily-propagating maximally-kinked hyperskew step avoids APF.

The amplification of APF with increasing d follows from the form of the MF-type dRDE. For vertical interfaces, the spatial coupling in MF-type dRDE is ~1/d [cf. (11)]. The diminution of this coupling with increasing d produces an amplification of APF. The same diminution of coupling persists upon introducing rare horizontal steps to a vertical interface [cf. (13)], thus preserving APF. However, introduction of rare hyperskew steps results in strong spatial coupling [cf. (14)], as for the hyperskew interface orientation [cf. (10)], thus avoiding APF.

Next, consider the d-dependence of the boundaries of the regime of 2PC. As noted above, there is a direct correspondence between $p_{eq}(111\ldots) = p_e$ (the upper boundary) in KMC analysis and MF-type treatments. However, due to APF, $p_{eq}(100\ldots)$ in MF-type treatments does not correspond to the lower boundary, p_f, of the 2PC regime (as it does in KMC analysis). We claim that p_f can be estimated in MF-type treatments from the stationary point for near vertical interfaces with rare hyperskew steps, i.e., $p_f = \lim_{S\to\infty} p_{eq}(1000\ldots HS)$, as such steps eliminate APF. Support for this claim comes from the results in Table IV. The behavior $p_{e(f)} \sim 0.2113765 + c_{e(f)}/d$, as $d\to\infty$, as determined from KMC analysis, is confirmed from the MF-type analysis where the 1/d-scaling is seen as a natural consequence of the form of the spatial coupling. As an aside, this strategy allows comparison of KMC and MF dRDE results for other orientations [25].

7. Conclusions

Our analysis indicates shrinking of the width, $\Delta p_{eq}(d) \approx 0.014/d$, of the regime of generic 2PC associated with the discontinuous transition in our QCP version of

Schloegl's second model on a hypercubic lattice with increasing dimension d. Appropriate application of MF-type dRDE is shown to be effective in elucidating this behavior particularly the scaling with *d*. These features and the utility of the dRDE analysis are expected to be general for non-equilibrium reaction models displaying discontinuous transitions. One could extend this analysis to consider nucleation of the more stable phase from the less stable one just outside the 2PC region. The orientation-dependence of interface propagation will be reflected in the shapes of evolving droplets [10,11], a feature which again can be elucidated by a MF-type dRDE analysis.

A significant feature of the MF-type dRDE treatment is the appearance of artificial propagation failure (APF). APF is artificial in the sense that it does not occur in the stochastic lattice-gas model due to fluctuations at the interface. Propagation failure in dRDE's of interest in its own right [26-28]. Studies often identify a critical value in spatial coupling below which there exists propagation failure, behavior which is amplified upon further reducing this coupling [28]. These observations are consistent with our observations, e.g., amplified APF for increasing *d*.

Acknowledgements

This work was supported by the U.S. Department of Energy (USDOE), Basic Energy Sciences, Division of Chemical Sciences, Geosciences, and Biosciences, through the Ames Laboratory Chemical Physics and PCTC projects. The Ames Laboratory is operated for the USDOE by Iowa State University under Contract No. DE-AC02-07CH11358.

Appendix A: Pair Discrete Reaction-Diffusion Equations (dRDE)

The pair approximation is applied to (1) and (3) for spatially inhomogeneous states corresponding to planar interfaces between active and vacuum states. For planar interfaces with a hyper-skew (1111…) orientation, so that $C_{i1,i2,\ldots,id} = C_{i1+i2+\ldots+id} = C_m$, we let $\varepsilon_m = 1\text{-}C_m$ denote the probability that a site on the hyper-skew plane $m=i_1+i_2+\ldots+i_d$ is empty. The probability of a NN empty pair with one site in plane m and the other in plane m+1 is denoted by $\phi_{m+1/2}$. Then, the corresponding dRDE have the form

$$d/dt\ \varepsilon_m = p(1\text{-}\varepsilon_m) - (2\varepsilon_m - \phi_{m+1/2} - \phi_{m-1/2})^2/(4\varepsilon_m), \tag{15a}$$

$$d/dt\ \phi_{m-1/2} = p(\varepsilon_m + \varepsilon_{m-1} - 2\phi_{m-1/2})$$

$$-\phi_{m-1/2}[d(\varepsilon_m - \phi_{m+1/2})^2 + 2(d\text{-}1)(\varepsilon_m - \phi_{m+1/2})(\varepsilon_m - \phi_{m-1/2}) + (d\text{-}2)(\varepsilon_m - \phi_{m-1/2})^2]/[4d(\varepsilon_m)^2]$$

$$-\phi_{m-1/2}[d(\varepsilon_{m-1} - \phi_{m-3/2})^2 + 2(d\text{-}1)(\varepsilon_{m-1} - \phi_{m-3/2})(\varepsilon_m - \phi_{m-1/2}) + (d\text{-}2)(\varepsilon_m - \phi_{m-1/2})^2]/[4d(\varepsilon_{m-1})^2]. \tag{15b}$$

These pair dRDE reduce to those of the MF dRDE in the limit as $d\rightarrow\infty$.

For a vertical (1000…) interface where $C_{i1,i2,\ldots,id} = C_{i1} = C_m$, we let $\varepsilon_m = 1\text{-}C_m$. The probability of a NN empty pair with one site in plane m and the other in plane m+1 [i.e., sites $(i_1,i_2,\ldots,i_d)$ and $(i_1+1,i_2,\ldots,i_d)$] is denoted by $\phi_{m+1/2}$. In addition, we must consider the distinct probability, ψ_m, of NN empty pair with both sites in plane m. The corresponding dRDE have the form

$$d/dt\ \varepsilon_m = p[1\text{-}\varepsilon_m] - [\varepsilon_m - \psi_m][d\varepsilon_m - (d\text{-}2)\psi_m - \phi_{m+1/2} - \phi_{m-1/2}]/[d\varepsilon_m], \tag{16a}$$

$$d/dt\ \phi_{m-1/2} = p[\varepsilon_m + \varepsilon_{m-1} - 2\phi_{m-1/2}]$$

$$-\phi_{m-1/2}[\varepsilon_m - \psi_m][(d-1)\varepsilon_m - (d-1)\psi_m - \phi_{m+1/2}]/[d(\varepsilon_m)^2]$$

$$-\phi_{m-1/2}[\varepsilon_{m-1} - \psi_{m-1}][(d-1)\varepsilon_{m-1} - (d-1)\psi_{m-1} - \phi_{m-3/2}]/[d(\varepsilon_{m-1})^2], \quad (16b)$$

$$d/dt\ \psi_m = 2p[\varepsilon_m - \psi_m] - \psi_m[\varepsilon_m - \psi_m][2(d-1)^2\varepsilon_m - 2(d-2)^2\psi_m$$

$$-(2d-3)(\phi_{m+1/2} + \phi_{m-1/2})]/[d(d-1)(\varepsilon_m)^2]. \quad (16c)$$

Examination of the form of (16) reveals that the active state cannot displace the vacuum state, consistent with exact behavior in the stochastic model.

Appendix B: dRDE Perturbation Analysis Vertical Interfaces as $d\to\infty$

For a stationary planar vertical interface between the vacuum state on the left for m = 0, -1, -2,…and a populated state on the right for m=1, 2,…, the MF dRDE (11) imply that

$$p - C_m(1-C_m) = d^{-1}(1-C_m)(C_{m+1} - 2C_m + C_{m-1}), \text{ for } m\geq 1, \quad (17)$$

where $C_0 = 0$. For large d, the RHS is small which forces $p - C_m(1-C_m) \approx 0$ or $C_m \approx C_{act}$. Thus, it is natural to write $C_m = C_{act} - \delta_m$ for $m\geq 1$ where $\delta_m << 1$ from which one obtains

$$(2C_{act} - 1)\delta_1 - d^{-1}C_{act}(1-C_{act}) - (\delta_1)^2 - d^{-1}(2-3C_{act})\delta_1 - d^{-1}(1-C_{act})\delta_2 - d^{-1}\delta_1(\delta_2 - 2\delta_1) = 0, \quad (18a)$$

$$(2C_{act} - 1)\delta_m - d^{-1}(1-C_{act})(\delta_{m+1} - 2\delta_m + \delta_{m-1}) - (\delta_m)^2 - d^{-1}\delta_m(\delta_{m+1} - 2\delta_m + \delta_{m-1}) = 0, \text{ for } m>1. \quad (18b)$$

First, we consider the general case of a stationary interface for fixed $p < p_{eq}(d)$ where $2C_{act} - 1 = (1-4p)^{1/2} = O(1)$. It follows from (18a) where the first two terms

dominate that $\delta_1 \approx d^{-1} C_{act}(1-C_{act})(2C_{act}-1)^{-1} = O(d^{-1})$. Then, considering the first two dominant terms in (18b) implies that $\delta_m \approx d^{-1}(1-C_{act})(2C_{act}-1)^{-1}\,\delta_{m-1}$, which in turn yields

$$\delta_m \approx C_{act}(1-C_{act})^m (2C_{act}-1)^{-m}\, d^{-m}, \text{ for } m \geq 1. \quad (19)$$

Second, in the special case of a stationary interface for $p=p_{eq}(d)$, one might anticipate distinct scaling behavior in the situation where $p_{eq}(d) \to \frac{1}{4}$, as $d \to \infty$. Indeed analysis of numerical data in **Table II** indicates that $\frac{1}{4} - p_{eq}(d) \approx A/d$ where $A \approx 0.25$, so that $2C_{act} - 1 = (1-4p)^{1/2} \approx B/d^{1/2}$ where $B \approx 1.0$. This forces modified scaling from (18) above. Now, the first three terms in (18a) dominate, and one concludes that $B \geq 1$ and $\delta_1 \approx E/d^{1/2}$ where $E = \frac{1}{2}[B \pm (B^2-1)^{1/2}]$. Then, considering the first two dominant terms in (18b) implies that $\delta_m \approx \frac{1}{2}\, d^{-1/2}\, B^{-1} \delta_{m-1}$ for $m>1$, which in turn yields

$$\delta_m \approx (2B)^{-m+1} E\, d^{-m/2}, \text{ for } m \geq 1. \quad (20)$$

Data from numerical analysis of the MF dRDE's supports this analysis. See **Table V**.

References

[1] J. Marro and R. Dickman, *Nonequilibrium Phase Transitions in Lattice Models* (Cambridge UP, Cambridge, 1999).

[2] G. Odor, Rev. Mod. Phys. **76**, 663 (2004).

[3] J. Cardy, *Scaling and Renormalization in Statistical Physics* (Cambridge University Press, Cambridge, 1996).

[4] F. Schloegl, Z. Phys. **253**, 147 (1972).

[5] P. Grassberger, Z. Phys. B Cond. Matt. **47**, 365 (1982).

[6] J.P. Boon, D. Dab, R. Kapral, and A. Lawniczak, Phys. Rep. **273**, 55 (1996).

[7] S. Prakash and G. Nicolis, J. Stat. Phys. **86**, 1289 (1997).

[8] R. Durrett, SIAM Rev. **41**, 677 (1999).

[9] D.-J. Liu, X. Guo, and J.W. Evans, Phys. Rev. Lett. **98**, 050601 (2007).

[10] X. Guo, J.W. Evans, and D.-J. Liu, Physica A **387**, 177 (2008).

Sites in the last two loss terms in eq. (17) are mislabeled. One should replace i with i-1.

[11] X. Guo, D.-J. Liu, and J.W. Evans, J. Chem. Phys. **130**, 074106 (2009).

[12] X. Guo, Y. de Decker, and J.W. Evans, Phys. Rev. E **82**, 021121 (2010).

[13] C.-J. Wang, X. Guo, D.-J. Liu, and J.W. Evans, J. Stat. Phys. **144**, 1308 (2011).

[14] A.L. Toom in *Multicomponent Random Systems*, edited by R.L. Dobrushin and Y.G. Sinai (Dekker, New York, 1980).

[15] C.H. Bennett and G. Grinstein, Phys. Rev. Lett. **55**, 657 (1985).

[16] R.S. MacKay, Nonlinearity **21**, T273 (2008).

[17] R.M. Ziff, E. Gulari, and Y. Barshad, Phys. Rev. Lett. **56**, 2553 (1986).

[18] P. Fischer and U.M. Titulaer, Surf. Sci. **221**, 409 (1989).

[19] J.W. Evans and T.R. Ray, Phys. Rev. E **50**, 4302 (1994).

[20] R. H. Goodman, D. S. Graff, L. M. Sander, P. Leroux-Hugon, and E. Clément, Phys. Rev. E **52**, 5904 (1995).

[21] Y. De Decker, G.A. Tsekouras, A. Provata, Th. Erneux, and G. Nicolis, Phys. Rev. E **69**, 036203 (2004).

[22] For systems with finite linear size, L, an alternative criterion is to balance rates for transitions between states due to homogeneous fluctuations. See G. Nicolis and J.W. Turner, Ann. NY Acad. Sci. **316**, 251 (1979), and J. Ross, K.L.C. Hunt, and M.O. Vlad,

J. Phys. Chem. C **106**, 10951 (2002). Only for L >> L_c (characteristic interface width) does this criterion match stationary interfaces.

[23] R.M. Ziff and B.J. Brosilow, Phys. Rev. A **46**, 4630 (1992).

[24] J.W. Evans, Rev. Mod. Phys. **65**, 1281 (1993).

[25] KMC estimates for p_{eq}(110…) of 0.1390, 0.1576 and 0.1682 compare with pair estimates of 0.1425, 0.1594 and 0.1694 for d=3, 4 and 5, respectively. KMC estimates for p_{eq}(1110…) of 0.1581 and 0.1688 compare with pair estimates of 0.1599 and 0.1700 for *d*=4 and 5, respectively.

[26] J.P. Keener, SIAM J. Appl. Math. **47**, 556 (1987).

[27] S.-N. Chow, J. Mallet-Paret, and E. S. Van Vleck, Int. J. Bifurc. Chaos 6, 1605 (1996).

[27] G. Fath, Physica D **116**, 176 (1998).

Figures

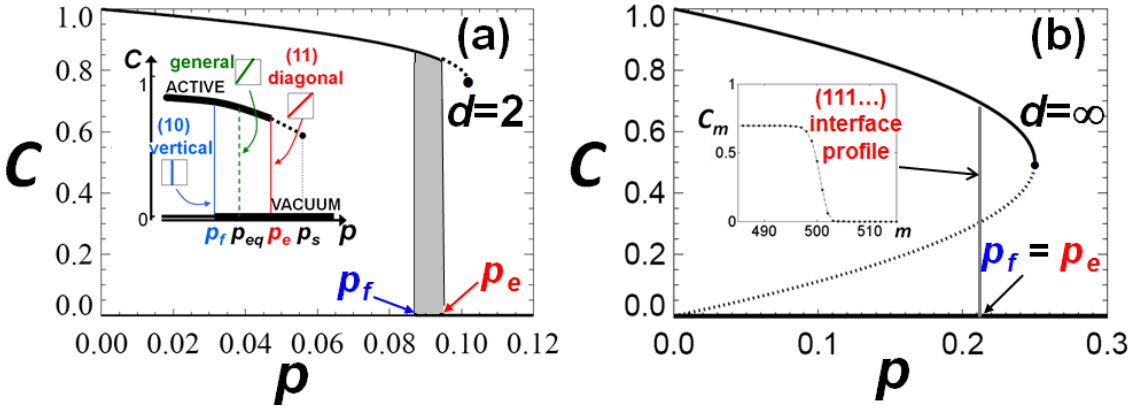

Fig.1. (Color online) Steady-state *C* versus *p* for: (a) *d*=2; (b) *d*→∞ MF behavior. p_e (p_f) = upper (lower) 2PC boundaries; p_s = spinodal. Inset to (a): dependence of equistability p_{eq} on interface orientation. Inset to (b): profile of a hyperskew interface for *d*→∞ at p_e = p_f = 0.2113765.

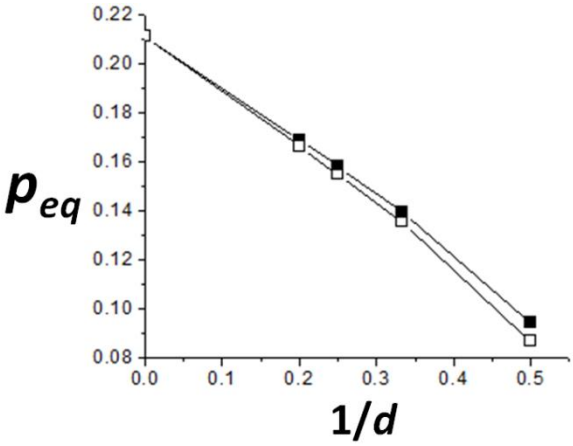

Fig.2. KMC results for p_{eq} versus $1/d$ for hyperskew (filled square) and vertical (open square) interfaces, where the exact result is also shown for $d\rightarrow\infty$.

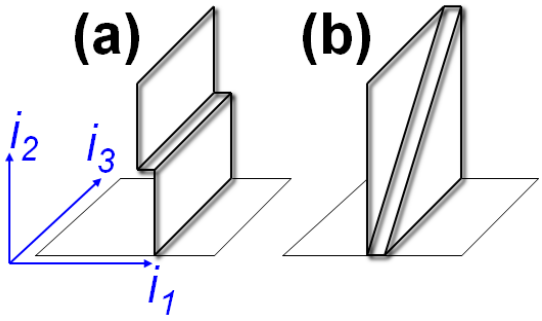

Fig.3. (Color online) Schematic for d=3 of a rare horizontal (a) and hyperskew (b) step on a vertical interface.

Tables

Table I. KMC values of $p=p_{eq}$ for stationary planar interfaces separating populated and vacuum states for orientations indicated before the colon; $p_{eq} \rightarrow 0.211377$, as $d\rightarrow\infty$, for all orientations.

d=2	10: 0.0871	11: 0.09440 (2)			
d=3	100: 0.1353	110: 0.139027(7)	111: 0.139386(7)		
d=4	1000: 0.1548	1100:	1110:	1111:	

		0.157593(9)	0.158091(8)	0.158284(8)	
d=5	10000: 0.1664	11000: 0.16824(1)	11100: 0.168847(7)	11110: 0.169055(6)	11111: 0.169137(6)

Table II. MF results for stationary points $p=p_{eq}$ or for regimes of propagation failure for planar interfaces separating populated and vacuum states.

	Vertical 1000…	Si_1+i_2	$Si_1+i_2+...+i_d$	Diagonal 11000…	$S(i_1+i_2)+i_3+...+i_d$	Skew 11100..	$S(i_1+i_2+i_3)+i_4+...+i_d$	Hyper-skew 111…
d=2	0.2071068	0.20505						0.2113765
d=3	0.21038	0.20602	0.20605	0.21023-0.21037	0.21030			0.2113765
d=4	0.21514	0.20720	0.20732	0.20949-0.21027	0.20990	0.21093	0.21092	0.2113765
d=5	0.21953	0.20782-0.20829	0.20834	0.20820-0.21099	0.20974	0.21060-0.21075	0.21068	0.2113765
d=6	0.22312	0.20717-0.20974	0.20906	0.20583-0.21246	0.20971	0.21024-0.21081	0.21053	0.2113765
d=7	0.22600	0.20468-0.21175	0.20957	0.20222-0.21437	0.20977	0.20959-0.21120	0.21045	0.2113765
d=10	0.23188	0.18816-0.21845	0.21039	0.18559-0.22035	0.21015	0.20496-0.21414	0.21039	0.2113765
d=100	0.24774	0.03235-0.24558	0.211365	0.03234-0.24566	0.21135	0.04977-0.24370	0.21134	0.2113765
d=1000	0.24976	0.00339-	0.211376	0.00340-	0.211376	0.00531-	0.211376	0.211376

		0.24952	4	0.24952	3	0.24929	5	5
$d=\infty$	0-0.25	0-0.25		0-0.25		0-0.25		0.211376 5

Table III. Pair approximation results for stationary points $p=p_{eq}$ or for regimes of propagation failure for planar interfaces separating populated and vacuum states. Results shown for S=1024.

	Vertical 100…	Si_1+i_2	$Si_1+i_2+\ldots+i_d$	Diagonal 11000…	$S(i_1+i_2)+i_3+\ldots+i_d$	Skew 11100…	$S(i_1+i_2+i_3)+i_4+\ldots+i_d$	Hyper-skew 111…
d=2	0.106016	0.105596		0.108312				0.108312
d=3	0.14123	0.13989	0.13989	0.14251	0.14251			0.14295
d=4	0.16084	0.15714	0.15716	0.15930-0.15941	0.15936	0.15990	0.15990	0.16014
d=5	0.17471	0.16784	0.16794	0.16902-0.16972	0.16939	0.17002	0.17001	0.17042
d=6	0.18500	0.17476-0.17533	0.17527	0.17460-0.17726	0.17608	0.17664-0.17677	0.17671	0.17726
d=7	0.19288	0.17860-0.18138	0.18055	0.17713-0.18349	0.18090	0.18120-0.18175	0.18149	0.18215
d=10	0.20814	0.17446-0.19593	0.19003	0.17204-0.19769	0.18985	0.18683-0.19256	0.19012	0.19093
d=100	0.24525	0.03219-0.24310	0.20932	0.03218-0.24318	0.20931	0.04952-0.24124	0.20930	0.20933
d=1000	0.24951	0.00339-0.24926	0.21117	0.00339-0.24927	0.21117	0.00539-0.24904	0.21117	0.21117
$d=\infty$	0-0.25	0-0.25		0-0.25		0-0.25		0.211376

								5

Table IV. KMC and pair estimates of p_e and p_f, and small errors $\delta p_{e(f)} = p_{e(f)}$(pair) - $p_{e(f)}$(KMC).

	KMC p_e	Pair p_e	δp_e		KMC p_f	Pair p_f	δp_f
d=2	0.09440	0.1083	0.0139		0.0871	0.1056	0.0185
d=3	0.13939	0.14295	0.0036		0.1353	0.1399	0.0046
d=4	0.15828	0.16014	0.0019		0.1548	0.1572	0.0024
d=5	0.16914	0.17042	0.0013		0.1664	0.1679	0.0015

Table V. Behavior of δ_m versus m and versus d from a MF dRDE analysis for vertical interfaces at $p = p_{eq}$.

d	δ_1	δ_2	δ_3	δ_4	δ_5	δ_6	δ_6
10	0.1687	2.02×10^{-2}	22.0×10^{-4}	2.39×10^{-4}	2.58×10^{-5}	2.78×10^{-6}	3.01×10^{-7}
100	0.0504	2.25×10^{-3}	9.79×10^{-5}	4.26×10^{-6}	1.85×10^{-7}		
1000	0.0161	2.44×10^{-4}	3.69×10^{-6}	5.57×10^{-8}			
10000	0.0077	3.56×10^{-5}	1.67×10^{-7}				

CHAPTER 4

THRESHOLD VERSION OF SCHLOEGL'S SECOND MODEL FOR AUTOCATALYSIS ON A SQUARE LATTICE

A paper to be submitted to *Physical Review E*

Chi-Jen Wang,[1,2] Da-Jiang Liu,[1] and J.W. Evans[1,2,3]

Ames Laboratory – USDOE[1] and Departments of Mathematics[2] and Physics & Astronomy[3], Iowa State University, Ames, Iowa 50011

1. Introduction

Stochastic lattice-gas reaction and reaction-diffusion models prescribe kinetic rules and rates for the annihilation, creation, and possibly hopping of diffusion of various species located at the sites of a periodic lattice [1]. The non-equilibrium steady states in these systems display phase transitions analogous to those in thermodynamic systems [1, 2]. A candidate for non-equilibrium discontinuous transitions is Schloegl's second model (S2M) for autocatalysis [3-13] (which also corresponds to a so-called quadratic contact process or QCP) on a lattice which involves: (i) spontaneous annihilation of particles at occupied sites, X, at rate p; and (ii) autocatalytic creation of particles at vacant sites, $\varnothing$, induced by nearby pairs of particles [7-12]. Schematically, the reaction steps are:

$$X \rightarrow \varnothing \text{ (spontaneous annihilation @ rate } p\text{)};$$

$$\varnothing + 2X \rightarrow 3X \text{ (autocatalytic creation).}$$

Mean-field (MF) analysis of the S2M or QCP suggests the existence of a discontinuous transition as the annihilation rate p increases through some p_{eq} from an active state with particle concentration $C>0$ for smaller p to an absorbing vacuum state $C=0$ for larger p. At the special equistability value $p = p_{eq}$, the two phases coexist and are equally stable. However, Kinetic Monte Carlo (KMC) analysis of Grassberger's version of S2M found only a continuous transition for a 2D lattice [4]. In contrast, analysis of a modified QCP version on a square lattice revealed a non-trivial *generic two-phase coexistence* (2PC) wherein the stable populated and vacuum phases coexist for a finite range of annihilation rate, p [8-12]. One quirk of standard QCP type models on a square lattice is that the vacuum state can always resist the growth of active droplets which cannot escape from any rectangular region containing them [7]. (One might describe this as trivial 2PC.) Similarly, the active state can never displace the vacuum state separated from it by a vertical interface. By perturbing the model (include particle hopping or spontaneous particle creation), this quirk and trivial 2PC disappear.

Non-trivial generic 2PC derives from an orientation-dependence of $p=p_{eq}$ for a stationary planar interface separating the two phases. This behavior contrasts phase coexistence in an equilibrium Hamiltonian system where planar interface separating phases is stationary at a unique point corresponding to equality of chemical potentials. As an aside, generic 2PC was first explored in Toom's model for voter dynamics [15,16] where the kinetic rules have an unappealing [17] asymmetry.

Our goal here is to analyze generic 2PC of discontinuous transitions in the "threshold" version [14] of the S2M or QCP on a square lattice [7, 8]. In Sec.2, we give

a detailed description of our stochastic gas-realization of this threshold version of Schloegl's second model on a 2D lattice, and present basic KMC simulation results. In Sec.3, we present the exact master equations describing spatially homogeneous and inhomogeneous states of the model, and perform MF and pair truncation analyses. From these approximations to the master equations for spatially heterogeneous states, we develop discrete reaction-diffusion equations (dRDE) in Sec.4. The interpretation of the dRDE results and their relationship to exact behavior of the stochastic reaction model is described in Sec.5. Further discussion and conclusions are provided in Sec.6.

2. Model Prescription and KMC Simulation

Various lattice-gas realizations of Schloegl's second model on a square lattice involve a spontaneous annihilation of particles at rate p and an autocatalytic creation at empty site given by nearby pairs of particles at rate dependent on the details of the local environment. The threshold version sets the creation rate of empty sites be a fixed rate 1 for two or more particles adjacent to the empty site [14]. It is instructive to note that previous studies considered an alternative specification or version known as Durrett's model which used $k/4$ as the creation rate of particles at empty sites where k is the number of "diagonal" pairs of particles on neighboring sites [7-13].

For spatially homogeneous states, we define the particle concentration, C, as the mean probability that a site is occupied, so $0 \leq C \leq 1$. We find that a stable "active" populated steady-state with concentration $C>0$ exists for a range of $0 \leq p \leq p_e$, and a vacuum state C=0 exists for all p. In the active populated state, particles are continually

created and annihilated, increasing p above p_e results in a discontinuous transition to a stable absorbing vacuum state with C=0. An ill-defined metastable extension of the active state exists for a small range, $p_e < p < p_s$, where p_s denotes the spinodal point. Our KMC studies found $p_e = 0.352$ for threshold model [14] (which should be compared with $p_e = 0.09443$ [8] for Durrett's model).

More detailed KMC studies of the threshold model for a square lattice [8,11] find *non-trivial* generic 2PC wherein stable active and vacuum states coexist for a finite range $p_f \leq p \leq p_e$. Specifically, we report that $p_f = 0.316$ and $p_e = 0.3518$. (For contrast, previous KMC simulation studies for Durrett's model revealed that $p_f = 0.0871$ and $p_e = 0.09443$.) This range is spanned by the orientation-dependent "equistability" values $p = p_{eq}$ corresponding to stationary planar interfaces separating these two states, and here $p_e = max\ p_{eq}$ corresponds to a diagonal interface. For a general orientation, for $0 \leq p < p_{eq}$, the active state displaces the vacuum state. For $p_{eq} < p < p_e$, the vacuum state displaces the active state. For $p_e < p < p_s$, the vacuum state transiently displaces the metastable active state until the latter spontaneously converts to the vacuum. One caveat is that for an exactly vertical interface, the active state can never propagate into the vacuum, because empty sites on the boundary of vacuum state have at most one occupied neighbor. More precisely, a vertical interface is stationary for all $p \leq p_f$, but the vacuum state expands for $p > p_f$, see [8-12].

From the above discussion, it is clear that the discontinuous phase transition behavior, and more generally the 2PC behavior, of threshold model is qualitatively similar to that of Durrett's model. However, because the autocatalytic creation rates are

generally higher in threshold model, all equistability values for p are much larger than in Durrett's model. Finally, as noted in the introduction, *trivial* 2PC occurs for all $p \leq p_e$ as the vacuum state is stable against expansion of droplets of the active state. We relegate an analysis of droplet dynamics, including a comparison between threshold and Durrett's model, to the **Appendix A**.

3. Master Equations for Homogeneous and Inhomogeneous States

Let *x (o)* denote a filled (empty) site on the square lattice, and let *P*'s denote the probabilities for various configurations of site clusters. For the general cases of spatially *inhomogeneous* states, the probability that a site is occupied or empty depends on its location. Thus, we let $C_{i,j} = P[x_{i,j}]$ denote the probability that the site (i, j) is occupied. Then, $P[o_{i,j}]$ (= 1 - $P[x_{i,j}]$ by conservation of probability) is the probability that site (i, j) is empty. Let $P[x_{i,j}\ x_{i,j+1}]$ ($P[o_{i,j}\ o_{i,j+1}]$) denotes the probability that sites (i, j) and $(i, j+1)$ are both occupied (empty). Also, $P[x_{i,j}\ o_{i,j+1}]$ and $P[o_{i,j}\ x_{i,j+1}]$ denote the probabilities of mixed occupied-empty pairs. Conservation of probability implies that $P[x_{i,j}\ o_{i,j+1}] + P[x_{i,j}\ x_{i,j+1}] = P[x_{i,j}]$, $P[o_{i,j}\ o_{i,j+1}] + P[o_{i,j}\ x_{i,j+1}] = P[o_{i,j}]$, etc. For spatially *homogeneous* case, these quantities do not depend on their locations, so $P[x_{i,j}] = P[x] = C$, $P[o_{i,j}] = P[o] = 1\text{-}C$, etc.

The exact master equations for our reaction model can be written as a coupled hierarchy for the evolution of the probabilities for empty single sites, empty pairs, etc. [18]. (We choose empty rather than occupied configurations, although the opposite choice is also possible.) In these equations for empty configurations, all gain terms are

associated with spontaneous particle annihilation, and all loss terms are associated with autocatalytic particle creation. Then, in terms of probabilities for empty configurations, the exact master equations for the threshold model have the form

$$d/dt\, P[o_{i,j}] = p \cdot P[x_{i,j}] - (P[o_{i,j}] - P\left[\begin{matrix} & o_{i,j+1} & \\ o_{i-1,j} & o_{i,j} & o_{i+1,j} \\ & o_{i,j-1} & \end{matrix}\right] - P\left[\begin{matrix} & x_{i,j+1} & \\ o_{i-1,j} & o_{i,j} & o_{i+1,j} \\ & o_{i,j-1} & \end{matrix}\right]$$

$$- P\left[\begin{matrix} & o_{i,j+1} & \\ o_{i-1,j} & o_{i,j} & x_{i+1,j} \\ & o_{i,j-1} & \end{matrix}\right] - P\left[\begin{matrix} & o_{i,j+1} & \\ o_{i-1,j} & o_{i,j} & o_{i+1,j} \\ & x_{i,j-1} & \end{matrix}\right] - P\left[\begin{matrix} & o_{i,j+1} & \\ x_{i-1,j} & o_{i,j} & o_{i+1,j} \\ & o_{i,j-1} & \end{matrix}\right]). \quad (1)$$

One can also develop a similar equation for $d/dt\ P[o_{i,\,j}\ o_{i,j+1}]$, and more complicated equations for the evolution of probabilities of larger configurations.

In order to analyze the infinite hierarchy including (1), a truncation approximation is needed which takes the form of a suitable factorization approximation for deriving the loss terms in (1), e.g., $P\left[\begin{matrix} & o_{i,j+1} & \\ x_{i-1,j} & o_{i,j} & o_{i+1,j} \\ & o_{i,j-1} & \end{matrix}\right]$ in terms of probabilities for simpler quantities. The site and pair approximations described below constitute the most natural lowest order factorization procedures. Taking the quantity $P\left[\begin{matrix} & o_{i,j+1} & \\ x_{i-1,j} & o_{i,j} & o_{i+1,j} \\ & o_{i,j-1} & \end{matrix}\right]$ as an example, the Mean-field (or site) truncation neglects all spatial correlations, so this treatment applies the following approximation

$$P\left[\begin{matrix} & o_{i,j+1} & \\ x_{i-1,j} & o_{i,j} & o_{i+1,j} \\ & o_{i,j-1} & \end{matrix}\right] \approx P[x_{i-1,j}]\, P[o_{i,j-1}]\, P[o_{i,j}]\, P[o_{i+1,j}]\, P[o_{i,j+1}].$$

The pair truncation attempts to account for correlation in the occupancy of the site (i,j) with its neighbors (and compensates for over-counting of this site), so this treatment applies the following approximation

$$P\left[\begin{matrix} & o_{i,j+1} & \\ x_{i-1,j} & o_{i,j} & o_{i+1,j} \\ & o_{i,j-1} & \end{matrix}\right] \approx P[x_{i-1,j}\ o_{i,j}] \cdot P[o_{i,j-1}\ o_{i,j}] \cdot P[o_{i+1,j}\ o_{i,j}] \cdot P[o_{i,j-1}\ o_{i,j}] / P[o_{i,j}]^3.$$

Because of accounting for correlations in the occupancy of the neighboring sites, predictions of pair approximation are closer to the precise KMC simulation results than those of the MF approximation.

3.1 Rate equations describing homogeneous states in the threshold model

Analysis of homogeneous states, where the probability of a site being occupied are the same for all site (i,j), provide an understanding of the basic behavior of S2M or QCP models on a 2D lattice. One can set $P[x]$ = C in the master equation (1), and use Mean-field and pair approximations for the loss terms.

Mean-field approximation. Let $P[x]$ = C, so $P[o]$ =1- C. It follows from the master equation that

$$dC/dt= -pC+(1-C)(C^2)(6-8C+3C^2). \qquad (2)$$

The steady state C satisfies $p=(1-C)C(6-8C+3C^2)$. The nonzero stable "active" state C_{act} has the following exact expression $C_{act} =11/12 -(1/2)(1/4+q)^{1/2}+(1/2)(1/2-q+85/(108(1/4+q)^{1/2}))^{1/2}$, where $q=2^{4/3}(-1+18p)/(9w)+w/(9(2)^{1/3})$, and $w=(88+243p-(3)^{3/2}(288+1520p+3339p^2-6912p^3)^{1/2})^{1/3}$. We deduce that the spinodal point p_s=0.815423. (p_s is the root of $288+1520p+3339p^2-6912p^3=0$.) For $p \leq p_s$, C_{act} (>0) is a stable active

state and C=0 is a stable vacuum state. For $p > p_s$ the vacuum state C=0 is the only steady state, see **Fig. 1(a)**.

Pair approximation. The simplest MF analysis for homogeneous states gives us a general qualitative idea of the steady state behavior, but in order to achieve at least a semi-quantitative picture capturing spatial correlations in the autocatalytic creation terms, we can consider the pair approximations. Let $\varepsilon = P[o]$ and $\phi = P[o\ o]$ be the probability of both nearest-neighbor empty pair are empty. For a spatially homogeneous state, these two quantities ε, ϕ satisfy the following evolution equations

$$\mathrm{d}/\mathrm{dt}\ \varepsilon = p(1-\varepsilon)-(\varepsilon-\phi)^2(\varepsilon^2+2\varepsilon\phi+3\phi^2)/(\varepsilon^3),$$

$$\mathrm{d}/\mathrm{dt}\ \phi = 2p(\varepsilon-\phi)-2(\varepsilon-\phi)^2\phi(\varepsilon+2\phi)/(\varepsilon^3). \qquad (3)$$

Stationary solutions satfies $\varepsilon = \sigma(1+2\sigma)/(1+2\sigma+3\sigma^2-3\sigma^3)$ and $p=(1-\sigma)\sigma(1+2\sigma)$, where $\sigma = \phi/\varepsilon$. It follows that $p_s(\mathrm{pair})=(10+7^{3/2})/54$ (~0.528153) at $\sigma = (1+7^{1/2})/6$ (~0.607625), see **Fig. 1(b)**.

3.2 Discrete RDE for inhomogeneous states in the site approximation:

For spatially inhomogeneous states, the equations of describing the evolution of the probabilities of single empty sites within the MF or site approximation have the form

$$d/dt P[o_{i,j}] = p\cdot(P[x_{i,j}]) - P[o_{i,j}]\ (\ 1 - P[o_{i-1,j}]\ P[o_{i+1,j}]\ P[o_{i,j-1}]\ P[o_{i,j+1}] - P[x_{i-1,j}]\ P[o_{i+1,j}]$$
$$P[o_{i,j-1}]\ P[o_{i,j+1}] - P[o_{i-1,j}]\ P[x_{i+1,j}]\ P[o_{i,j-1}]\ P[o_{i,j+1}] - P[o_{i-1,j}]\ P[o_{i+1,j}]\ P[x_{i,j-1}]$$
$$P[o_{i,j+1}] - P[o_{i-1,j}]\ P[o_{i+1,j}]\ P[o_{i,j-1}]\ P[x_{i,j+1}]). \qquad (4)$$

The detailed analysis of orientation-dependent equistability within this approximation is provided in section 4. We report that p_e(MF)= 0.70284 and p_f(MF)= 0.68468.

3.3 Discrete RDE for inhomogeneous states in the pair approximation:

For spatially inhomogeneous states, the pair approximation produces a coupled set of equations for the probabilities of single empty sites, and for the horizontal pair probabilities $P[o_{i-1,j}\ o_{i,j}]$ and vertical pair probabilities $P[o_{i,j-1}\ o_{i,j}]$. These evolution equations have the following form

$$
\begin{aligned}
d/dt\ P[o_{i,j}] &= p\cdot(P[x_{i,j}]) - P[o_{i,j}] +(P[o_{i-1,j}\ o_{i,j}]\ P[o_{i+1,j}\ o_{i,j}]\ P[o_{i,j-1}\ o_{i,j}]\ P[o_{i,j+1}\ o_{i,j}] \\
&\quad + P[x_{i-1,j}\ o_{i,j}]\ P[o_{i+1,j}\ o_{i,j}]\ P[o_{i,j-1}\ o_{i,j}]\ P[o_{i,j+1}\ o_{i,j}]+ P[o_{i-1,j}\ o_{i,j}]\ P[x_{i+1,j}\ o_{i,j}] \\
&\quad P[o_{i,j-1}\ o_{i,j}]\ P[o_{i,j+1}\ o_{i,j}]+ P[o_{i-1,j}\ o_{i,j}]\ P[o_{i+1,j}\ o_{i,j}]\ P[x_{i,j-1}\ o_{i,j}]\ P[o_{i,j+1}\ o_{i,j}] \\
&\quad + P[o_{i-1,j}\ o_{i,j}]\ P[o_{i+1,j}\ o_{i,j}]\ P[o_{i,j-1}\ o_{i,j}]\ P[x_{i,j+1}\ o_{i,j}]) / (P[o_{i,j}])^3.
\end{aligned}
$$

$$
\begin{aligned}
d/dt\ P[o_{i-1,j}\ o_{i,j}] &= p\cdot\ (P[o_{i-1,j}\ x_{i,j}] +P[x_{i-1,j}\ o_{i,j}]) - P[o_{i-1,j}\ o_{i,j}]\ (1 -P[o_{i+1,j}\ o_{i,j}]\ P[o_{i,j-1}\ o_{i,j}] \\
&\quad P[o_{i,j+1}\ o_{i,j}] - P[x_{i+1,j}\ o_{i,j}]\ P[o_{i,j-1}\ o_{i,j}]\ P[o_{i,j+1}\ o_{i,j}] - P[o_{i+1,j}\ o_{i,j}]\ P[x_{i,j-1}\ o_{i,j}] \\
&\quad P[o_{i,j+1}\ o_{i,j}] - P[o_{i+1,j}\ o_{i,j}]\ P[o_{i,j-1}\ o_{i,j}]\ P[x_{i,j+1}\ o_{i,j}])/ (P[o_{i,j}])^3 - P[o_{i-1,j}\ o_{i,j}] \\
&\quad (1 -P[o_{i-2,j}\ o_{i-1,j}]\ P[o_{i-1,j-1}\ o_{i-1,j}]\ P[o_{i-1,j+1}\ o_{i-1,j}] -P[x_{i-2,j}\ o_{i-1,j}]\ P[o_{i-1,j-1}\ o_{i-1,j}] \\
&\quad P[o_{i-1,j+1}\ o_{i-1,j}] -P[o_{i-2,j}\ o_{i-1,j}]\ P[x_{i-1,j-1}\ o_{i-1,j}]\ P[o_{i-1,j+1}\ o_{i-1,j}] - P[o_{i-2,j}\ o_{i-1,j}] \\
&\quad P[o_{i-1,j-1}\ o_{i-1,j}]\ P[x_{i-1,j+1}\ o_{i-1,j}])/ (P[o_{i-1,j}])^3.
\end{aligned}
$$

$$
\begin{aligned}
d/dt\ P[o_{i,j-1}\ o_{i,j}] &= p\cdot\ (P[o_{i,j-1}\ x_{i,j}] +P[x_{i,j-1}\ o_{i,j}]) - P[o_{i,j-1}\ o_{i,j}]\ (1 -P[o_{i+1,j}\ o_{i,j}]\ P[o_{i-1,j}\ o_{i,j}] \\
&\quad P[o_{i,j+1}\ o_{i,j}] - P[x_{i+1,j}\ o_{i,j}]\ P[o_{i-1,j}\ o_{i,j}]\ P[o_{i,j+1}\ o_{i,j}] - P[o_{i+1,j}\ o_{i,j}]\ P[x_{i-1,j}\ o_{i,j}] \\
&\quad P[o_{i,j+1}\ o_{i,j}] - P[o_{i+1,j}\ o_{i,j}]\ P[o_{i-1,j}\ o_{i,j}]\ P[x_{i,j+1}\ o_{i,j}])/ (P[o_{i,j}])^3 - P[o_{i,j-1}\ o_{i,j}] \\
&\quad (1 -P[o_{i,j-2}\ o_{i,j-1}]\ P[o_{i-1,j-1}\ o_{i,j-1}]\ P[o_{i+1,j-1}\ o_{i,j-1}] - P[x_{i,j-2}\ o_{i,j-1}]\ P[o_{i-1,j-1}\ o_{i,j-1}] \\
&\quad P[o_{i+1,j-1}\ o_{i,j-1}]- P[o_{i,j-2}\ o_{i,j-1}]\ P[x_{i-1,j-1}\ o_{i,j-1}]\ P[o_{i+1,j-1}\ o_{i,j-1}] - P[o_{i,j-2}\ o_{i,j-1}] \\
&\quad P[o_{i-1,j-1}\ o_{i,j-1}]\ P[x_{i+1,j-1}\ o_{i,j-1}])/ (P[o_{i,j-1}])^3. \qquad (5)
\end{aligned}
$$

The analysis of orientation-dependent equistability within this pair approximation will be presented in section 4. We find that p_e(pair)= 0.44253 and p_f(pair)= 0.41872.

4. Detailed Discrete RDE Analysis: Site and Pair Approximations

We consider the evolution of planar interfaces separating the active and vacuum states with orientations such that site probabilities only depend on the combination m=a*i*+b*j*. Thus, a≠0 and b=0 corresponds to a vertical interface, etc. Below, interface orientation is labeled by (a b). Results presented below are obtained from numerical integration of the MF and Pair dRDE's. The initial evolution data corresponds to a sharp interface with the active state $C_m = C_{act} = [1+ (1-4p)^{1/2}]/2$ on the left m<m* and the vacuum state $C_m = 0$ on the right m>m*. The mean interface location during subsequent motion is determined by the center of mass, $\langle m \rangle = \sum_m C_m/C_{act}$ for a large finite system about 1000 sites. The asymptotic interface velocity, V(*p*) = d/dt <m>, for large t is determine by integrating the dRDE's up to time $t \approx 4\times10^4$. Note that V(*p*) < 0 corresponds to the vacuum state displacing the active state for larger $p < p_s$.

Our focus is on determining stationarity and propagation failure by assessing variation of V(*p*) versus *p*. Since these features correspond to time-independent steady-states of the dRDE's, one could anticipate that direct analysis is possible without consideration of interface evolution. This can be achieved using iterated map techniques described in Appendix B. Results are consistent with those from numerical integration in time of the dRDE.

The inhomogenuous analysis allows us to assess the concentration profiles across the interfaces and equistability or propagation failure features of interface propagation as a function of orientation. Next, we will analyze three special orientations: diagonal, vertical, and near-vertical.

4.1. dRDE: mean-field results

Diagonal (11) interface. Here the probability $P[x_{i,j}]$ are the same for the site (i,j) located on diagonal lines with $i+j$ constant. Thus, we set $C_m=C_{i+j}= P[x_{i,j}]$, and from (4) it follows that

$$d/dt\ C_m= -pC_m+(1-C_m)[1-(1-C_{m-1})(1-C_{m+1})(1+C_{m+1}+C_{m-1}-3C_{m+1}C_{m-1})]. \qquad (6)$$

From numerical integration of (6) with initial data $C_m=C_{act}$, for $m < m^*$, and $C_m=0$, for $m > m^*$, we find that $p_{eq}(11, MF)= 0.70284$. Additional analysis below reveals that this value constitutes the maximum of p_{eq} for all orientations.

Vertical(10) interface. Here the $P[x_{i,j}]$ only depend on i. Thus, we set $C_m=C_i= P[x_{i,j}]$, and then C_m satisfies

$$d/dt\ C_m= -pC_m+(1-C_m)[1-2(1-C_{m-1})(1-C_{m+1})(1-C_m)C_m-(1-C_m)^2(1-C_{m+1}C_{m-1})]. \qquad (7)$$

Analysis of these equations yields $p_{eq}(10, MF)= 0.69131$. Propagation failure occurs for this vertical orientation for $p<p_{eq}(10, MF)$ due to the impossibility of particle creation at the vertical boundary of the vacuum state (i.e., the vertical interface is stationary in this regime). However, for $p>p_{eq}(10, MF)$, the vacuum states expands displacing the active state. In order to remove this trivial propagation failure in vertical orientation, we can

mis-orient the interface slightly so that $P[x_{i,j}] = C_{Si+j}$ with large S depends only on Si+j. This orientation tends towards vertical as S -> ∞, so we describe it as "near vertical".

Near vertical interface. Adding a small amount of misorientation to a vertical interface, now allows particle creation on the boundary of vaccuum state. Let $C_m = C_{Si+j} = P[x_{i,j}]$ for some large integer S, so then C_m satisfies

$$d/dt\ C_m = -pC_m+(1-C_m)[1-(1-C_{m-1})(1-C_{m+1})(1-C_{m-S})(1-C_{m+S}) -C_{m-1}(1-C_{m+1})(1-C_{m-S})(1- C_{m+S})-(1-C_{m-1})C_{m+1}(1-C_{m-S})(1-C_{m+S})-(1-C_{m-1})(1-C_{m+1})C_{m-S}(1-C_{m+S})-(1-C_{m-1})(1-C_{m+1})(1-C_{m-S})C_{m+S}]. \quad (8)$$

Numerical analysis reveals that as S→∞, one has p_{eq}(near-vert, MF)=0.68468, see **Table 1**. This value corresponds to the minimum of p_{eq} for all orientations.

4.2. dRDE: pair results

In the higher-order pair approximation, one accounts for spatial correlations by factorizing probabilities larger configurations of clusters of sites in terms of pairs (compensating for over-counting of some sites. Below we analyze special cases of the corresponding dRDE.

Diagonal interface. Let $\varepsilon_m=1-C_m=1-C_{i+j} =1-P[x_{i,j}]=P[o_{i,j}]$ and $\phi_{m+1/2}$ is the probability of a nearest-neighbor empty pair with one site in plane m and the other in plane m+1. Notice that, for diagonal interface, $\phi_{m+1/2} = \phi_{(2i+2j+1)/2}$ = horizontal pairs $P[o_{i,j}\ o_{i+1,j}]$ = vertical pairs $P[o_{i,j}\ o_{i,j+1}]$. From (5), ε_m and $\phi_{m+1/2}$ satisfy the following equations

$$d/dt\ \varepsilon_m = p(1-\varepsilon_m)-[((\varepsilon_m-\phi_{m+1/2})^2+(\varepsilon_m-\phi_{m-1/2})^2)(\varepsilon_m)^2+(\varepsilon_m-\phi_{m+1/2})(\varepsilon_m-\phi_{m-1/2})$$

$$(4\phi_{m+1/2}\phi_{m-1/2}-(\varepsilon_m-\phi_{m+1/2})(\varepsilon_m-\phi_{m-1/2}))]\ /(\varepsilon_m)^3,$$

$$d/dt\ \phi_{m-1/2} = p(\varepsilon_{m-1}+\varepsilon_m-2\phi_{m-1/2})-\phi_{m-1/2}((\varepsilon_m-\phi_{m+1/2})^2\varepsilon_m+2\phi_{m+1/2}(\varepsilon_m-\phi_{m+1/2})$$
$$(\varepsilon_m-\phi_{m-1/2}))/(\varepsilon_m)^3-\phi_{m-1/2}((\varepsilon_{m-1}-\phi_{m-3/2})^2\varepsilon_{m-1}+2\phi_{m-3/2}(\varepsilon_{m-1}-\phi_{m-3/2})$$
$$(\varepsilon_{m-1}-\phi_{m-1/2}))/(\phi_{m-1})^3. \qquad (9)$$

Analysis of these equations yields p_{eq}(11, pair)=0.442525.

<u>*Vertical interface.*</u> Let ε_m=1-C_m=1-C_i =1-$P[x_{i,j}]$=$P[o_{i,j}]$, ψ_m be the probability of a empty pair with both sites in the plane $i+j= m$, and $\phi_{m+1/2}$ be the probability of a nearest-neighbor empty pair with one site in the plane $i+j =m$ and the other in the plane $i+j =m+1$. Then ε_m , ψ_m, and $\phi_{m+1/2}$ satisfy the equations:

$$d/dt\ \varepsilon_m= p(1-\varepsilon_m)-((\varepsilon_m)^4-(\psi_m)^2\phi_{m-1/2}\phi_{m+1/2}-2(\varepsilon_m-\psi_m)\ \psi_m\ \phi_{m-1/2}\phi_{m+1/2}-(\psi_m)^2$$
$$(\varepsilon_m-\phi_{m-1/2})\phi_{m+1/2}-\ (\psi_m)^2\phi_{m-1/2}(\varepsilon_m-\phi_{m+1/2}))/(\varepsilon_m)^3;$$

$$d/dt\ \psi_m=2p(\varepsilon_m-\psi_m)-2\psi_m(\varepsilon_m-\phi_{m-1/2})(\varepsilon_m-\phi_{m+1/2})/(\varepsilon_m)^2-2\psi_m(\varepsilon_m-\psi_m)(\varepsilon_m(\phi_{m-1/2}+\phi_{m+1/2})$$
$$-2\phi_{m-1/2}\phi_{m+1/2})/(\varepsilon_m)^3;$$

$$d/dt\ \phi_{m-1/2}= p(\varepsilon_{m-1}+\varepsilon_m-2\phi_{m-1/2})-\phi_{m-1/2}(\varepsilon_m-\psi_m)((\varepsilon_m-\psi_m)^2+2\psi_m(\varepsilon_m-\phi_{m+1/2}))/(\varepsilon_m)^3$$
$$-\phi_{m-1/2}(\varepsilon_{m-1}-\psi_{m-1})((\varepsilon_{m-1}-\psi_{m-1})^2+2\psi_{m-1}(\varepsilon_{m-1}-\phi_{m-3/2}))/(\varepsilon_{m-1})^3; \qquad (10)$$

Analysis of these equations yields p_{eq}(10, pair)=0.421254.

<u>*Near vertical interface.*</u> We let ε_m=1-C_m=1-C_i =1-P$[x_{i,j}]$=P$[o_{i,j}]$, $\phi_{m+1/2}$ be the probability of a nearest-neighbor empty pair with one site in the plane m and the other in the plane m+1, and $\varphi_{m+S/2}$ is the probability of a nearest-neighbor empty pair with one site in the plane m and the other in plane the m+S. We report these particularly

complicated equations in **Appendix C**. Numerical analysis reveals that as $S \rightarrow \infty$, one obtains p_{eq}(near-vert, pair)= 0.418723, see **Table 2**.

5. dRDE Predictions Versus Precise Stochastic Model Behavior (from KMC)

Mean-field type treatments of stochastic lattice-gas models with discontinuous transitions are expected to predict bistability, and furthermore will also produce generic 2PC as illustrated by the above analyses. For a comparison between MF-type dRDE predictions and stochastic reaction model behavior, it is instructive to focus on equistability for the principal diagonal and vertical orientations and a near-vertical orientation.

For a diagonal (11) interface, there is no propagation failure for the MF-type dRDE, so the predicted stationary p_{eq}(11) corresponds to that in the stochastic model. A large discrepancy occurs at the MF level where p_{eq}(11, MF)= 0.70284 (as expected), but there is much better (although still not quantitative) agreement between p_{eq}(11, pair) ≈ 0.44253 and p_{eq}(11, KMC) ≈ 0.3518.

For a vertical (10) interface, propagation failure is expected for p below some critical value as the active state cannot displace the vacuum state. This feature applies to both the stochastic model and to various dRDE's. However, we claim that p_{eq}(10) from the MF or pair approximation does *not* correspond to the p_{eq}(10, KMC) since these MF type formulations "artificially extend" the propagation failure regime. The stochastic models always produce a roughened (10) interface with steps, a feature not reflected in MF analysis of a perfectly vertical interface in MF analysis. Thus, p_{eq} for stationarity of

a slightly misoriented interface better reflects the p_{eq}(10, KMC). Specifically, we identify p_{eq}(near-vert) from MF or pair approximations, which corresponds to stationarity of a (10) interface with rare diagonal steps, to compare with the p_{eq}(10, KMC). A large discrepancy occurs between these quantities at the MF level where p_{eq}(near-vert, MF)=0.68468 (as expected), but there is much better (although still not quantitative) agreement between p_{eq}(near-vert, pair) ≈0.41872 and p_{eq}(10, KMC) ≈0.316. We show an appropriate schematic summary in **Fig. 1**.

In the above analysis, absolute values of various equistabilty points are dramatically shifted from KMC values at the lowest MF level, and still significantly shifted at the pair level. However, it is instructive to also compare KMC versus MF type predictions for differences between these points, as these describe the width of the 2PC regime which is of particular interest. For a precise estimate of the width of the 2PC regime, we consider KMC values for Δp_{eq}(2PC width) = p_{eq}(11) - p_{eq}(10). Furthermore, rather than just comparing KMC and MF type predictions for absolute values of the 2PC width, it is also natural to compare rescaled values (where one for example rescales by p_e). See **Table 3** for a summary of these comparisons. For the threshold model, the pair approximation estimates improve those of the simplest MF approximation. Given the subtle nature of the orientation-dependence of interface propagation, we regard the pair approximation is being quite effective reflecting behavior in the stochastic model.

Finally, it is instructive to consider the extent of *artificial propagation failure* (APF) for vertical interfaces occurring in the MF type treatments as measured by

$\Delta p_{apf}(10) = p_{eq}(10) - p_{eq}(10D)$. This difference decreases from $\Delta p_{apf}(10) = 0.0066$ for the MF treatment to $\Delta p_{apf}(10) = 0.0025$ for the higher-order pair treatment.

6. Conclusions

Our stochastic lattice-gas realization of a threshold version of Schloegl's second model for autocatalysis on a square lattice exhibits generic 2PC associated with an orientation dependence of the stationary point for planar interfaces separating coexisting active and vacuum states. We have demonstrated that dRDE associated with MF approximations to the master equations for spatially non-uniform states of the reaction model are effective in capturing and elucidating this behavior. The higher-order pair approximation exhibits improved predictive capability.

One subtlety in making this comparison is that MF-type dRDE analysis reveals artificial propagation failure (APF) for vertical interfaces. MF dRDE analysis for near-vertical interfaces shows that p_{eq}(near-vert) lies strictly below p_{eq}(vert) for an exactly vertical interface. We claim that p_{eq}(near-vert) which corresponds to p_f(KMC) as the presence of kinks on the near-vertical interface is needed to mimic a vertical interface in KMC simulations where kinks are formed spontaneously. Diagonal interfaces exhibit no propagation failure in MF type treatments, and p_{eq}(diag) corresponds to p_e(KMC).

Previous limited analysis of the threshold version of the S2M or QCP [14] did not report orientation dependence or 2PC, rather incorrectly claiming that there was a unique equistability point. This study also claimed a lack of metastability for the model, in contrast to our expectations.

It is appropriate to comment on whether the phenomenology and dRDE methodology discussed here apply for broader classes of reaction models. Threshold modification of QCP and Schloegl's second model reveals analogous behavior to Durrett's model square lattice [9, 19]. We expect other modifications also reveal similar behavior.

Appendix A: Droplet Dynamics in the Threshold and Durrett Models

Stability of a state in a system with two states is usually taken to mean that embedded droplets of the other phase will always shrink. In contrast, a droplet of the more stable phase embedded in the less stable phase will grow provided it exceeds a critical size. For the models described here, the active state is more stable than vacuum state for small p. (However, a quirk is that trivial 2PC occurs for all $p \leq p_e$ as the vacuum state is stable against expansion of droplets of the active state.) The vacuum state is more stable than active state for large p.

Specifically, here we consider the situation for p larger than p_e where a vacuum droplet embedded in active state will shrink for small initial area, and grow for large initial area. There is a critical vacuum droplet that remains unchanged in the active state.

Let Rc(p) be the critical radius of vacuum droplet embedded in active state, and the radius is defined as $R=(A/\pi)^{1/2}$, where A is the area of vacuum droplet. For p well above p_e (but still below p_s), the vacuum state is much more stable than the active state and the vacuum droplet grows easily, therefore the critical droplet is small. When p is closer to p_e, the vacuum droplet shrinks easily, so the corresponding critical droplet must

be very big. We have analyzed the asymptotic divergence of Rc(p) as $p \to p_e+$ by assessing the relation between 1/Rc and p_1, where $p_1=(p-p_e)/p_e$ is the rescaled p value. See **Fig. 3**.

Appendix B: Iterated Map for MF Treatment of Stationary Interfaces

The time-independent discrete RDE describing stationary planar interfaces can be converted to an *iterated map* for $[u_m, v_m] = [C_{m-1}, C_m]$ of the form

$$u_{m+1} = v_m \text{ and } v_{m+1} = F(u_m, v_m, p).$$

The uniform active and vacuum steady-states correspond to fixed points of the map, $[u,v] = [C_{act}(p), C_{act}(p)]$, with $C_{act}(p)= (1+(1-4p)^{1/2})/2$, and $[u,v] = [0,0]$, respectively. Except for a vertical interface, the stationary concentration profiles smoothly approach the active and vacuum state away from the interface. Correspondingly, orbits of the above map smoothly connect the fixed points, while remaining within the physical domain $0 \leq u, v \leq 1$. The orbit goes through the active fixed point and intersects physical domain boundary for $p \leq p_{eq}(10)$, tangentially for $p=p_{eq}(10)$.

To generate these orbits, we choose an initial point $[u_1, v_1] = [C_{act} + \varepsilon, C_{act} + \varepsilon\lambda]$ for small ε, where the exact value of λ can be determined by stationary evolution equation (and describes the asymptotic form of the interface). Then, we iterate the map for a selected value of p, and determine whether the orbit has the desired form. For example, in the case of a *diagonal interface*, if one chooses $p<p_{eq}(11)$, the orbit exits the physical domain (see **Fig. 4a**). At the unique value of $p=p_{eq}(11)$, the orbit will smoothly

approach [0,0] (see **Fig. 4b**). For $p>p_{eq}(11)$, the orbit remains within this domain (see **Fig. 4c**). The *vertical interface*, we show the orbit for $p<p_{eq}(10)$ in **Fig. 5a;** $p=p_{eq}(10)$ in **Fig. 5b;** $p>p_{eq}(10)$ in **Fig. 5c.**

To provide one example of the function $F(u_m, v_m, p)$, we consider a vertical interface. If we let $(u_m, v_m) = (C_m, C_{m+1})$ in (7), then the stationary states u_m, v_m, v_{m+1} satisfy the equation

$$0= -pv_m+ (1-v_m)[1-2(1-u_m)(1-v_{m+1})(1-v_m)v_m-(1-v_m)^2(1-v_{m+1}u_m)].$$

So we can rewrite the term v_{m+1} as a function of the quantities (u_m, v_m, p), that is,

$$v_{m+1}=F(u_m, v_m, p)= (1+v_m-2u_mv_m-1/(1-v_m)+pv_m/(1-v_m)^2)/(u_m+2v_m-3u_mv_m).$$

Appendix C: dRDE for Near-Vertical Planar Interfaces in the Pair Approximation

For a pair approximation treatment of near-vertical interface orientation, we let $\varepsilon_m=1-C_m=1-C_i =1- P[x_{i,j}]=P[o_{i,j}]$, $\phi_{m+1/2}$ is the probability of a nearest-neighbor empty pair with one site in plane m and the other in plane m+1, and $\varphi_{m+S/2}$ is the probability of a nearest-neighbor empty pair with one site in plane m and the other in plane m+S. Then, one has that

$$d/dt\ \varepsilon_m= p(1-\varepsilon_m)-((\varepsilon_m)^4-\phi_{m+1/2}\phi_{m-1/2}\varphi_{m+S/2}\varphi_{m-S/2}-(\varepsilon_m-\phi_{m+1/2})\phi_{m-1/2}\varphi_{m+S/2}\varphi_{m-S/2}$$
$$-\phi_{m+1/2}(\varepsilon_m-\phi_{m-1/2})\varphi_{m+S/2}\varphi_{m-S/2}-\phi_{m+1/2}\phi_{m-1/2}(\varepsilon_m-\varphi_{m+S/2})\varphi_{m-S/2}-\phi_{m+1/2}\phi_{m-1/2}\varphi_{m+S/2}$$
$$(\varepsilon_m-\varphi_{m-S/2}))/(\varepsilon_m)^3;$$

$$d/dt\ \phi_{m-1/2}= p(\varepsilon_{m-1}+\varepsilon_m-2\phi_{m-1/2})-\phi_{m-1/2}((\varepsilon_m-\phi_{m+1/2})(\varepsilon_m-\varphi_{m-S/2})(\varepsilon_m-\varphi_{m+S/2})+\phi_{m+1/2}$$
$$(\varepsilon_m-\varphi_{m-S/2})\ (\varepsilon_m-\varphi_{m+S/2})+(\varepsilon_m-\phi_{m+1/2})\varphi_{m-S/2}(\varepsilon_m-\varphi_{m+S/2})+(\varepsilon_m-\phi_{m+1/2})$$

$(\varepsilon_m-\varphi_{m-S/2})\varphi_{m+S/2})/(\varepsilon_m)^3-\phi_{m-1/2}$ $((\varepsilon_{m-1}-\phi_{m-3/2})(\varepsilon_{m-1}-\varphi_{m-1+S/2})(\varepsilon_{m-1}-\varphi_{m-1-S/2})+$

$\phi_{m-3/2}(\varepsilon_{m-1}-\varphi_{m-1+S/2})(\varepsilon_{m-1}-\varphi_{m-1-S/2})+$ $(\varepsilon_{m-1}-\phi_{m-3/2})\varphi_{m-1+S/2}(\varepsilon_{m-1}-\varphi_{m-1-S/2})+(\varepsilon_{m-1}-$

$\phi_{m-3/2})(\varepsilon_{m-1}-\varphi_{m-1+S/2})$ $\varphi_{m-1-S/2})/(\varepsilon_{m-1})^3$;

$d/dt\ \varphi_{m-S/2}= p(\varepsilon_{m-S}+\varepsilon_m-2\varphi_{m-S/2})-\varphi_{m-S/2}((\varepsilon_m-\varphi_{m+S/2})(\varepsilon_m-\phi_{m-1/2})(\varepsilon_m-\phi_{m+1/2})+\varphi_{m+S/2}$

$(\varepsilon_m-\phi_{m-1/2})(\varepsilon_m-\phi_{m+1/2})+(\varepsilon_m-\varphi_{m+S/2})\phi_{m-1/2}(\varepsilon_m-\phi_{m+1/2})+(\varepsilon_m-\varphi_{m+S/2})$

$(\varepsilon_m-\phi_{m-1/2})\phi_{m+1/2})/(\varepsilon_m)^3-\varphi_{m-S/2}((\varepsilon_{m-S}-\varphi_{m-3S/2})(\varepsilon_{m-S}-\phi_{m-S+1/2})(\varepsilon_{m-S}-\phi_{m-S-1/2})+$

$\varphi_{m-3S/2}(\varepsilon_{m-S}-\phi_{m-S+1/2})(\varepsilon_{m-S}-\phi_{m-S-1/2})+$ $(\varepsilon_{m-S}-\varphi_{m-3S/2})\phi_{m-S+1/2}(\varepsilon_{m-S}-\phi_{m-S-1/2})+$

$(\varepsilon_{m-S}-\varphi_{m-3S/2})(\varepsilon_{m-S}-\phi_{m-S+1/2})\phi_{m-S-1/2})/(\varepsilon_{m-S})^3$;

Numerical analysis of these equations yields p_{eq}(near-vert, pair)=0.418723.

References

[1] J. Marro and R. Dickman, *Nonequilibrium Phase Transitions in Lattice Models* (Cambridge UP, Cambridge, 1999).

[2] G. Odor, Rev. Mod. Phys. **76**, 663 (2004).

[3] F. Schloegl, Z. Phys. **253**, 147 (1972).

[4] P. Grassberger, Z. Phys. B Cond. Matt. **47**, 365 (1982).

[5] J.P. Boon, D. Dab, R. Kapral, and A. Lawniczak, Phys. Rep. **273**, 55 (1996).

[6] S. Prakash and G. Nicolis, J. Stat. Phys. **86**, 1289 (1997).

[7] R. Durrett, SIAM Rev. **41**, 677 (1999).

[8] D.-J. Liu, X. Guo, and J.W. Evans, Phys. Rev. Lett. **98**, 050601 (2007).

[9] X. Guo, J.W. Evans, and D.-J. Liu, Physica A **387**, 177 (2008).

Sites in the last two loss terms in eq. (17) are mislabeled. One should replace i with i-1.

[10] X. Guo, D.-J. Liu, and J.W. Evans, J. Chem. Phys. **130**, 074106 (2009).

[11] X. Guo, Y. de Decker, and J.W. Evans, Phys. Rev. E **82**, 021121 (2010).

[12] C.-J. Wang, X. Guo, D.-J. Liu, and J.W. Evans, J. Stat. Phys. **144**, 1308 (2011).

[13] C.-J. Wang, X. Guo, D.-J. Liu, and J.W. Evans, Phys. Rev. E. **85**, 041109 (2012).

[14] da Silva, E.F., de Oliveira, M.J.; J. Phys. A: Math. Theor. **44,** 135002 (2011)

[15] A.L. Toom in *Multicomponent Random Systems*, edited by R.L. Dobrushin and Y.G. Sinai (Dekker, New York, 1980).

[16] C.H. Bennett and G. Grinstein, Phys. Rev. Lett. **55**, 657 (1985).

[17] R.S. MacKay, Nonlinearity **21**, T273 (2008).

[18] J.W. Evans, Rev. Mod. Phys. **65**, 1281 (1993).

[19] Liu, D.-J.; J. Stat. Phys. **135**, 77 (2009)

Figures

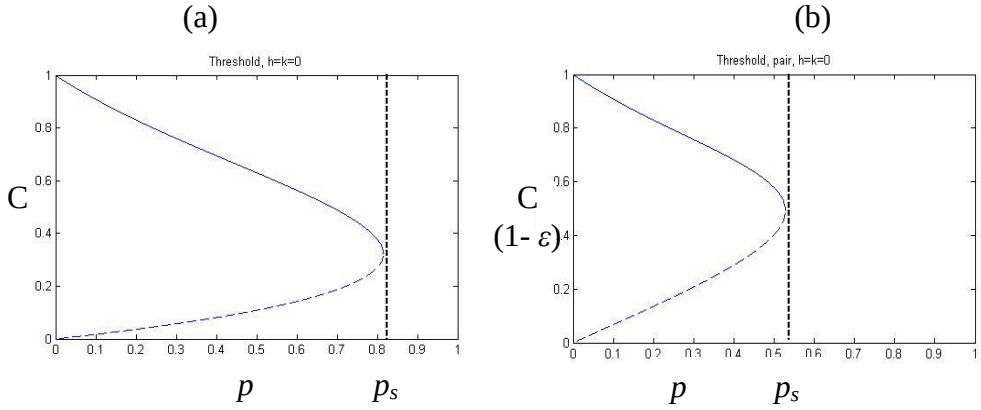

Fig.1. The steady states C versus the annihilation rate p. The dashed curve is the curve of the unstable solution; the solid curve is the stable active steady state $C_{act}(p)$ of the master equation for (a) MF (b) pair approximations.

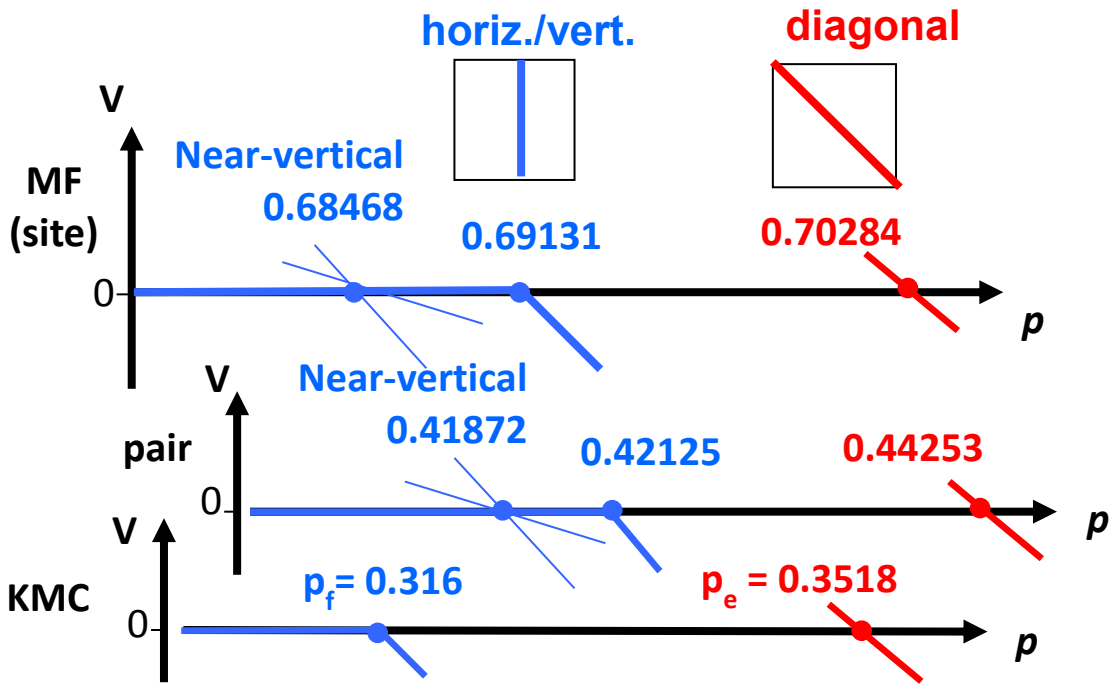

Fig.2. Schematic summary of MF dRDE, pair dRDE, and KMC results for propagation velocity, V(*p*), versus particle annihilation rate, *p*, of planar interfaces separating the active and vacuum states for various orientations.

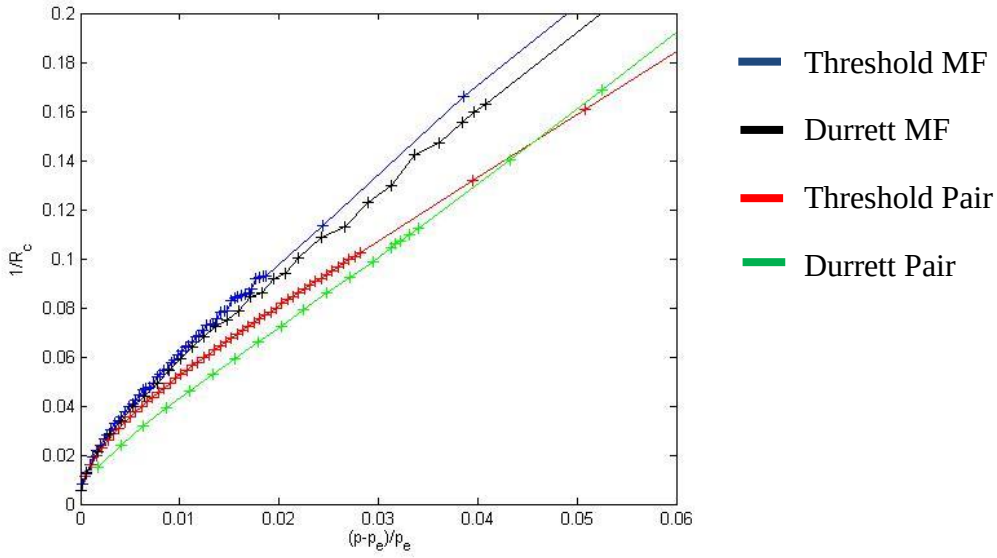

Fig.3. Schematic 1/Rc behavior of MF and pair results in threshold and Durrett's models as $p_1 \to 0$.

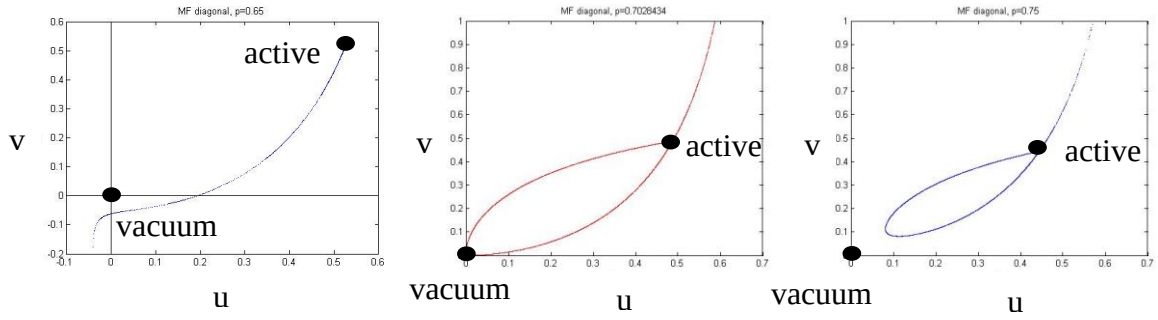

(a) p=0.65 (b) p=0.7028434 (c) p=0.75

Fig.4. Orbits of the iterated map associated with the MF dRDE for a diagonal interface with: (a) $p = 0.65 < p_{eq}(11) \approx 0.70284$; (b) $p = p_{eq}(11)$; (c) $p = 0.75 > p_{eq}(11)$.

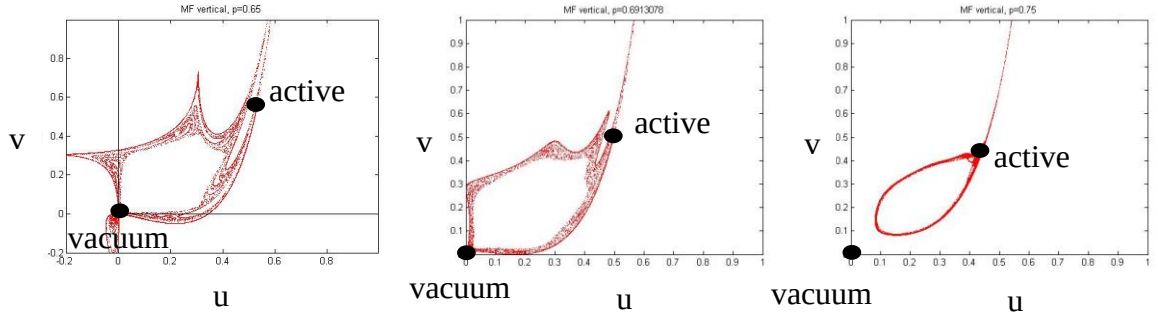

(a) p=0.65 (b) p=0.6913078 (c) p=0.75

Fig.5. Orbits of the iterated map associated with the MF dRDE for a vertical interface with: (a p) = $0.65 < p_{eq}(10) \approx 0.69131$; (b) $p = p_{eq}(10)$; (c) $p = 0.75 > p_{eq}(10)$.

Tables

Table 1. The equistability value p_{eq} of MF approximation for the orientation 64i+j, 256i+j, and 1024i+j.

S=	64	256	1024
p_{eq}(MF, Si+j)=	0.6846768	0.6846768	0.6846768

Table 2. The equistability value p_{eq} of pair approximation for the orientation 64i+j, 256i+j, and 1024i+j.

S=	64	256	1024

p_{eq}(pair, Si+j)=	0.418723	0.418723	0.418723

Table 3. Differences in stationary values for p for various interface orientations.

Treatment	Threshold MF	Threshold Pair	Threshold KMC		Durrett MF	Durrett Pair	Durrett KMC
Δp_{eq}(2PC width)	0.0182	0.0238	0.0358		0.0063	0.0027	0.0073
Δp_{eq}(2PC width) /p_e	0.0259	0.0538	0.1018		0.0298	0.0249	0.0773

CHAPTER 5

SCHLOEGL'S SECOND MODEL FOR AUTOCATALYSIS ON A SQUARE LATTICE WITH SPONTANEOUS PARTICLE CREATION OR HOPPING

A paper to be submitted

Chi-Jen Wang,[1,2] Da-Jiang Liu,[1] and J.W. Evans[1,2,3]

Ames Laboratory – USDOE[1] and Departments of Mathematics[2] and Physics & Astronomy[3], Iowa State University, Ames, Iowa 50011

1. Introduction

Stochastic lattice-gas reaction and reaction-diffusion models prescribe kinetic rules and rates for the annihilation, creation, and possibly hopping of diffusion of various species located at the sites of a periodic lattice [1]. The non-equilibrium steady states in these systems display phase transitions analogous to those in thermodynamic systems [1, 2]. A candidate for non-equilibrium discontinuous transitions is Schloegl's second model (S2M) for autocatalysis [3-13] (which also corresponds to a so-called quadratic contact process or QCP) on a square or cubic lattice. The simplest version of the model involves just: (i) spontaneous annihilation of particles at occupied sites, X, at rate p; and (ii) autocatalytic creation of particles at vacant sites, $\varnothing$, induced by nearby particles [7,8-12]. These reaction steps can be represented schematically as: $X \rightarrow \varnothing$ (spontaneous annihilation @ rate p) and $\varnothing + 2X \rightarrow 3X$ (autocatalytic creation). More general versions of

the model can include: (iii) spontaneous creation of particles at rate k; and (iv) diffusive hopping of particles to adjacent empty sites at rate h (per direction). These steps can be represented as: $\varnothing \rightarrow X$ (spontaneous creation @ rate k) and $\varnothing+X \rightarrow X+\varnothing$ (hopping @ rate h).

Mean-field (MF) analysis of the S2M or QCP suggests the existence of a discontinuous transition as p increases through some equistability p_{eq} from an active state with particle concentration $C>0$ for smaller p to an inactive state with small C (or C=0 for k=0) for larger p. However, Kinetic Monte Carlo (KMC) analysis of Grassberger's version of S2M found only a continuous transition for 2D and 3D lattices [4]. In contrast, analysis of basic QCP version on a square lattice excluding (iii) spontaneous creation and (iv) hopping revealed a non-trivial *generic two-phase coexistence* (2PC) wherein the stable populated and inactive phases coexist for a finite range of annihilation rate, p [8-12]. The non-trivial 2PC derives from an orientation-dependence of $p=p_{eq}$ for a stationary planar interface separating the two phases. This behavior contrasts phase coexistence in an equilibrium Hamiltonian system where planar interface separating phases is stationary at a unique point corresponding to equality of chemical potentials. One quirk of basic QCP type models [excluding mechanisms (iii) and (iv)] on a square or cubic lattice is that the active state can never displace the inactive vacuum state separated from it by a vertical interface. "Perturbing" the basic model to include spontaneous particle creation (iii) or particle hopping (iv) removes this quirk.

Our goal here is to analyze generic 2PC associated with the discontinuous transition in the perturbed model with either autocatalytic creation at a small rate $k<<1$ or hopping at a small rate $h<<1$. This will be done just at the level of the simplest MF approximation. In Sec.2, we give a detailed description of our stochastic gas-realization of Schloegl's second model on a square lattice, and present the exact master equations for spatially homogeneous states. In Sec.3, we use MF truncation analyses for spatially heterogeneous states to develop orientation-dependent discrete reaction-diffusion equation (dRDE). The interpretation of propagation failure and the asymptote behavior of the interface velocity are in Sec.4. The stability of states analysis is described in Sec.5. Further discussion and conclusions are provided in Sec.6.

2. Model Prescription and Mean-Field Analysis for Homogeneous States

Our Schloegl's second model in the square lattice involves: (i) a spontaneous annihilation rate p; (ii) an autocatalytic creation of particles at empty sites at rate $r/4$, where r is the number of diagonal pairs of particles on neighboring sites; and either (iii) spontaneous creation small rate k at empty sites [8, 14], or (iv) hopping to neighboring empty sites at small rate h [10, 11]. A schematic of these steps is shown in **Fig. 1.**

Previous studies of this Schloegl's second model for $h=k=0$ [15, 16] found a non-trivial generic *two phase coexistence* (2PC) wherein stable active and inactive vacuum states coexist for a finite range $p_f \leq p \leq p_e$. This range is spanned by the orientation-dependent "equistability" values $p = p_{eq}$ for stationary planar interfaces separating these states. The *max* p_{eq} (defined as p_e) corresponds to a diagonal interface, and *min* p_{eq}

(defined as p_s) corresponds to a near-vertical interface. For a general (non-vertical) orientation, when $0 \le p < p_{eq}$, the active state displaces the poisoned state. For $p_{eq} < p < p_e$, the poisoned state displaces the active state. For $p_e < p < p_s$, the poisoned state transiently displaces the metastable active state until the latter spontaneously converts to the poisoned.

For the exactly vertical interface when h=k=0, the active state can never propagate into the inactive vacuum state (empty sites in this poisoned state have at most one occupied neighbor). The trivial 2PC occurs for all $p \le p_e$ as the vacuum state is stable against expansion of droplets of the active state. By adding "perturbations" of spontaneous creation k>0 or hopping h>0, particles can now be formed at the vertical boundary of the inactive state (which is no longer a vacuum state for k>0). Thus, we might expect that the region of propagation failure where a vertical interface is stationary when h=k=0 is completely removed (as the active state can now displace the inactive state). However, the analysis below shows that it is not completely removed but just becomes narrower.

Let x(o) denote a filled (empty) site, and let P's denote probabilities of various configurations of such sites. For spatially homogeneous states, we define the particle concentration, C=P[x], as the mean probability that a site is occupied, so P[o] = 1-C. Then, for spatially homogeneous states, the lowest-order equations in the exact master equations have the form:

<u>*with hopping*</u>: $d/dtP[o] = p \cdot P[x] - ¼ \left(P\begin{bmatrix} x & \\ o & x \end{bmatrix} + P\begin{bmatrix} o & x \\ x & \end{bmatrix} + P\begin{bmatrix} x & o \\ & x \end{bmatrix} + \right.$

$$P\begin{bmatrix} & x \\ x & o \end{bmatrix}) + (-h\cdot P[o\ x] + \text{other hopping terms}), \qquad (1)$$

with spontaneous creation: $d/dtP[o] = p\cdot P[x] - ¼\,(P\begin{bmatrix} x & \\ o & x \end{bmatrix} + P\begin{bmatrix} o & x \\ x & \end{bmatrix} +$

$$P\begin{bmatrix} x & o \\ & x \end{bmatrix} + P\begin{bmatrix} & x \\ x & o \end{bmatrix}) - k\cdot P[o]. \qquad (2)$$

The first gain terms in (1) and (2) correspond to spontaneous the particle annihilation producing desired empty configurations. The second loss terms correspond to autocatalytic particle creation destroying the empty configurations under consideration, and involve summing contributions over various relevant configurations multiplied by the appropriate rates. The last term corresponds to the hopping or spontaneous particle creation perturbations.

2.1 Mean-field type equations with hopping *h*.

The simplest mean-field (MF) approximation ignores all spatial correlations in occupancy of different sites and thus factors multi-site probabilities in terms of $P[x]$ and $P[o]$. Applying factorization directly to the exact equation (1), and noting that $d/dtP[o] = -dC/dt$ yields the MF kinetic equation

$$d/dtC = -p\cdot C + (1-C)C^2.$$

This homogeneous equation is independent of *h* and exactly the same with the previous analysis of the model without adding the perturbation terms. We find that there is a stable active state $C_{act} = [1+(1-4p)^{1/2}]/2$ for $p<p_s$ and a vacuum state C=0, where $p_s = 0.25$ is the spinodal point.

2.2 Mean-field type equations with spontaneous creation rate k

Using the same Mean-Field approximation as in 2.1, the master equation (2) yields the following equation

$$d/dtC = -p\cdot C + k\cdot(1-C) + (1-C)C^2.$$

In the model including small spontaneous creation rate k, the vacuum state C=0 is not a steady state, instead there exists a nonzero low-concentration stable "inactive" steady-state $C \sim k/(p+k)$ for $p \geq ps_-$, where ps_- is a spinodal point. Also another stable high-concentration active steady state $C_{act}>0$ exists for $p \leq ps_+$, where ps_+ is the other spinodal point.

More specifically, for k in [0, 1/27), there are two spinodal points ps_- and ps_+, where $0< ps_- < ps_+ <1$. If $p< ps_-$, there is only one active steady state; $ps_- \leq p \leq ps_+$, there are two stable states; $p> ps_+$, there is only one low-concentration steady state, see **Fig. 2 (a)** for k=0.001 and **(b)** for k=0.01. For $k \geq 1/27$, there is only one stable state for all p, *e.g.* k=0.05 in **Fig. 2(c).** The bistability of stationary states disappears in the model with higher spontaneous creation rate $k>1/27$.

3. Inhomogeneous States: Hierarchical Equations and Discrete Reaction-Diffusion Equations (dRDE) Analysis

The homogeneous master equation and the associated MF analysis provide basic insight into the behavior of the S2M or QCP models. However, considerable additional insight comes from consideration of spatially inhomogeneous states including planar

interfaces separating the active and inactive states. The lowest-order equations in the exact master equations for these states have the form

<u>*with hopping*</u>: $d/dtP[o_{i,j}] = p\cdot P[x_{i,j}] - ¼(P[\begin{smallmatrix} x_{i,j+1} & \\ o_{i,j} & x_{i+1,j} \end{smallmatrix}] + P[\begin{smallmatrix} & o_{i,j} & x_{i+1,j} \\ x_{i,j-1} & & \end{smallmatrix}] +$

$P[\begin{smallmatrix} x_{i-1,j} & o_{i,j} \\ & x_{i,j-1} \end{smallmatrix}] + P[\begin{smallmatrix} & x_{i,j+1} \\ x_{i-1,j} & o_{i,j} \end{smallmatrix}]) + (-h\cdot P[o_{i,j}\, x_{i+1,j}] +$

$h\cdot P[x_{i,j}\, o_{i+1,j}]$+ other hopping terms),

<u>*with spontaneous creation*</u>: $d/dtP[o_{i,j}] = p\cdot P[x_{i,j}] - k\cdot P[o_{i,j}] - ¼(P[\begin{smallmatrix} x_{i,j+1} & \\ o_{i,j} & x_{i+1,j} \end{smallmatrix}] +$

$P[\begin{smallmatrix} & o_{i,j} & x_{i+1,j} \\ x_{i,j-1} & & \end{smallmatrix}] + P[\begin{smallmatrix} x_{i-1,j} & o_{i,j} \\ & x_{i,j-1} \end{smallmatrix}] + P[\begin{smallmatrix} & x_{i,j+1} \\ x_{i-1,j} & o_{i,j} \end{smallmatrix}])$

In order to analyze the above infinite hierarchy, a truncation approximation is needed which takes the form of a suitable factorization approximation for deriving the terms of multiple sites, e.g., $P[\begin{smallmatrix} x_{i,j+1} & \\ o_{i,j} & x_{i+1,j} \end{smallmatrix}]$ in terms of probabilities for simpler quantities. The mean-field (or site) approximations described below constitute the most natural lowest order factorization procedures. Taking the quantity $P[\begin{smallmatrix} x_{i,j+1} & \\ o_{i,j} & x_{i+1,j} \end{smallmatrix}]$ as an example, the MF truncation neglects all spatial correlations, so this treatment applies the following approximation

$$P\,[\begin{smallmatrix} x_{i,j+1} & \\ o_{i,j} & x_{i+1,j} \end{smallmatrix}] \approx P[o_{i,j}]\; P[x_{i+1,j}]\; P[x_{i,j+1}].$$

A MF-type treatment of these equations can provide qualitative insight into the basic behavior of their solutions. It is a suitable candidate to catch the site dependent

model. For spatially inhomogeneous states, these MF equations for single empty sites have the following form:

<u>with hopping *h*</u>: $d/dtP[o_{i,j}] = p\cdot P[x_{i,j}] - ¼\, P[o_{i,j}]\,(P[x_{i-1,j}] + P[x_{i+1,j}])(P[x_{i,j-1}] + P[x_{i,j+1}])$

$+h\cdot P[x_{i,j}](P[o_{i-1,j}] + P[o_{i+1,j}] + P[o_{i,j-1}] + P[o_{i,j+1}])$

$- h\cdot P[o_{i,j}]\,(P[x_{i-1,j}] + P[x_{i+1,j}] + P[x_{i,j-1}] + P[x_{i,j+1}])$, (3)

<u>with spontaneous creation *k*</u>: $d/dtP[o_{i,j}] = p\cdot P[x_{i,j}] - k\cdot P[o_{i,j}] - ¼\, P[o_{i,j}]\,(P[x_{i-1,j}]$

$+P[x_{i+1,j}])\,(P[x_{i,j-1}] + P[x_{i,j+1}])$. (4)

This MF approximation applied to assess equistability of planar interfaces reveals an orientation dependence of the value of the annihilation rate $p=p_{eq}$ corresponding to a stationary planar interface separating the two states. The upper bound of p_{eq} corresponds to the diagonal orientation, and we might expect the lower bound of p_{eq} corresponds to the near vertical interface.

We now present results from numerical integration of the dRDE's for evolution of planar interfaces between two steady states. The initial data are chosen as a sharp interface between the active state $C_m = C_{act}$ for $m<m^*$, and the inactive state $C_m=C_{inact}=0$ in hopping model; $C_m = C_{inact} \sim k/(p+k)$ in the model with spontaneous creation) for $m\geq m^*$. The interface location is determined from $\langle m\rangle = \sum_m C_m/(C_{act}+C_{inact})$ for a 1000 sites system. The interface velocity, $V(p) = d/dt \langle m\rangle$, is determined for long times $t \approx 4\times10^4$. Our focus is on assessing variation of $V(p)$ with p to determine stationarity and propagation failure.

3.1. Mean-field dRDE with hopping rate $h>0$

Diagonal(11) interface. Assume the probability $P[x_{i,j}]$ are the same for the site (i,j) located on the same diagonal line $i+j$=constant. We let $C_m=C_{i+j}= P[x_{i,j}]$, from (3) it follows that

$$d/dt\ C_m= -pC_m+¼\ (1-C_m)(C_{m-1}+C_{m+1})^2+2h(C_{m-1}+C_{m+1}-2C_m).$$

Taking h=0.01 as an example, $p_{eq}(11)$= 0.21273 (versus $p_{eq}(11)$=0.21138 for h=0).

Vertical(10) interface. Assume the $P[x_{i,j}]$ only deponds on i. We let $C_m=C_i = P[x_{i,j}]$, then C_m satisfies

$$d/dt\ C_m= -pC_m+½\ (1-C_m)C_m(C_{m-1}+C_{m+1})+h(C_{m-1}+C_{m+1}-2C_m).$$

The propagation failure occurs over a finite range of p, i.e., the interface separating active and inactive states is stationary. When h=0.01, the "artificial" propagation failure region (APF) is [0.20708, 0.20972]. If we misorientate the interface a slighly away from vertical, then propagation failure disappears.

Near vertical interface. We set $C_m=C_{Si+j}=P[x_{i,j}]$ for large S, so then C_m satisfies

$$d/dt\ C_m= -pC_m+ ¼\ (1-C_m)\ (C_{m-S} + C_{m+S})(\ C_{m-1} + C_{m+1}\ )$$
$$+ h(C_{m-S} + C_{m+S} + C_{m-1} + C_{m+1} -4C_m\ )$$

When h=0.01, p_{eq}(near-vert)= 0.209034. The summary of these various stationary values of p for h=0.01 is given in **Fig. 3 (a).**

3.2. Mean-field dRDE with spontaneous creation rate k

Diagonal(11) interface. Let $C_m=C_{i+j}= P[x_{i,j}]$, the corresponding dRDE is

$$d/dt\ C_m= -pC_m+ k(1-C_m)+¼\ (1-C_m)(C_{m-1}+C_{m+1})^2.$$

p_{eq}(diag, k=0.001)= 0.214100.

Vertical(10) interface. $C_m=C_i= P[x_{i,j}]$, and C_m satisfies

$$d/dt\ C_m= -pC_m+ k(1-C_m)+ ½\ (1-C_m)C_m(C_{m-1}+C_{m+1})$$

p_{eq}(vert, k=0.001)= 0.206062-0.210363. The APF still occurs for $0<k<1/27$.

Near vertical interface. We set $C_m=C_{Si+j}=P[x_{i,j}]$ for large S, so then C_m satisfies

$$d/dt\ C_m= -pC_m+ k(1-C_m)+ ¼\ (1-C_m)\ (C_{m-S} + C_{m+S})(C_{m-1} + C_{m+1})$$

p_{eq}(near-vert, k=0.001)= 0.208932. The summary of these various stationary p values for k=0.001 is given in **Fig. 3 (b).**

For a perturbation of the standard QCP model introducing $h(k)$ is small, APF occurs for interfaces between active and inactive states with a vertical orientation. However, increasing $h(k)$, the width of the region of propagation failure is greatly reduced. Next, we explore in more detail APF with for very small perturbations.

4. Asymptotic Behavior of Artificial Propagation Failure (APF) for Small *k and h*

Introducing perturbations to the basic QCP removes extreme propagation failure for vertical interfaces where the active state can never displace the inactive state for the entire range $0 < p < 0.207107$. Now for a *perfect vertical interface* with small annihilation rate p, the active state does displaces to the other state, so the corresponding interface velocity is positive. There is still artificial propagation failure but the width of the APF regime is smaller than 0.207107 (the width in the $h=k=0$ model).

As h (or k) $\rightarrow 0$, the corresponding APF does not tend to $h=k=0$ behavior, but converges to a fixed finite interval. Defining $P_{eq}(10)^-$ ($P_{eq}(10)^+$) as the lower (upper) bound of APF, we found that $P_{eq}(10)^- \rightarrow 0.19613$, and $P_{eq}(10)^+ \rightarrow 0.20711$, so that the

width of APF → 0.011, as h (or k) →0. See **Table 1**. Further, we report that the asymptotic behavior of the APF width as h (k) →0 satisfies

$$\log(\text{APF width}) = -4.513 - 13\sqrt{h} \text{ (or } -4.513 - 23\sqrt{k}). \quad (5)$$

See **Fig. 4.**

For $p < P_{eq}(10)^{-}$, the active state is more stable than and displaces the inactive state, the wave speed is roughly proportional to $P_{eq}(10)^{-} - p$. **Fig. 5**. We assume the interface velocity $V(p,h)$ is *separable*, that is $V(p,h) = V(0,h)\ [1 - p/P_{eq}(10)^{-}]$, where $V(0,h)$ is a nonlinear function of h. Numerical analysis indicates that $V(0,h) = 0.515 / |\log(h)|^{1.06}$, **Fig. 6(a)**. Similarly, for the model with spontaneous creation rate k, $V(p,k) = V(0,k)\ [1 - p/P_{eq}(10)^{-}]$, where $V(0,k) = 1.95 / |\log(k)|^{1.34}$. See **Fig. 6(b)**.Therefore, as h (k) →0, we can write

$$V(p,h) = 0.515 * [1 - p/P_{eq}(10)^{-}] / |\log(h)|^{1.06},$$

$$V(p,k) = 1.95 * [1 - p/P_{eq}(10)^{-}] / |\log(k)|^{1.34}.$$

5. Droplet Dynamics in the Perturbed Models

The inactive state is more stable than the active state $p > p_e$. Thus a sufficiently large droplet of the inactive state embedded in the active state will always grow. More precisely, an inactive droplet embedded in active state will shrink for small initial area, but grow for sufficiently large size. There is a critical size such that the droplet remains the same (i.e., is stationary).

Let Rc(p) be the critical radius of inactive droplet embedded in active state, and the radius is defined as $R = (A/\pi)^{1/2}$, where A is the area of the droplet. For large p, the

inactive droplet grows easily for most sizes of droplet, and therefore the critical droplet must be small. When p is close to p_e+, the inactive droplet shrinks more easily, so the corresponding critical droplet must be very big. So by letting $p_1=(p-p_e)/p_e$, $1/Rc(p_1) \to 0$ as $p_1 \to 0^+$. **Fig. 7**.

2PC occurs in the region $p_f < p < p_e$. For small p, the active state is more stable than the inactive state. Without perturbations to the QCP, trivial 2PC occurs for all $p \leq p_e$ as the inactive vacuum state is stable against expansion of droplets of the active state. For the QCP with hopping h or spontaneous creation k, the trivial 2PC disappears, and the artificial propagation failure (APF) regime shrinks to a smaller region. For active droplets for p below this APF regime, sufficiently large active droplets can expand. Here we just show behavior for the critical radius of these active droplets plotting 1/Rc versus p for the two different perturbations. In **Fig. 8**, we focus on behavior as $p_2 \to 0$, where $p_2=(p-p_f)/p_f$.

6. Conclusions

Our perturbations of the basic Schloegl's second model for autocatalysis (or the QCP) exhibits generic 2PC associated with an orientation dependence of the stationary point for planar interfaces separating coexisting active and poison states. We have demonstrated that MF dRDE for spatially non-uniform states do correctly capture the feature that the active state can displace the inactive state separated from it by vertical interfaces. However, they do predict a small regime of artificial propagation failure not seen the stochastic model.

References

[1] J. Marro and R. Dickman, Nonequilibrium Phase Transitions in Lattice Models (Cambridge UP, Cambridge, 1999).

[2] G. Odor, Rev. Mod. Phys. **76**, 663 (2004).

[3] F. Schloegl, Z. Phys. **253**, 147 (1972).

[4] P. Grassberger, Z. Phys. B Cond. Matt. **47**, 365 (1982).

[5] J.P. Boon, D. Dab, R. Kapral, and A. Lawniczak, Phys. Rep. **273**, 55 (1996).

[6] S. Prakash and G. Nicolis, J. Stat. Phys. **86**, 1289 (1997).

[7] R. Durrett, SIAM Rev. **41**, 677 (1999).

[8] D.-J. Liu, X. Guo, and J.W. Evans, Phys. Rev. Lett. **98**, 050601 (2007).

[9] X. Guo, J.W. Evans, and D.-J. Liu, Physica A **387**, 177 (2008).
Sites in the last two loss terms in eq. (17) are mislabeled. One should replace i with i-1.

[10] X. Guo, D.-J. Liu, and J.W. Evans, J. Chem. Phys. **130**, 074106 (2009).

[11] X. Guo, Y. de Decker, and J.W. Evans, Phys. Rev. E **82**, 021121 (2010).

[12] C.-J. Wang, X. Guo, D.-J. Liu, and J.W. Evans, J. Stat. Phys. **144**, 1308 (2011).

[13] C.-J. Wang, X. Guo, D.-J. Liu, and J.W. Evans, Phys. Rev. E. **85**, 041109 (2012).

[14] Liu, D.-J.; J. Stat. Phys. **135**, 77 (2009)

[15] Guo, X., Liu D.-J., Evans, J.W.; Phys. Rev. E **75**, 061129 (2007)

[16] Guo, X., Evans, J.W., Liu, D.-J.; Physica A **387**, 177 (2008). Note the error in site labeling in the last two loss terms in (17): replace i with i-1.

Figures

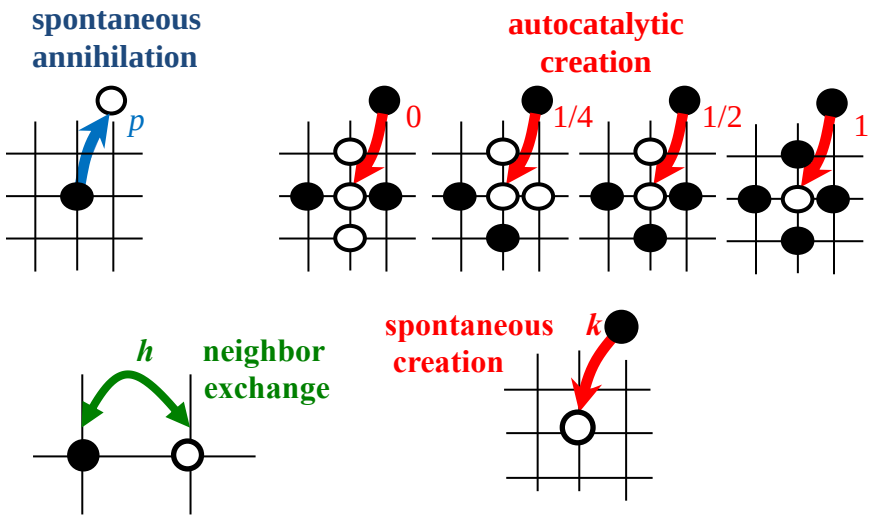

Fig. 1. Schematic of spontaneous particle annihilation (at rate *p*), neighbor exchange (at rate *h*), spontaneous particle creation (at rate *k*), and configurations for autocatalytic particle creation (at rate *k*/4) for our realization of Schloegl's second model, where *k* is the number of diagonal neighboring pairs of particles.

(a)

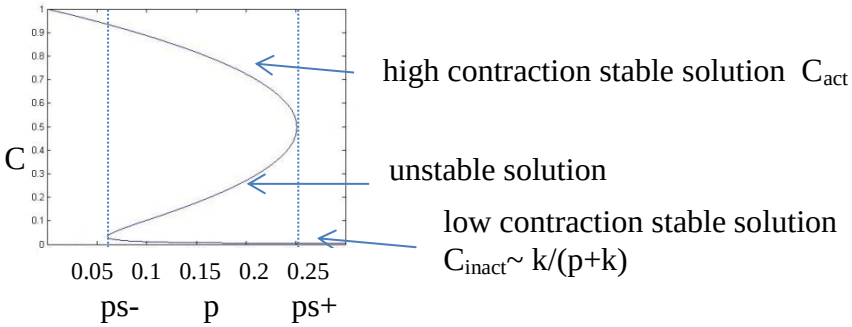

(b)

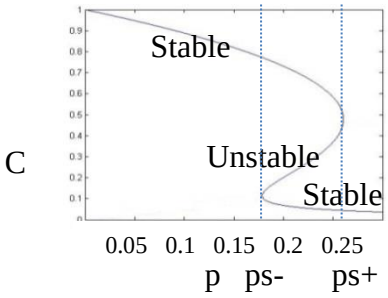

(c)

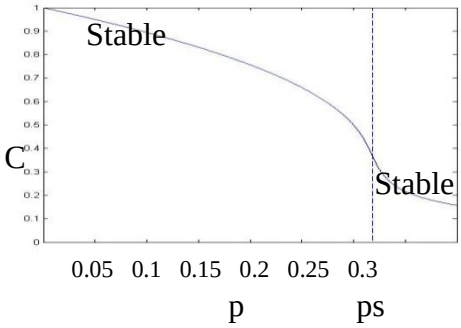

Fig. 2. Steady-state C versus p for: (a) k=0.001(b) k=0.01(<1/27), where the bistabilities occurs and p_{s-}, p_{s+} are the corresponding spinodal points; (c) k=0.05(>1/27), unique positive stable solution.

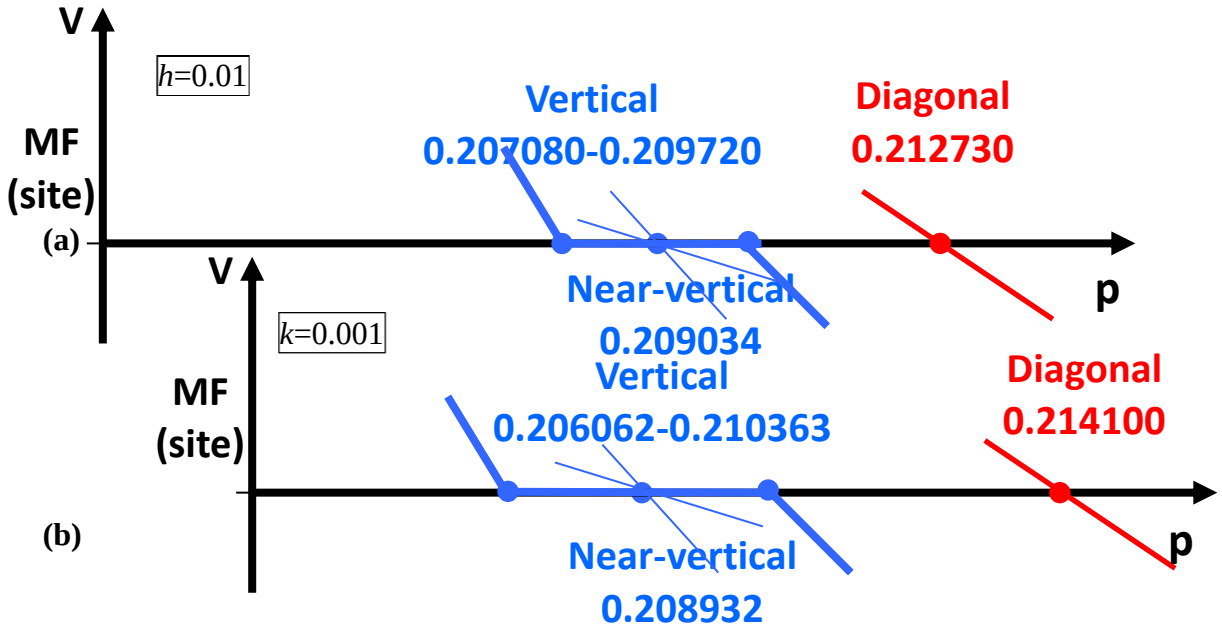

Fig. 3. Schematic summary of results for propagation velocity, V(p), versus particle annihilation rate p for (a) h=0.01 (b) k=0.001.

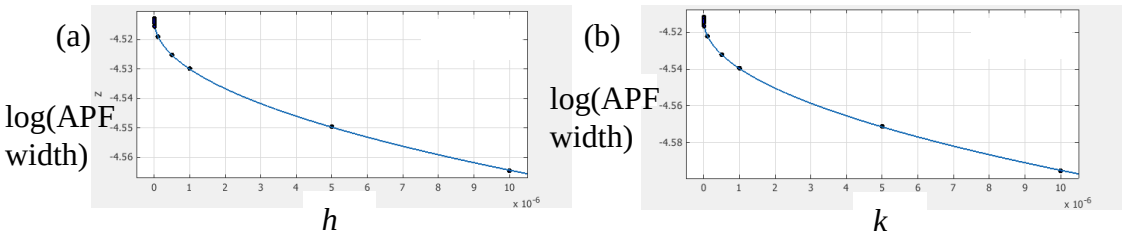

Fig. 4. For vertical interface, log(APF width) verse h (or k) (a) −4.513−13h^(0.487) (b) −4.513−23k^(0.491).

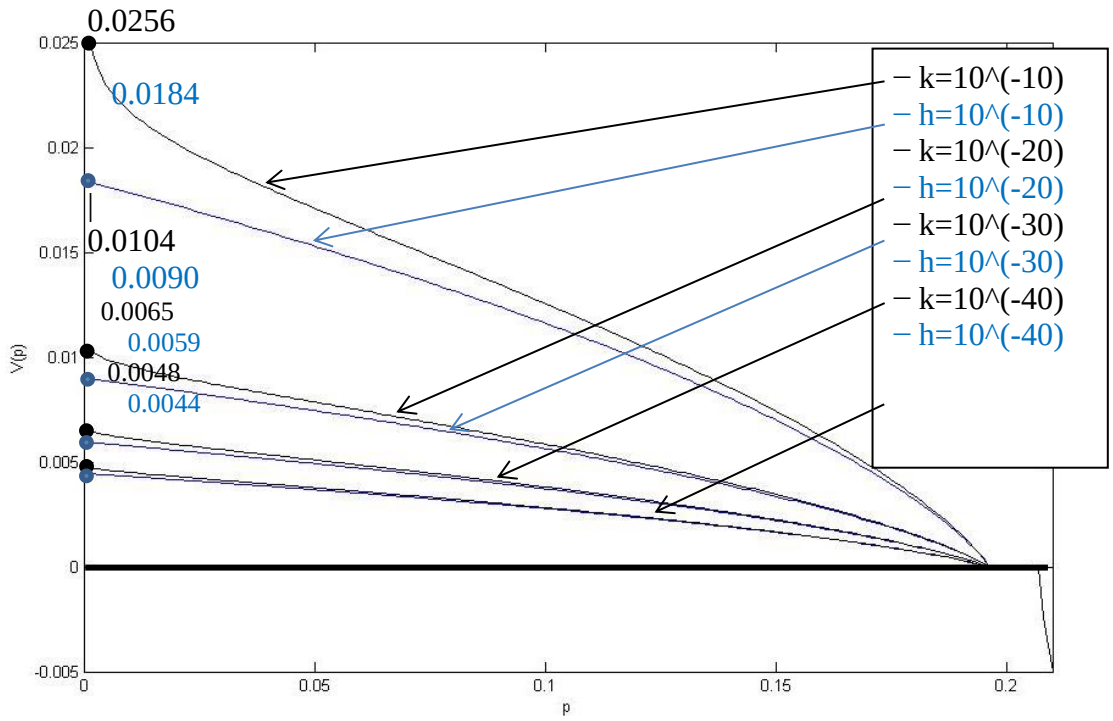

Fig. 5. The velocity of vertical interfaces $V(p)$ vs p, especially focus on $p<p_-$.

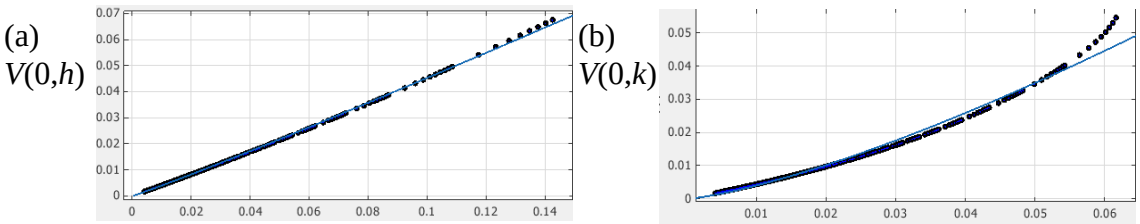

Fig. 6. (a) V vs $1/|\log(h)|$, where h is from 10^{-3} to 10^{-103}. Fit $V(0, h)$ by $0.5145/|\log(h)|^{1.056}$; (b) V vs $1/|\log(k)|$, where k is from 10^{-7} to 10^{-105}. Fit $V(0, k)$ by $1.95/|\log(k)|^{1.343}$.

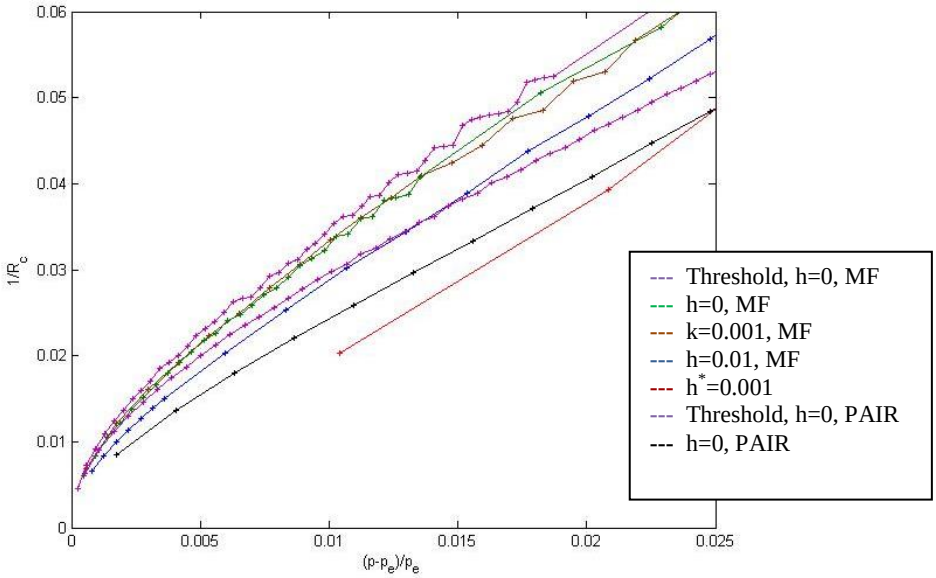

Fig. 7. Schematic 1/Rc behavior of different models as $p_1 \rightarrow 0$.

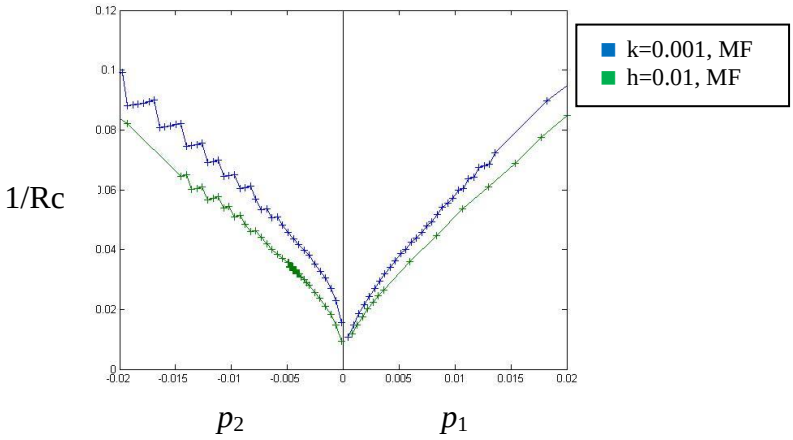

Fig. 8. Schematic of 1/Rc behavior of two different perturbations as $p_1(p_2) \rightarrow 0$.Where $p_1 = (p-p_e)/p_e$, $p_2 = (p-p_f)/p_f$. For h=0.01, p_e=0.212730 and p_f=0.209034. For k=0.001, p_e=0.214100 and p_f=0.208932.

Tables

Table 1. Artificial Propagation Failure (APF) Region and its width versus h or k for vertical interfaces. (The upper limit on k of 1/27 corresponds to the disappearance of bistability.)

		APF ($p_- < p < p_+$)	APF width
h= 0	k= 0.000000000000001	0.196134-0.207107	0.010973
	k= 0.00000000000001	0.196136-0.207107	0.010971
	k= 0.0000000000001	0.196141-0.207107	0.010966
	k= 0.000000000001	0.196144-0.207107	0.010963
	k= 0.00000000001	0.196149-0.207107	0.010958
	k= 0.0000000001	0.196152-0.207107	0.010955
	k= 0.000000001	0.196160-0.207107	0.010947
	k= 0.00000001	0.196180-0.207107	0.010927
	k= 0.0000001	0.196240-0.207107	0.010867
	k= 0.000001	0.196431-0.207110	0.010679
	k= 0.00001	0.197041-0.207140	0.010099
	k= 0.0001	0.199038-0.207437	0.008399
	k= 0.001	0.206062-0.210363	0.004301
	k= 0.01	0.235978-0.236103	0.000125
	k= 0.02	0.260233	~0
	k= 0.03703(~1/27)	0.296282	~0
k= 0	h= 0.000000000000001	0.196133-0.207107	0.010974
	h= 0.00000000000001	0.196135-0.207107	0.010972
	h= 0.0000000000001	0.196140-0.207107	0.010967
	h= 0.000000000001	0.196144-0.207107	0.010963
	h= 0.00000000001	0.196146-0.207107	0.010961
	h= 0.0000000001	0.196150-0.207107	0.010957
	h= 0.000000001	0.196156-0.207107	0.010951
	h= 0.00000001	0.196169-0.207107	0.010938

	h= 0.0000001	0.196207-0.207107	0.010900
	h= 0.000001	0.196325-0.207107	0.010782
	h= 0.00001	0.196695-0.207110	0.010415
	h= 0.0001	0.197821-0.207139	0.009318
	h= 0.001	0.200998-0.207420	0.006422
	h= 0.01	0.208085-0.209731	0.001636
	h= 0.02	0.210898-0.211529	0.000631
	h= 0.03703	0.213431-0.213607	0.000176
	h= 0.05	0.214624-0.214700	0.000076

CHAPTER 6

FAMILIES OF CRITICAL DROPLETS FOR NON-EQUILIBRIUM PHASE TRANSITIONS IN BISTABLE SYSTEMS DESCRIBED BY LATTICE REACTION-DIFFUSSION TYPE EQUATIONS

A paper to be submitted to *PNAS*

Chi-Jen Wang[1,2], Xiaofang Guo[1,3], Da-Jiang Liu[1], and James W. Evans[1,3]

Ames Laboratory[1] – USDOE, Departments of Mathematics[2] and Physics & Astronomy[3], Iowa State University, Ames Iowa 50011

1. Introduction

Discontinuous phase transitions are common in the steady-states of diverse non-equilibrium systems describing catalytic reaction-diffusion processes, biological transport and regulation, spatial epidemics, etc. These transitions often display similarities to those in thermodynamic equilibrium systems, such as hysteresis and metastability [1-3]. Such transitions are usually associated with equistability of two stable states, as can be determined by stationarity of a planar interface separating the states. For equilibrium systems, this criterion is equivalent to the Maxwell construction determining coexistence of two states at a unique equistability point. Analyses of nucleation phenomena near such transitions aims in part to characterize critical droplets of the more stable state embedded in the less stable metastable state, where these droplets correspond to stationary curved interfaces between the two states. The critical

droplet size is expected to diverge approaching the transition. A general dynamically-based derivation of this result follows from analysis of the non-conserved phase-field or Cahn-Allen equations for thermodynamic systems or the reaction-diffusion type equations (RDE) for non-equilibrium systems, most clearly by taking the sharp interface limit for isotropic systems. This analysis shows that propagation of an advancing interface is retarded linearly by curvature. The critical curvature which arrests propagation should vanish linearly approaching the transition.

However, analysis of discontinuous transitions in spatially discrete non-equilibrium systems, which are of interest here, also reveals a richer variety of behavior than in equilibrium systems. This includes interface propagation failure at the mean-field (MF) level, and orientation-dependent equistability producing generic two-phase coexistence over a finite range of some control parameter [4-10]. As a non-equilibrium counterpart to the classic Ising model, we consider stochastic lattice-versions of Schloegl's 2nd model (S2M) [11] involving spontaneous annihilation $X \rightarrow \varnothing$ of particles X residing at the sites of a periodic lattice, and autocatalytic creation of particles at empty sites induced by nearby particle pairs $\varnothing + 2X \rightarrow 3X$ [10,12-14]. This model is equivalent to a quadratic contact process (QCP) [13] describing spatial epidemics where sick individuals (S) residing at households arranged on a regular lattice or grid spontaneously recover $S \rightarrow H$, and healthy individuals (H) are infected by sick pairs of neighbors $H + 2S \rightarrow 3S$. A MF treatment of the homogeneous steady-states of the S2M or QCP produces bistability [11], analogous to a Bragg-Williams treatment of the Ising model. Our focus is on MF treatments of spatially inhomogeneous states based on

discrete RDE [15] or lattice differential equations [16], which reveal propagation failure, generic two-phase coexistence, and an unprecedented richness in critical or stationary droplet behavior.

2. Reaction Model, Discrete RDE, and Planar Interface Propagation

We analyze behavior for a class of S2M with particles X residing on a 2D square lattice. Spontaneous annihilation of particles occurs at rate p, and autocatalytic creation of particles at empty sites ∅ occurs provided there exist two or more suitably-configured nearby particles. The standard requirement is that these particles be on nearest-neighbor (NN) sites, but this leaves many choices of creation rates k: the "threshold" choice sets k = 1 for all configurations with two or more NN particles, and k=0 otherwise [14]; the more restrictive Durrett choice sets k = m/4 for configurations with m=0, 1, 2, or 4 diagonal NN particle pairs [13]; etc. Below, we will actually focus on various "perturbations" of these basic models. See **Fig.1.**

If $C_{i,j}$ denotes the probability that site (i,j) is occupied by a particle, i.e., the concentration at (i,j), then one has d/dt $C_{i,j}$ = -p$C_{i,j}$ + gain terms. The gain terms involve sum over configurations contributing to autocatalytic creation of the configuration probability times the relevant rate. These configuration probabilities involve spatial correlations between the occupancy of distinct sites, so the d/dt $C_{i,j}$ equations are not closed but constitute the lowest-order entries in an infinite hierarchy of exact master equations. However, our MF-level analysis of spatially heterogeneous states closes the hierarchy by neglecting these correlations. Thus, e.g., the probability of a configuration

allowing particle creation at empty site (i,j), where (i+1,j) & (i,j+1) are occupied, and (i,j-1) & (i,j-1) are empty is set to $(1-C_{i,j})C_{i+1,j}C_{i-1,j}(1-C_{i,j+1})(1-C_{i,j-1})$. Accounting for all creation terms produces a set of lattice differential equations, which given the spatial coupling may be regarded as discrete RDE. For example, for Durrett's choice of rates, one obtains after reduction using the binomial summation formula (cf. [15])

$$d/dt\ C_{i,j} = -pC_{i,j} + ¼(1-C_{i,j})[C_{i+1,j}C_{i,j+1} + C_{i,j+1}C_{i-1,j} + C_{i-1,j}C_{i,j-1} + C_{i,j-1}C_{i+1,,j}]$$

$$= R(C_{i,j}) + D(C_{i,j})\Delta C_{i,j} + \ldots$$

where $R(C) = -pC+C^2(1-C)$, $D(C) = ½\ C(1-C)$, $\Delta C_{i,j} = C_{i+1,j}+C_{i,j+1}+C_{i-1,j}+C_{i,j-1} -4C_{i,j}$ is the discrete Laplacian. The terms … [17] are quadratic in discrete gradients $\nabla_i^{\pm}C_{i,j} = C_{i\pm1,j} - C_{i,j}$.

For homogeneous states where $C_{i,j}=C$, for all (i,j), where d/dt C = R(C), analysis of steady-states reveals bistability between a higher-concentration "active" populated state and a static vacuum state for $0=p_{s-} < p < p_{s+}$ [10,11,13]. See **Fig.2a.** Analysis of the discrete RDE for the evolution of planar interfaces separating these states reveals that interface propagation depends on orientation or slope S. Generally, the active state displaces the vacuum state with velocity $V_p >0$ for $p_{s-} < p < p_{eq}(S)$, and the opposite applies so $V_p <0$ for $p_{eq}(S) < p < p_{s+}$. The equistability $p_{eq}(S)$ is maximum for diagonal interfaces S=1, so the propensity of the active state to displace the vacuum state is highest for S= 1. However, the active state cannot displace the vacuum state for vertical interfaces orientations $S=\infty$, as empty sites in the vacuum state have at most one neighboring particle and thus are inaccessible to autocatalytic particle creation. Thus,

vertical interfaces are stationary (V_p =0) for all of $0 < p < p_{eq}(\infty)$, but still have V_p <0 for $p>p_{eq}(S)$.

To remove the "extreme" propagation failure of vertical interfaces, we consider "perturbations" of the basic model to include either: (a) hopping of particles to adjacent empty sites at small rate h [18]; or (b) spontaneous creation at small rate ε [19], in which case the vacuum state is replaced by a low-concentration state and p_{s-} becomes non-zero [20]. However, for vertical interfaces, we find that propagation failure still occurs for a finite range $p_-(S=\infty) < p < p_+(S=\infty)$. As h or $\varepsilon \to 0+$, one finds that $p_+(\infty) \to p_{eq}(\infty)$ as expected, but $p_-(\infty)$ does not vanish. **Fig.2b** summarizes this interface propagation behavior showing the propagation velocity, V_p, versus p, for S≥1 in the Durrett model with small h=0.01. **Table 1** summarizes of key p-values for this and related models. One subtle feature is that near-vertical interfaces for $S\to\infty$ do not exhibit propagation failure, and have a unique equistability point $p=p_{eq}(S\to\infty)$ between p-(∞) and p+(∞). To explain this feature, we note that near-vertical interfaces can be regarded as vertical interfaces decorated with far-separated kinks which flow so as to expand the active (vacuum) state for $p<p_{eq}(S\to\infty)$ ($p>p_{eq}(S\to\infty)$). Kinks are stationarity for $p= p_{eq}(S\to\infty)$. See again **Fig.2b.**

Extensive analyses of lattice differential equations in the mathematics literature [16] have been motived by reaction-diffusion systems. This work invariably adopts the simpler traditional form $d/dt\ C_{i,j} == R(C_{i,j}) + D\Delta C_{i,j}$ with constant D, rather than the more complex forms deriving from hierarchical master equations. Non-trivial propagation failure is often found, so such behavior for vertical interfaces [21] should

not be regarded as a quirk of our model. However these mathematical analyses have not considered curvature effects on interface propagation, a central issue in this study.

3. Overview of Droplet Dynamics and Stationarity

We now provide a brief but comprehensive summary of evolving and stationary of droplet-like solutions to the discrete RDE for the perturbed SCM models. Here, we consider only the case where droplets have the 4-fold rotational symmetry of the underlying square lattice. First, it is appropriate to make some general comments on droplet shape. In thermodynamic lattice-gas models, shapes of equilibrium droplets of specified size are determined by a Wulff construction from their orientation-dependent line tension so as to minimize energy cost. While 2D equilibrium droplets do not exhibit true straight facets, for the square lattice considered here, it is instructive to discuss shape in terms of the appearance of near-diagonal and near-horizontal/vertical segments of their edges (for convenience described here as α=(11) and α=(10) facets, respectively). The Wulff construction shows that the distance, d_α, from the island center to the middle of a facet α is proportional to the line tension, γ_α, of that facet, i.e., $d_\alpha = c_{eq}\ \gamma_\alpha$. Thus, facets with high line tension are further from the droplet center, and constitute a correspondingly smaller fraction of the periphery. The Wulff construction also determines periphery curvature, κ, so that radius of curvature, $R=\kappa^{-1}$, is proportional to the stiffness (which is related to γ), and ensures that edge orientation varies smoothly. Note that the Wulff construction also determines the shape of critical droplets which minimize excess energy at the critical size.

For growing droplets in non-equilibrium systems, where facet α has growth velocity V_α, the above is naturally replaced by a kinetic Wulff construction which gives $d_\alpha = c_g V_\alpha$. Thus, faster growing facets are further from the droplet center, and are a smaller fraction of the periphery. In non-equilibrium systems, there is no generic prescription for edge curvature, an issue to which we return later. Extending these ideas, it is appropriate to also note that for shrinking droplets, shape is primarily controlled by the fastest receding orientation.

Typical droplet behavior is summarized for the Durrett model perturbed with particle hopping with h=0.01 in **Fig.3** and perturbed with spontaneous particle creation with ε=0.001 in **Fig.4.** It is instructive to divide description of behavior is separated into four p-regimes:

(i) For "higher" $p_{eq}(S=1) < p < p_{s+}$, the vacuum (or low-concentration) state is unambiguously more stable than the active state and displaces the latter separated from it by any planar interface. However, the expansion of a vacuum droplets embedded in the active state is inhibited by the curvature at the droplet interface. Vacuum droplets only grow above a critical size, A_c, with smaller ones shrinking. The growing droplets are limited by the slowest growing diagonal orientation, so these are predominantly diamond shaped. A_c diverges as $p \to p_{eq}(S=1)$.

(ii) For $p_{s-} < p < p_{-}(S=\infty)$, the active state is unambiguously more stable than the vacuum (or low-concentration) state. Analogous to the above case, active droplets embedded in the vacuum state only grow above a critical size A_c^+ which diverges as $p \to p_{-}(S=\infty)$. Their shapes reflect the slowest growing horizontal/vertical orientations,

and are predominantly square. However, only active droplets below a distinct smaller critical size A_c^- shrink, and we find an entire discrete family of droplets which are stationary between these limits.

(iii) For $p_-(S=\infty) < p < p_{eq}(S\to\infty)$, again small droplets of the active state embedded in the vacuum state shrink below the critical size A_c^-, which diverges as $p\to p_{eq}(S\to\infty)$. All larger droplets evolve to one of an infinite discrete set of stationary active droplets, with no droplets growing indefinitely. This behavior is readily understood as stationarity of vertical and horizontal interfaces in this regime blocks active droplet growth.

(iv) For $p_{eq}(S\to\infty) < p < p_{eq}(S=1)$, both vacuum and active droplets embedded in the other state always shrink. The shapes of shrinking droplets controlled by fastest shrinking orientations. Thus, shrinking vacuum droplets are always diamond shaped. Shrinking active droplets are effectively square at least for higher p in this regime.

As a result of this analysis, we identify the latter regime, $p_{eq}(S\to\infty) < p < p_{eq}(S=1)$, as "generic two-phase coexistence (2PC)" since each state is stable against local perturbations of the other state in this regime, and furthermore such perturbations dissipate. [The latter standard feature for 2PC does not apply for $p_-(S=\infty) < p < p_{eq}(S\to\infty)$.]

4. Detailed Droplet Analysis

Below we consider only the Durrett model perturbed by particle hopping with h=0.01. Results are obtained from numerical integration of the dRDE's for evolution of

droplet-like solutions separating the active and vacuum states. The initial data in Sec.4.1 are chosen as four-fold symmetric vacuum (active) embedded in the active (vacuum) state. This symmetry constraint is relaxed in Sec.4.2. We select various sizes of initial droplet, and explore evolution as a function of initial size. For droplets of the more stable state embedded in a less stable state, one generally expects large initial droplets expand, small ones shrink, and for a special initial size evolution to a stationary critical droplet for long times. To assess whether a stationary droplet is actually achieved, we perform numerical integration up to times $t \approx 5\times10^4$. However, more complex behavior is sometimes found, as described below. For a (large) finite simulation system of N^2 sites, the area and radius of active droplets droplet are determined from $A=\pi R^2= \sum_{i,j} C_{i,j}/C_{act}$), and of vacuum droplets from $A=\pi R^2 = N^2-\sum_{i,j} C_{i,j}/C_{act}$. The critical droplet area (radius) is denoted as A_c (R_c). One issue of particular interest is the variation of $R_c(p)$ with p.

4.1 Analysis for four-fold symmetric initial droplets

Here, we use a four-fold symmetric droplet shape as the initial data in our studies of droplet evolution, where this shape can be that of an octagon, diamond, or square. We find that the long time behavior does not depend on the specific initial shape within this symmetry class.

(i) Vacuum droplets for $0.21273 = p_{eq}(S=1) < p < p_{s+} = 0.25000$. **Fig.5a-c** shows the examples of the evolution of 4-fold symmetric vacuum droplets for p=0.214. As noted in Sec.3, large growing droplets are predominantly diamond shaped for p just above $p_{eq}(S=1)$, being limited by the slowest-advancing diagonal orientations. See

Fig.5c. Discussion in following sections shows that the same applies for the critical droplet. See **Fig.5b.** Smaller shrinking droplets also tend to be diamond shaped, as curved diagonal orientations are the fastest receding orientation. See **Fig.5a.** Finally, in **Fig.6**, we provide R versus t curves showing evolution to the unique critical droplet only for a unique initial size.

(ii) Active droplets for $p_{s-} < p < p_{-}(S=\infty) = 0.20809$. **Fig.7a-c** present the examples of the evolution of 4-fold symmetric active droplets for p=0.206, and **Fig.8a-e** present examples for p=0.207. As noted in Sec.3, large growing droplets are predominantly square, being limited by the slowest-advancing horizontal/vertical orientations. See **Fig.7c** and **Fig.8e.** Smaller shrinking droplets also tend to be square, as curved horizontal/vertical orientations are the fastest receding orientation. See **Fig.7a** and **Fig.8a.** For p=0.206, there is a unique critical droplet of size R_c =15.4877. See **Fig.7b**. However, for p=0.207 there are three distinct stationary sizes $R_c^- = 19.6266$, $R_c = 20.9199$, and $R_c^+ = 22.1870$. See **Fig.8b-d.** The former and latter correspond to the upper and lower limits on critical areas, $A_c^{\pm}$, described in Sec.3. All these stationary droplets tend to have a square shape. Finally, we provide R versus t curves showing evolution to the unique critical droplet for p=0.206 in **Fig.9**, and to the family of three stationary solutions for p=0.207 in **Fig.10a.** We should also emphasize that as $p \to p_{-}(\text{vert})$ from below, the number of stationary droplets diverges.

(iii) Active droplets for $0.20809 = p_{-}(S=\infty) < p < p_{eq}(S\to\infty) = 0.20903$. **Fig.11a-d** present the examples of the evolution of 4-fold symmetric active droplets for p=0.2085. The behavior is similar to case (ii) above in that small droplets shrink, and

there exists a well-defined minimum size of stationary droplets corresponding here to R_c = 38.9322. However, now there is an infinite discrete set of larger stationary active droplets and there are no droplets which grow indefinitely. The shrinking droplets and all of the stationary droplets tend to be square. Finally, we provide R versus t curves showing evolution to the smallest few dozen stationary solutions in **Fig.12a.**

(iv) Vacuum and active droplets in the regime of generic two-phase coexistence for 0.20903 = peq(S$\rightarrow\infty$) < p < peq(S=1) = 0.21273. **Fig.13** provides examples for p=0.2093 [< p_+(S=∞) = 0.20973] and p= 0.211 [> p_+(S=∞) = 0.20973]. For vacuum droplets, in either case, the fastest receding orientation is diagonal, so these droplets tend to be diamond shaped. For active droplets, the fastest receding orientation is horizontal/vertical at least for p= 0.211, so these droplets tend to be square. For lower p around p=0.2093 where orientations with slope S~ 16 or 1/16 shrink fastest (see **Fig.2b**), these can instead be 8-sided (although this feature is difficult to discern).

4.2 Analysis for asymmetric initial droplets

For p_{eq}(S=1) < p < p_{s+}, it appears that a unique diamond-shaped critical droplet is achieved irrespective of whether one starts with 4-fold symmetric or asymmetric initial conditions. **Fig.5d-f** provide examples for p=0.214 for various asymmetric initial shapes where the final stationary critical droplet matches that obtained in **Fig.5a-c.**

For p < p_-(S=∞) = 0.20809 but sufficiently close to this value, numerical simulations indicate that in addition to the finite family of stationary droplets with 4-fold

symmetry, there is another finite family of stationary droplets which can have 2-fold symmetry with a rectangular-like shape. **Fig.7d-f** and **Fig.8f-h** provides examples for p=0.206 and p=0.207, respectively (although for p=0.206 just one asymmetric droplet is found). Analogous to the 4-fold symmetric family, the number of members in the asymmetric family and their maximum size diverges as $p \to p_{-}(S=\infty)$. **Fig.7b** and **Fig.9b** show the corresponding R versus t plots for p=0.206 and 0.207.

For $0.20809 = p_{-}(S=\infty) < p < p_{eq}(S\to\infty) = 0.209034$, the same applies except that now there are distinct infinite families of 4-fold symmetric and asymmetric stationary droplets. **Fig.11e-g** provides examples for p=0.2085. **Fig.12b** show the corresponding R versus t plots for p=0.2085.

5. Detailed Analysis of Critical Vacuum Droplets for $p_{eq}(S=1) < p < p_{s+}$

5.1 Behavior of critical droplet curvature and size

For $p_{eq}(S=1) < p < p_{s+}$, our analysis indicates that there is a unique critical vacuum droplet analogous to traditional equilibrium systems for which there are extensive studies of nucleation phenomena. As indicated in the introduction, in a traditional isotropic analysis for these systems, it is expected that the propagation velocity, $V(\kappa)$, of advancing interfaces is inhibited linearly by curvature κ. The critical curvature κ_c is given by $V(\kappa_c)=0$ which determines the critical radius $R_c = 1/\kappa_c$. If V_p denotes the velocity of a planar interface (as above), then one expects that $V_p \approx a\delta p$, where δp denotes the distance to the equistability point (i.e., the distance to the phase transition) in terms of a control parameter p. Then, it follows that

$$V(\kappa) \approx V_p - b\kappa, \text{ so that } \kappa_c \approx V_p/b \text{ and } R_c = 1/\kappa_c \approx b/V_p \approx ba^{-1}/\delta p,$$

so that $\kappa_c = 1/R_c \approx ab^{-1}\,\delta p$ vanishes linearly as $\delta p \to 0$.

However, results for the perturbed Durrett model with h=0.01 shown in **Fig.14** reveal a different more complicated behavior for critical vacuum droplets. In fact for a broad range of $p > p_{eq}(S=1)$, not too close to $p_{eq}(S=1)$, one has linear behavior $\kappa_c = 1/R_c \propto (p - p^*)$ where $p^* \approx 0.2111$ is between $p_{eq}(S\to\infty) = 0.209034$ and $p_{eq}(S=1) = 0.21273$. This is perhaps not too surprising if one recognizes that in this p-regime, the velocities of diagonal and vertical interfaces roughly satisfy $V_p(S=1) \propto [p-p_{eq}(S=1)]$ and $V_p(S=\infty) \propto [p-p_{eq}(S\to\infty)]$ (see **Fig.15**), and that the critical droplet periphery includes significant portions of diagonal and horizontal/vertical orientations. Thus, the growth of R_c reflects and average of contributing effects from these orientations, and one can think of p* as an effective average of $p_{eq}(S=1)$ and $p_{eq}(S\to\infty)$. As $p \to p_{eq}(S=1)$, it is clear from **Fig.14** that the influence of the S=1 orientations begins to dominate causing a transition in the behavior of $\kappa_c = 1/R_c$ which vanishes in this limit.

Any quantitative analysis of critical vacuum droplet size and shape for the perturbed Durrett model with h=0.01 will rely on a reliable characterization of the dependence of the critical curvature on planar interface velocity, $\kappa_c \approx f(V_p)$ for the two dominant interface orientations S=1 and S=∞ (anticipating possible deviations from the classic behavior $\kappa_c \approx V_p/b$).

5.2 Detailed Analysis of Critical Curvature

First, we introduce a procedure to estimate the curvature at the edge of critical vacuum droplets for the two primary orientations S=1 and S=∞. The critical droplet is diamond-like shaped with rounded corners as shown in Sec.4. Thus, the droplet boundary at the corners is a near-vertical (or near horizontal) interface. Given that concentration profiles across interfaces in two-phase systems typically have a hyperbolic tangent form, we use the hyperbolic tangent function to provide a local fit the $C_{i,j}$ of the form

$$C_{i,j} \approx C_{act}/2 * (1+\tanh(\frac{j-\bar{j}+(k(i-\bar{\imath}))^2}{\sigma})), \text{ for } |i-\bar{\imath}| \leq 3, and\ |j-\bar{j}| \leq 3,$$

where C_{act} the value of active state, $(\bar{\imath}, \bar{j})$ is the effective vertex on the vertical boundary, and $\kappa = \kappa_c(S=\infty)$ is the desired curvature. These three parameters are obtained by least-square fitting to the numerical data for $C_{i,j}$. Similarly, we fit the local concentration profile on the diagonal sides of critical droplets to the form

$$C_{i,j} \approx C_{act}/2 * (1+\tanh(\frac{\frac{i+j-\overline{\imath+j}}{\sqrt{2}}+(k(\frac{i-j}{\sqrt{2}}))^2}{\sigma})) \text{ for } |i-\bar{\imath}| \leq 3, and\ |j-\bar{j}| \leq 3\ ,$$

where $(\bar{\imath}, \bar{j})$ is the vertex on the diagonal boundary, $\kappa = \kappa_c(S=1)$ is the desired curvature. For various p values, the corresponding curvatures are listed in **Table 2**. Using this data to obtained the dependence of critical curvature κ_c on corresponding planar interface velocity, V_p, shows a complete breakdown from the traditional proportionality described above. Instead, one finds that $|\kappa_c(S=\infty)| \approx 0.08023 + 21.6|V_p(S=\infty)|$ in the narrow range of $V_p(S=\infty)$ analyzed here, and that $|\kappa_c(S=1)| \approx 0.05558 + 38.85|V_p(S=1)|$ at least provided that $|V_p(S=1)|$ is not too small. We still expect that $\kappa_c(S=1) \approx f(V_p(S=1))$ vanishes as $V_p(S=1) \to 0$, but the cross-over must occur for small values of $V_p(S=1)$ and

is difficult to assess numerically. This deviation fom traditional proportionality must impact the dependence of the $\kappa_c = 1/R_c$ on p in part contributing to the unusual form described above.

6. Conclusions

Discontinuous phase transitions and associated nucleation phenomena (i.e., analysis of the formation of droplets of the more stable phase embedded in a metastable phase) have been studies for decades. Usually this is done for thermodynamic systems and within a quasi-continuum framework. The general view from these studies is that there is a unique critical size above which droplets grow and below which they shrink. For the discrete non-equilibrium model analyze here, we find much richer as a result of both generic two-phase coexistence and propagation failure. In the two-phase coexistence region, droplets always shrink. Outside this region, sometimes entire families of stationary droplets exist.

References

[1] G. Nicolis and I. Prigogine, Self-Organization in Nonequilibrium Systems (Wiley, New York, 1977).

[2] A.S. Mikhailov, Foundations of Synergetics I (Springer, Berlin, 1994).

[3] J. Marro and R. Dickman, Nonequilibrium phase transitions in lattice models (Cambridge UP, Cambridge, 1999).

[4] A.L. Toom, in Multicomponent random systems, edited by R.L. Dobrushin and Y.G. Sinai Marcel Dekker, New York, 1980).

[5] C.H. Bennett and G. Grinstein, Phys. Rev. Lett. **55**, 657 (1985).

[6] Y. He, C. Jayaprakash, and G. Grinstein, Phys. Rev. A **42**, 3348 (1990).

[7] G. Grinstein, IBM J. Res. & Dev. **48**, 5 (2004).

[8] H. Hinrichsen, R. Livi, D. Mukamel, and A. Politi, Phys. Rev. E **61**, R1032 (2000).

[9] M.A. Munoz, F. de los Santos, and M.M.T. da Gama, Euro. Phys. J. B **43**, 73 (2005).

[10] D.-J. Liu, Xiaofang Guo, and J.W. Evans, Phys. Rev. Lett. **98**, 050601 (2007).

[11] F. Schloegl, Z. Phys. **253**, 147 (1972).

[12] P. Grassberger, Z. Phys. B Cond. Matt. **47**, 365 (1982).

[13] R. Durrett, SIAM Rev. **41**, 677 (1999).

[14] S. J. Hanjini, J. Theor. Probability **10**, 737 (1997).

[15] C.-J. Wang, D.-J. Liu, and J.W. Evans, Phys. Rev. E **85**, 041109 (2012).

[16] S.-N. Chow, J. Mallet-Paret, and E. S. Van Vleck, Int. J. Bifurc. Chaos **6**, 1605 (1996).

[17] These terms are $\frac{1}{4}(1-C_{i,j})[\nabla_i^+ C_{i,j}\, \nabla_j^+ C_{i,j} + \nabla_i^+ C_{i,j}\, \nabla_j^- C_{i,j} + \nabla_i^- C_{i,j}\, \nabla_j^+ C_{i,j} + \nabla_i^- C_{i,j}\, \nabla_j^- C_{i,j}]$

[18] This adds a term $h(C_{i+1,j} + C_{i,j+1} + C_{i-1,j} + C_{i,j-1} - 4C_{i,j})$ to the discrete RDE.

[19] This adds a term $\varepsilon(1-C_{i,j})$ to the discrete RDE.

[20] An alternative to remove extreme propagation failure is to include autocatalytic creation with small rate δ given at least one adjacent NN and one diagonal NN particle. This adds a term $\delta(1-C_{i,j})[1- C'_{i+1,j}\, C'_{i,j+1} C'_{i-1,j} C'_{i,j-1} - C'_{i+1,j+1}\, C'_{i-1,j-1} C'_{i-1,j+1} C'_{i+1,j-1}$

+ $C'_{i+1,j}\,C'_{i,j+1}C'_{i-1,j}C'_{i,j-1}C'_{i+1,j+1}\,C'_{i-1,j-1}C'_{i-1,j+1}C'_{i+1,j-1}$], to the discrete RDE, where $C'_{i,j} = 1-C_{i,j}$.

[21] Note that for vertical interfaces, our discrete RDE reduce to the simpler traditional form except for including a concentration-dependent D.

Figures

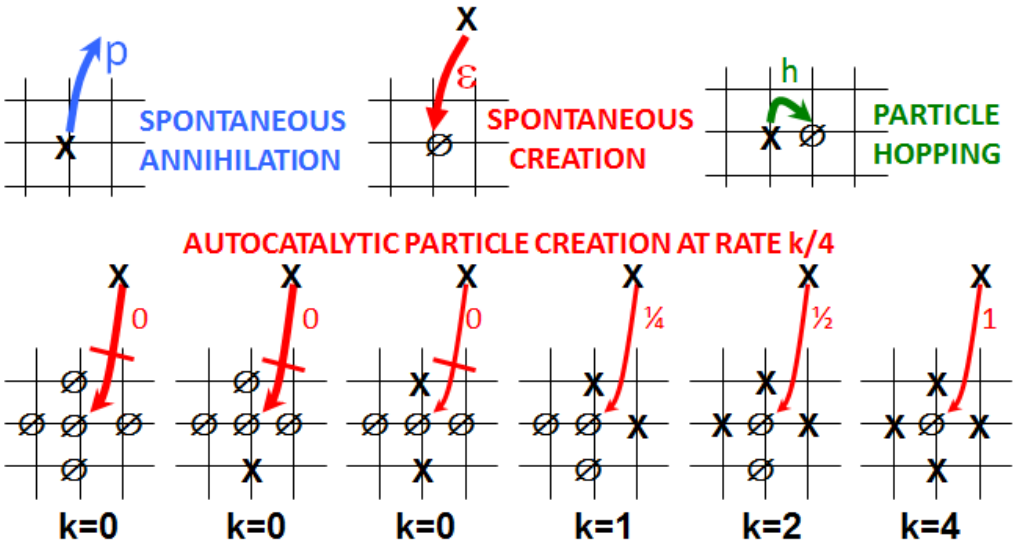

Fig. 1. Schematic of the Durrett version of Schloegl's second model allowing with spontaneous annihilation and autocatalytic creation of particles, but also allowing for spontaneous creation and particle hopping.

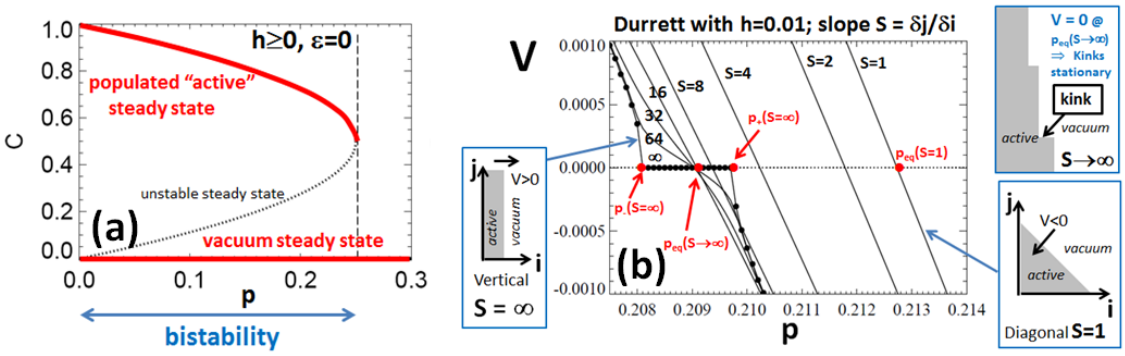

Fig. 2. (a) Steady-state concentration versus p for Durrett's model with h≥0, and ε=0. (b) Propagation velocity of planar interfaces, V, for Durrett's model perturbed with h=0.01. V>0 corresponds to the active state displacing the inactive vacuum state. Slope S=1 diagonal interfaces have the highest equistability $p=p_{eq}(S=1)$. Slope S=∞ vertical interfaces exhibit propagation failure for a range $p_{-}(S=\infty) < p < p_{+}(S=\infty)$ below $p_{eq}(S=1)$. Near-vertical interfaces do not exhibit propagation failure and have an equistability $p=p_{eq}(S\to\infty)$.

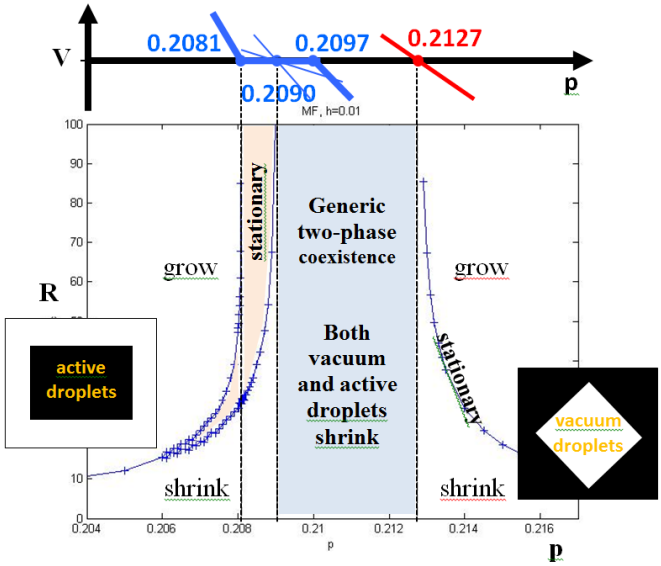

Fig. 3. Comprehensive summary of the evolution and stationarity of droplet-like solutions to the discrete RDE for the perturbed Durrett model with h=0.01.

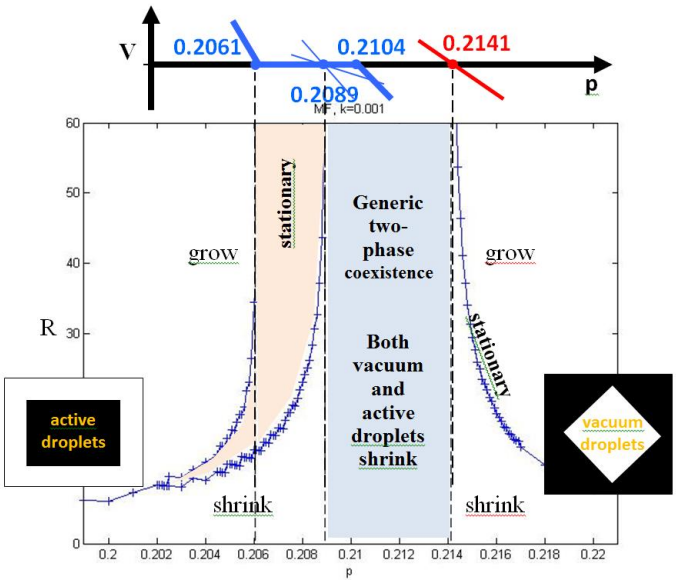

Fig. 4. Comprehensive summary of the evolution and stationarity of droplet-like solutions to the discrete RDE for the perturbed Durrett model with ε=0.001.

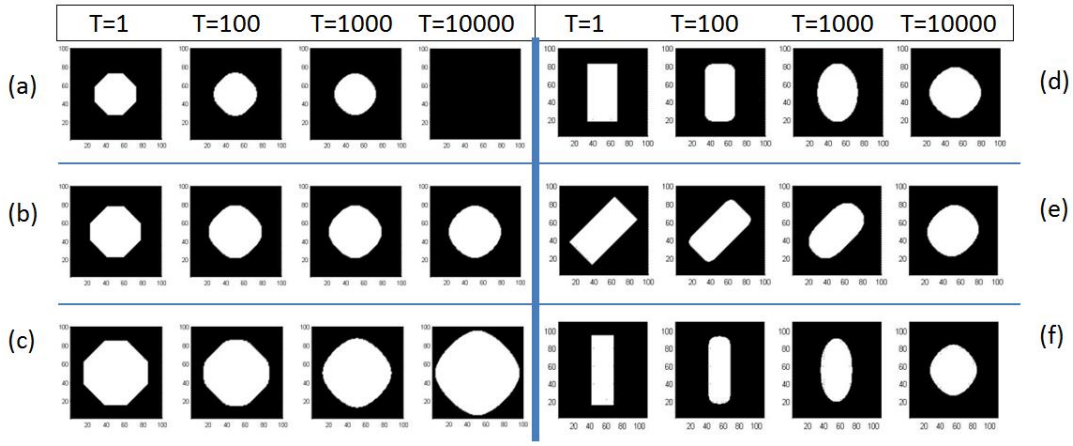

Fig. 5. Evolution of vacuum droplets of different initial sizes embedded in the active steady state for p=0.214 [> $p_{eq}(S=1)$]. For 4-fold symmetric initial data: (a) Small initial droplet shrinks; (b) stationary droplet with R_c =27.8822; (c) large initial droplet grows. For asymmetric initial data: (d) stationary droplet with R_c=27.8822 from 2x1 rectangle; (e) stationary droplet with R_c=27.8822 from oblique rectangle; (f) stationary droplet with R_c=27.8822 from 3x1 rectangle. Note that all critical vacuum droplets are the same.

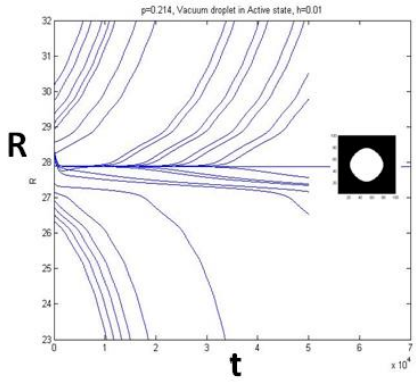

Fig. 6. R versus t for 4-fold symmetric vacuum droplets for p=0.214 for various initial sizes showing selection of unique critical vacuum droplet. The stationary solution has R_c=27.8822.

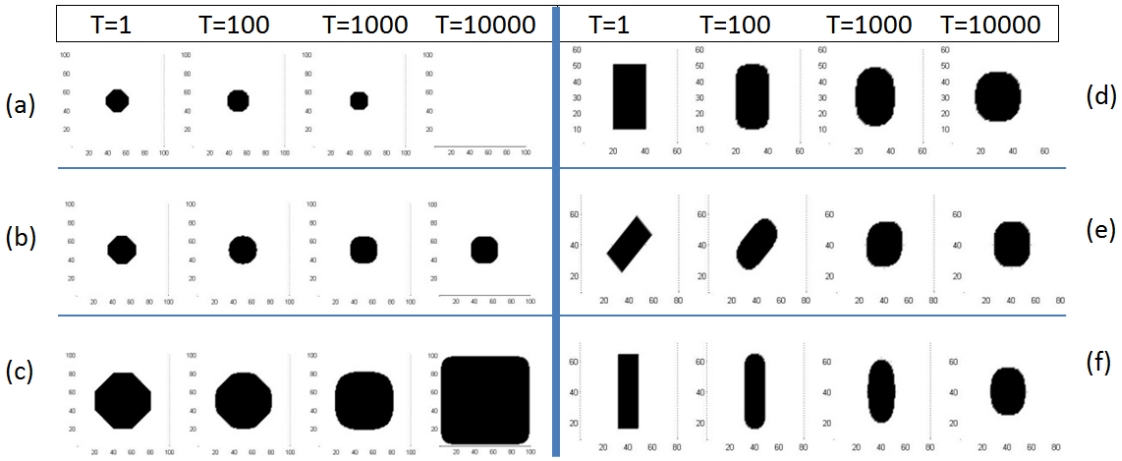

Fig. 7. Evolution of active droplets of different initial sizes embedded in the vacuum steady state for p=0.206 [< $p_c(S=\infty)$ = 0.20809]. For 4-fold symmetric initial data: (a) small initial droplet shrinks; (b) stationary droplet with R_c=15.4877; (c) large initial droplet grows. For asymmetric initial data: (d) stationary droplet with R_c=15.5026 from 2x1 rectangle; (e) stationary droplet with R_c=15.4877 from oblique 2x1 rectangle; (f) stationary droplet with R_c=15.8363 from 3x1 rectangle. Notice that the stationary sizes for (d) and (f) differs from (b), but that of (c) matches (b).

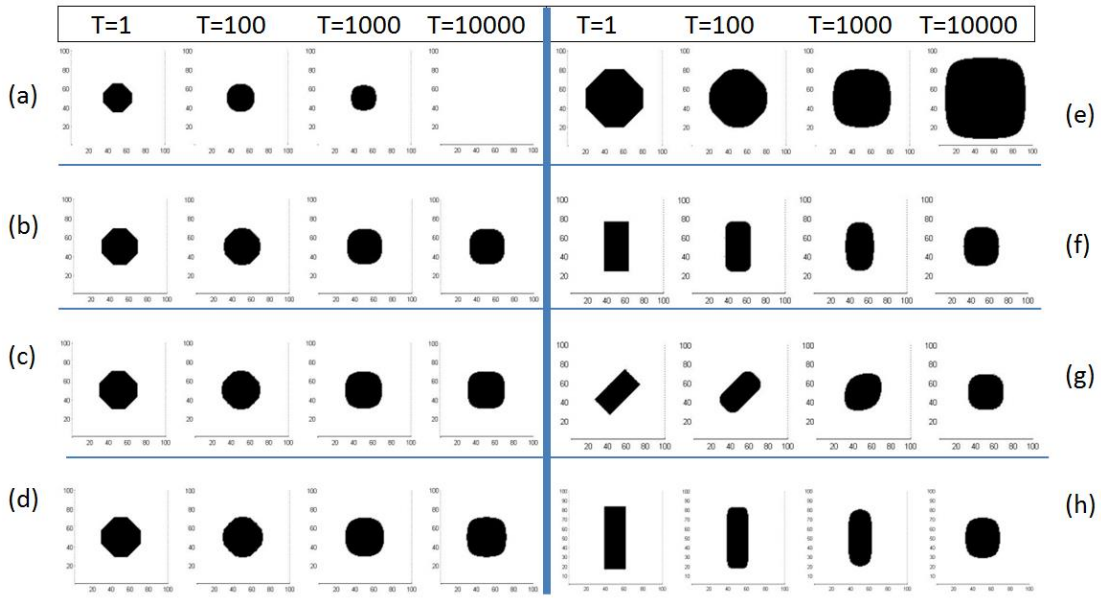

Fig. 8. Evolution of active droplets of different initial sizes embedded in the vacuum steady state p=0.207 [< $p_c(S=\infty)$ = 0.20809]. For 4-fold symmetric initial data: (a) small initial droplet shrinks; (b) stationary droplet with minimum R_c^- = 19.6266; (c) stationary droplet with Rc = 20.9199; (d) stationary droplet with maximum R_c^+ = 22.1870; (e) large initial droplet grows. For asymmetric initial data: (f) stationary droplet with R_c=20.8862 from 2x1 rectangle; (g) stationary droplet with R_c =19.6266 from oblique 2x1 rectangle; (h) stationary droplet with R_c=20.8862 from 3x1 rectangle initials. Notice that stationary droplets in (f) and (h) differ from (b)-(d), but (g) matches (b).

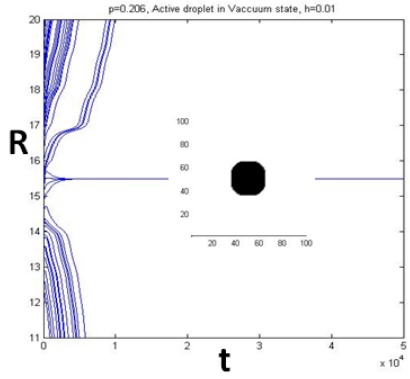

Fig. 9. R versus t for 4-fold symmetric active droplets for *p*=0.206 for various initial sizes showing selection of unique critical vacuum droplet. The stationary solution has R_c=15.4877.

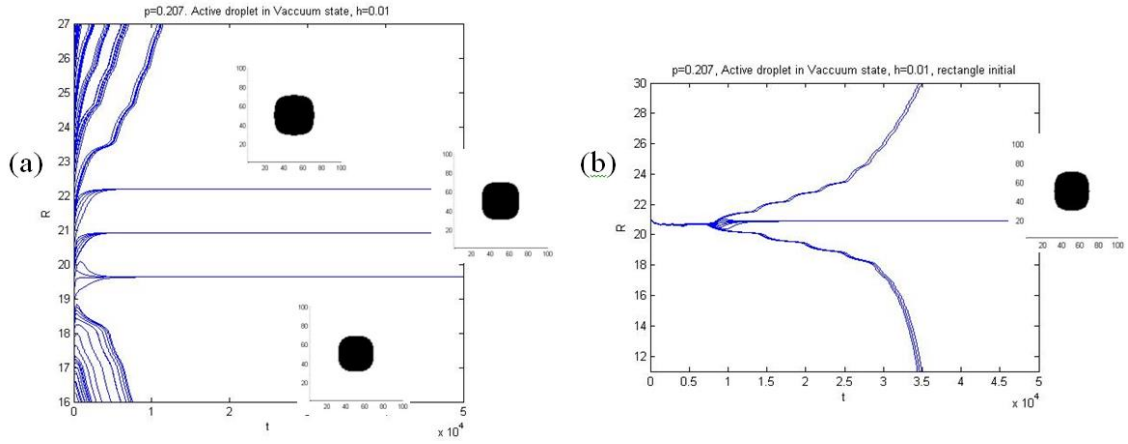

Fig. 10. R versus t for active droplets for p=0.207. (a) 4-fold symmetric initial condition; (b) 2x1 rectangular initial condition. There are three stationary solutions in (a) with R_c = 19.6266, 20.9199, 22.1870, but only one stationary solution in (b) with R_c=20.8862 which is distinct from those in (a).

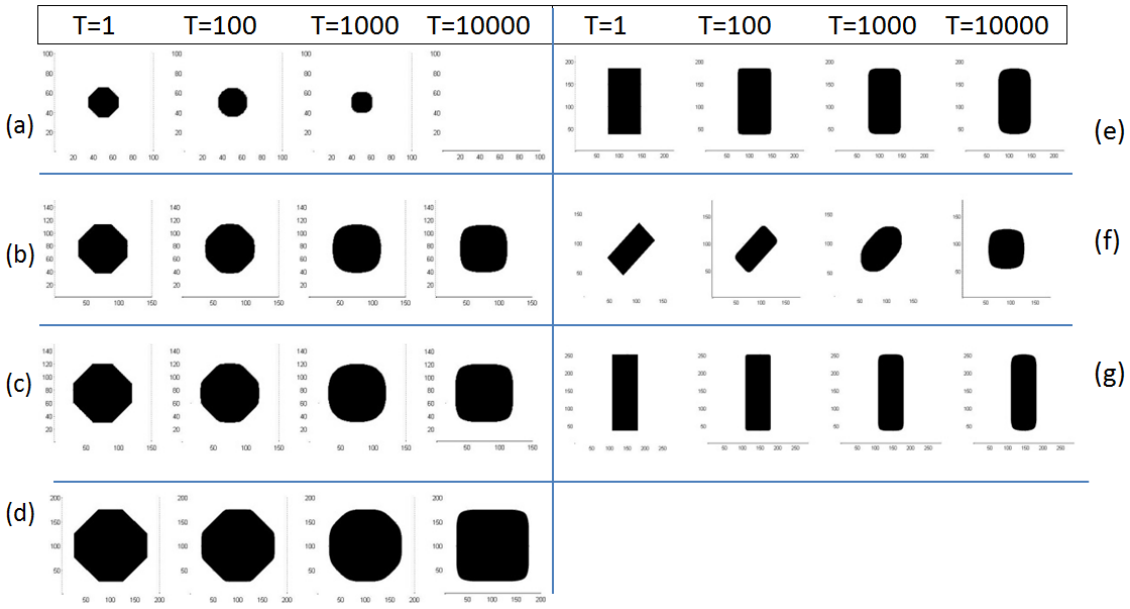

Fig. 11. Evolution of active droplets of different initial sizes embedded in the vacuum steady state for p=0.2085 [where 0.20809 = p-(S=∞) < p < p_{eq}(S→∞) = 0.20903]: For 4-fold symmetric initial data: (a) small initial droplet shrinks; (b) stationary droplet with minimum R_c^- = 38.9322; (c) stationary droplet with Rc = 40.1661; (d) stationary droplet with R_c = 41.3758. For asymmetric initial data: (e) stationary droplet with R_c=57.0258 from 2x1 rectangle; (f) stationary droplet with R_c =38.9322 from oblique 2x1 rectangle;

(g) stationary droplet with R_c=69.9412 from 3x1 rectangle. Notice that stationary droplets in (e) and (g) differ from (b)-(d), but (f) matches (b).

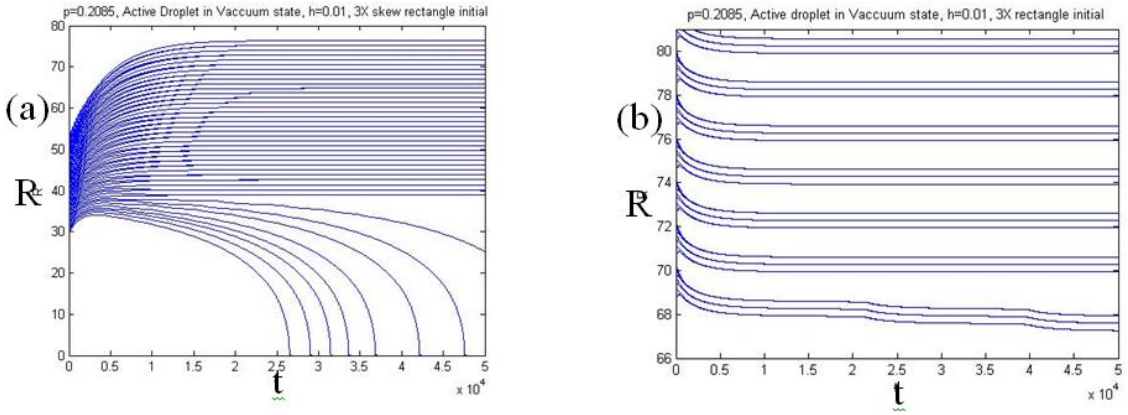

Fig. 12. R versus t for active droplets for p=0.2085. (a) 4-fold symmetric initial condition; (b) 3x1 rectangular initial condition. The infinite discrete set of stationary solutions in (a) has R_c = 38.9322, 40.1661, 41.3758,... The different infinite discrete set of stationary solutions in (b) has R_c = 69.9412, 70.2753, 70.6079,…

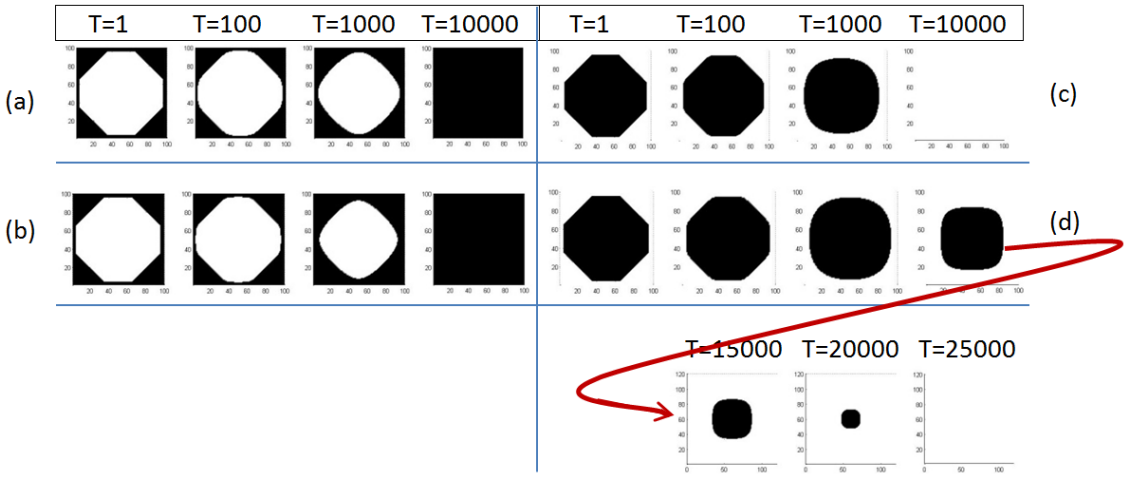

Fig. 13. Shrinking vacuum and active droplets in the 2PC region 0.20903 = peq(S→∞) < p < peq(S=1) = 0.21273. Vacuum droplets for: (a) p=0.211 [> p_+(S=∞) = 0.20973]; (b) p=0.2093 [< p_+(S=∞)]. Active droplet for: (c) p=0.211 [>p_+(S=∞)]; (d) p=0.2093 [< p_+(S=∞)].

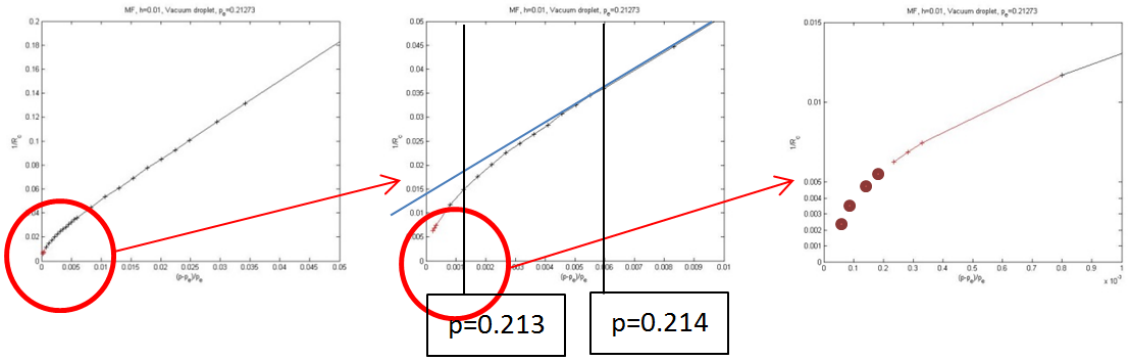

Fig. 14. $\kappa_c = 1/R_c$ VS $\delta p/p_{eq}(S=1)$: (a) $0 < \delta p/p_{eq}(S=1) < 0.05$; and expanded views for (b) $0 < \delta p/p_{eq}(S=1) < 0.01$ (c) $0 < \delta p/p_{eq}(S=1) < 0.001$.

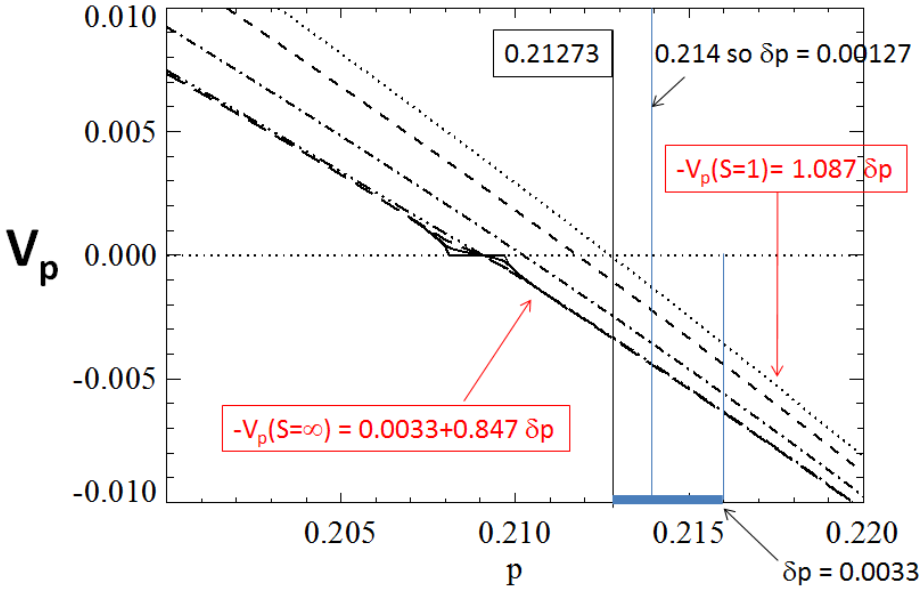

Fig. 15. Propagation velocity of planar interfaces, V, for Durrett's model perturbed with h=0.01. V>0 corresponds to the active state displacing the inactive vacuum state. Slope S=1 diagonal interfaces have the highest equistability $p=p_{eq}(S=1)$. Slope S=∞ vertical interfaces exhibit propagation failure for a range $p_-(S=\infty) < p < p_+(S=\infty)$ below $p_{eq}(S=1)$. Near-vertical interfaces do not exhibit propagation failure and have an equistability $p=p_{eq}(S\to\infty)$.

(a)

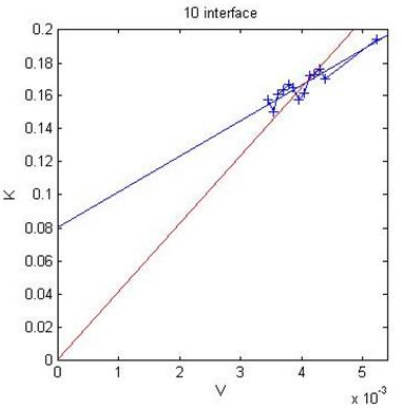

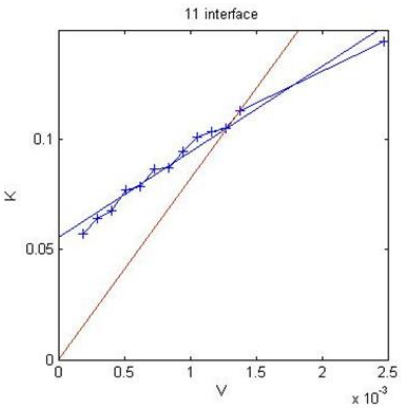

(b)

Fig. 16. κ versus V_p plots for: (a) vertical-oriented; (b) diagonally-oriented portions of the interface of the critical vacuum droplet. The blue straight line is the best-fit curve than the red straight line gives the poor "traditional" fit $\kappa \propto V_p$. (a) $|\kappa_c(S=\infty)| = 0.08023 + 21.6|V_p(S=\infty)|$ or $41.37|V_p(S=\infty)|$ (b) $|\kappa_c(S=1)| = 0.05558 + 38.85|V_p(S=1)|$ or $82.41|V_p(S=1)|$.

Tables

Table 1. Results the upper and lower limits of the regime of propagation failure, $p_{\pm}$(vert), for vertical interfaces, and the stationary point, p_{eq}(~vert), for a near vertical interface. For h=ε=0, p-(vert) =0 $p_{s\pm}$ denote upper and lower (spinodal) limits of the bistable region. For the perturbed models, we find $p_{\pm}(\text{vert}) \approx p_{\pm}(\text{vert})|_{h=0} + c_{\pm} h^{1/2}$ ($c_{\pm} \varepsilon^{1/2}$) for small h (ε) where $c_+ - c_- \approx 0.252$ (0.143) for Durrett. Higher p-values for the threshold model simply reflect higher typical autocatalytic creation rates.

	p_{s-}	p-(S=∞)	p_{eq}(S→∞)	p_+ (S=∞)	p_{eq}(S=1)	p_{s+}
Threshold (ε,h=0+)	0	0.657108	0.684667	0.691308	0.702843	0.815423
Threshold (ε=0.001,h=0)						
Threshold (ε=0, h=0.01)	0	0.682019	0.690245	0.694729	0.704709	0.815423
Durrett (ε,h=0+)	0	0.196134	0.205051	0.207107	0.211377	0.250000
Durrett (ε=0.001,h=0)	0.061212	0.206062	0.208932	0.210363	0.214100	0.251004
Durrett (ε=0, h=0.01)	0	0.208085	0.209034	0.209731	0.212730	0.250000

Table 2. The curvatures $\kappa_c(S=\infty)$ and $\kappa_c(S=1)$ for vertical and diagonal portions of the periphery of critical vacuum droplets.

p	$\kappa_c(S=\infty)$	$V_p(S=\infty)$	$\kappa_c(S=1)$	$V_p(S=1)$
0.2150	0.1946	0.00522	0.1450	0.01702
0.2140	0.1701	0.00438	0.1131	0.01221
0.2139	0.1766	0.00429	0.1055	0.01206
0.2138	0.1730	0.00421	0.1036	0.01123
0.2137	0.1722	0.00412	0.1015	0.01039
0.2136	0.1615	0.00404	0.09492	0.00996
0.2135	0.1574	0.00395	0.08745	0.00957
0.2134	0.1652	0.00387	0.08689	0.00923
0.2133	0.1668	0.00378	0.07892	0.00785
0.2132	0.1635	0.00370	0.07736	0.00660
0.2131	0.1609	0.00361	0.06755	0.00595
0.2130	0.1501	0.00353	0.06413	0.00458
0.2129	0.1579	0.00344	0.05736	0.00322

CHAPTER 7

ANALYTIC FORMULATIONS FOR ONE-DIMENSIONAL DECAY OF RECTANGULAR HOMOEPITAXIAL ISLANDS DURING COARSENING ON ANISOTROPIC FCC(110) SURFACES

A paper submitted to *Physical Review B*

Chi-Jen Wang[1], Yong Han[2], Holly Walen[3], Selena M. Russell[3*], Patricia A. Thiel[3,4,5], and James W. Evans[1,2,5]

Departments of Mathematics[1], Physics & Astronomy[2], Chemistry[3], and Materials Science & Engineering[4], and Ames Laboratory – USDOE[5], Iowa State University, Ames, Iowa 50011

Abstract

Submonolayer homoepitaxial fcc(110) systems display behavior reflecting strong anisotropy at lower temperatures, including one-dimensional decay during Ostwald ripening of rectangular islands. This decay process preserves a constant island width in the $\langle 001 \rangle$ direction. We develop appropriate analytic formulations to describe this behavior. *First*, a refined continuum Burton-Cabrera-Frank formalism is described which accounts for a lack of equilibration of island shape, and importantly also for inhibited incorporation of adatoms at almost-facetted $\langle \bar{1}10 \rangle$ island edges. *Second*, a further refined formalism is developed which incorporates separate terrace and edge adatom density fields in a continuum setting, or alternatively captures these distinct

densities utilizing spatially-discrete diffusion equations (i.e., lattice differential equations). The second approach allows more flexibility in accounting for edge diffusion kinetics including corner rounding, and in treating any lack of equilibration of the edge adatom density at $\langle \bar{1}10 \rangle$ island edges. These approaches are implemented to describe net adatom detachment fluxes from the $\langle 001 \rangle$ ends of islands, and thus island evolution in various local environments.

1. Introduction

Submonolayer homoepitaxial films consist of arrays of single-atom-high two-dimensional (2D) islands on perfectly flat terraces of extended single crystal surfaces. These provide ideal systems for analysis of the details of 2D coarsening processes [1,2]. The most common scenario for coarsening is Ostwald Ripening (OR) [3] wherein smaller than average islands shrink, transferring their adatoms by terrace diffusion to larger islands. Typically, equilibration of island shape is facile during the coarsening process, individual islands maintaining their equilibrium shape which is determined according to the Wulff construction by the orientation-dependent edge energies for 2D clusters [4]. The thermodynamic driving force for coarsening process derives from the reduction in the energy cost associated with broken bonds at island edges which is achieved by reducing in overall island perimeter length [5]. The preferential dissolution of smaller clusters with higher average edge curvatures reflects their higher chemical potential, a quantity which is well-defined given the assumed equilibrium island shapes.

A basic understanding of island evolution during OR is often provided by a continuum Burton-Cabrera-Franck (BCF) [6] type "step dynamics" formulation [4,7]. This formulation involves analysis of a boundary value problem for the diffusion equation describing the density of mobile adatoms on the terraces between islands with appropriate boundary conditions (BCs) at island edges. These BCs account for both the island chemical potentials and for the ease or difficulty of adatom attachment-detachment through so-called kinetic coefficients. It suffices to adopt a steady-state approximation since the adatom density relaxes quickly to the local island configuration. Solution of this boundary value problem gives net fluxes for attachment-detachment, and thus island growth or decay rates. Thus, the island configuration is incrementally updated using these rates, the boundary value problem is resolved to obtain new rates, the island configuration is further evolved, etc. Often instead of analyzing this many-island problem, just the evolution of a single island within a "typical environment" is determined to provide input to the continuity equation for evolution of the island size distribution in a Lifshitz-Slyozov-Wagner theory [5,2].

The above picture applies to isotropic systems, and also to mildly anisotropic systems. However, for strongly anisotropic systems, one might anticipate qualitatively different behavior. The traditional expectation is for a complete *absence* of deterministic OR in purely one-dimensional (1D) systems where all islands have the same chemical potential [8]. In contrast, coarsening does occur in strongly anisotropic 2D systems. For example, Scanning tunneling microscopy (STM) studies by Morgenstern *et al.* [9,10] revealed coarsening for rectangular Ag islands on an Ag(110) surface at a lower

temperature (T) of around 220 K or below, but via an unusual 1D decay mode. Smaller islands shrank in length while retaining *fixed* width in the ⟨001⟩ direction, and thus were unequivocally *not* shape equilibrated [11,12]. Our goal here is to develop appropriate analytical formalisms to describe this 1D decay behavior.

In Sec. II, we provide a brief atomistic-level description of the thermodynamics and surface diffusion kinetics for submonolayer fcc(110) homoepitaxial systems. Experimental observations for 1D decay of Ag islands on Ag(110), and kinetic Monte Carlo (KMC) simulation results for an atomistic model for this process, are also presented. Then, in Sec. III, we refine the standard continuum BCF formulation to treat these strongly anisotropic systems. Refined BCF predictions for decay rates of islands in strongly anisotropic fcc(110) homoepitaxial systems are presented various local environments, demonstrating that this formalism captures the key dependencies on geometry and temperature. However, this refined BCF approach does not have the flexibility to describe the details of edge diffusion kinetics and neglects any lack of local equilibration of edge adatoms. Thus, in Sec. IV, we present a further refined formalism with multiple adatom density fields to better capture edge diffusion kinetics first within a continuum framework, and then through an alternative spatially-discrete diffusion equation (or lattice differential equation) formalism [13]. A comparison with the refined BCF formalism is also presented.

2. Review of Homoepitaxial FCC(110) Surface Dynamics and 1D Island Decay

2A. Atomistic models for surface diffusion kinetics

An fcc(110) surface consists of an array of parallel channels as shown in **Fig. 1**. The surface unit cell is rectangular with shorter side length b in the $\langle \bar{1}10 \rangle$ direction, and longer side length $a = \sqrt{2}b$ in the $\langle 001 \rangle$ direction, so its area is given by $\Omega = ab$. Adatoms hop between the preferred in-channel adsorption sites (supported by four atoms in the underlying surface layer) through bridge-site transition states (TS). These bridge sites differ for in-channel and cross-channel hopping, and correspondingly there are different diffusion barriers $E_{\mathrm{d}}^{\parallel}$ and $E_{\mathrm{d}}^{\perp}$, respectively. These barriers just correspond to the difference between the energy, E_{ads}, at adsorption site and the TS energy for an isolated adatom. Here, one caveat is that cross-channel diffusion could instead occur preferentially via exchange for some homoepitaxial fcc(110) systems.

A complete characterization of surface diffusion kinetics, including edge diffusion and detachment, requires specification of "conventional" interactions between adatoms on preferred adsorption sites. We assume nearest-neighbor pairwise attractions with a larger (smaller) magnitude $E_{\mathrm{b}}^{\parallel} < 0$ ($E_{\mathrm{b}}^{\perp} < 0$), for atoms separated b (a) in the $\langle \bar{1}10 \rangle$ ($\langle 001 \rangle$) direction. In addition, for our *multisite lattice-gas (msLG) models* [14,15,16], we prescribe as second set of "unconventional" interactions between one adatom at a TS and others at nearby adsorption sites. Again, just short range pairwise attractions are assumed ($E'^{\parallel}_{\mathrm{b}} < 0$ and $E'^{\perp}_{\mathrm{b}} < 0$). See **Fig. 1**. These unconventional interactions are set to zero in common initial value approximation (IVA) models [17,18]. However, allowing non-zero $E'^{\parallel}_{\mathrm{b}}$ and $E'^{\perp}_{\mathrm{b}}$ provides additional flexibility and accuracy in simultaneously describing both thermodynamics and edge diffusion kinetics [19]. The total energy E_{i} in the initial state before hopping, and the total TS energy E_{TS} can be

determined as the sum of the relevant adsorption energy and pairwise interactions; then the activation barrier for hopping is simply determined as $E_{\rm act} = E_{\rm TS} - E_{\rm i}$ [14,15,16]. Hop rates are described by an Arrhenius form, $h = \nu e^{-\beta E_{\rm act}}$, with common prefactor $\nu = 10^{13}$/s and inverse temperature $\beta \equiv 1/(k_{\rm B}T)$ ($k_{\rm B}$ is the Boltzmann constant). For Ag/Ag(110), an appropriate choice of energetics is described in Ref. [11]. For this study, the parameters of most importance are $E_{\rm d}^{\parallel} = 0.28$ eV, $E_{\rm d}^{\perp} = 0.38$ eV, $E_{\rm b}^{\parallel} = -0.18$ eV, $E_{\rm b}^{\perp} = -0.045$ eV, and a fast corner rounding barrier $E_{\rm cr} = 0.39$ eV. See Fig. 1. Here, we also should mention that earlier IVA modeling used a low value of $E_{\rm b}^{\perp} = -0.02$ eV, which is not consistent with observed equilibrium island shapes. However, later this value was increased in IVA modeling to $E_{\rm b}^{\perp} = -0.04$ eV [20], which is similar to our choice [11].

The key features proposed to produce the type of 1D island decay for Ag/Ag(110) at lower temperatures described in Sec. I are [9,11]: (i) Detachment of atoms almost exclusively from the short $\langle 001 \rangle$ ends of islands. (ii) A lack of detachment from the long $\langle \bar{1}10 \rangle$ sides, and a lack of corner rounding from the $\langle 001 \rangle$ ends to the $\langle \bar{1}10 \rangle$ sides (but see Sec. IV B). (iii) Inhibited nucleation of new layers on the $\langle \bar{1}10 \rangle$ sides, and facile corner rounding of edge atoms from the $\langle \bar{1}10 \rangle$ sides to the $\langle 001 \rangle$ ends. See **Fig. 1** for our notation. We expect that 1D island decay is a general phenomenon for fcc(110) homoepitaxial systems, and for other systems with strong anisotropy.

2B. Key experimental observations for Ag/Ag(110)

The key experimental STM observations for coarsening of rectangular Ag islands on the anisotropic Ag(110) surface have been described in Morgenstern *et al.* [9,10] and Han *et al.* [11]. Details of the experimental setup and procedures can be found in those publications. Above about 220 K, classic OR behavior is observed with individual islands retaining their equilibrium shapes during growth or decay [9]. If $L^{\parallel}$ ($L^{\perp}$) denotes the length (width) of rectangular islands in the $\langle\bar{1}10\rangle$ ($\langle 001\rangle$) direction, then the area satisfies $A \approx L^{\parallel}L^{\perp}$ and the aspect ratio is given by $R \equiv L^{\parallel}/L^{\perp}$. For equilibrated island shapes, one has that $R = R_{\mathrm{eq}} \approx 3$ [9]. However, at 220 K and below, a 1D decay mode is observed: smaller (and narrower) islands shrink in length, $L^{\parallel}$, while retaining constant width, $L^{\perp}$. This behavior is observed down to about 175 K at which point the coarsening process becomes too slow to be readily observed. To motivate subsequent analysis, in Figs. 2 and 3 we provide examples of this 1D island decay process with time t. Detailed images for the selected examples have not been shown previously. It is clear that the island decay rate $K = -\mathrm{d}A/\mathrm{d}t$ increases with T. Indeed, a more comprehensive analysis which better captures typical decay behavior shows that $K \propto e^{-\beta E_{\mathrm{OR}}}$ defining the Arrhenius energy which here adopts the value $E_{\mathrm{OR}} \approx 0.32$ eV [11].

2C. KMC simulation results for 1D island decay on Ag/Ag(110)

Fig. 4. shows the results of extensive simulations of the 1D decay process for the island shown in **Fig. 2(a)** at 190 K. These simulations were performed using our atomistic msLG model described in Sec. II A and in Ref. [11]. Input to the simulations is the multi-island configuration mimicking the local environment of the decaying island.

In addition, we perform "atom-tracking" KMC simulations where we label the adatoms originally in the decaying island with a different color so as to track their transfer to other islands. Given the small island size and low temperature, there are significant fluctuations in the decay process. As a consequence, to reliably assess typical or average behavior, we perform ~100 trials and average the results. From the decrease of the average area of the decaying island, we extract an initial decay rate of $K_{\mathrm{msLG}} \approx 0.0026$ nm^2/s. However, after a transient period of ~750 s, there appears to be a slight increase in rate to $K_{\mathrm{msLG}} \approx 0.0033$ nm^2/s (measured between ~750 s and ~1500 s). This may reflect the "idealized" initial conditions in our simulations with perfect rectangular islands. The apparent discrepancy between the average msLG rates and the experimental rate $K_{\mathrm{expt}} \approx 0.007$ nm^2/s is expected given the very large fluctuations in the results for individual simulation trials.

3. Refined BCF Theory for Anisotropic Systems without Island Equilibration

Here, we show how traditional continuum BCF type formulations might be refined to better describe coarsening in strongly anisotropic systems, and specifically 1D island decay corresponding to a large deviation from island shape equilibration. Our focus is on determining for the decay rate, $K_{\mathrm{rBCF}} = -\mathrm{d}A/\mathrm{d}t$, of smaller narrower islands from our refined-BCF (rBCF) theory.

3A. Constrained thermodynamics

For fcc(110) homoepitaxial systems with rectangular monolayer islands, the key thermodynamic parameters in our atomistic model are: the chemical potential for an infinite island $\mu_\infty = \mu_{\rm ads} + \mu_{\rm int}$ where $\mu_{\rm ads} = E_{\rm ads}$ and $\mu_{\rm int} = E_{\rm b}^{\parallel} + E_{\rm b}^{\perp}$; and the higher (lower) step energy per unit length $\gamma_{001} = |E_{\rm b}^{\parallel}|/(2a)$ ($\gamma_{\bar{1}10} = |E_{\rm b}^{\perp}|/(2b)$) for steps aligned in the $\langle 001\rangle$ ($\langle \bar{1}10\rangle$) direction. See **Fig.** 1. The energy of an island with linear dimension $L^{\parallel}$ ($L^{\perp}$) in the $\langle \bar{1}10\rangle$ ($\langle 001\rangle$) direction and area $A \approx L^{\parallel}L^{\perp}$ can be written as

$$E_{\rm isl} = \frac{A}{\Omega}\mu_\infty + (2\gamma_{\bar{1}10}L^{\parallel} + 2\gamma_{001}L^{\perp}). \quad (1)$$

Given the lack of island shape equilibration, we introduce *partial chemical potentials*, μ_M, for different possible modes, M, of island evolution [11,21, 22]. For this study, the most relevant mode $M = 001$ involves changing length $L^{\parallel}$ with constant width $L^{\perp}$. Then, $\mu_{001} = \Omega {\rm d}E_{\rm isl}/{\rm d}A$ obtained using ${\rm d}A = L^{\perp}{\rm d}L^{\parallel}$ with fixed $L^{\perp}$ yields

$$\mu_{001} = \mu_\infty + 2\Omega\gamma_{\bar{1}10}/L^{\perp}. \quad (2)$$

The introduction of μ_{001} assumes a degree of local equilibration which should also apply for the dilute ideal 2D adatom gas at the $\langle 001\rangle$ island edge. If $n_{\rm eq}$ denotes the locally equilibrated gas density per site at the $\langle 001\rangle$ island edge, then its chemical potential is given by $\mu_{\rm gas} = \mu_{\rm ads} + k_{\rm B}T\ln n_{\rm eq}$. Since $\mu_{\rm gas}$ must match μ_{001}, it follows that $n_{\rm eq}$ equals [11,23]

$$n_{001} = n_\infty e^{2\beta\Omega\gamma_{\bar{1}10}/L^{\perp}}. \quad (3)$$

Here, $n_\infty = e^{\beta\mu_{\rm int}}$ denotes the equilibrium adatom density at an extended straight step. Finally, for the observed 1D decay mode $M = 001$, Eqs. (2) and (3) indicate that

narrower islands with smaller $L^{\perp}$ and therefore higher μ_{001} and n_{001} should shrink, while wider islands with bigger $L^{\perp}$ and therefore lower μ_{001} and n_{001} grow.

Similarly, defining a mode $M = \bar{1}10$ for changing width $L^{\perp}$ with fixed length $L^{\parallel}$, one has that $\mu_{\bar{1}10} = \mu_{\infty} + 2\Omega\gamma_{001}/L^{\parallel}$ and $n_{\bar{1}10} = n_{\infty}e^{2\beta\Omega\gamma_{001}/L^{\parallel}}$ at $\langle\bar{1}10\rangle$ island edges. Now, for equilibrated island shapes (occurring at higher T), one must have that $\mu_{001} = \mu_{\bar{1}10}$ which yields the equilibrium aspect ratio $R_{\mathrm{eq}} \equiv L^{\parallel}_{\mathrm{eq}}/L^{\perp}_{\mathrm{eq}} = \gamma_{001}/\gamma_{\bar{1}10}$, a result traditionally obtained by minimizing energy E_{isl} for constant area A.

3B. Refined BCF formulation for kinetics

As noted in Sec. I, analytic BCF formulations of OR are based on a steady-state analysis of the diffusion equation for the adatom density, n, which for fcc(110) homoepitaxial systems has the form

$$\frac{\partial}{\partial t}n = D^{\parallel}\frac{\partial^2}{\partial x^2}n + D^{\perp}\frac{\partial^2}{\partial y^2}n \approx 0, \tag{4}$$

where $D^{\parallel} \equiv D_0^{\parallel}e^{-\beta E_{\mathrm{d}}^{\parallel}}$ ($D^{\perp} \equiv D_0^{\perp}e^{-\beta E_{\mathrm{d}}^{\perp}}$) is the larger (smaller) diffusion coefficient in the $\langle\bar{1}10\rangle$ ($\langle 001\rangle$) x- (y-) direction given that $0 < E_{\mathrm{d}}^{\parallel} < E_{\mathrm{d}}^{\perp}$. In this work, we will assume a common attempt frequency for hopping, ν, so that $D_0^{\parallel} = b^2\nu$ and $D_0^{\perp} = a^2\nu$. Appropriate BCs must be imposed at island edges. The lack of island shape equilibration might be addressed by assigning separate partial chemical potentials and equilibrium adatom densities to the $\langle\bar{1}10\rangle$ and $\langle 001\rangle$ edges (cf. Sec. III A).

In a general Chernov formulation, the boundary conditions are written as [7]

$$\pm D^{\parallel}\frac{\partial n}{\partial x} = k_{001}(n - n_{001}) \tag{5(a)}$$

at $\langle 001 \rangle$ edges, and

$$\pm D^{\perp} \frac{\partial n}{\partial y} = k_{\bar{1}10}(n - n_{\bar{1}10}) \qquad 5(b)$$

at $\langle \bar{1}10 \rangle$ edges. The $+(-)$ sign applies for the right (left) edge of the island in Eq. 5(a), and the upper (lower) edge in Eq. 5(b). In a traditional "macroscopic setting" [24], the kinetic coefficients, k_{001} and $k_{\bar{1}10}$, which describe the ease of attachment, would traditionally be taken as $k_{001}^{\text{macro}} = D^{\parallel}/\left(e^{\beta\delta_{001}} - 1\right)$ and $k_{\bar{1}10}^{\text{macro}} = D^{\perp}/\left(e^{\beta\delta_{\bar{1}10}} - 1\right)$ where δ_{001} and $\delta_{\bar{1}10}$ denote the additional energy barriers for attachment at $\langle 001 \rangle$ and $\langle \bar{1}10 \rangle$ steps, respectively [25,13]. Such barriers are generally zero for homoepitaxial systems, and thus the kinetic coefficients are generally taken as infinite for so-called terrace-diffusion limited coarsening. Then, Eqs. (5a) and (5b) reduce to simple Dirichlet BCs: $n = n_{001}$ at $\langle 001 \rangle$ edges, and $n = n_{\bar{1}10}$ at $\langle \bar{1}10 \rangle$ edges, respectively.

Solution of this Dirichlet boundary value problem allows determination of the integrated net detachment flux for each edge of each island. These determine the rate at which the island dimensions change if one assumes negligible transfer of adatoms by edge diffusion between different island edges. However, even for small $D^{\perp}$, these traditional Dirichlet BCs would lead to a tendency for widening of islands for aspect ratio $R > R_{\text{eq}}$ where $n_{\bar{1}10} < n_{001}$. Likewise, there is a tendency for narrowing when $R < R_{\text{eq}}$ and $n_{001} < n_{\bar{1}10}$. This is *not* consistent with the 1D decay observed in experiment.

Our resolution to this dilemma is to argue that the traditional macroscale Chernov-type kinetic coefficients in a BCF formulation must be modified for analysis of

nanoscale evolution. Specifically, this modification is required when the characteristic length scale of the decaying objects does not greatly exceed the characteristic separation, L_{kink}, between kinks at island edges [13]. The underlying concept is that true attachment at steps requires incorporation at kink sites, and is thus inhibited for low kink densities even in the absence of an additional energetic barrier for attachment. This is the case for the smooth almost-facetted $\langle\bar{1}10\rangle$ island edges. As a result, we introduce a more appropriate "very small" effective kinetic coefficient, $k_{\bar{1}10}{\sim}D^{\perp}/L_{\mathrm{kink}}^{2}$ for attachment to the $\langle\bar{1}10\rangle$ step edge [13], which would be negligible for an almost-facetted step edge with large L_{kink}. The kinetic coefficient k_{001} can reasonably be taken as infinite since $\langle 001\rangle$ steps are highly kinked. Within this formalism incorporating $k_{\bar{1}10}=0$, it is immediately clear that one recovers 1D decay which is *independent* of the value of $n_{\bar{1}10}$.

In closing, we note a previous BCF-type treatment by Yao *et al.* [23] for Ag island decay on Ag(110). They incorporated finite kinetic coefficients $k^{\parallel}\ll k^{\perp}$, based on the inequality $D^{\parallel}\ll D^{\perp}$, although this only follows in the traditional macroscopic theory for non-zero δ_{001} and $\delta_{\bar{1}10}$, However, Yao *et al.* did not discuss the assignment of finite $k^{\parallel}$ and $k^{\perp}$ in the absence of energetic barriers to attachment. They also predicted a different scaling in time for the island decay rate from the behavior which we describe below.

3C. Refined BCF analysis for benchmark aligned island configurations

Here, we perform an analysis of the diffusion problem in Sec. III B for a "benchmark" island configuration motivated by the observation that islands in

experimental distributions are often reasonably well aligned end-to-end with their neighbors in the $\langle\bar{1}10\rangle$ direction [11]. Thus, we consider a configuration with just two aligned islands of differing widths in a rectangular simulation cell with periodic boundary conditions. See **Fig. 5.** This enables more systematic analysis and elucidation of the fundamental behavior. We set $E_{\mathrm{d}}^{\perp} - E_{\mathrm{d}}^{\parallel} = 0.1$ eV for Ag/Ag(110), and set the temperature to 190 K unless otherwise stated. This implies that $\varepsilon \equiv D^{\perp}/D^{\parallel} = 0.00445$. Below, $L_{\mathrm{cell}}^{\perp}$ will denote the width of the simulation cell, and $L_{\mathrm{narrow}}^{\perp}$ ($L_{\mathrm{wide}}^{\perp}$) the width of the narrow (wide) island in the $\langle 001\rangle$ direction. Also, $L_{\mathrm{cell}}^{\parallel} = 2L_{\mathrm{sep}} + L_{\mathrm{narrow}}^{\parallel} + L_{\mathrm{wide}}^{\parallel}$ denotes the length of the simulation cell in terms of the length of the narrow (wide) island, $L_{\mathrm{narrow}}^{\parallel}$ ($L_{\mathrm{wide}}^{\parallel}$), and the separation, L_{sep}, between them in the $\langle\bar{1}10\rangle$ direction.

Precise determination of the decay rate, K_{rBCF}, for the narrower island from our refined-BCF theory, and its dependence on various geometric and model parameters, is achieved from numerical analysis of the diffusion problem using FEMLAB software [26]. An example of the results from such an analysis is shown in **Fig. 5**, where we define $R_{\mathrm{narrow}} \equiv \frac{L_{\mathrm{narrow}}^{\parallel}}{L_{\mathrm{narrow}}^{\perp}}$, $k \equiv \frac{L_{\mathrm{cell}}^{\perp}}{L_{\mathrm{narrow}}^{\perp}}$, $l \equiv \frac{L_{\mathrm{sep}}}{L_{\mathrm{narrow}}^{\parallel}}$, $m \equiv \frac{L_{\mathrm{wide}}^{\parallel}}{L_{\mathrm{narrow}}^{\parallel}}$, and $s \equiv \frac{L_{\mathrm{wide}}^{\perp}}{L_{\mathrm{narrow}}^{\perp}}$. If "narrow" ("wide") denotes quantities for the narrower (wider) island, then the bottom frame shows results for the rescaled adatom density, $\delta n^{*} \equiv (n - n_{001}^{\mathrm{wide}})/(n_{001}^{\mathrm{narrow}} - n_{001}^{\mathrm{wide}})$. Thus, δn^{*} takes values of 1 (0) at the end of the narrower (wider) island. From these results, we can calculate the net detachment fluxes integrated along $\langle 001\rangle$ island

ends after multiplying integrated rescaled fluxes, $\int \frac{\partial}{\partial x}\delta n^* \mathrm{d}y$, by $D^{\parallel}(n_{001}^{\mathrm{narrow}} - n_{001}^{\mathrm{wide}})$. Selected results are shown in Table I.

For this aligned island geometry, given the strong anisotropy in terrace diffusion at 190 K, it is natural to assess the effectiveness of a quasi-1D estimate, $K_{1\mathrm{D}}$, of the island decay rate. This estimate corresponds to the diffusion flux in the $\langle \bar{1}10 \rangle$ (x-) direction rate for $D^{\perp} = 0$ (and therefore $\varepsilon = 0$), and has the form

$$K_{1\mathrm{D}} = 2D^{\parallel}\frac{L_{\mathrm{narrow}}^{\perp}}{L_{\mathrm{sep}}}\left(n_{001}^{\mathrm{narrow}} - n_{001}^{\mathrm{wide}}\right) \approx \frac{4D^{\parallel}n_{\infty}\beta\Omega\gamma_{\bar{1}10}}{L_{\mathrm{sep}}}\left(1 - \frac{L_{\mathrm{narrow}}^{\perp}}{L_{\mathrm{wide}}^{\perp}}\right). \quad (6)$$

The latter expression follows after adopting an approximation for the adatom density $n_{001} = n_{\infty}e^{2\beta\Omega\gamma_{\bar{1}10}/L^{\perp}} \approx n_{\infty} + 2n_{\infty}\beta\Omega\gamma_{\bar{1}10}/L^{\perp}$.

Results shown in Table I directly compare K_{rBCF} and $K_{1\mathrm{D}}$. The agreement is particularly good if the separation, L_{sep}, between the islands is comparable to the island length. For larger L_{sep}, the agreement is better for narrower simulation cells. A key feature reflecting quasi-1D behavior is the dependence of $K_{\mathrm{rBCF}} \sim 1/L_{\mathrm{sep}}$ on L_{sep} where all other parameters are fixed. This inverse proportionality is satisfied best for narrow simulation cells with width not much greater than the wider island. Such a decrease in K_{rBCF} with increasing L_{sep} is much stronger than the logarithmic dependence found in isotropic systems [11]. This feature impacts the temperature-dependence of island decay, as discussed in Sec. III F.

We can also assess the dependence of K_{rBCF} on other model parameters. *First*, we recall the feature that the thermodynamic driving force for island decay derives from the difference in width between islands. Thus, it is natural to analyze the change in K_{rBCF}

upon varying $L^{\perp}_{\mathrm{wide}}$. We choose $L^{\perp}_{\mathrm{wide}} = (k-1)L^{\perp}_{\mathrm{narrow}}$ and increase k. In this analysis, we fix $R_{\mathrm{narrow}} = 3$, $l = 3/2$, $m = 2$, $s = 3/2$, and $\varepsilon = 0.00445$. If we define $\delta n_{001} \equiv n^{\mathrm{narrow}}_{001} - n^{\mathrm{wide}}_{001}$, then results from this analysis are instructively presented as

$$K_{\mathrm{rBCF}} = c_k \delta n_{001} \tag{7}$$

with $c_k/c_{5/2} = 0.97$, 1.02, and 0.98 for $k = 3$, $k = 5$, and $k > 9$ (i.e., c_k is roughly independent of k). Thus, the enhanced decay rate for wider islands primarily results from the increased thermodynamic driving force. The limiting value for $k > 9$ corresponds to decay of an island between two infinite steps.

Second, consistent with the quasi-1D estimate, we find a negligible dependence of K_{rBCF} on the length, $L^{\parallel}_{\mathrm{wide}} \equiv mL^{\parallel}_{\mathrm{narrow}}$, of the larger island: $\frac{K_{\mathrm{rBCF}}(m)}{K_{\mathrm{rBCF}}(m=1)} = 1$, 1.000, 0.981, 0.969 for $m = 1$, 2, 4, and 8, respectively, fixing other parameters: $R_{\mathrm{narrow}} = 3$, $k = 2$, $l = 3/2$, $s = 3/2$, and $\varepsilon = 0.00445$.

Third, we explore how the dependence of K_{rBCF} on $L_{\mathrm{sep}} \equiv lL^{\parallel}_{\mathrm{narrow}}$ varies with the degree of anisotropy ε in terrace diffusion. For the benchmark geometry with fixed $R_{\mathrm{narrow}} = 3$, $k = 5/2$, $m = 2$, and $s = 3/2$, we find that the dependence, $K_{\mathrm{rBCF}} \sim 1/L_{\mathrm{sep}}$, does not degrade upon increasing ε from 0.00445 to 0.0102 (i.e., increasing T from 190 K to 220 K for Ag/Ag(110)) to $\varepsilon = 1$ (isotropic diffusion). See Table II. The key point is that quasi-1D behavior is induced not just by small ε, but also by the "quasi-1D channel" geometry in which we solve boundary value problem for the diffusion equation. This feature of our benchmark geometry for larger L_{sep} reflects experimental

geometries given the presence of highly elongated large islands formed during deposition [11]. See **Fig. 2.**

3D. Refined BCF analysis for non-aligned island configurations

Certainly, there are examples in experimental island distributions where neighboring islands in the $\langle \bar{1}10 \rangle$ direction are *completely misaligned*. It is clear that the net flux of diffusing adatoms between such islands (which is mediated by slow cross-channel diffusion) will be relatively small. There are also cases, as shown in Sec. III E, where neighboring islands are *marginally misaligned*, so that the top $\langle \bar{1}10 \rangle$ edge of one island is aligned with the bottom $\langle \bar{1}10 \rangle$ edge of the neighbor. The net flux between such islands for large anisotropy, $\varepsilon \ll 1$ should be significantly higher than for completely misaligned islands. Separate analysis for the simpler benchmark configurations shown in **Fig. 6** reflecting these possibilities for misalignment will help elucidate evolution for general arrays of islands.

The FEMLAB results for island decay rates, K_{rBCF}, are shown in Table III comparing behavior for marginally misaligned and completely misaligned islands in **Fig. 6** with that for aligned islands in **Fig. 5.** We vary ε to check for scaling of the form $K_{\mathrm{rBCF}} \sim \varepsilon^{\sigma}$, as $\varepsilon \to 0$, where σ is an exponent to be determined. For aligned islands, one has $K_{\mathrm{rBCF}} \to K_{1\mathrm{D}} > 0$ (the 1D estimate), as $\varepsilon \to 0$. For *marginally aligned islands*, data in Table III together with more extensive analysis shows that $K_{\mathrm{rBCF}} \sim \varepsilon^{1/2}$, as $\varepsilon \to 0$, a feature clarified in Sec. III F. Note that K_{rBCF} in this case is a significant fraction ($\sim 1/3$) of that for aligned islands despite the strong diffusional anisotropy of $\varepsilon = 0.00445$

corresponding to $T = 190$ K for Ag/Ag(110). For *completely misaligned islands*, K_{rBCF} decreases much more quickly with ε, so the flux becomes substantially smaller than that for marginally aligned islands. From Table III supplemented by additional analysis, one finds that $K_{\mathrm{rBCF}} \sim \varepsilon^1$, as $\varepsilon \to 0$. See also Sec. III F.

3E. Refined BCF analysis for an experimental island configuration

For configurations of multiple islands, including those extracted from experimental STM images, it is also viable to solve the rBCF boundary value problem numerically using FEMLAB software. In this way, one can compare theoretical predictions for island evolution, and particularly the 1D decay of narrower islands, with experimental observations or corresponding KMC simulations. To this end, we input to our numerical analysis a configuration of several islands shown in **Fig. 7** (top) which constitute the local environment of the narrow decaying island tracked in **Fig. 2(a).** One constraint for our FEMLAB analysis is that we choose the boundary of the simulation region to roughly correspond at least approximately to a zero flux boundary. Note however that the specific treatment of the outer boundary will not greatly affect the evolution of the "far removed" small narrow central island. For each of the islands, we impose a zero-flux boundary condition on the top and bottom $\langle \bar{1}10 \rangle$ edges, and a suitable Dirichlet BC on the $\langle 001 \rangle$ ends. From Eq. (3), the latter BC sets the adatom densities, n, to

$$n_{001} = n_\infty e^{2\beta\Omega\gamma_{\bar{1}10}/L^\perp} = n_\infty e^{\beta a|E_{\mathrm{b}}^\perp|/L^\perp} \approx n_\infty e^{1.124/L^\perp} \tag{8}$$

at 190 K, with $\left|E_{\mathrm{b}}^\perp\right| = 0.045$ eV for Ag/Ag(110) [11] and with $L^\perp$ in nm.

Results of our FEMLAB analysis for the rescaled density field $n^{\dagger} = n/n_{\infty}$ are shown in **Fig. 7** (bottom). From these results, we can calculate the net detachment fluxes integrated along ⟨001⟩ island ends after multiplying integrated rescaled fluxes $\int \frac{\partial}{\partial x} n^{\dagger} \mathrm{d}y$ by $D^{\parallel} n_{\infty} = 0.0336$ nm^2/s at 190 K using parameters for Ag/Ag(100) in Ref. [11]. The calculated net detachment rate from the right side of the small central island 1 is $K_{\mathrm{rBCF,1R}} = 0.00147$ nm^2/s, and from the left side is $K_{\mathrm{rBCF,1L}} = 0.00073$ nm^2/s. Thus, the total rate of decay of the area of island 1 is $K_{\mathrm{rBCF},1} = 0.0022$ nm^2/s.

It is natural to compare the value of $K_{\mathrm{rBCF,1R}}$ with a simple 1D estimate. We note that a segment of length $L'^{\perp} = 1.7$ nm on the right end of island 1 (with $L_1^{\perp} = 2.5$ nm) is directly aligned with the left end of the island 5 to the right (with $L_5^{\perp} = 3.3$ nm) which is separated from island 1 by a distance $L_{\mathrm{sep}}^{1\to5} = 8.3$ nm. Thus, it follows that

$$K_{\mathrm{1D,1R}} = D^{\parallel} n_{\infty} \left(e^{1.124/L_1^{\perp}} - e^{1.124/L_5^{\perp}} \right) L'^{\perp} / L_{\mathrm{sep}}^{1\to5} = 0.0011 \text{ nm}^2/\text{s}. \quad (9)$$

$K_{\mathrm{1D,1R}}$ is somewhat below $K_{\mathrm{rBCF,1R}}$, as expected from the results in Sec. III C. We also emphasize that the left end of island 1 provides an example of "marginal alignment" with the neighboring island to the left. Despite only marginal alignment, $K_{\mathrm{rBCF,1L}}$ is still significant relative to $K_{\mathrm{rBCF,1R}}$, as might also be anticipated from the results in Sec. III D.

From the FEMLAB analysis, one can also extract integrated diffusional fluxes at the ends of all islands. The results are as expected. For example, the largest fluxes, $K_{\mathrm{rBCF,4L}} = 0.00448$ nm^2/s and $K_{\mathrm{rBCF,3R}} = -0.00462$ nm^2/s, are associated with the smallest island 4.

Next, we compare the above results with the *experimental observations* in Sec. II B. The effective comparison is complicated by two factors. *First*, the island decay process has significant stochastic nature as shown in Sec. II, especially for small islands at 190 K. Thus, experimentally observed behavior may not be typical. *Second*, the actual shapes of islands neighboring the decaying island 1 are not perfect rectangles or even rectangles with rounded corners. The feature that these islands often do not have straight $\langle\bar{1}10\rangle$ sides means that there are significantly more traps for diffusing adatoms than for more perfect islands such as those in our rBCF analysis. This is consistent with the high experimental decay rate, $K_{\mathrm{expt},1} \approx 0.007$ nm^2/s (with large uncertainty) relative to the rBCF analysis.

Finally, we compare the rBCF results with those from *KMC simulation of our msLG model* in Sec. II C for the experimental island configuration. This avoids some of the above complications in comparing with experiment. *First*, by repeating the simulation multiple times for a single initial configuration of island 1 and its local environment, we not only assess the extent of fluctuations in decay, but also obtain precise results for the mean decay rate. *Second*, we can choose the initial shapes of the islands to match the perfect rectangular rBCF shapes rather than including the experimental imperfections. Comparing the initial decay rate for island 1 from our msLG model averaging over 99 trials (see Sec. II C) with the rBCF result yields the good agreement

$$K_{\mathrm{msLG},1} = 0.0026 \text{ nm}^2/\text{s versus } K_{\mathrm{rBCF},1} = 0.0022 \text{ nm}^2/\text{s}. \quad (10)$$

However, complications include possible initial transients in our KMC simulations as noted in Sec. II C, and limitations of the rBCF theory as discussed in Sec. IV.

3F. Discussion of rBCF analysis

Our rBCF analysis has been effective in characterizing dependence of the island decay rate on geometry. However, a simple observation further elucidates the results in Secs. III C and III D, including the effectiveness of the quasi-1D analysis: expanding the y-axis by a (large) factor of $r \equiv \varepsilon^{-1/2} \equiv (D^{\parallel}/D^{\perp})^{1/2} = (b/a)e^{\beta(E_{\mathrm{d}}^{\perp}-E_{\mathrm{d}}^{\parallel})/2}$ converts the boundary value problem into one with isotropic diffusion. Since $r = e^{0.05\beta}/\sqrt{2} \approx 15.0$ (here and later, β is always in eV^{-1} for any similar expression) is large for Ag/Ag(110) at 190 K, our benchmark geometry with two *aligned* islands in the simulation cell transforms into a geometry with two closely-spaced wide islands with long parallel nearby edges. Thus, one naturally expects quasi-1D behavior. To obtain the island decay rate, K_{rBCF}, for misaligned islands, one solves for rate, K_{iso}, in the rescaled isotropic problem, and then multiplies by $1/r$ (accounting for expanded $\langle 001 \rangle$ island edge lengths) to recover the flux in the original problem. Then, for the marginally misaligned case, it is clear that K_{iso} achieves a finite limiting value as $r \to \infty$, and thus $K_{\mathrm{rBCF}} \sim K_{\mathrm{iso}}/r \sim \varepsilon^{1/2}$, as $\varepsilon \to \infty$. For the completely misaligned case, one has that $K_{\mathrm{iso}} \sim 1/r$, so that $K_{\mathrm{rBCF}} \sim 1/r^2 \sim \varepsilon$, as $\varepsilon \to 0$.

The rBCF formalism also elucidates basic dependencies of the decay rate, K_{rBCF}, on time and temperature. The form of K_{1D} indicates that K_{rBCF} should be roughly constant, or even decrease with time if L_{sep} increases, consistent with experiment and

simulation in Sec. II. Previous studies proposed that $A \sim (t_0 - t)^p$, where t_0 is the time of island disappearance, disagreeing on whether $p = 2/3$ [9] or 1/2 [23]. In either case, since $p < 1$, it follows that $K \sim A^{-(1-p)/p}$ diverges as $A \to 0$. However, these fits were applied to both to the 1D decay regime, and a subsequent 2D late-stage regime which occurs for $R < R_{\min} \sim 1$ [11]. Thus, their analysis was skewed by the latter regime. This regime is described by $p = 2/3$ just as for terrace-diffusion limited coarsening in isotropic systems [11].

Finally, we consider the effective Arrhenius energy $E_{\rm OR} = -\frac{\rm d}{{\rm d}\beta}\ln K$ for 1D island decay at lower T versus conventional 2D decay at higher T. We assign a Arrhenius dependence, $L_{\rm sep} \sim e^{-\beta E_{\rm sep}}$, for the typical distance between $\langle 001 \rangle$ island ends [11], and write $E_{\rm form} = -\mu_{\rm int} > 0$ for the energy cost to form a 2D gas adatom by extraction of an adatom from a large 2D island. Then, since roughly speaking, one has that $K_{\rm 1D} \sim D^{\parallel} n_\infty / L_{\rm sep}$ versus $K_{\rm 2D} \sim (D^{\parallel} D^{\perp})^{1/2} n_\infty / \ln L_{\rm sep}$ for 2D decay [23,11], it follows that

$$E_{\rm OR,1D} = E_{\rm d}^{\parallel} + E_{\rm form} - E_{\rm sep} \text{ versus } E_{\rm OR,2D} = (E_{\rm d}^{\parallel} + E_{\rm d}^{\perp})/2 + E_{\rm form}. \quad (11)$$

The low value of $E_{\rm OR,1D}$ using $E_{\rm sep} \approx 0.2$ eV is consistent with experiment [11].

4. Multi-Density Field and Spatially Discrete Analytic Formalisms

More detailed analytic treatment of the 1D island decay processes requires incorporation into the modeling of edge diffusion kinetics which is missing in the refined-BCF formulation of Sec. III. In Sec. IV A below, we suggest a possible

formalism still within a continuum BCF-type framework, but which includes an additional diffusion field for edge adatoms. However, in any system with nanoscale island dimensions of $\mathcal{O}(10^1)$ lattice constants, one could argue that it is more appropriate to retain a spatially discrete model. Then, BCF-type diffusion equations are replaced by so-called lattice differential (diffusion) equations. In fact, such a discrete framework is extremely versatile being readily amenable to including details of edge diffusion kinetics, e.g., associated with the above edge adatom diffusion field, as well as other features of nanoscale geometry [13]. Thus, this approach is developed in Sec. IV B, and results are presented in Secs. IV C and IV D.

4A. Analytic continuum formalism

To account for the lack of equilibration of edge adatoms at $\langle\bar{1}10\rangle$ step edges and to capture the details of edge diffusion kinetics, we introduce a separate diffusion field, n_{edge}, to describe the density per site of edge adatoms at the $\langle\bar{1}10\rangle$ edges (in addition to the adatom density, n, on terraces). See Ref. [27,28,29] for somewhat related formalisms. The terrace adatom density, n, satisfies the BCF diffusion equation Eq. (4) together with a Dirichlet BC, $n = n_{001}$, at $\langle 001\rangle$ islands ends (as in Sec. III), and now another Dirichlet BC, $n = e^{\beta E_{\text{b}}^{\perp}} n_{\text{edge}}$, on $\langle\bar{1}10\rangle$ island edges. The latter condition reflects the feature that n_{edge} is enhanced relative to the nearby adatom density on terraces due to bonding to the step edge with strength determined by $E_{\text{b}}^{\perp} < 0$.

Let $J_y(x) = \pm a^{-1} D^{\perp} \frac{\partial}{\partial y} n$ denote the net flux of terrace adatoms per unit length attaching at position x along the $\langle \bar{1}10 \rangle$ edge of an island, where the $+(-)$ sign applies for the lower (upper) $\langle \bar{1}10 \rangle$ edge. Then, it follows that

$$\frac{\partial}{\partial t} n_{\text{edge}} = D_{\text{e}}^{\parallel} \frac{\partial^2}{\partial x^2} n_{\text{edge}} + J_y(x) \approx 0, \tag{12}$$

where $D_{\text{e}}^{\parallel} \equiv b^2 h_{\text{e}}^{\parallel}$ is the edge diffusion coefficient with $h_{\text{e}}^{\parallel} \equiv \nu e^{-\beta E_{\text{e}}^{\parallel}}$. To complete this formulation for n_{edge}, we must impose BCs at the corners of the island. To this end, we introduce an *effective rate*, $h_{\text{cr}} \equiv \nu e^{-\beta E_{\text{cr}}}$ (see **Fig. 1**) for corner rounding from $\langle \bar{1}10 \rangle$ to $\langle 001 \rangle$ edges. The rate for corner rounding in the reverse direction is determined by detailed-balance, a feature incorporated in the following treatment. Then, by matching edge diffusion flux and the net corner rounding flux, J_{cr}, from $\langle \bar{1}10 \rangle$ to $\langle 001 \rangle$ edges, this BC becomes

$$D_{\text{e}}^{\parallel} \frac{\partial}{\partial x} n_{\text{edge}} = \pm J_{\text{cr}} = \pm b h_{\text{cr}} \left(n_{\text{edge}} - e^{-\beta E_{\text{b}}^{\perp}} \right) n_{001}, \tag{13}$$

the $+(-)$ sign applies for left (right) island corners. The first (second) term on the right hand side corresponds to corner rounding from $\langle \bar{1}10 \rangle$ to $\langle 001 \rangle$ edges (from $\langle 001 \rangle$ to $\langle \bar{1}10 \rangle$ edges). The extra factor of $e^{-\beta E_{\text{b}}^{\perp}}$ in the negative contribution to J_{cr} ensures that for a single island, the equilibrated $\langle \bar{1}10 \rangle$ edge density satisfies $n_{\text{edge}} = e^{-\beta E_{\text{b}}^{\perp}} n_{001}$, i.e., n_{edge} is enhanced relative to n_{001} which also corresponds to the local adatom density on terraces consistent with the above Dirichlet BC for n at $\langle \bar{1}10 \rangle$ step edges.

For further analysis, it is instructive to note that detachment from the $\langle\bar{1}10\rangle$ edge occurs with rate $h_{\rm det} \equiv \nu e^{-\beta E_{\rm det}^{\perp}}$, where $E_{\rm det}^{\perp} = E_{\rm d}^{\perp} - E_{\rm b}^{\perp}$. Consequently, the net attachment flux can be decomposed as

$$J_y = J_{y,\rm attach} - J_{y,\rm detach}, \tag{14}$$

where $J_{y,\rm detach} = h_{\rm det} n_{\rm edge}$. It is also useful to define $L_{\rm cr}^{\parallel} \equiv 2bh_{\rm cr}/h_{\rm det}$ as a characteristic length for corner rounding in competition with detachment. Next, we note that if $h_{\rm edge}/h_{\rm det}$ and $h_{\rm edge}/h_{\rm cr}$ are high (realistic values are ~10^3 for Ag/Ag(110) at 200 K), it follows that $n_{\rm edge}$ is effectively uniform along the $\langle\bar{1}10\rangle$ edge. Then, integrating Eq. (12) along this edge and applying Eqs. (13) and (14) yields

$$L^{\parallel} n_{\rm edge} + L_{\rm cr}^{\parallel}\left(n_{\rm edge} - e^{-\beta E_{\rm b}^{\perp}} n_{001}\right) \approx L^{\parallel}\langle J_{y,\rm attach}\rangle / h_{\rm det}, \tag{15}$$

where $\langle J_{y,\rm attach}\rangle$ denotes the average of $J_{y,\rm attach}$ along the step edge.

A previous perspective on the kinetics of 1D island decay [9] assumed a significant $J_{\rm cr} > 0$ and implicitly that $L_{\rm cr}^{\parallel} \gg L^{\parallel}$. In this case, Eq. (15) indicates that $J_{\rm cr} \sim L^{\parallel}$ decreases with shrinking $L^{\parallel}$ suggesting enhanced rate of decay of the small island. In Sec. IV B, we will reassess this picture and analyze 1D island decay incorporating a detail description of edge diffusion kinetics utilizing the spatially discrete formalism.

4B. Discrete diffusion equations (lattice differential equations)

Formalisms based on spatially-discrete diffusion equations (DDE), i.e., lattice differential equations, have great flexibility to describe the details of edge diffusion

kinetics and to capture nanoscale behavior [13]. Furthermore, one could argue that continuum formulations are inappropriate or misapplied when the spatial grid size for accurate numerical solution is below that of the physical surface lattice constant. To develop and illustrate the DDE formalism, we first consider the benchmark geometry of two aligned islands in a simulation cell with periodic BCs as described in Sec. III C. This geometry and the labeling of a spatially discrete grid of adsorption sites (i, j) is shown in **Fig. 8.** The adatom density at site (i, j) is denoted as $n_{i,j}$.

The generic equation for the adatom densities, $n_{i,j}$, has the form

$$\frac{\mathrm{d}}{\mathrm{d}t} n_{i,j} = h^{<}_{i+1,j} n_{i+1,j} + h^{>}_{i-1,j} n_{i-1,j} + h^{\vee}_{i,j+1} n_{i,j+1} + h^{\wedge}_{i,j-1} n_{i,j-1} - (h^{<}_{i,j} + h^{>}_{i,j} + h^{\vee}_{i,j} + h^{\wedge}_{i,j}) n_{i,j}, \tag{16}$$

where $h^{<}_{i,j}$, $h^{>}_{i,j}$, $h^{\vee}_{i,j}$, and $h^{\wedge}_{i,j}$ denote the rates to hop left, right, down, up from site (i, j), respectively. For *sites in the middle of the terrace*, one has that $h^{<}_{i,j} = h^{>}_{i,j} = h^{\parallel} \equiv \nu e^{-\beta E_{\mathrm{d}}^{\parallel}}$ and $h^{\vee}_{i,j} = h^{\wedge}_{i,j} = h^{\perp} \equiv \nu e^{-\beta E_{\mathrm{d}}^{\perp}}$. For *sites near* $\langle \bar{1}10 \rangle$ *edges* (i.e., for sites adjacent to those at the $\langle \bar{1}10 \rangle$ edge), rates for hopping into those sites from edge sites are reduced by a factor of $e^{\beta E_{\mathrm{b}}^{\perp}}$ relative to $h^{\perp}$, so this feature modifies certain terms in Eq. (16). For *sites at* $\langle \bar{1}10 \rangle$ *edges*, a distinct edge diffusion rate is applied, i.e., $h^{\parallel}$ is replaced by $h_{\mathrm{e}}^{\parallel} \equiv \nu e^{-\beta E_{\mathrm{e}}^{\parallel}}$ [19]. Also, the rate to hop from such sites to near-edge terrace sites is reduced by a factor of $e^{\beta E_{\mathrm{b}}^{\perp}}$ relative to $h^{\perp}$. Examples of the equations for edge, near-edge, corner, and near-corner sites, as well as the generic equation for terrace sites, are given in **Fig. 8.** For boundaries across which there is no diffusion flux (such as $\langle \bar{1}10 \rangle$ island edges and the outer boundaries of the simulation cell), we simply set to zero the

rates for hops which would cross those boundaries. For sites at $\langle 001 \rangle$ island edges (in the light grey shaded region in **Fig. 8**), we impose a Dirichlet BC, $n_{i,j} = n_{001}$, where n_{001} is determined for the appropriate island width, and thus is higher for the left island than the right island [30].

Finally, for the *corner sites just above or below the* $\langle 001 \rangle$ *edges*, we introduce special equations and rates to capture corner-rounding diffusion kinetics. The rate to hop up or down from these corner sites to the $\langle 001 \rangle$ edge sites is taken as $h_{\rm cr} \equiv \nu e^{-\beta E_{\rm cr}}$, where we will set $E_{\rm cr} = 0.39$ eV (see **Fig. 1**) consistent with the model in Ref. [11]). The reverse rate is taken as $c_{\rm r} e^{-\beta E_{\rm b}^{\perp}} h_{\rm cr}$ with $c_{\rm r} = 1$, reflecting the feature that the equilibrium edge density is enhanced by a factor of $e^{-\beta E_{\rm b}^{\perp}}$ relative to the equilibrium terrace density. We include the factor $c_{\rm r}$, as it is instructive to compare behavior for $c_{\rm r} = 1$ with that for $c_{\rm r} = 0$ (artificially enforcing one-way corner rounding).

Deeper insight into the form of the solutions of Eq. (16) comes from a natural rescaling where we set $n^*_{i,j} = n_{i,j}$ for all terrace sites, and $n^*_{i,j} = e^{\beta E_{\rm b}^{\perp}} n_{i,j}$ for $\langle \bar{1}10 \rangle$ edge sites. Then, for all terrace sites including near $\langle \bar{1}10 \rangle$ edge sites (but not for $\langle \bar{1}10 \rangle$ edge sites), Eq. (16) adopts the generic form

$$\frac{\rm d}{{\rm d}t} n^*_{i,j} = h^{\parallel}(n^*_{i+1,j} - 2n^*_{i,j} + n^*_{i-1,j}) + h^{\perp}(n^*_{i,j+1} - 2n^*_{i,j} + n^*_{i,j-1}). \qquad (17)$$

For the edge of the simulation cell, terms corresponding to crossing the boundary are removed. For most $\langle \bar{1}10 \rangle$ edge sites, one has that

$$\frac{\rm d}{{\rm d}t} n^*_{i,j} = h^{\parallel}_{\rm e}(n^*_{i+1,j} - 2n^*_{i,j} + n^*_{i-1,j}) + e^{\beta E_{\rm b}^{\perp}} h^{\perp}(n^*_{i,j\pm1} - n^*_{i,j}), \qquad (18)$$

where the $+(-)$ applies for the upper (lower) $\langle\bar{1}10\rangle$ edge. For the edge sites just above the right $\langle 001\rangle$ island end, one has the special equation

$$\frac{\mathrm{d}}{\mathrm{d}t}n_{i,j}^{*} = h_{\mathrm{e}}^{\parallel}\left(n_{i-1,j}^{*} - n_{i,j}^{*}\right) + e^{\beta E_{\mathrm{b}}^{\perp}}h^{\parallel}\left(n_{i+1,j}^{*} - n_{i,j}^{*}\right)$$
$$+e^{\beta E_{\mathrm{b}}^{\perp}}h^{\perp}(n_{i,j+1}^{*} - n_{i,j}^{*}) + h_{\mathrm{cr}}^{\perp}(c_{\mathrm{r}}n_{i,j-1}^{*} - n_{i,j}^{*}). \qquad (19)$$

An analogous equation applies for edge sites just below the right $\langle 001\rangle$ island end, as well as just above and below the left $\langle 001\rangle$ end.

For the standard choice $c_{\mathrm{r}} = 1$ (satisfying detailed-balance), each term in the rescaled equations just involves the difference between two densities of adjacent lattice sites. Thus, for the case where both islands have the same width and the same BC: $n^{*} = n_{001}$, it is immediately clear that one recovers the correct equilibrium steady-state solution, $n_{i,j}^{*} = n_{001}$, for all sites. For different widths, one might introduce the quantity $\delta n_{i,j}^{*} = (n_{i,j}^{*} - n_{001}^{\mathrm{wide}})/(n_{001}^{\mathrm{narrow}} - n_{001}^{\mathrm{wide}})$, which satisfies the same equation as the $n_{i,j}^{*}$. Analogous to δn^{*} in Secs. III C and III D, the $\delta n_{i,j}^{*}$ has BCs of 1 and 0 on the $\langle 001\rangle$ ends of the narrow and wide islands, respectively. Instead, analogous to Sec. III E, we consider the variable $n_{i,j}^{\dagger} \equiv n_{i,j}^{*}/n_{\infty}$ also satisfying the same equation as $n_{i,j}^{*}$. From Eq. (3), the BC on the end of an island of width $L^{\perp} = \delta j a$ [where δj is the difference between the coordinates (in units of a) of upper and lower $\langle\bar{1}10\rangle$ edges of the island, see **Fig. 8**] is simply $n_{001}^{\dagger} = e^{\beta a|E_{\mathrm{b}}^{\perp}|/L^{\perp}} \approx e^{2.748/\delta j}$ for $E_{\mathrm{b}}^{\perp} = -0.045$ eV matching Ag/Ag(110) at 190 K. Finally, note that for one-way corner rounding ($c_{\mathrm{r}} = 0$), one never obtains a simple equilibrium steady-state solution.

4C. Lattice differential equations results for aligned islands

We first assess 1D island decay behavior for the configuration of *aligned islands* shown in **Fig. 8** with a realistic choice of parameters corresponding to the msLG model for Ag/Ag(110) at 190 K. In **Fig. 9(a)**, we show sample simulation results for $n_{i,j}^{\dagger} \equiv n_{i,j}^{*}/n_{\infty}$ with $c_{\mathrm{r}} = 1$ and choosing geometric parameters: $L_{\mathrm{narrow}}^{\perp} \approx 2.5$ nm and $L_{\mathrm{narrow}}^{\parallel} \approx 6.9$ nm for the small narrow island ($\delta j = 6$ with the BC $n_{001,\mathrm{narrow}}^{\dagger} = 1.581$); $L_{\mathrm{wide}}^{\perp} \approx 4.1$ nm and $L_{\mathrm{wide}}^{\parallel} \approx 11.0$ nm for the wider island ($\delta j = 10$ with the BC $n_{001,\mathrm{wide}}^{\dagger} = 1.316$); $L_{\mathrm{sep}} \approx 12.1$ nm. It is straightforward to determine the diffusion flux between islands summing differences in densities, $\delta n_{i,j}^{\dagger} = n_{i+1,j}^{\dagger} - n_{i,j}^{\dagger}$, for adjacent columns of sites, $K_{\mathrm{DDE}} = 2h^{\parallel} n_{\infty} \left(\sum_j \delta n_{i,j}^{\dagger} = 0.0504 \right)$. One can also evaluate the net corner rounding flux from the $\langle \bar{1}10 \rangle$ to the $\langle 001 \rangle$ edge of the narrow island given the adatom density $n_{\mathrm{corner,narrow}}^{\dagger} = 1.441$ at the sites just above the $\langle 001 \rangle$ ends relative to $n_{001,\mathrm{narrow}}^{\dagger} = 1.581$. Using $J_{\mathrm{cr}} = 2h_{\mathrm{cr}} n_{\infty} e^{-\beta E_{\mathrm{b}}^{\perp}} \left(n_{\mathrm{corner,narrow}}^{\dagger} - n_{001,\mathrm{narrow}}^{\dagger} \right)$, one finds that $J_{\mathrm{cr}} < 0$, i.e., the net corner-rounding flux is from $\langle 001 \rangle$ to $\langle \bar{1}10 \rangle$ edges, and that $|J_{\mathrm{cr}}|/K_{\mathrm{DDE}} = 0.052$ is small. As an aside, J_{cr} is positive for the wider island.

These results present a *different picture* from that suggested previously [9] of effective one-way corner rounding ($c_{\mathrm{r}} = 0$) with a significant positive corner rounding flux, $J_{\mathrm{cr}} > 0$ for the narrow decaying island. Such a flux could inhibit the overall 1D decay of the island by feeding detached adatoms back to the $\langle 001 \rangle$ end. We can mimic this picture by artificially setting $c_{\mathrm{r}} = 0$ in our equations which does produce a significantly lower island decay rate to $K_{\mathrm{DDE}} = 2h^{\parallel} n_{\infty} \left(\sum_j \delta n_{i,j}^{\dagger} = 0.0248 \right)$ and large

one-way corner rounding flux $J_{\rm cr}/K_{\rm DDE} = 1.55$ determined from $n^{\dagger}_{\rm corner} = 1.018$. However, examination of the boundary value problem for our rescaled equations for the physical choice of $c_{\rm r} = 1$ (consistent with detailed-balance) makes it clear that the rescaled densities at all sites on the surface, including those at corners, $n^{\dagger}_{\rm corner,narrow}$, cannot exceed the maximum value of $n^{\dagger}_{001,\rm narrow}$ for the narrower island. Thus, $J_{\rm cr}$ must always be negative [31].

Another key comparison follows from adjusting the model parameters to mimic the rBCF treatment which does not incorporate binding to $\langle\bar{1}10\rangle$ edges and does not explicitly treat corner rounding. To this end, we simply set $E_{\rm b}^{\perp} = 0$, $h^{\parallel} = h_{\rm e}^{\parallel}$, and also set $h_{\rm cr} = 0$ to capture the feature of no direct corner rounding [32]. See **Fig. 9(b)**. Analyzing the associated discrete diffusion equations for the same geometry as above yields $\sum_j \delta n^{\dagger}_{i,j} = 0.0466$. Consequently, $K_{\rm DDE}$ is somewhat reduced by a factor of 0.92 relative to our above model with realistic treatment of edge diffusion for Ag/Ag(110) at 190 K. This reduction is consistent with the observation in Sec. III that the rBCF prediction for the rate of decay of the island in **Fig. 2(a)** is slightly below the value obtained from KMC simulation.

4D. Lattice differential equations results for different geometries

The discrete formulation can also be used to compare behavior for aligned islands and misaligned islands (not shown). To analyze the case of *marginally misaligned islands*, we start with the island geometry as in **Fig. 8** but shift the two

islands relative to each other in the y-direction from perfect alignment to marginal misalignment and slightly increase the y-dimension of the simulation cell (so now $j_{\mathrm{R1}} = 4,\ j_{\mathrm{R2}} = 15,\ j_{\mathrm{L1}} = 14,\ j_{\mathrm{L2}} = 21,$ and $j_{\mathrm{M}} = 24$). Retaining parameters for Ag/Ag(110) at 190 K with $c_{\mathrm{r}} = 1$, we find that $\sum_j \delta n_{i,j}^{\dagger} = 0.0142$ for marginally aligned islands, well below $\sum_j \delta n_{i,j}^{\dagger} = 0.0504$ for aligned islands. However, K_{DDE} is still significant, consistent with the results of Sec. III D. For *completely misaligned islands* (but with a small misalignment gap) where now $j_{\mathrm{R1}} = 4$, $j_{\mathrm{R2}} = 15$, $j_{\mathrm{L1}} = 16$, $j_{\mathrm{L2}} = 23$, and $j_{\mathrm{M}} = 26$, we find the expected further reduction in $\sum_j \delta n_{i,j}^{\dagger} = 0.0087$.

Finally, we further highlight the versatility of the discrete diffusion equation formalism to capture features of nanoscale island geometry by refining the aligned island geometry shown in **Fig. 8** to *add kinks on the* $\langle \bar{1}10 \rangle$ *edges of the wider island*. See **Fig. 10**. In our corresponding analysis, we retain all the geometric parameters used in Sec. IV C including $i_{\mathrm{R}} = 54$, $j_{\mathrm{R1}} = 4$, and $j_{\mathrm{R2}} = 15$, but add the kinks at $i_{\mathrm{k}} = 59$. These kinks will act as additional traps for adatoms diffusing from the narrower island. This feature is reflected in the assignment $n_{\mathrm{kink}}^{\dagger} \equiv n_{\mathrm{kink}}/n_{\infty} = 1$ which is below the value $n_{001}^{\dagger} = e^{\beta |E_{\mathrm{b}}^{\perp}|/\delta j}$ at the $\langle 001 \rangle$ end of either island. For this geometry and retaining parameters for Ag/Ag(110) at 190K with $c_{\mathrm{r}} = 1$, we find that $\sum_j \delta n_{i,j}^{\dagger} = 0.0554$ has *increased* somewhat above the value of $\sum_j \delta n_{i,j}^{\dagger} = 0.0504$ for the corresponding geometry without kink sites. This enhancement is also consistent with the observation in Sec. III that the rBCF prediction for the rate of decay of the island in **Fig. 2(a)** is slightly below the value

obtained from KMC simulation of our msLG model (noting that kinks can form spontaneously in the KMC simulations).

5. Conclusions

Our rBCF modeling in Sec. III provides an effective and instructive modeling tool which captures the basic features of 1D decay of islands in strongly anisotropic fcc(110) homoepitaxial systems. This includes description of the unusual dependence of island decay rate on both island geometry and temperature. In particular, rBCF modeling obtains good agreement with (being only slightly below) precise results for the island decay rate obtained from extensive KMC simulations modeling experimentally observed 1D decay of Ag islands on Ag(110) homoepitaxial at 190 K. However, the rBCF theory assumes equilibration of edge adatoms and does not incorporate edge diffusion kinetics, the details of which could have at least some influence on the decay rate. A modified treatment within the framework of discrete differential equations can account for these features. The result of this approach is to produce a slight enhancement of the island decay rates relative to the rBCF treatment. The discrete diffusion equation formalism also has the flexibility to allow incorporation of kinks on the $\langle \bar{1}10 \rangle$ island edges. We note that such kinks are absent in the rBCF treatment which includes perfect rectangular islands, but formed spontaneously in KMC simulations of a msLG model. Incorporating kinks also slightly enhances the island decay rate. Both effects improve the already good agreement of the predictions of analytic theory with KMC simulation.

Acknowledgements

This work was supported by NSF Grant CHE-1111500. It was performed at Ames Laboratory which is operated for the USDOE by Iowa State University under Contract No. DE-AC02-07CH11358. We thank Tony Layson for providing some of the STM data discussed in this work.

*Current address: Electrochemistry Branch, Power and Energy Division, Sensor and Electron Devices Directorate, U.S. Army Research Laboratory, Adelphi, Maryland 20783

References

[1] K. Morgenstern, Phys. Stat. Sol. B 242, 773 (2005).

[2] P. A. Thiel, M. Shen, D.-J. Liu, and J. W. Evans, J. Phys. Chem. C 113, 5047 (2009).

[3] W. Ostwald, Lehrbuch der Allgemeinen Chemie (Verlag von W. Engelmann, Leipzig, Germany, 1887), Vol. 2, Part 1.

[4] M. Giesen, Prog. Surf. Sci. 68, 1 (2001).

[5] L. Ratke and P. W. Voorhees, Growth and Coarsening: Ripening in Materials Processing (Springer, Berlin, 2001).

[6] W. K. Burton, N. Cabrera, and F. C. Frank, Philos. Trans. Roy. Soc. London Series A 243, 299 (1951).

[7] H.-C. Jeong and E. D. Williams, Surf. Sci. Rep. 34, 171 (1999).

[8] L. D. Landau and E. M. Lifshitz, Course on Theoretical Physics: Statistical Physics (Permagon, New York, 1959), Vol. 5, p. 482.

[9] K. Morgenstern, E. Lægsgaard, I. Stensgaard, and F. Besenbacher, Phys. Rev. Lett. 83, 1613 (1999).

[10] K. Morgenstern, E. Lægsgaard, I. Stensgaard, F. Besenbacher, M. Böhringer, W.-D. Schneider, R. Berndt, F. Mauri, A. De Vita, and R. Car, Appl. Phys. A 69, 559 (1999).

[11] Y. Han, S. M. Russell, A. R. Layson, H. Walen, C. D. Yuen, P. A. Thiel, and J. W. Evans, Phys. Rev. B 87, 155420 (2013).

[12] Eventually, when the island aspect ratio becomes small enough, there is a transition to 2D decay before island disappearance [11].

[13] D. M. Ackerman and J. W. Evans, Multiscale Model. Simul. 9, 59 (2011).

[14] T. Duguet, Y. Han, C. Yuen, D. Jing, B. Ünal, J. W. Evans, and P. A. Thiel, Proc. Nat. Acad. Sci. 108, 989 (2011).

[15] Y. Han, B. Ünal, D. Jing, P. A. Thiel, and J. W. Evans, J. Chem. Phys. 135, 084706 (2011).

[16] Y. Han, D. Jing, B. Ünal, P. A. Thiel, and J. W. Evans, Phys. Rev. B 84, 113414 (2011).

[17] R. Ferrando, F. Hontinfinde, and A. C. Levi, Phys. Rev. B 56, R4406 (1997).

[18] C. Mottet, R. Ferrando, F. Hontininde, and A. C. Levi, Surf. Sci. 417, 220 (1998).

[19] The edge diffusion barrier on $\langle\bar{1}10\rangle$ edges is $E_{\mathrm{e}}^{\parallel} = E_{\mathrm{d}}^{\parallel} - E_{\mathrm{b}}^{\perp} + 2E'^{\perp}_{\mathrm{b}} = E_{\mathrm{d}}^{\parallel} + \left|E_{\mathrm{b}}^{\perp}\right| - 2\left|E'^{\perp}_{\mathrm{b}}\right|$ which can be comparable to $E_{\mathrm{d}}^{\parallel}$ in contrast to the higher IVA value.

[20] C. D. Giorgi, P. Aihemaiti, F. B. de Mongeot, C. Boragno, R. Ferrando, and U. Valbusa, Surf. Sci. 487, 49 (2001).

[21] Y. Han, J. Y. Zhu, F. Liu, S.-C. Li, J.-F. Jia, Y.-F. Zhang, and Q.-K. Xue, Phys. Rev. Lett. 93, 106102 (2004).

[22] M. Li, C. Z. Wang, J. W. Evans, M. Hupalo, M. C. Tringides, and K. M. Ho, Phys. Rev. B 79, 113404 (2009).

[23] Y. Yao, Ph. Ebert, M. Li, Z. Zhang, and E. G. Wang, Phys. Rev. B 66, 041407 (2002). Note the typographic error in the expressions for equilibrium adatom densities at island edges.

[24] In this traditional "macroscopic setting", the characteristic length describing the surface morphology is assumed to far exceed any microscopic length scales.

[25] J. W. Evans, P. A. Thiel, and M. C. Bartelt, Surf. Sci. Rep. 61, 1 (2006).

[26] COMSOL Multiphysics® (formerly FEMLAB®) is a finite element analysis, solver, and simulation software developed by Comsol Inc. (www.comsol.com).

[27] R. E. Caflisch, E. Weinan, M. F. Gyure, B. Merriman, and C. Ratsch, Phys. Rev. E 59, 6879 (1999).

[28] R. E. Caflisch and D. Margetis, Multiscale Model. Simul. 7, 242 (2008).

[29] O. Pierre-Louis and M. I. Haftel, Phys. Rev. Lett. 87, 048701 (2001).

[30] An alternative formulation of BC for $\langle 001 \rangle$ ends of islands follows in spirit Ref. [13]. Here, one sets $n_{001} = 1$ at the island ends, but then the rate for detachment from these $\langle 001 \rangle$ ends in the x-direction is $e^{-\beta E_{\mathrm{form}}} h^{\|}$, and there are related modifications for corner rounding. We make the choice in the text as this is more analogous to the refined BCF treatment.

[31] In equilibrium, there is a balance in the corner-rounding flux in both directions. Imbalance is created in non-equilibrium situations such as coarsening or growth during deposition. Our analysis shows that coarsening cannot create a net flux from $\langle\bar{1}10\rangle$ to $\langle 001\rangle$ edges in the narrowest islands. Such a flux could be created by deposition.

[32] Similar behavior ($\sum_j \delta n^{\dagger}_{i,j} = 0.0472$) is obtained in a rBCF model with $E^{\perp}_{\mathrm{b}} = 0$ and $h_{\mathrm{cr}} = h^{\perp}$ (and retaining $c_{\mathrm{r}} = 1$).

Figures

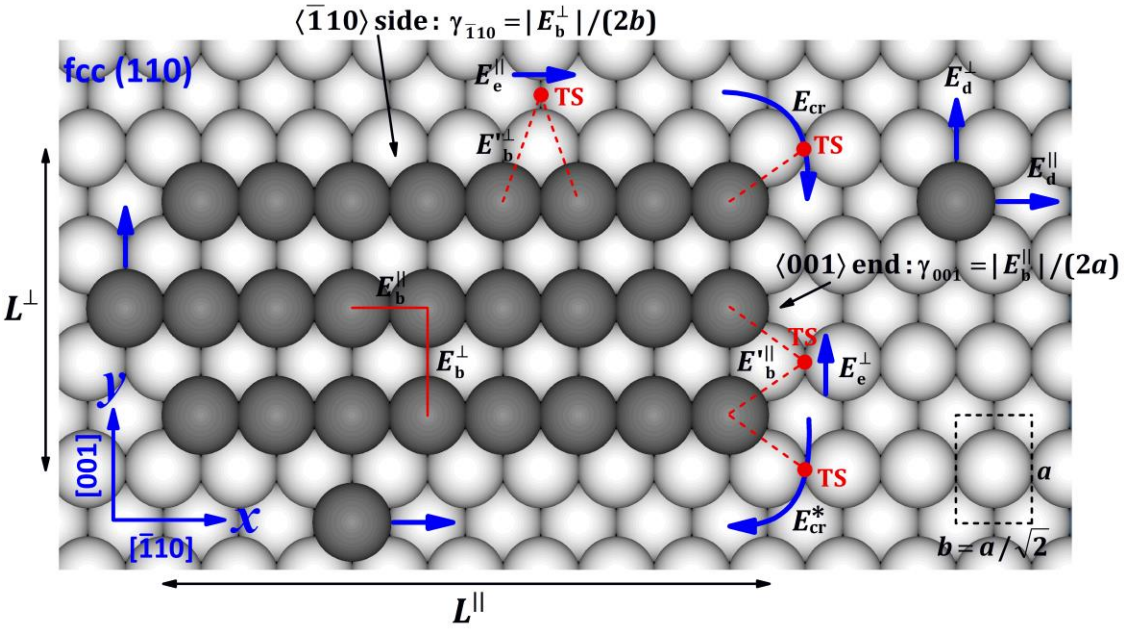

Fig. 1. (Color online) Schematic of a 2D rectangular homoepitaxial island on an fcc(110) surface. Also indicated are: anisotropic terrace diffusion barriers ($E^{\parallel}_{\mathrm{d}}$ and $E^{\perp}_{\mathrm{d}}$); conventional pairwise interactions ($E^{\parallel}_{\mathrm{b}}$ and $E^{\perp}_{\mathrm{b}}$) and associated step energies ($\gamma_{\bar{1}10}$ and γ_{001}); unconventional interactions ($E'^{\parallel}_{\mathrm{b}}$ and $E'^{\perp}_{\mathrm{b}}$) for an adatom at a transition state (TS) for edge diffusion; edge diffusion barriers ($E^{\parallel}_{\mathrm{e}}$ and $E^{\perp}_{\mathrm{e}}$); corner rounding barriers (E_{cr} and E^{*}_{cr}); examples of hopping adatoms on terrace and along edges. We also show the surface unit cell as well as notations for island dimensions and in-surface directions.

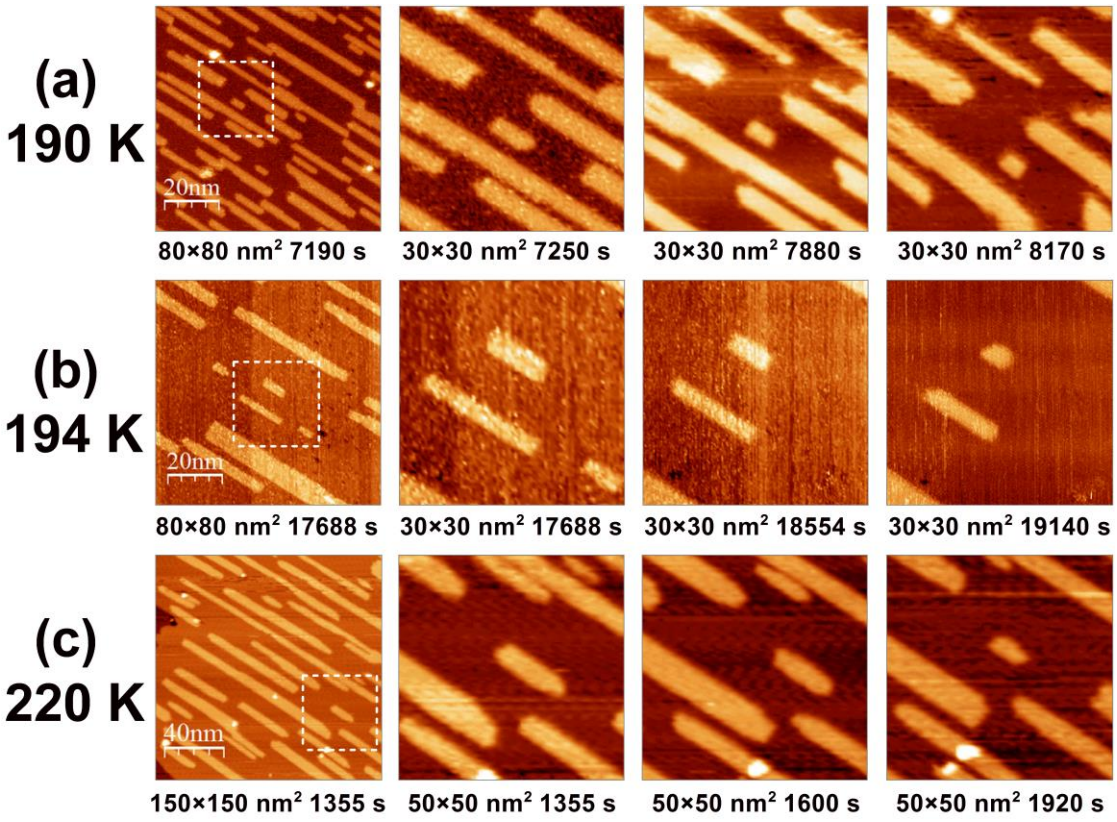

Fig. 2. (Color online) STM images for 1D decay of rectangular Ag islands on Ag(110) at: (a) 190 K with island decay rate $K_{\text{expt}} \approx 0.007$ nm^2/s for the central small island; (b) 194 K with $K_{\text{expt}} \approx 0.011$ - 0.013 nm^2/s for both islands after exposure of 1.0 L oxygen (which does not affect behavior [11]); (c) 220 K with $K_{\text{expt}} \approx 0.058$ nm^2/s for the central island. The left column shows a larger region, and the other columns magnify the sub-region indicated of 30×30 nm^2 for (a) and (b), and 50×50 nm^2 for (c). Also shown are times since Ag deposition.

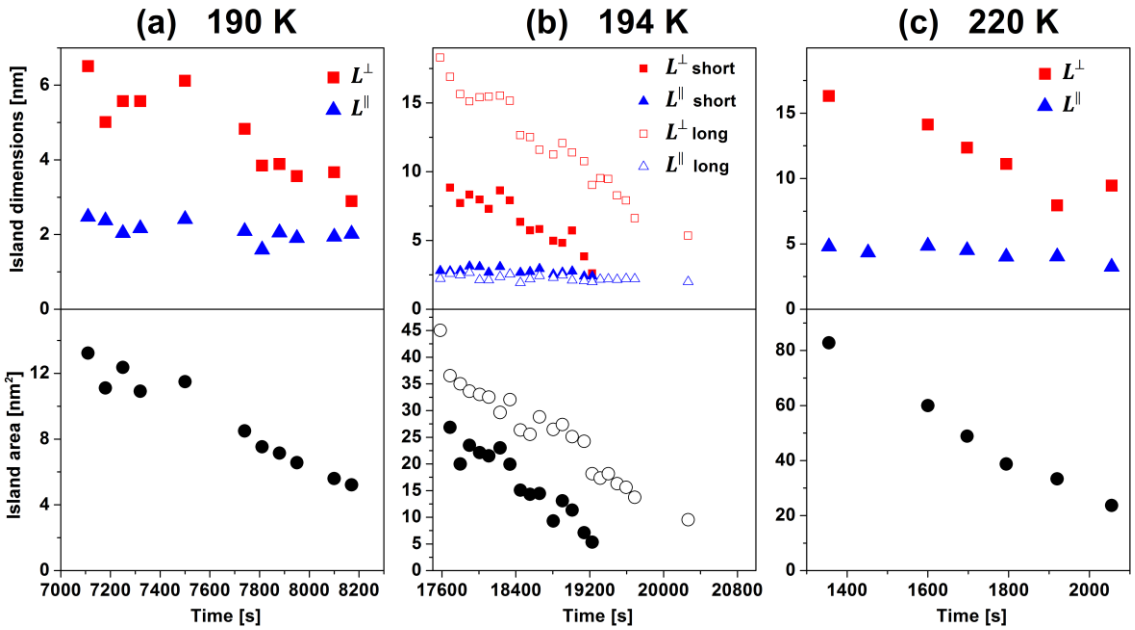

Fig. 3. (Color online) Island decay at (a) 190 K (left column); (b) 194 K (middle column); (c) 220 K (right column), for the islands shown in **Fig. 2.** Top row: island linear dimensions ($L^{\parallel}$ and $L^{\perp}$) versus time since Ag deposition. Bottom row: island area versus time.

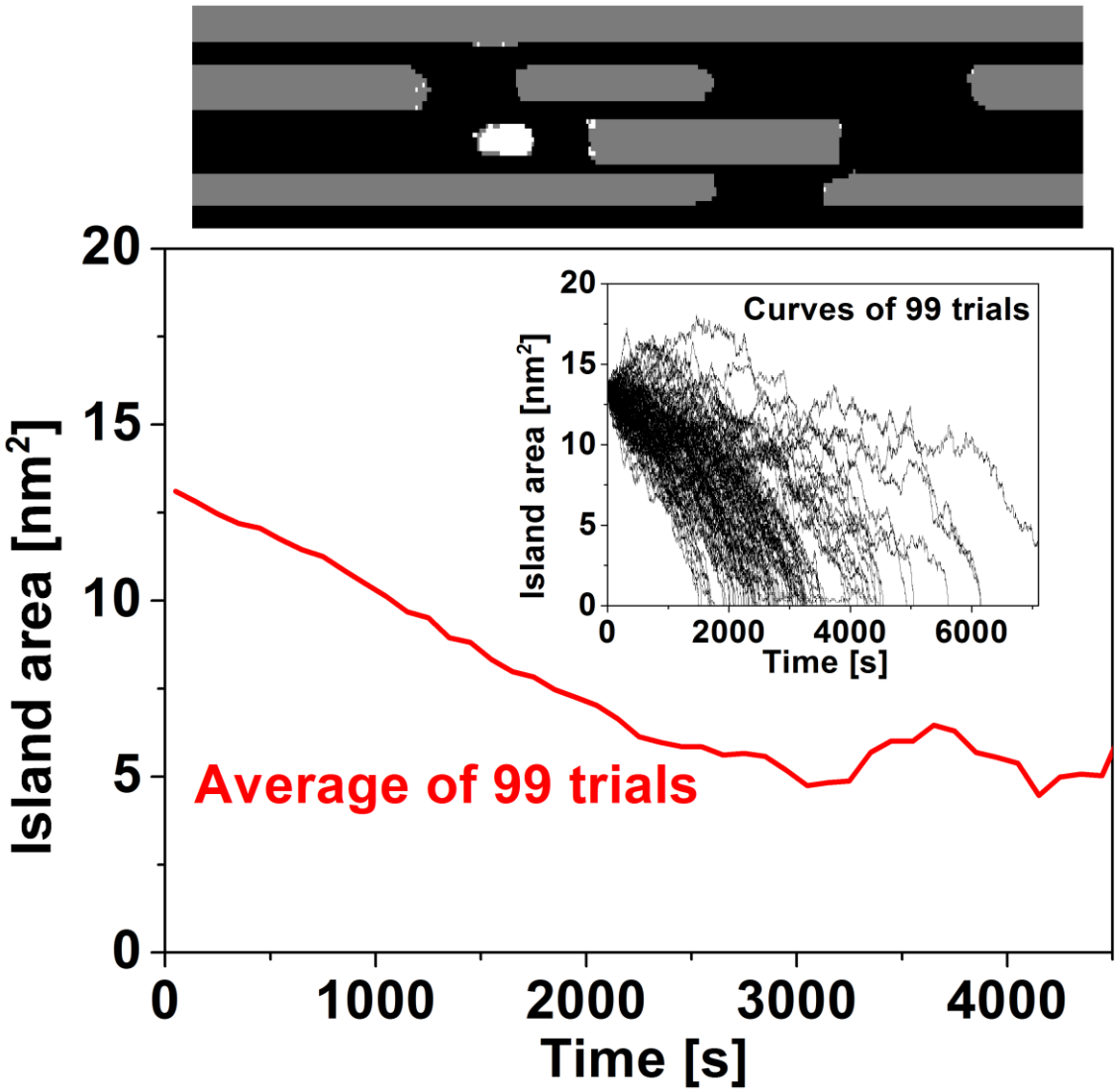

Fig. 4. (Color online) Results from KMC simulation of our atomistic msLG model [11] for decay at 190 K of the Ag island on Ag(110) shown in **Fig. 2(a).** The top frame shows a snapshot of the simulated island configuration early in the decay process. Atoms initially in the decaying island of interest are colored white. The bottom frame shows the area versus time averaged over 99 simulation trials. The areas for individual trials, illustrating very large fluctuations in the decay process, are shown in the inset. The noise in the average area for time $t > 2000$ s reflects the limited number of trials with a surviving island.

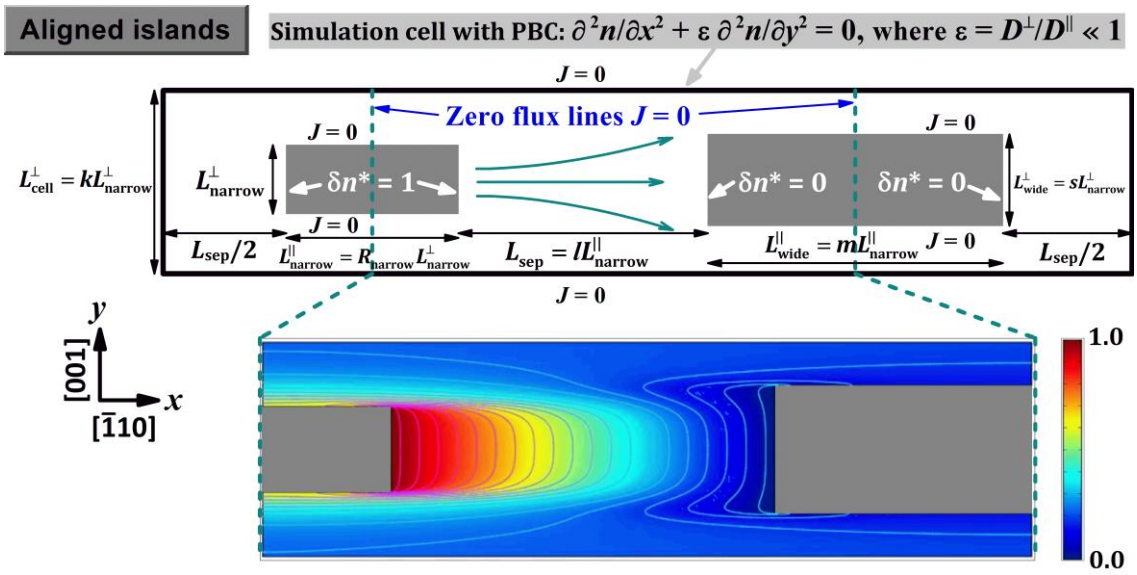

Fig. 5. (Color online) Benchmark configuration with a pair of islands aligned end-to-end shown (top row), and rescaled adatom density $\delta n^* \equiv (n - n_{001}^{\text{wide}})/(n_{001}^{\text{narrow}} - n_{001}^{\text{wide}})$ in the refined-BCF problem for the central portion of the benchmark configuration (FEMLAB results is shown in bottom row). Rescaled Dirichlet BCs at island ends are $\delta n^*_{001} = 1$ and 0. Geometric parameters for the above island configuration are defined as $R_{\text{narrow}} \equiv \frac{L^{\parallel}_{\text{narrow}}}{L^{\perp}_{\text{narrow}}}$, $k \equiv \frac{L^{\perp}_{\text{cell}}}{L^{\perp}_{\text{narrow}}}$, $l \equiv \frac{L_{\text{sep}}}{L^{\parallel}_{\text{narrow}}}$, $m \equiv \frac{L^{\parallel}_{\text{wide}}}{L^{\parallel}_{\text{narrow}}}$, and $s \equiv \frac{L^{\perp}_{\text{wide}}}{L^{\perp}_{\text{narrow}}}$. In the adatom density field analysis of bottom row, we choose $\varepsilon = 2e^{-\beta(E_{\text{d}}^{\perp} - E_{\text{d}}^{\parallel})} = 0.00445$ at $T = 190$ K for Ag/Ag(110), $R_{\text{narrow}} = 3$, $k = 5/2$, $l = 3/2$, $m = 5/2$, and $s = 3/2$.

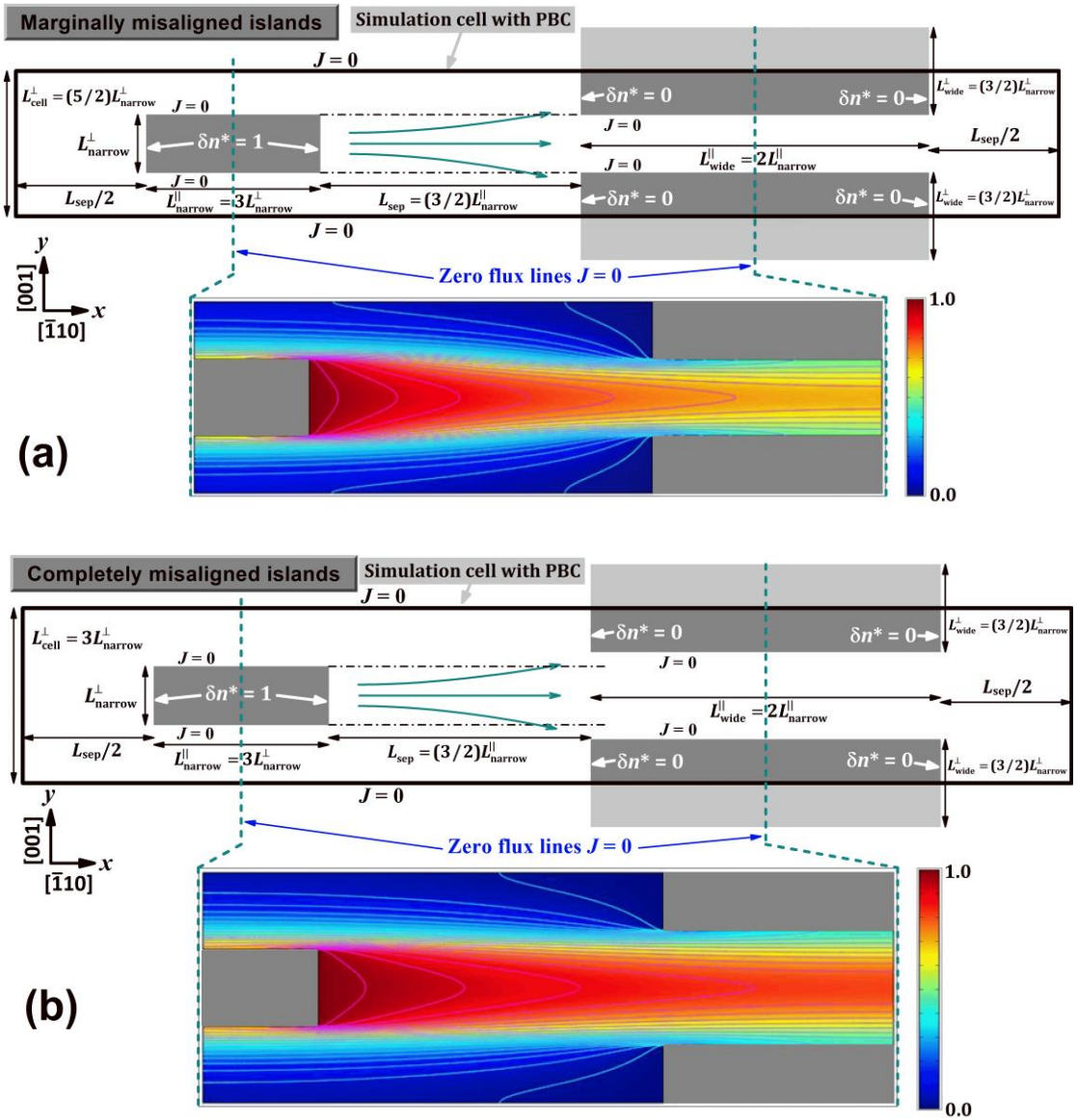

Fig. 6. (Color online) Benchmark configurations for (a) marginally misaligned islands with $k = 5/2$, and (b) completely misaligned islands with $k = 3$. FEMLAB results of rescaled adatom density field from $\delta n^* \equiv (n - n_{001}^{\text{wide}})/(n_{001}^{\text{narrow}} - n_{001}^{\text{wide}})$ in the rBCF problem are shown in bottom rows of (a) and (b). We use rescaled Dirichlet BCs $\delta n_{001}^* = 1$ and 0 at island ends, and $\varepsilon = 0.00445$ for Ag/Ag(110) at 190 K.

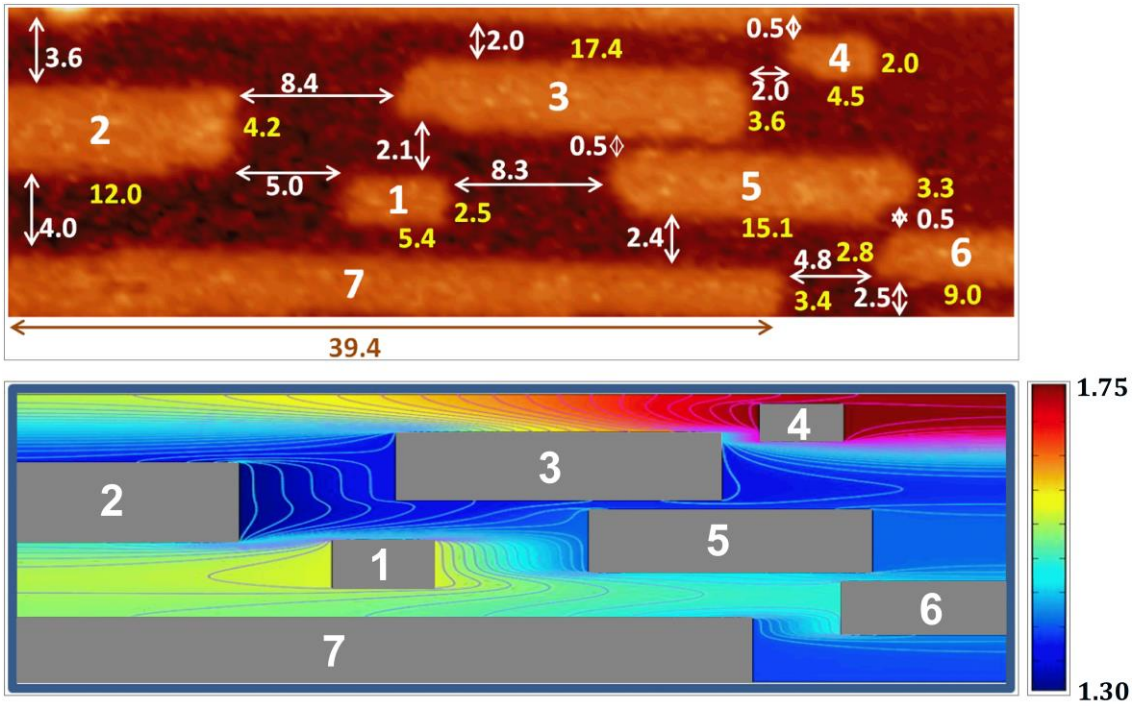

Fig. 7. (Color online) Top: Magnified STM image (50.0×15.5 nm^2) for the local environment of the small narrow island decaying shown in **Fig. 2(a).** Island dimensions are shown in yellow and separations in white (in nm). Bottom: FEMLAB results for the rescaled adatom density field, $n^{\dagger} \equiv n/n_{\infty}$, in the rBCF treatment for the island configuration (top). The simulation cell has zero-flux boundary conditions at the outer edges.

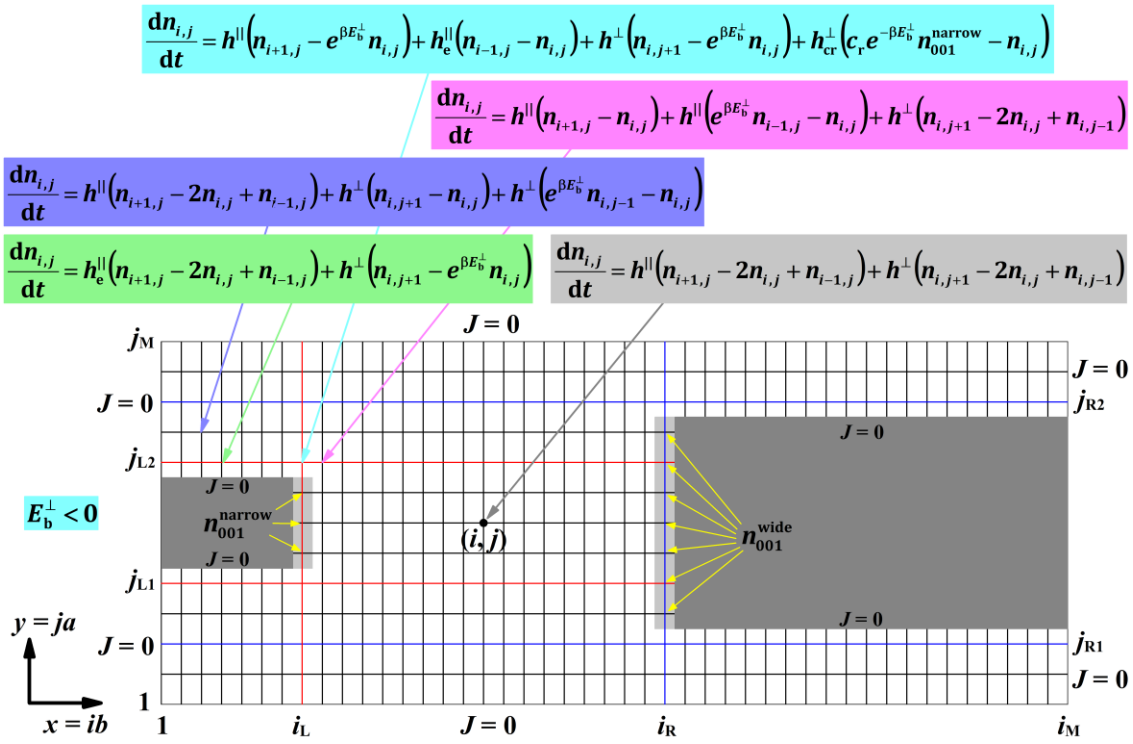

Fig. 8. (Color online) Discrete diffusion equations for the benchmark geometry with a pair of aligned islands. The region shown corresponds to the central portion of the top row, and all of bottom row in **Fig. 5** (so only half the length of each island is shown). Examples of Eq. (16) are given for edge, near-edge, corner, and near-corner sites, as well as the generic equation for terrace sites. Arrows indicate the sites to which the equations correspond. The positions of the island edges are given in terms of the coordinate system shown in the lower left.

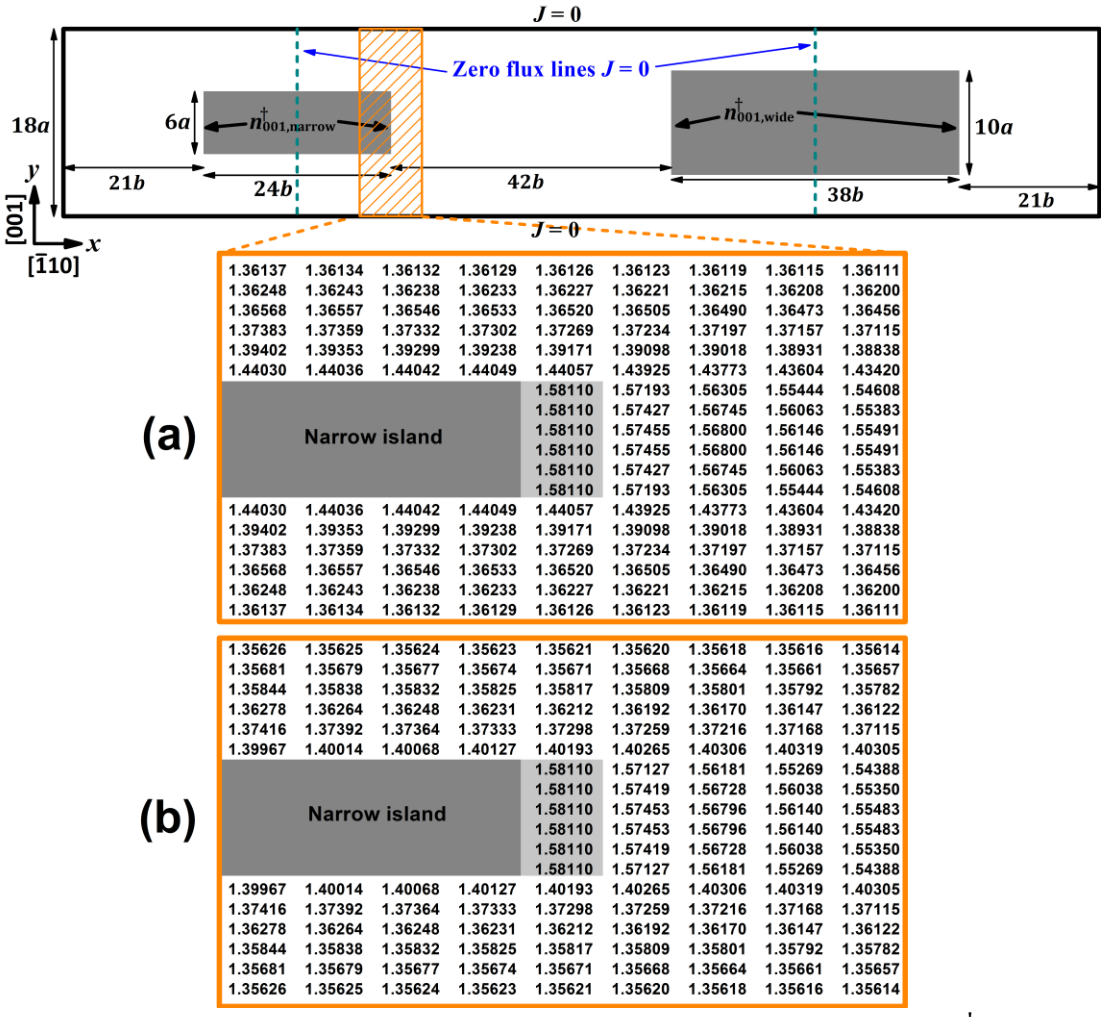

1.36137	1.36134	1.36132	1.36129	1.36126	1.36123	1.36119	1.36115	1.36111
1.36248	1.36243	1.36238	1.36233	1.36227	1.36221	1.36215	1.36208	1.36200
1.36568	1.36557	1.36546	1.36533	1.36520	1.36505	1.36490	1.36473	1.36456
1.37383	1.37359	1.37332	1.37302	1.37269	1.37234	1.37197	1.37157	1.37115
1.39402	1.39353	1.39299	1.39238	1.39171	1.39098	1.39018	1.38931	1.38838
1.44030	1.44036	1.44042	1.44049	1.44057	1.43925	1.43773	1.43604	1.43420
Narrow island				1.58110	1.57193	1.56305	1.55444	1.54608
				1.58110	1.57427	1.56745	1.56063	1.55383
				1.58110	1.57455	1.56800	1.56146	1.55491
				1.58110	1.57455	1.56800	1.56146	1.55491
				1.58110	1.57427	1.56745	1.56063	1.55383
				1.58110	1.57193	1.56305	1.55444	1.54608
1.44030	1.44036	1.44042	1.44049	1.44057	1.43925	1.43773	1.43604	1.43420
1.39402	1.39353	1.39299	1.39238	1.39171	1.39098	1.39018	1.38931	1.38838
1.37383	1.37359	1.37332	1.37302	1.37269	1.37234	1.37197	1.37157	1.37115
1.36568	1.36557	1.36546	1.36533	1.36520	1.36505	1.36490	1.36473	1.36456
1.36248	1.36243	1.36238	1.36233	1.36227	1.36221	1.36215	1.36208	1.36200
1.36137	1.36134	1.36132	1.36129	1.36126	1.36123	1.36119	1.36115	1.36111

(a)

1.35626	1.35625	1.35624	1.35623	1.35621	1.35620	1.35618	1.35616	1.35614
1.35681	1.35679	1.35677	1.35674	1.35671	1.35668	1.35664	1.35661	1.35657
1.35844	1.35838	1.35832	1.35825	1.35817	1.35809	1.35801	1.35792	1.35782
1.36278	1.36264	1.36248	1.36231	1.36212	1.36192	1.36170	1.36147	1.36122
1.37416	1.37392	1.37364	1.37333	1.37298	1.37259	1.37216	1.37168	1.37115
1.39967	1.40014	1.40068	1.40127	1.40193	1.40265	1.40306	1.40319	1.40305
Narrow island				1.58110	1.57127	1.56181	1.55269	1.54388
				1.58110	1.57419	1.56728	1.56038	1.55350
				1.58110	1.57453	1.56796	1.56140	1.55483
				1.58110	1.57453	1.56796	1.56140	1.55483
				1.58110	1.57419	1.56728	1.56038	1.55350
				1.58110	1.57127	1.56181	1.55269	1.54388
1.39967	1.40014	1.40068	1.40127	1.40193	1.40265	1.40306	1.40319	1.40305
1.37416	1.37392	1.37364	1.37333	1.37298	1.37259	1.37216	1.37168	1.37115
1.36278	1.36264	1.36248	1.36231	1.36212	1.36192	1.36170	1.36147	1.36122
1.35844	1.35838	1.35832	1.35825	1.35817	1.35809	1.35801	1.35792	1.35782
1.35681	1.35679	1.35677	1.35674	1.35671	1.35668	1.35664	1.35661	1.35657
1.35626	1.35625	1.35624	1.35623	1.35621	1.35620	1.35618	1.35616	1.35614

(b)

Fig. 9. (Color online) Simulation results for rescaled adatom densities, $n^{\dagger}_{i,j} \equiv n^{*}_{i,j}/n_{\infty}$, near the right end of the narrower island for a simple geometry with two aligned islands. The top frame shows the island geometry and the sub-region for which rescaled densities are shown in (a) and (b). We choose $h^{\perp}/h^{\parallel} = e^{-0.10\beta}$, $h^{\parallel}_{\mathrm{e}}/h^{\parallel} = 1$, and set $T = 190$ K. The system size parameters: $i_{\mathrm{M}} = 73$ and $j_{\mathrm{M}} = 18$. Narrow island parameters: $j_{\mathrm{L1}} = 6$ and $j_{\mathrm{L2}} = 13$ so that $L^{\perp}_{\mathrm{narrow}} = (j_{\mathrm{L2}} - j_{\mathrm{L1}} - 1)a = 6a \approx 2.5$ nm; $i_{\mathrm{L}} = 13$ so that $L^{\parallel}_{\mathrm{narrow}} = 2(i_{\mathrm{L}} - 1)b = 24b \approx 6.9$ nm. Wider island parameters: $j_{\mathrm{R1}} = 4$ and $j_{\mathrm{R2}} = 15$ so that $L^{\perp}_{\mathrm{wide}} = (j_{\mathrm{R2}} - j_{\mathrm{R1}} - 1)a = 10a \approx 4.1$ nm; $i_{\mathrm{R}} = 54$ so that $L^{\parallel}_{\mathrm{wide}} = 2(i_{\mathrm{M}} - i_{\mathrm{R}})b = 38b \approx 11.0$ nm. Island separation: $L_{\mathrm{sep}} = (i_{\mathrm{R}} - i_{\mathrm{L}} + 1)b = 42b \approx 12.1$ nm. (a) Realistic model for Ag/Ag(110) with $c_{\mathrm{r}} = 1$, $h_{\mathrm{cr}}/h^{\parallel} = e^{-0.11\beta}$, and $E^{\perp}_{\mathrm{b}} = -0.045$ eV. (b) Simplified model mimicking rBCF theory with $h_{\mathrm{cr}}/h^{\parallel} = 0$, and $E^{\perp}_{\mathrm{b}} = 0$. Note the reduced edge adatom density in (b) relative to (a) is associated with a lack of binding to the $\langle\bar{1}10\rangle$ edge.

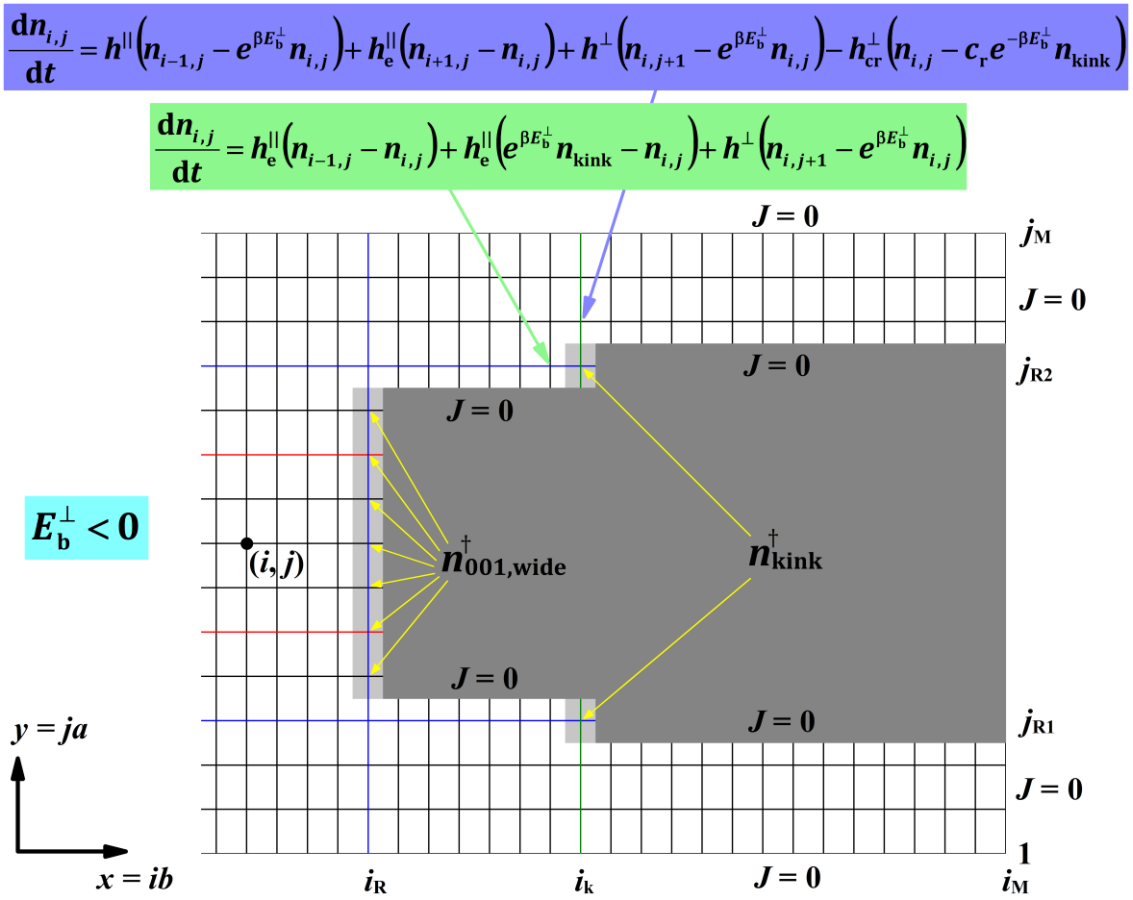

Fig. 10. (Color online) Portion of modified discrete diffusion equations geometry showing the addition of kinks on the $\langle \bar{1}10 \rangle$ edges of the wider island. Examples are given of additional equations needed for adatom densities near the kink site.

Tables

Table I. Rescaled island decay rates $\frac{K_{\mathrm{rBCF}}(L_{\mathrm{sep}})}{K_{\mathrm{1D}}(L_{\mathrm{sep}})}$ and $\frac{K_{\mathrm{rBCF}}(L_{\mathrm{sep}})}{K_{\mathrm{rBCF}}(L^{\parallel}_{\mathrm{narrow}})}$ versus $L_{\mathrm{sep}} \equiv lL^{\parallel}_{\mathrm{narrow}}$ for the configuration in **Fig. 5** from FEMLAB analyses. Choice of parameters: $\varepsilon = 0.00445$ at 190 K for Ag/Ag(110), $R_{\mathrm{narrow}} = 3$, $m = 5/2$, $s = 3/2$, and various k and l. For $k = 3/2$, the wider island corresponds to a vertical strip. The complete adatom density field for $k = 5/3$ and $l = 3/2$ is shown in the bottom portion of **Fig. 5.**

$l \equiv \frac{L_{\mathrm{sep}}}{L^{\parallel}_{\mathrm{narrow}}}$		$l = 1$	$l = 2/3$	$l = 1/2$	$l = 1/4$	$l = 1/8$	$l = 1/16$
$k = 3/2$	$\frac{K_{\mathrm{rBCF}}(L_{\mathrm{sep}})}{K_{\mathrm{1D}}(L_{\mathrm{sep}})}$	1.121	1.153	1.195	1.271	1.310	1.330

	$\frac{K_{\mathrm{rBCF}}(L_{\mathrm{sep}})}{K_{\mathrm{rBCF}}(L^{\parallel}_{\mathrm{narrow}})}$	1	0.686	0.533	0.284	0.146	0.074
$k = 5/2$	$\frac{K_{\mathrm{rBCF}}(L_{\mathrm{sep}})}{K_{\mathrm{1D}}(L_{\mathrm{sep}})}$	1.051	1.162	1.222	1.358	1.594	1.781
	$\frac{K_{\mathrm{rBCF}}(L_{\mathrm{sep}})}{K_{\mathrm{rBCF}}(L^{\parallel}_{\mathrm{narrow}})}$	1	0.737	0.581	0.323	0.190	0.106
$k = 4$	$\frac{K_{\mathrm{rBCF}}(L_{\mathrm{sep}})}{K_{\mathrm{1D}}(L_{\mathrm{sep}})}$	1.076	1.103	1.208	1.376	1.670	2.098
	$\frac{K_{\mathrm{rBCF}}(L_{\mathrm{sep}})}{K_{\mathrm{rBCF}}(L^{\parallel}_{\mathrm{narrow}})}$	1	0.684	0.561	0.319	0.194	0.122

Table II. Rescaled island decay rate $\frac{K_{\mathrm{rBCF}}(L_{\mathrm{sep}})}{K_{\mathrm{rBCF}}(L^{\parallel}_{\mathrm{narrow}})}$ versus $L_{\mathrm{sep}} \equiv lL^{\parallel}_{\mathrm{narrow}}$ for different diffusional anisotropies ε for the configuration in **Fig. 5** from FEMLAB analyses.

$l \equiv \frac{L_{\mathrm{sep}}}{L^{\parallel}_{\mathrm{narrow}}}$	$l = 1$	$l = 2/3$	$l = 1/2$	$l = 1/4$	$l = 1/8$	$l = 1/16$
$\varepsilon = 0.00445$	1	0.737	0.581	0.323	0.190	0.106
$\varepsilon = 0.0102$	1	0.725	0.578	0.328	0.189	0.102
$\varepsilon = 1$	1	0.671	0.537	0.277	0.142	0.071

Table III. Dependence of rescaled rBCF island decay rates $K_{\mathrm{rBCF}}/K^{*}_{\mathrm{rBCF}}$ on the degree of diffusional anisotropy ε from FEMLAB analyses for the configurations of aligned islands in **Fig. 5**, and marginally and completely misaligned islands in **Fig. 6**. Here K^{*}_{rBCF} is the decay rate for aligned islands when $\varepsilon = 1$ with fixed other parameters as in **Fig.6**.

$\varepsilon \equiv D^{\perp}/D^{\parallel}$	$\varepsilon = 1$	$\varepsilon = 0.1$	$\varepsilon = 0.01$	$\varepsilon = 0.00445$	$\varepsilon = 0.001$	$\varepsilon = 0.0001$
Aligned	1	0.882	0.677	0.622	0.557	0.519
Marginally misaligned	1.037	0.869	0.471	0.326	0.142	0.0275
Completely misaligned	1.174	0.871	0.342	0.199	0.054	0.0050

CHAPTER 8

LANGEVIN AND FOKKER-PLANK ANALYSIS OF INHIBITED MOLECULAR PASSING PROCESSES CONTROLLING REACTIVITY IN NANOPOROUS CATALYTIC MATERIALS

A paper to be submitted *Physical Review Letter*

Chi-Jen Wang[1,3], David M. Ackerman[1,2], Igor I. Slowing[1,2], and James W. Evans[1,3,4]

Division of Chemical & Biological Sciences, Ames Laboratory – USDOE[1] and

Departments of Chemistry[2], Mathematics[3], and Physics & Astronomy[4],

Iowa State University, Ames, Iowa 50011

Abstract

The propensity for reactant and product molecules to pass each other within the pores of catalytic nanoporous materials strongly impacts reaction yield. For overdamped Langevin molecular dynamics, we describe the dependence of the passing propensity, P, on pore radius, R, including the scaling, $P \sim (R-R_c)^{\sigma}$, as $R \rightarrow R_c$ (the critical radius below which passing is sterically blocked). The exponent, σ, is generally lower than transition state type theory predictions. Precise numerical analysis of the Langevin and equivalent Fokker-Planck equations is provided for rotationally symmetric molecules. This facilitates development of a general picture for the dependence of passing propensity on molecular degrees of freedom including shape and rotational motion.

1. Introduction

It has long been recognized that in catalytically active nanoporous materials such as zeolites, the yield of conversion reactions is very low in the so-called single-file diffusion (SFD) regime [1]. SFD applies when reactant and product molecules cannot pass each other within narrow pores. In this regime, the reactant is restricted to near the pore openings, and the pore interior is exclusively populated by product which cannot be readily extruded. Increasing pore width to allow the onset of inhibited passing results in a strong increase in reactant penetration into the pore, and thus in the yield.

The delicate interplay between reaction and inhibited transport in these systems has typically been described by spatially coarse-grained models wherein the pore is divided into cells with width d~1 nm matching the mean length of reactant and product molecules [1-6]. Then, transport subject to SFD is simply described by hopping to adjacent empty sites in cells at rate h_α for species α. This corresponds to a low-concentration diffusion coefficient of $D_\alpha = d^2 h_\alpha$. Passing can be incorporated by allowing exchange of species α and β in adjacent cells with rate $h_{\alpha,\beta} p_{ex}$, where $h_{\alpha,\beta}$ is a suitable average of h_α and h_β, and the $p_{ex}>0$ reflects the passing propensity. Adsorption-desorption at pore openings, as well as reaction, must also be specified. Then, model behavior can be analyzed precisely via Kinetic Monte Carlo simulation [1-5] or via a suitable "generalized hydrodynamic theory" capturing both fluctuation effects and restricted transport [6].

However, a key requirement for application of the model to specific systems is to reliably assess the key input parameter, p_{ex}. Clearly, p_{ex} will depend strongly on the size

of the molecules relative to the pore radius, R, and will vanish at a critical pore radius, R_c, where passing is sterically blocked. Close to this threshold, roughly spherical molecules must misalign on opposite sides of the pore in order to pass. For elongated rod-like molecules, orientational alignment will also be required both with the pore axis and with each other. Detailed behavior will depend on system details although some general features may exist.

Despite the significance of passing propensity in determining catalytic yield, the only previous direct study of passing behavior is for spherical molecules utilizing a transition state theory (TST) type approximation [7]. Here, we apply overdamped Langevin molecular dynamics [8] to describe the motion of reactants and products through a solvent in the pore and to provide a basic assessment of passing processes controlled by steric effects. Numerical analysis of the appropriate Langevin equations quantifies the passing propensity, P, versus pore radius, R. However, for a more fundamental understanding, it is instructive to also consider an equivalent formulation in terms of a Fokker-Planck equation [9] (which corresponds to a high-dimensional diffusion equation). This also enables a particularly effective reformulation to explore asymptotic behavior as $R \rightarrow R_c$. Precise numerical analysis is provided for the case of rotationally symmetric molecules. Insights from this analysis provide a general picture for the dependence of passing propensity on molecular degrees of freedom including shape and rotational motion. Actual behavior differs in all cases from predictions of a transition state type theory formulation of passing.

2. Langevin Formulation and Analysis of Passing Propensity

We consider overdamped Langevin dynamics for a pair of reactant and product molecules, i = 1, 2, inside a pore which is aligned with the z-axis. We treat only steric interactions between the pair of molecules, and between the molecules and the pore (i.e., we impose a no overlap condition). The analysis is formulated for possibly non-spherical elongated molecules in 3D which exhibit rotational symmetry about a long axis. Thus, each has three translation degrees of freedom (DOF) and two angular DOF. The passing of spherical molecules within a 3D cylindrical pore is analyzed in detail. To obtain broader insight into the effect on passing propensity of the number of molecular DOF, we consider analogous 2D cases, i.e., elongated molecules with two translational DOF and one additional rotational DOF, and analyze in detail the passing of circular molecules

For an elongated molecule with mass m, it is convenient to implement incremental changes in coordinates in the body-fixed frame as follows. For translational motion, we assign drag forces $F_{\|}^{drag} = -m\zeta_{\|}\, d/dt\, x_{\|}$ and $F_{\perp,i}^{drag} = -m\zeta_{\perp}\, d/dt\, x_{\perp,i}$ for changes in position $x_{\|}$ and $x_{\perp,i}$ parallel to and orthogonal to the long axis, for translational drag coefficients $\zeta_{\|}$ and $\zeta_{\perp}$, respectively. (The two orthogonal directions in 3D are labeled by i.) Translational induced by random forces $F_{\|}$ and $F_{\perp,i}$ is implemented via [8,9]

$m\zeta_{\|}\, dx_{\|} = F_{\|}(t)\, dt$, where $\langle F_{\|}(t)\rangle = 0$ and $\langle F_{\|}(t)F_{\|}(t')\rangle = 2k_BTm\zeta_{\|}\,\delta(t-t')$, and (1a)

$m\zeta_{\perp}\, dx_{\perp,i} = F_{\perp,i}(t)\, dt$, where $\langle F_{\perp,i}(t)\rangle = 0$ and $\langle F_{\perp,i}(t)F_{\perp,j}(t')\rangle = 2k_BTm\zeta_{\perp}\,\delta_{i,j}\delta(t-t')$, (1b)

consistent with the fluctuation-dissipation relation. This prescription induces diffusive dynamics, e.g., $<dx_{\|}> = 0$ and $<(dx_{\|})^2> = 2D_{II}\ dt$, where $D_{\|} = k_BT/(m\zeta_{\|})$. We assign rotational drag torques $\tau_i^{drag} = -I_{\|}\ \zeta_{rot}\ d/dt\ \theta_i$ for rotation about the long axis with rotational drag coefficient ζ_{rot}. Here, the θ_i are most conveniently selected as polar rotations about the long axis in two orthogonal planes which include the long axis Also, $I_{\|}$ is the moment of inertia for the long axis. Re-orientation induced by random torques τ_i is implemented via [10]

$$I_{\|}\ \zeta_{rot}\ d\theta_i = \tau_i(t)\ dt \text{ where } <\tau_i(t)> = 0 \text{ and } <\tau_i(t)\ \tau_i(t)> = 2k_BTI_{\|}\ \zeta_{rot}\ \delta_{i,j}\ \delta(t-t'), \quad (2)$$

resulting in orientational diffusive dynamics with $<d\theta_i>=0$ and $<(d\theta_i)^2> = 2D_{rot}\ dt$ and $D_{rot} = k_BT/(I_{\|}\zeta_{rot})$. [This specification of orientational dynamics neglects coupling of the θ_i dynamics to spinning about the long axis.] Such spinning can produce an angular momentum in the direction of the long axis. After incremental motion, we accept the move only if it satisfies the non-overlap conditions, and the new coordinates are transformed back to a space-fixed frame which is used to track absolute and relative molecular locations. For the case of rotationally symmetric molecules, one has that $\zeta_{\|} = \zeta_{\perp}$ and there is no angular motion. In this case, one can use a space-fixed frame with z-axis along the pore to implement translational motion, and naturally replaces two coordinates z_i for the pair of molecules by $\delta z = z_1 - z_2$. The associated drag coefficient for δz-evolution is reduced by half, and the associated diffusivity is doubled.

Next, we describe the setup of our Langevin simulations to obtain passing propensities, P. Since only steric interactions are included, results for P just depend on

geometric factors. As above, we let $\delta z = z_1 - z_2$ denote the center-of-mass separation for the pair of molecules along the pore axis. We consider the initial value problem where adjacent molecules start with separation $\delta z = d$ and follow their evolution either until they separate (defined as reaching $\delta z=2d$) or pass (defined as reaching $\delta z = -d$). This specification of passing is compatible with the coarse-grained models described above. Note that in the initial configuration, there is no hindrance of rotation of one molecule by the other in the case of elongated molecules. We select all other initial translational and rotational coordinates randomly, subject to the constraint that the molecules are within the pore. From a large number N simulation trials with N_{pass} passing and N_{sep} separation outcomes (so $N = N_{pass}+N_{sep}$), we estimate $P \approx N_{pass}/N$. For this definition, the maximum value of P is $P_{max} = 1/3$ for very wide pores where molecules do not interact (reflecting the feature that δz changes by -2d for passing and only +d for separation.) One can also show that P is related to the parameter, p_{ex}, in the coarse-grained models described above by $P = p_{ex}/(2+p_{ex})$ consistent with $p_{ex}=1$ corresponding to unhindered passing.

First, we present a detailed analysis of passing for the case of rotationally symmetric molecules. For radius r and linear size is d=2r, the critical pore diameter is $R_c = 2d$. It is useful to introduce a gap size, $g = 2(R-R_c)$, anticipating that $P \sim (g/r)^{\sigma}$, as $g \to 0$. **Fig.**1 shows a typically trajectories for two spheres separating (left) and passing (right) in a cylindrical pore. The passing propensity, P, versus gap size, g, is shown in **Fig.2** for spheres in a 3D cylindrical pore (left), and circles in a 2D rectangular pore (right). **Fig.2** (top) show that P(spheres) exceeds P(circles) for all g/r above about 0.05. This is expected from a simple analysis (see below)? On the other hand, for small g, we

find from **Fig.2** (bottom), together with the FPE analysis below, that $\sigma \approx 1.7$ for spheres, and $\sigma \approx 1.4$ for circles. Thus, P(circles) dominates P(spheres), as $g \to 0$. Finally, we mention some challenges to obtaining precise P-values. Firstly, large N is required particularly for small g and small P, e.g., we choose N up to 5×10^6 for spheres. Another more subtle issue is the choice of time step dt. For large dt, molecules can artificially jump by each other, so P is overestimated. However, for suitable small dt, we find that P increases with decreasing dt towards its limiting exact value. This reflects the feature that small steps are required to negotiate narrow gaps. Thus, for gap sizes below about 0.1r, our Langevin estimates of P are imprecise even for our smallest time step.

3. Fokker-Planck Equation Analysis of Passing Propensity

Langevin dynamics can be described by the equivalent Fokker-Plank equation (FPE), which for the above problems with steric blocking just corresponds to a diffusion equation in high dimensions. It is convenient to introduce coordinates in the space-fixed frame for the molecules $\underline{Q}_i = (\underline{q}_i, z_i)$ where z_i is the center-of-mass z-coordinate, and $\underline{q}_i$ is the collection of center-of-mass lateral coordinates orthogonal to the pore axis and angular coordinates. The relevant time-dependent FPE problem considers the probability distribution $f(\underline{q}_1, \underline{q}_2, \delta z; t)$ for the probability of finding two molecules confined inside the pore aligned with a finite range of center-of-mass z-coordinate separations δz. In our analysis of passing propensity, P, adjacent molecules start with center-of-mass separation along the pore axis $\delta z = z_1 - z_2 = d$, so that

$$f(\underline{q}_1, \underline{q}_2, \delta z; t=0) = V_d^{-1} \, \delta(\delta z - d), \text{ where } V_d = \int d\underline{q}_1 d\underline{q}_2 \, d(\delta z) \, \delta(\delta z - d) , \qquad (3)$$

is a normalization constant. Since we follow evolution either until the molecules separate (reaching $\delta z=2d$) or pass (reaching $\delta z = -d$), this corresponds to imposing adsorbing Dirichlet boundary conditions (BCs) $f=0$ for $\delta z = -d$ and $+2d$. We also impose zero-flux Neumann BCs at the boundary of the physically region for other coordinates. Evolution of f is described by a FPE incorporating these BCs of the form [9]

$$\partial/\partial t\, f(\underline{q}_1,\underline{q}_2,\delta z;\, t) = L_{FPE}\, f(\underline{q}_1,\underline{q}_2,\delta z;\, t) \quad \text{with self-adjoint } L_{FPE} = \nabla\, \underline{\underline{D}}\, \nabla. \qquad (4)$$

The symmetric diffusion tensor $\underline{\underline{D}}$, has components reflecting the amplitude of the noise terms in the LE and the molecular orientation relative to the body-fixed frame. For rotationally invariant molecules, $\underline{\underline{D}}$ is diagonal with entries $D = D_{\|} = D_{\perp}$ for lateral coordinates, and $2D$ for the coordinate δz.

The above constitutes a diffusion problem in a high-dimensional constricted channel as shown schematically in **Fig.3** (center). From $f(\underline{q}_1,\underline{q}_2,\delta z;\, t)$, one accumulates over time the probability flux reaching $\delta z = -d$ and $+2d$ [see **Fig.3** (right)], and thereby determines the probability of passing $P=P_{pass}$ or separation P_{sep} as

$$P_{pass(sep)} = \pm \int_{0<t<\infty} \iint d\underline{q}_1 d\underline{q}_2\, \underline{e}_{\delta z} \cdot \underline{\underline{D}}\, \nabla\, f|_{\delta z = 2d,-d}, \text{ for unit vector } \underline{e}_{\delta z} \text{ in } \delta z\text{-direction.} \quad (5)$$

Numerical analysis of this FPE initial value problem was performed using a hypercubic mesh in $(\underline{q}_1,\underline{q}_2,\delta z)$-space. Accuracy is limited by the mesh spacing which was varied from r to r/16. We find good agreement with Langevin results for large gap sizes, but deviations (see below) for the regime of smaller sizes which is of particular interest.

To resolve the computational challenges for small gap size, we first note that there is an equivalent time-independent FPE formulation of the "passing problem" which

considers the steady-state probability, f^{ss}, with probability continually fed into the system at $\delta z = d$, i.e.,

$$0 = L_{FPE}\, f^{ss}(\underline{q}_1,\underline{q}_2, \delta z) \; + V_d^{-1}\, \delta(\delta z - d). \qquad (6)$$

Now the probability of passing $P=P_{pass}$ or separation P_{sep} are obtained from the steady-state fluxes

$$P_{pass(sep)} \; = \iint d\underline{q}_1 d\underline{q}_2\, \underline{n} \cdot \underline{\underline{D}}\, \nabla f^{ss}|_{\delta z = 2d,-d}. \qquad (7)$$

Proof of the equivalence of these formulations follows from an eigenfunction expansion of their solutions in terms of the orthonormal eigenfunctions of the self-adjoint L_{FPE}. See the Appendix.

While this steady-state problem is similar in complexity to the time-dependent problem, there is a natural simplification for very small gap size. It is clear that in this regime, f_{ss} should be roughly constant for $0 < \delta z < d$ and decrease linearly in δz for $\delta z > d$ to zero at $\delta z = 2d$. It should drop dramatically as δz decreases through $\delta z = 0$ to small values for $-d < \delta z < 0$. See **Fig.3** (left) for a schematic of this behavior. Thus, it is clear that behavior in this regime can be determined from the simpler and more conventional Dirichlet boundary value problem, $0 = L_{FPE}\, f^{ss}(\underline{q}_1,\underline{q}_2, \delta z)$ for $-d < \delta z < d$, with $f^{ss} = 0$ at $\delta z = -d$ and $f^{ss} = c$ (constant) at $\delta z = d$. Again, we impose zero flux BCs at the other boundaries. Flux at $\delta z = -d$ is determined non-trivially from this solution, and at $\delta z = +2d$ trivially given the linear profile of f^{ss} for $+d < \delta z < +2d$. Thus, analysis with standard (and precise) adaptive-grid finite-element methods and software is viable [11].

A detailed comparison of different approaches was made for two circular molecules passing in a 2D rectangular channel. **Fig.4** shows estimates of P versus g/r.

Precise results are obtained small g/r utilizing FEMLAB analysis [11] of the steady-state problem (in a phase space with two lateral positions and δz). These smoothly connect to results from the time-dependent analysis, which are accurate for large g/r above about unity. Thus, together, these approaches give an accurate global characterization of behavior. Langevin equation agree with the time-dependent FPE results for larger g/r above unity, and agree with the FEMLAB results d for smaller g/r down to below which they become inaccurate. The FEMLAB analysis provides a precise estimate of the exponent $\sigma \approx 1.4$ for circles. This supports our estimate of exponents from Langevin data in the regime of g/r from around 0.1 to 1 indicating $\sigma \approx 1.7$ for spheres.

4. TST Analysis and Effective 2-Variable FPE Analysis

A broader perspective on passing behavior comes from consideration of a TST type analysis of the free energy barrier to be surmounted during passing. In these models with just steric interactions, free energy is purely entropic, $F_{\delta z} = -kT \ln(V_{\delta z})$, where $V_{\delta z}$ is the volume of accessible $(\underline{q}_1,\underline{q}_2)$ phase space for fixed δz. Thus, the free energy barrier for passing satisfies $\delta F = k_B T \ln(V_{|\delta z|>d}/V_{\delta z^*})$, where δz^* is the transition state corresponding to minimum $V_{\delta z}$. Thus, the TST estimate for the passing probability scales like $P_{TST} \sim \exp[-\delta F/(k_B T)] \sim V_{\delta z^*}/ V_{|\delta z|>d}$. For circular molecules, trivially one has $\delta z^*=0$ and $P_{TST} \sim V_0 \sim (g/r)^2$, as $g \to 0$ (i.e., $\sigma_{TST} =2$) since both molecules are confined to a distance of order g/r from the pore wall. For spherical molecules in a cylindrical pore, orienting the configuration at $\delta z^*=0$ so that molecule 1 is on the vertical axis through the pore center, it is clear that both molecules are confined to a distance of order g/r from the

wall, and the center of molecule 2 is confined to an angle or order $(g/r)^{1/2}$ from the vertical axis. Thus, one has that $P_{TST} \sim V_0 \sim (g/r)^{2.5}$ as $g \to 0$ (i.e., $\sigma_{TST} = 2.5$). See **Fig.5**. Thus, in both cases, σ_{TST} exceeds the actual value of σ, a feature which we claim is general.

To elucidate the deviation of exact behavior from TST predictions, it is instructive to consider an effective reduced-dimensional FPE analysis of the passing process. It is natural to consider replacing all the variables ($\underline{q}_1,\underline{q}_2$) by a single effective variable q_{eff}, and then considering 2-variable FPE problem in $(q_{eff},\delta z)$-space with an effective pore of width $V_{\delta z}$ at position δz. See **Fig.6.** Detailed analysis of the passing propensity, P_{eff}, for the effective 2-variable Dirichlet problem appropriate for the regime of small gap size (using FEMLAB) reveals that $P_{eff} \sim (V_{\delta z^*})^{\nu}$ as $V_{\delta z} \to 0$, where ν is not necessarily unity as in TST. In fact, ν can vary from values as low as ~0.15 to unity. See **Fig.6.** The key point is that the solution of the FPE problem and the behavior of the passing propensity depends not just on the size at the smallest constriction in the effective pore, but on the entire shape of the constriction. This should be anticipated since the exact solution of the effective 2-variable Dirichlet problem can be obtain by applying a conformal mapping to transform the constricted pore into a rectangular pore (a transformation which requires increasing dilation in the δz direction as the gap vanishes). The conformal mapping depends on the entire shape.

Future work will explore in detail whether analysis of an effective 2-variable FPE can give a reasonable estimate of exact passing behavior, i.e., of the solution of the high-dimensional FPE). For the case of two circle in a rectangular channel where $V_{\delta z^*}$

$=V_0 \sim (g/r)^2$, a value of $\nu \approx 0.7$ would exactly recover the true scaling for small gap size (but the above comments and preliminary analysis suggest that ν will be just above 0.5 for this system).

5. Extension to General Molecular Shapes

The TST formulation naturally extends to general molecular shapes. For example, for an elliptical and circular molecule in a 2D rectangular channel, there is an additional angular DOF for the ellipse which is restricted to a range of order g for small gaps at the transition state $\delta z^*=0$ (see **Fig.5**). Thus, one has that $P_{TST} \sim g^3$. Similarly, for an ellipsoidal and spherical molecule in a 3D cylindrical channel, there are two additional angular DOF for the ellipsoid each of which is restricted to a range of order g for small gaps at the transition state $\delta z^*=0$. Thus, one has that $P_{TST} \sim g^{4.5}$. For a pair of elliptical or ellipsoidal molecules, additional rotational degrees of freedom will further increase the exponents in the above scaling relations. Based on the above analysis for rotationally symmetric molecules we expect that the actual exponents, σ, for these cases are smaller than the TST predictions.

It should also be emphasized that the passing propensity, and in particular its scaling as $g \rightarrow 0$, depends on molecular shape. The above results for elongated molecules are specific to their convex shape. For contrast, consider the case of a circular and dumbbell shaped molecule (composed of two joined spheres) in a 2D rectangular pore. It is clear that the transition state no longer occurs at $\delta z=0$, but rather there are two transition states corresponding to when one of the spheres in the dimer aligns with the

spherical molecule. See **Fig.5.** In each of these, dumbbell orientation is not increasingly restricted as $g \to 0$, and as a result the scaling corresponds to that for a pair of circular molecules ($P_{TST} \sim g^2$ and the exact $P \sim g^{1.4}$). The actual value of P for substantial g should be significantly reduced from the latter case, and the onset of the scaling regime should be modified. Analogous comments apply for a spherical and dumbbell molecule in a 3D cylindrical pore where $P_{TST} \sim g^{2.5}$ and the exact $P \sim g^{1.7}$.

6. Conclusions

We have successfully provided a general picture for the behavior of molecular passing processes in narrow pores. The passing propensity is not described by a simple transition state theory, but rather depends on more global features of the confined geometry during the passing process. Behavior also depends strongly on molecular shape.

Appendix: Equivalence of Time-Dependent and Time-Independent FPE Approaches

We consider solutions of FPE-type problems for the probability of finding two molecules with coordinates $\underline{Q}_i = (\underline{q}_i, z_i)$ for i=1,2 confined inside the pore aligned with a finite range of center-of-mass z-coordinate separations δz between –d and +2d. We impose adsorbing Dirichlet boundary conditions (BCs) for δz = -d and +2d, and zero-flux Neumann BCs at the boundary of the physically region for other coordinates. Then,

for these BC's, the associated eigenvalue problem for the self-adjoint FPE operator, $L_{FPE} = \nabla \underline{\underline{D}} \nabla$, with symmetric diffusion tensor $\underline{\underline{D}}$, has the form

$$L_{FPE}\, u_n(\underline{q}_1,\underline{q}_2, \delta z) = -\lambda_n\, u_n(\underline{q}_1,\underline{q}_2, \delta z) \quad \text{where} \iiint d\underline{q}_1 d\underline{q}_2\, d(\delta z)\, u_n^* u_m = \delta_{n,m}.$$

An eigenfunction expansion of the solution for the <u>time-dependent initial value problem</u> for the FPE described in the text yields

$$f(\underline{q}_1,\underline{q}_2, \delta z; t) = \sum_n c_n \exp(-\lambda_n t)\, u_n(\underline{q}_1,\underline{q}_2, \delta z) \quad \text{with } c_n = V_d^{-1} \iint d\underline{q}_1 d\underline{q}_2\, u_n^*(\underline{q}_1,\underline{q}_2, \delta z = d),$$

the coefficients c_n being selected to recover the initial conditions. An eigenfunction expansion of the solution for the <u>time-independent formulation</u> of the "passing problem" yields

$$f^{ss}(\underline{q}_1,\underline{q}_2, \delta z) = \sum_n b_n\, u_n(\underline{q}_1,\underline{q}_2, \delta z) \quad \text{with } b_n = V_d^{-1} \iint d\underline{q}_1 d\underline{q}_2\, u_n^*(\underline{q}_1,\underline{q}_2, \delta z = d)/\lambda_n.$$

Determination of the probabilities for separation and passing from either of these problems yields the same result

$$P_{pass(sep)} = \sum_n V_d^{-1} \iint d\underline{q}_1' d\underline{q}_2'\, u_n^*(\underline{q}_1',\underline{q}_2', \delta z = d) \iint d\underline{q}_1 d\underline{q}_2\, \underline{n} \cdot \underline{\underline{D}} \nabla\, u_n(\underline{q}_1,\underline{q}_2, \delta z = 2d, -d)/\lambda_n.$$

References

[1] C. Rodenbeck, J. Karger, and K. Hahn, J. Catal. 157, 656 (1995).

[2] J.G. Tsikoyiannis and J.E. Wei, Chem. Eng. Sci 46, 233 (1991).

[3] M.S. Okino, R.Q. Snurr, H.H. Kung, J.E. Ochs, and M.L. Mavrovouniotis, J. Chem. Phys. 111, 2210 (1999).

[4] S.V. Nedea, A.P.J. Jansen, J.J. Lukkien, and P.A.J. Hilbers, Phys. Rev. E 65, 066701 (2002)

[5] D.M. Ackerman, J. Wang, J.H. Wendel, D.-J. Liu, M. Pruski, and J.W. Evans, J. Chem. Phys. 134, 114107 (2011).

[6] D.M. Ackerman, J. Wang, and J.W. Evans, Phys. Rev. Lett., 108, 228301 (2012).

[7] D.S. Sholl, Chem. Eng. J. 74, 25 (1999).

[8] W.T. Coffery, Yu. P. Kalmykov, and J.T. Waldron, "The Langevin Equation" (World Scientific, Singapore, 2004).

[9] C.W. Gardiner, "Hanndbook of Stochastic Methods" (Springer, Berlin, 2002).

[10] I. Snook, "The Langevin and Generalized Langevin Equation Approach to the Dynamics of Atomic, Polymeric, and Colliodal Systems", (Elsevier, Amsterdam, 2007).

[11] COMSOL Multiphysics ® (formerly FEMLAB ®) is a finite element analysis, solver, and simulation software developed by Comsol Inc. (www.comsol.com).

Figures

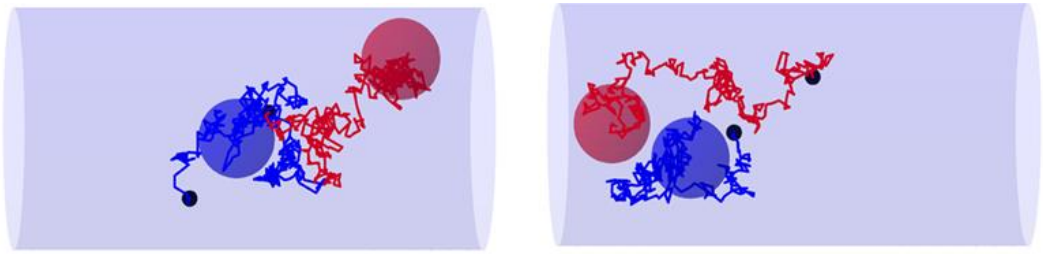

Fig.1. Simulated trajectories for separating spheres (left) and passing spheres (right) in a cylindrical pore for gap size g = 2r where P ≈ 0.20.

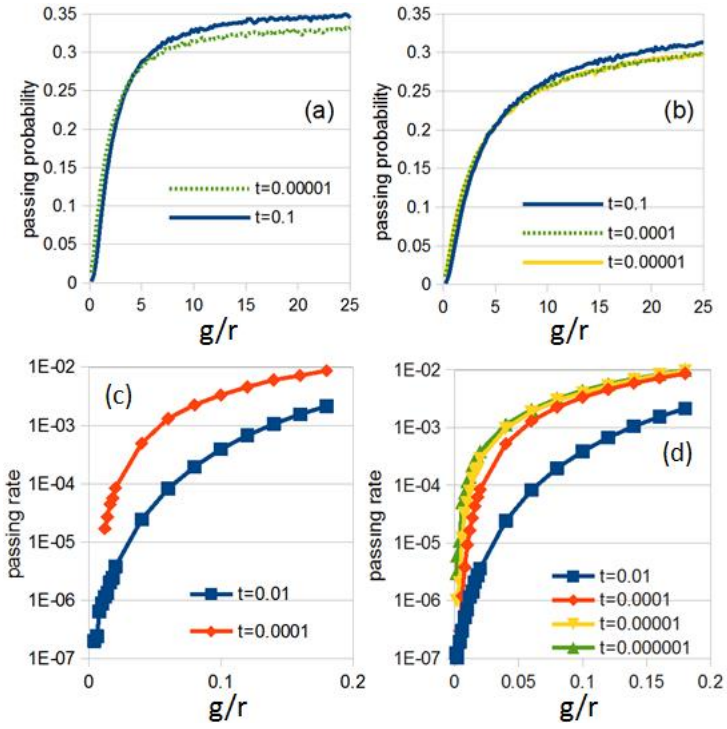

Fig.2. Passing probability, P, versus scaled gap size, g/r, for spheres in a 3D cylindrical pore (left: a, c) and circles in a 2D rectangular pore (right: b, d). Results for various numerical time steps, dt, are also shown. Note the convergence $P \to 1/3$, as $g \to \infty$.

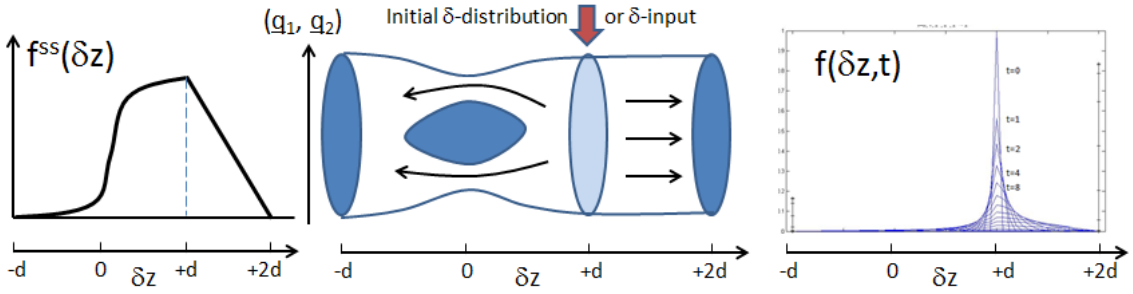

Fig.3. Schematics for FPE analysis of passing. Center: the region of $(\underline{q}_1,\underline{q}_2,\delta z)$-phase space for the FPE problem with adsorbing BCs (f=0) on the left and right ends (δz = -d, +2d), and zero flux BCs on the sides; note that the region generally has missing inclusions reflecting the feature than molecules center-of-mass cannot get close. Right: reduced time-dependent probability distributions $f(\delta z,t) = \iint d\underline{q}_1 d\underline{q}_2\ f(\underline{q}_1,\underline{q}_2,\delta z;\ t)$. Left: reduced steady-state probability distribution $f^{ss}(\delta z) = \iint d\underline{q}_1 d\underline{q}_2\ f^{ss}(\underline{q}_1,\underline{q}_2,\delta z)$.

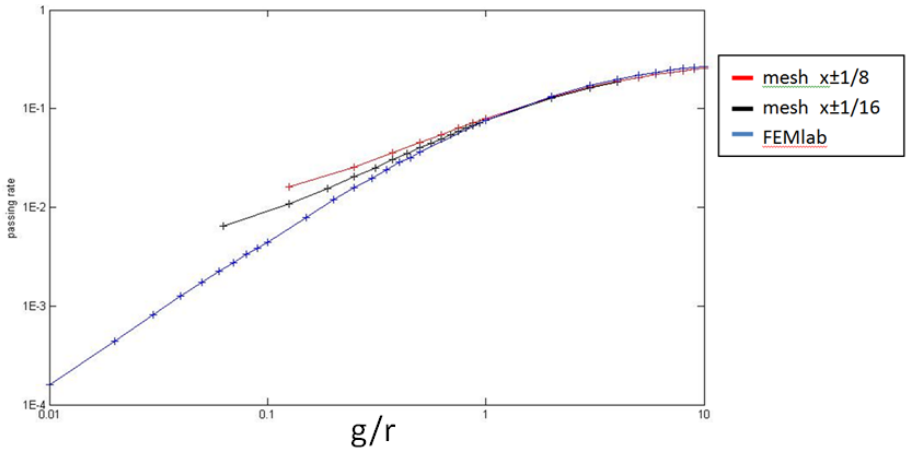

Fig.4. Comparison of results for the passing probability for two circular molecules in a rectangular channel from solution of time-dependent and time-independent FPE problems.

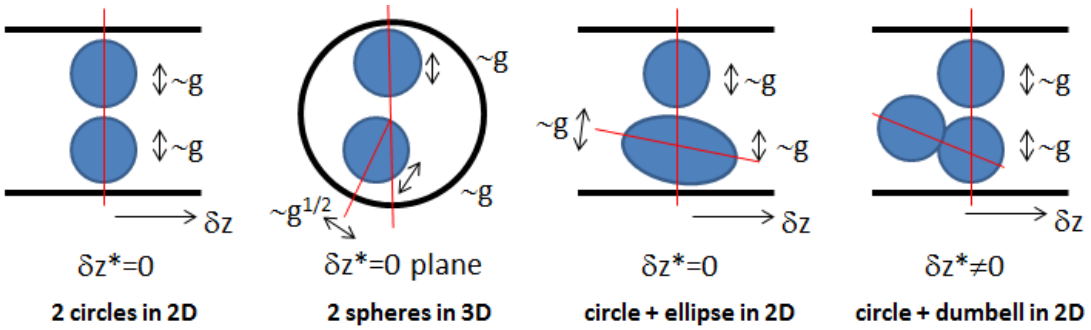

Fig.5. Restricted dynamics at the transition state for passing. Range of allowed translational and rotational motion in indicated in terms of the (small) gap size.

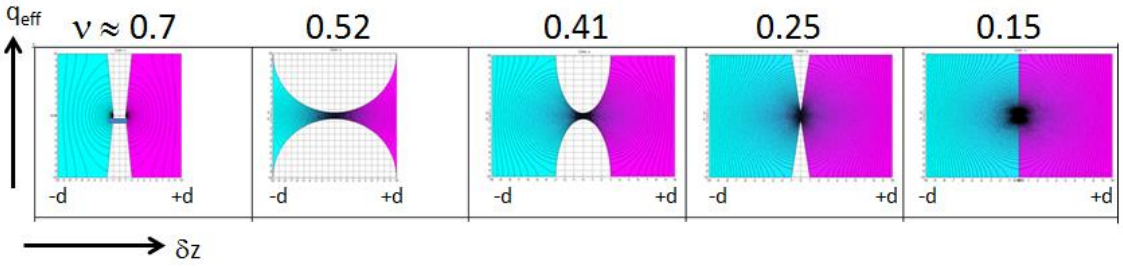

Fig.6. Solution of the effective 2-variable Dirichlet problem for a reduced dimensional pore of width $V_{\delta z}$ at position δz. Values for the effective exponent, ν, are shown, where $P_{eff} \sim (V_{\delta z})^{\nu}$, and $V_{\delta z} \to 0$.

CHAPTER 9

GENERAL CONCLUSION

The first part of this thesis focuses on analysis of a non-equilibrium stochastic model for reactions, specifically a realization of Schloegl's second model for autocatalysis (or quadratic contact process) on lattices. The Durret's model and other similar models exhibit some features with the equilibrium Hamiltonian systems, but there are still some differences. The most significant feature is the generic two-phase coexistence for a finite range of control parameter. This contrasts the behavior in the equilibrium systems which two-phases coexist only at a single parameter value. We present a detailed analysis of this novel phenomenon for the Schloegl's second model and its generalizations. Another extended topic is the analysis of nucleation phenomena in these non-equilibrium systems where the standard tools and concepts of thermodynamics are not available to facilitate understanding. The behavior of the rich droplet dynamics has been successfully predicted and described.

The second component of this thesis has focused on the spatially continuous diffusion equations or Fokker-Planck equations for transport problems on surfaces and in nanopores. One of the transport problems is a coarsening and decay problem in strongly anisotropic systems. Our rBCF modeling obtains good agreement with the results for the island decay rate obtained from extensive KMC simulations. A modified treatment can account for edge diffusion kinetics and allow the kinks on the $\langle \bar{1}10 \rangle$ island edges which are absent in the rBCF theory. Our analysis successfully describes and elucidates

experimental scanning tunneling microscopy (STM) observations for the Ag/Ag(110) system. Another class of transport problems involves diffusion and passing of pairs of overdamped Langevin molecules in narrow nanopores. The passing propensity is not described by a simple transition state theory, but rather depends on more global features of the confined geometry during the passing process. Precise numerical analysis of the Langevin and equivalent Fokker-Planck equations are given for rotationally symmetric molecules. We have successfully provided a general picture for the dependence of passing propensity on molecular degrees of freedom including shape and rotational motion.

To summarize the discoveries and developments presented in this thesis, we provide the following list of the main highlights:

(A) Discontinuous phase-transitions in non-equilibrium systems

1. Discovery utilizing kinetic Monte Carlo simulation of generic two-phase coexistence (2PC) in a stochastic realization of Schloegl's second model for autocatalysis (or quadratic contact process) on cubic or hypercubic lattices.

2. Development of exact master equations and approximate hierarchical truncations to provide an effective treatment of the above models.

3. Analysis of the generic 2PC regions and propagation failure regions of the above models on hypercubic lattices.

4. Comparison between the above models from the Durrett model to threshold model or models with particle diffusion.

5. Detailed analysis of metastability associated with the discontinuous phase transition in the above models at the level of the site-approximation.

6. Discovery of droplet dynamics exhibiting a classical family of critical solutions for vacuum droplets and nonclassical family for active droplets.

(B) Inhibited passing of overdamped Langevin particles in narrow pores and Coarsening and decay

1. Development of an instructive modeling tool to capture the basic features of island decay in strongly anisotropic systems.

2. Successful description and elucidation of experimental scanning tunneling microscopy (STM) observations.

3. Agreement with precise results for the island decay rate obtained from extensive KMC simulations modeling and rBCF treatment.

4. Interpretation of molecular shape-dependence passing behavior in narrow pores.

5. Successful agreement with the numerical results from Langevin and equivalent Fokker-Planck equations.